Active and Passive Multi-Functional Filtering Circuits Based on Collaborative Techniques

A Dissertation Submitted for the Degree of Doctor of Philosophy

Candidate：Jin-Xu Xu

Supervisor：Dr. Yang Yang

Co-supervisor: Prof. Eryk Dutkiewicz

Faculty of Engineering and Information Technology (FEIT),

University of Technology Sydney,

Ultimo, NSW 2007, Australia.

August, 2020

CERTIFICATE OF ORIGINAL AUTHORSHIP

I, Jin-Xu Xu declare that this thesis, is submitted in fulfilment of the requirements for the award of Doctoral Degree, in the School of Electrical and Data Engineering, Faculty of Engineering and Information Technology at the University of Technology Sydney.

This thesis is wholly my own work unless otherwise reference or acknowledged. In addition, I certify that all information sources and literature used are indicated in the thesis.

This document has not been submitted for qualifications at any other academic institution. I certify that the work in this thesis has not previously been submitted for a degree nor has it been submitted as part of the requirements for a degree at any other academic institution except as fully acknowledged within the text. This thesis is the result of a Collaborative Doctoral Research Degree program with South China University of Technology.

This research is supported by the Australian Government Research Training Program.

Production Note:
Signature: Signature removed prior to publication.

Date: 2020-08-25

Related Published Works in This Thesis

Since I am in a Collaborative Doctoral Research Degree program with South China University of Technology (SCUT), this thesis includes both the works during my PhD period in UTS and SCUT. The results presented in this thesis discuss both the published works during my PhD candidature in UTS and SCUT, which are detailed as follows.

[1]. J.-X. Xu, H.-Y. Li, X. Y. Zhang, Y. Yang, Q. Xue and E. Dutkiewicz, "Compact dual-channel balanced filter and balun filter based on quad-mode dielectric resonator," *IEEE Trans. Microw. Theory Tech.,* vol. 65, no. 11, pp. 4636-4644, Feb. 2019.

[2]. J.-X. Xu, X. Y. Zhang, H.-Y. Li, Y. Yang, E. Dutkiewicz and Q. Xue, "Ultra-compact multi-channel bandpass filter based on tri-mode dielectric resonator for 5G massive MIMO antenna system," *IEEE Trans. Microw. Theory Tech.,* vol. 68, no. 5, pp. 1668-1677, May 2020.

[3]. J.-X. Xu, X. Y. Zhang, H.-Y. Li, and Y. Yang, "Narrow-band single-pole double throw filtering switch based on dielectric resonator," *IEEE Microw. Wireless Compon. Lett.*, vol. 28, no. 7, pp. 594-596, Jul. 2018.

[4]. J.-X. Xu, L. Yang, Y. Yang, and X. Y. Zhang, "High-Q-factor tunable bandpass filter with constant absolute bandwidth and wide tuning range based on coaxial resonators," *IEEE Trans. Microw. Theory Tech.,* vol. 67, no. 10, pp. 4186-4195, Oct. 2019.

[5]. J.-X. Xu, X. Y. Zhang and Y. Yang, "High-Q-Factor Dual-Band Bandpass Filter and Filtering Switch Using Stub-Loaded Coaxial Resonators," *2019 IEEE MTT-S International Wireless Symposium (IWS)*, Guangzhou, China, 2019, pp. 1-3.

[6]. J.-X. Xu and X. Y. Zhang, "Single- and dual-band LTCC filtering witch with high isolation based on coupling control," *IEEE Trans. Ind. Electron.* vol. 64, no. 4, pp. 3137-3146, Apr. 2017.

[7]. X. Y. Zhang, J.-X. Xu and J. X. Chen, "High-power filtering witch with

low loss and high isolation based on dielectric resonator," *IEEE Trans. Microw. Theory Tech.,* vol. 65, no. 6, pp. 2101-2110, Jun. 2017.

[8]. J.-X. Xu, X. Y. Zhang and X. Q. Song, "High-efficiency filter-integrated class-F power amplifier based on dielectric resonator," *IEEE Microw. Wireless Compon. Lett.*, vol. 27, no. 9, pp. 827-829, Sep. 2017.

[9]. J.-X. Xu, X. Y. Zhang and X. L. Zhao, "Compact LTCC balun with bandpass response based on Marchand balun," *IEEE Microw. Wireless Compon. Lett.*, vol. 26, no. 7, pp. 493-495, Jul. 2016.

[10]. J.-X. Xu and X. Y. Zhang, "Compact high-isolation LTCC diplexer using common stub-loaded resonator with controllable frequencies and bandwidths," *IEEE Trans. Microw. Theory Tech.,* vol. 67, no. 2, pp. 494-504, Nov. 2017.

[11]. J.-X. Xu, X. Y. Zhang and H.-Y. Li, "Compact narrow-band filtering rat-race coupler using quad-mode dielectric resonator," *IEEE Trans. Microw. Theory Tech.,* vol. 66, no. 9, pp. 4029-4039, Sep. 2018.

[12]. J.-X. Xu and X. Y. Zhang, "Dual-channel dielectric resonator filter and its application to Doherty power amplifier for 5G massive MIMO system," *IEEE Trans. Microw. Theory Tech.,* vol. 66, no. 7, pp. 3297-3305, Jul. 2018.

Abstract

In radio frequency front ends, there are lots of active and passive circuits, such as filters, power amplifiers (PAs), switches, couplers and so on. Generally, they are cascaded in wireless systems, which suffer from the large size, high loss, or efficiency degradation due to impedance mismatching. To solve these problems, novel methods for collaborative designs of multiple circuits are proposed, and overall performance is improved by the complementation of different circuits. Design methods for fusion of multiple circuits are also proposed by constructing one circuit function into another circuit, which can simplify the structures to reduce the size and loss. Lots of active and passive multi-functional filtering circuits are proposed, including the following three sections:

1. To improve overall efficiency of the PA, switch, and filter, integration of filters and active circuits are conducted. To reduce the total loss and improve isolation of the switch and filter, coupling control method is proposed to fuse the functions of filter and switch. To avoid efficiency degradation by impedance mismatching, the collaborative design of a class-F PA and a high-selectivity filter is presented.

2. To reduce the loss and size, filters are integrated with other passive circuits. The functions of a balun circuit and a rat-race coupler are fused to a filter to realize the miniaturized filtering balun and filtering rat-race coupler, respectively. By using a common dual-mode resonator, a compact LTCC diplexer with controllable frequencies and bandwidths is designed.

3. For high integration, dual-/multi-channel filtering circuits are proposed. Based on a quad-mode dielectric resonator, two filters are integrated as one dual-channel filter, and then collaborative-designed with a two-input two-output Doherty PA for high integration and high efficiency. For further integration, multi-channel filters and dual-channel balanced/balun filters are also proposed.

In this thesis, design methods and working mechanisms of proposed multi-functional filtering circuits are detailed. Measured results are given to show the validity of the proposed designs. As compared to reported designs or products from

some international companies, the proposed designs show advantages of miniaturization or low power consumption, which are useful in wireless applications.

Keywords: Active multi-functional filtering circuit, filtering switch, filtering power amplifier, passive multi-functional filtering circuit, multi-channel filtering circuit, collaborative-design

Acknowledgement

I am very thankful to Dr. Yang Yang and Prof. Eryk Dutkiewicz who are my supervisors during the Collaborative Doctoral Research Degree Program in University of Technology, Sydney (UTS). They provide me with a good learning platform, enrich my research experience and also improve my PhD thesis. Especially for Dr. Yang Yang who also helps me a lot in my daily life.

I would like to express my sincere gratitude to my supervisor Prof. Xiu Yin Zhang in South China University of Technology (SCUT). Prof. Zhang is a knowledgeable and experienced supervisor. Under his supervision and support, I have a good accumulation of professional research knowledge and have obtained a great improvement in practical ability, and also have successfully completed my research subject and published several international-referred journal papers. Moreover, I would like to thank Prof. Zhang for recommending me to study in UTS. He definitely makes a crucial role in my research achievements and will also make a significant influence on my future life.

I am grateful to Prof. Quan Xue for offering me the opportunity of internship before my doctoral admission so that I can accumulate the scientific research background and experience, which is of great help for my PhD study.

I give my sincere acknowledgement to all teachers who helped me a lot during my PhD study, including Prof. Xiaolan Zhao, Prof. Binjie Hu, Prof. Yongmei Pan, Prof. Huifen Huang, Dr. Yang Jun, Dr. Honglin Zhang and so on. Their joint efforts have created a good academic atmosphere for the lab. Particularly, I thank Prof. Xiaolan Zhao for her care and help in my scientific research and daily life.

I would like to thank all the students who studied with me together in UTS, for making me feel in a comfortable and harmonious scientific research environment abroad. I also would like to express my thanks to all my colleagues in SCUT. I have benefited a lot from learning and discussing with them.

In addition, I would like to express my special thanks to my family as well as my

girlfriend, Ms. Huiyang Li, for their care, encouragement, and support all the time.

Finally, I would like to thank the experts and teachers who provided their suggestions on my thesis revision, which will definitely improve the quality of my thesis and make me have a deeper understanding of my thesis work.

Jinxu Xu

Aug. 2020

Contents

List of Figures

List of Tables

Chapter 1 Introduction

1.1 Research Background and Significance

With the rapid development of wireless communications, a variety of wireless services and wireless products have also developed rapidly. Nowadays, wireless systems integrate a lot of wireless technologies and the functions of the system become more and more complex. Thus, more radio frequency (RF) circuits and components are integrated into one wireless system. Especially, in 5G or future wireless systems, the number of transceivers in a wireless system will be greatly increased as compared to 4G wireless systems. For example, in a 5G massive multiple-input multiple-output (MIMO) antenna system, the number of transceivers can be larger than one hundred, which put forward strict requirements for a wireless system to have a high degree of integration. Moreover, such a large number of transceivers also make wireless systems bulky in size, which leads to increasing difficulty in site selection and engineering construction of base stations, as well as increasing cost. Thus, it is of great importance to miniaturize the size of wireless systems. On the other hand, the power consumption in future wireless communications is expected to be greatly reduced, so that the system should have low power consumption. In summary, with the development of wireless technologies, miniaturization, low power consumption and high integration of wireless systems have an important significance.

Microwave circuits are essential in wireless systems. As shown in Figure 1.1, there are lots of microwave circuits in a time division duplexer (TDD) wireless system, such as the power amplifier, switch, bandpass filter, balun and so on. As the wireless system is evolving with a tendency of high integration, miniaturization, and low power consumption, the microwave circuits are required to have a compact size, low loss, and high efficiency.

Over the last few decades, a lot of research on the miniaturized or high-efficiency

single-functional microwave circuits has been conducted and significant progress has been made. For active circuits, their performance and circuit size are mainly limited by the fabrication process of semiconductor materials. For example, although various methods have been proposed to design the GaN power amplifier, the power added efficiency is limited by the GaN transistor process and maintained at about 80% for many years. For passive circuits, the insertion loss is determined by the circuit quality (Q) factor and the size is related to the wavelength at their operating frequencies. Since a smaller size generally leads to a lower Q factor, it is very difficult to further reduce the size and loss simultaneously.

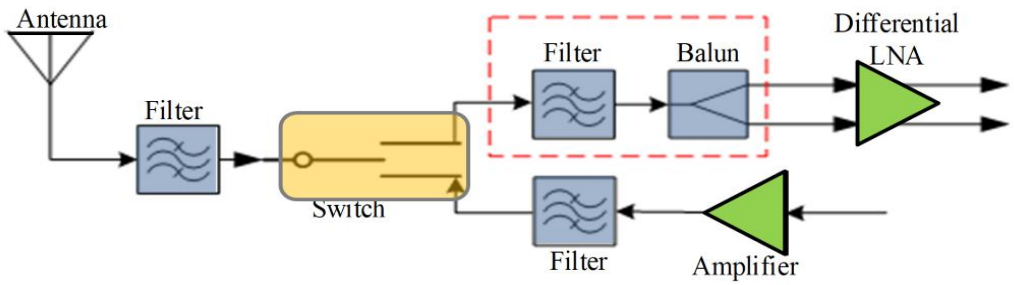

Figure 1.1. Schematic of a TDD wireless system.

In order to make a further breakthrough in respect to the miniaturization, low loss and high efficiency of microwave circuits to meet the requirements of rapid-developed wireless technologies, research on multi-functional filtering circuits is carried out in this thesis. The collaborative-design methods of multiple circuits are proposed, which can improve the overall circuit performance through the complementary use of multiple circuits. Design methods for constructing one circuit function into another circuit are also proposed to enable the fusion of multiple circuit functions, which can simplify the circuit structures as well as reduce the size and loss. A variety of active, passive and dual-/multi-channel filtering circuits are designed and implemented in this thesis. The proposed multi-functional circuits will contribute to the miniaturization of wireless devices, which can also be used to reduce power consumption and thus extend the standby time of wireless

devices. Thus, the proposed multi-functional circuits will have important significance and application values to help achieve green wireless communications.

1.2 Introduction of Multi-Functional Filtering Circuits

The bandpass filter plays an important role in wireless systems [1]-[6], which is one of the most important circuits to realize high-quality wireless communications, such as the microwave filters, LTCC filters, dielectric resonator filters presented in Figures 1.2 and 1.3. In order to realize miniaturization and low power consumption of a wireless system, a lot of research on co-designs and multifunctional fusion of filter and other circuits has been reported in recent years, which can be mainly divided into two categories: active multi-functional filtering circuits and passive multi-functional filtering circuits. In the following two parts, the research of these two kinds of multi-functional filtering circuits will be reviewed. Then, existing problems of the reported multi-functional filtering circuits will be summarized, and the research of this thesis is focused on solving the existing problems.

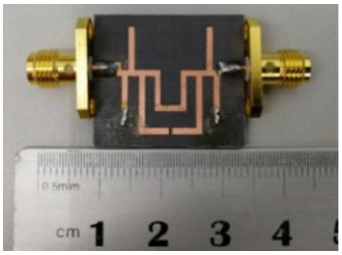

(a)

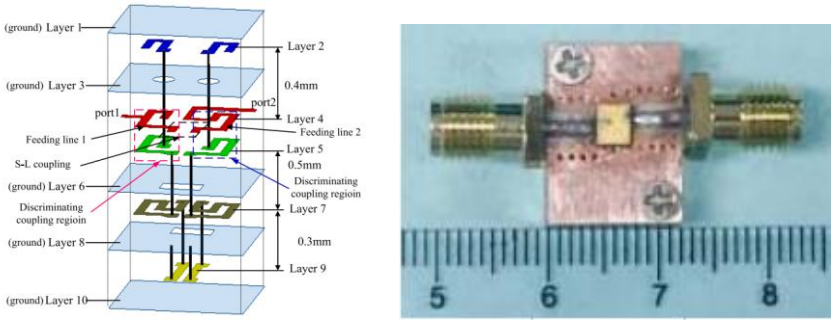

(b)

Figure 1.2. (a) Photograph of a microwave filter in [2]; (b) 3-D structure and photograph of a LTCC filter in [3].

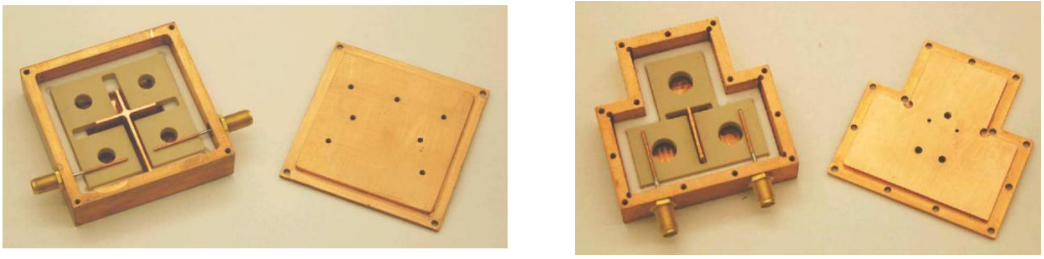

Figure 1.3. Photographs of dielectric resonator filters in [5].

1.2.1 Active Multi-Functional Filtering Circuits

In RF transmitters, the power amplifier [7]-[9] is one of the main active circuits and it is generally cascaded with the switch [10], [11] and bandpass filter [12]-[14]. The efficiency of an RF transmitter is influenced by the efficiency of the power amplifier and the total loss of the switch and filter. In order to improve the overall efficiency, two typical active multi-functional filtering circuits, including the filtering switch and filtering power amplifier, are proposed.

As for the integration of the filter and the switch, PIN diodes or transistors are often embedded into the filter structures to realize the function fusion of these two circuits. One of the methods is to design the switchable structures using PIN diodes or transistors, and then use them in the filter designs [15]-[17]. For example, in [15], transmission lines with PIN diodes are used to enable the switching of the filter between wideband and narrowband applications, whereas the insertion loss in this design is high. By designing a switchable delay line using PIN diodes, a filtering switch with Chebyshev and quasi-elliptic responses is realized in [16], as shown in Figure 1.4. In [17], a switchable connected line using PIN diodes is utilized as an admittance inverter (*J* inverter) in a bandpass filter to design a filtering switch. Figure 1.5 shows the circuit structure as well as simulated and measured results. As can be seen, high OFF-state isolation of 48 dB is achieved. Nevertheless, in the ON-state, the insertion loss of 1.8 dB is high. It is because the signals pass through the PIN diodes and introduce additional loss. As compared to the classic cascaded filter and switch, it seems the advantage of the filtering switch in [17] is not obvious in terms of insertion losses.

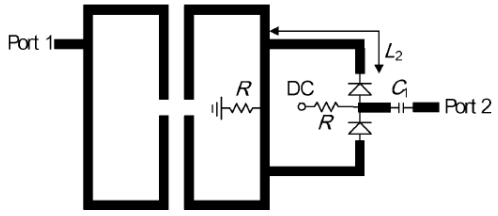

(a)

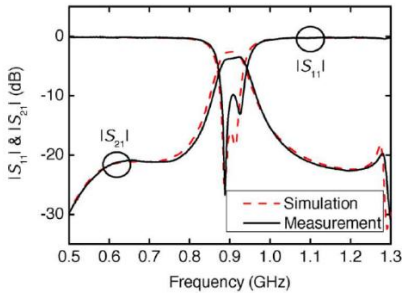

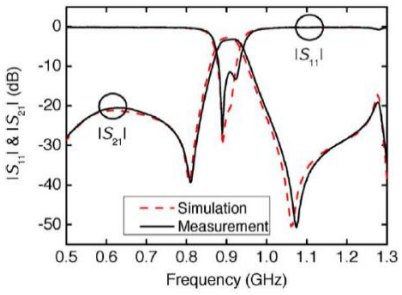

(b) (c)

Figure 1.4. A filtering switch based on a switchable delay line [16] (a) Structure; (b) With Chebyshev filtering responses; (c) With quasi-elliptic filtering responses.

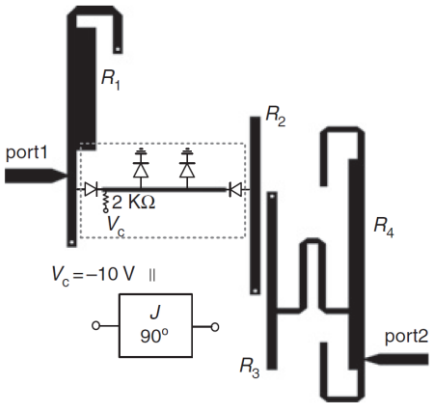

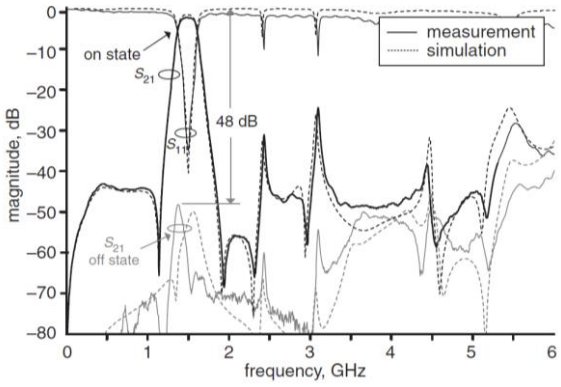

(a) (b)

Figure 1.5. A filtering switch using switchable connect line in [17] (a) Circuit structure; (b) Simulated and measured results.

In addition, the filtering switch can also be realized by controlling the resonant frequencies of the resonators in a filter by using PIN diodes or transistors [18]-[22]. By using the stepped impedance half-wavelength resonators with PIN diodes, a filtering switch with wide stopband is realized in [18]. The circuit structure and S parameters are shown in Figure 1.6. In order to reduce the size, a similar design using quarter-wavelength resonators is presented in [19]. By employing two sets of resonators with different frequencies or dual-mode resonators, dual-band filtering

switches can also be achieved [20], [21]. Figure 1.7 shows the structure and S parameters of a dual-band filtering switch based on dual-mode stub-loaded resonators [21]. As can be seen, the two passbands of this filtering switch can be switched on and off independently.

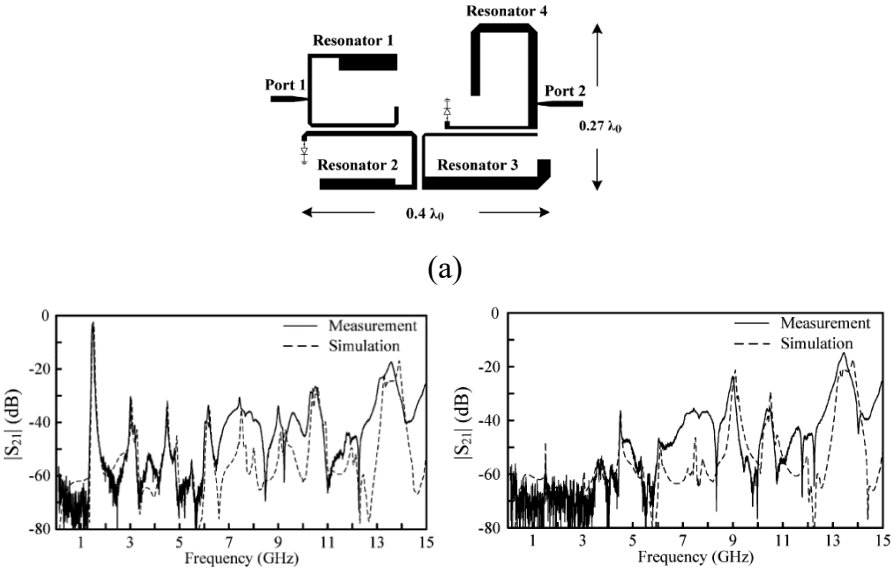

(a)

(b) (c)

Figure 1.6. Wide stopband filtering switch [18] (a) Structure; (b) ON-state responses; (b) OFF-state responses.

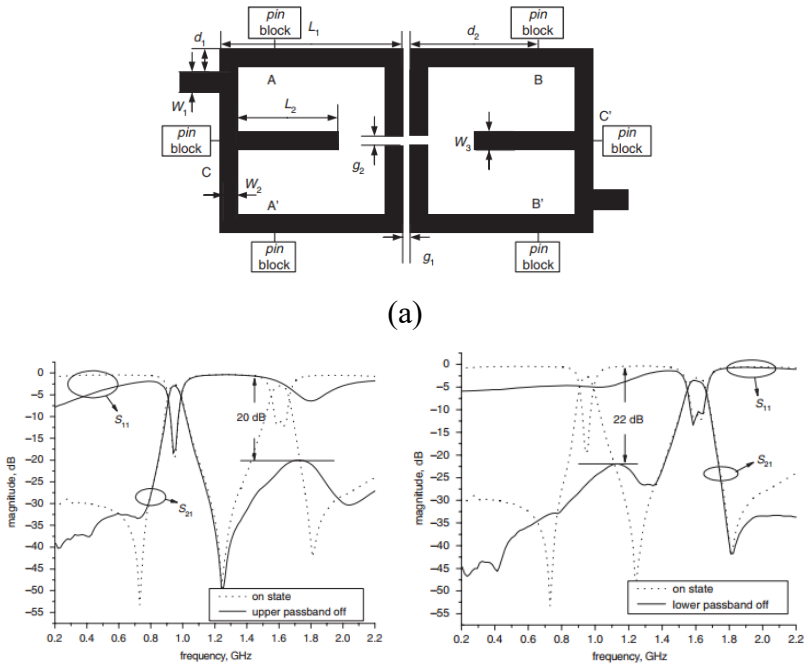

(a)

(b) (c)

Figure 1.7. Dual-band filtering switch using stub-loaded resonators [21] (a) Circuit structure; (b) Lower passband is turned on; (c) Upper passband is turned on.

The above-mentioned filtering switches are designed with the single-pole single-throw (SPST) working mode. Besides, the single-pole double-throw (SPDT) switches are also important in wireless applications, such as the time-division duplexer (TDD) system. Thus, SPDT filtering switches are also presented [22], [23]. Figure 1.8(a) shows the structure of an SPDT filtering switch [22]. It consists of five coupled resonators that form two filtering channels. One of the filters locating at the center is utilized as the common resonator of the two filtering channels, which can reduce the number of resonators to reduce the circuit size. PIN diodes and their biasing circuits are connected to the resonators. For the working mechanism, when one of the filtering channels works in the ON-state, the PIN diodes in this channel are turned off. No signals pass through these PIN diodes and thus can reduce the loss. For the other filtering channel, the PIN diodes are turned on and the capacitors are loaded to the resonators in this channel. The resonant frequencies of these resonators are different from the operating passband, realizing high isolation. Figure 1.8(b) shows the simulated and measured results of the SPDT filtering switch in [22]. As can be seen, a low insertion loss of 0.97 dB in the ON-state channel is realized and high isolation of 40 dB in the OFF-state channel is achieved, showing good SPDT filtering switch performance.

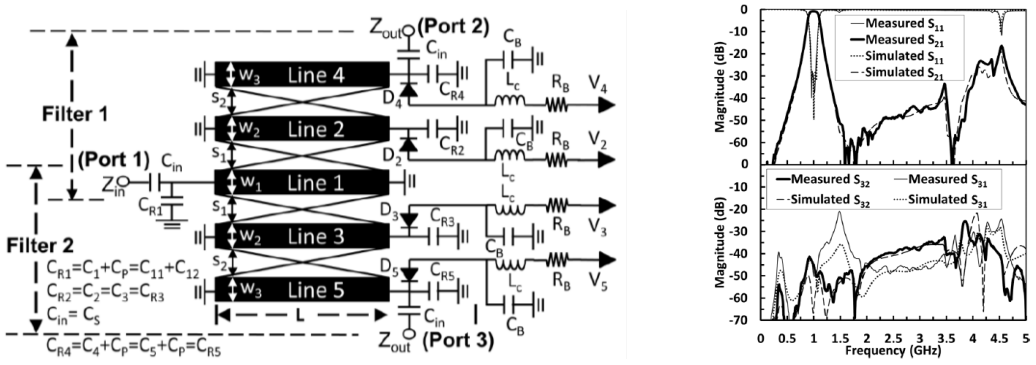

(a) (b)

Figure 1.8. SPDT filtering switch in [22] (a) Circuit structure; (b) Simulated and measured results.

Except for the above filtering switches using printed circuit board (PCB)

technology, the multilayer low temperature co-fired ceramic (LTCC) filtering switches with more compact size have also been reported. In [24], an LTCC filtering switch with the switchable center frequencies is designed. Figure 1-9(a) shows its schematic. When the PIN diodes are turned off, the resonators resonate at a higher frequency and thus the passband is located at the higher frequency. However, if the PIN diodes are turned on, the loading capacitors make the resonators resonate at a lower frequency. In this case, the passband is switched to a lower frequency. By using the multilayer low temperature co-fired ceramic (LTCC) structure, a very compact size can be achieved. Figures 1.4(b) and (c) show the photograph of the fabricated circuit and measured results, respectively. As can be seen, the filtering responses are not good and the isolation can be further improved.

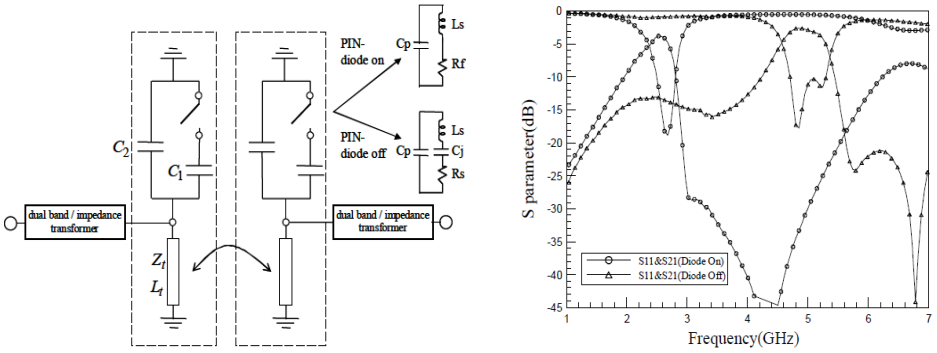

(a) (b)

Figure 1.9. LTCC filtering switch in [24] (a) Schematic; (b) Measured results.

Apart from the switches, power amplifiers can also be co-designed with filters. On one hand, filters can be utilized to control the harmonic impedance of a power amplifier, so as to improve the performance of the power amplifier. On the other hand, filters can be designed with impedance conversion functions and then can be used to replace the output matching networks in the power amplifiers. By using this method, the loss by the output matching networks in the power amplifier designs can be eliminated and the impedance mismatching by the cascaded filter and power amplifier can be avoided, resulting in efficiency improvement.

In [25], a CMRC structure is employed in a class-F power amplifier design, as

shown in Figure 1-10(a). In this structure, the CMRC features lowpass filter responses, which can generate a transmission zero at the third harmonic frequency, as shown in Figure 1-10(b). When it is used as the harmonic control network of the power amplifier, the third harmonic impedance approaches to infinity, which can satisfy the requirement of a class-F power amplifier. In this case, the harmonic control network is simplified. Figure 1-10(c) shows the measured results, where the power added efficiency (PAE) is higher than 74%. In [26], the ultra-wideband bandpass filter with a notched band can also be used to control the harmonic impedance of a class-F power amplifier to realize high efficiency.

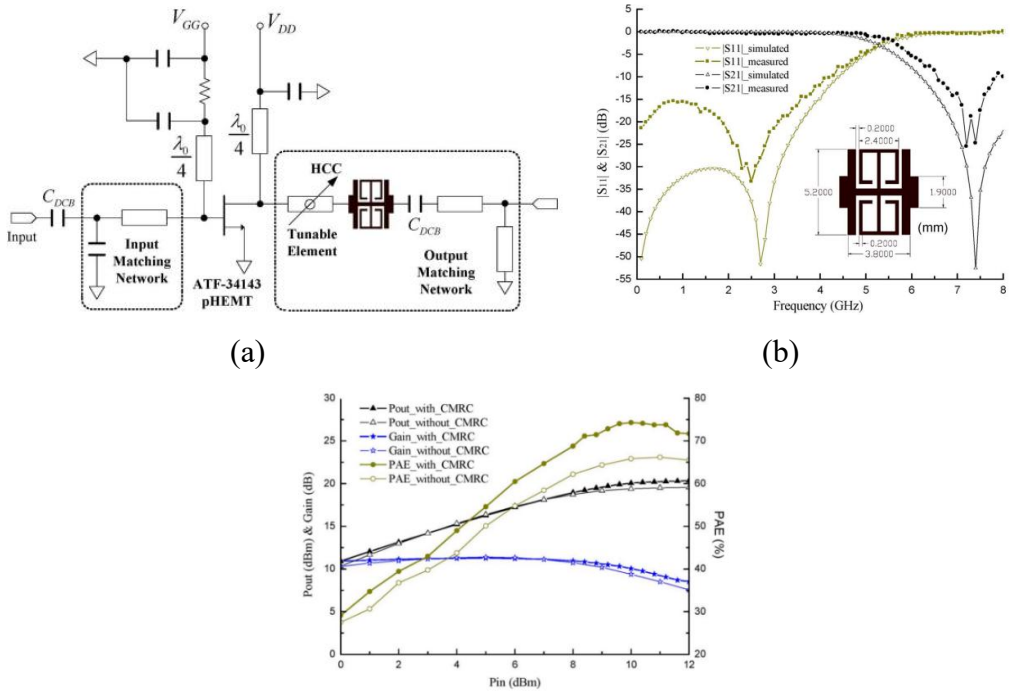

Figure 1.10. A class-F power amplifier based on CMRC [25] (a) Schematic; (b) Structure and simulated results of the CMRC; (c) Measured results of the power amplifier.

Wideband power amplifiers are useful in industrial applications, and thus co-designs of filter and power amplifiers are also used to realize wideband power amplifiers. Figure 1.11(a) shows the schematic of a wideband power amplifier [27]. A wideband low-pass filter is utilized as the output matching network of a class-E

power amplifier, whose harmonic impedances can also meet the requirements of this class-E power amplifier. Figure 1.11(b) shows the simulated and measured efficiencies. As can be seen, high efficiency of better than 80% is achieved in a wide frequency range from 1.2 to 2 GHz.

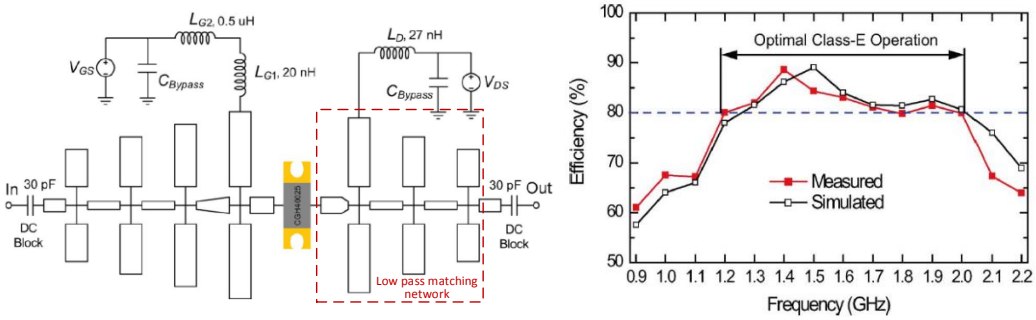

(a) (b)

Figure 1.11. A class-E power amplifier in [27] (a) Schematic; (b) Simulated and measured drain efficiencies.

For the co-designs of the filter and power amplifier in [25]-[27], the performance of power amplifiers, such as the efficiency and bandwidth, can be improved. However, these power amplifiers do not integrate bandpass responses. In order to realize the filtering power amplifiers, bandpass filters are usually used as output matching networks of power amplifiers [28]-[33]. Figure 1.12(a) shows the structure of a power amplifier in [28]. The bandpass filter based on two half-wavelength resonators in this design can achieve the phase shift of ±90º. By controlling the locations of the ports, this filter can realize different input impedance. Thus, it can be utilized as the output matching network of the power amplifier. Figures 1.12(b) and (c) show the simulated and measured results. As can be seen, both the bandpass filter and power amplifier responses are realized, whereas the in-band flatness is not so good. Based on this design, a bandpass filter is designed with wider bandwidth in [29] and a filtering power amplifier is proposed, as shown in Figure 1.13. The in-band flatness is improved and the filtering power amplifier realizes a higher efficiency.

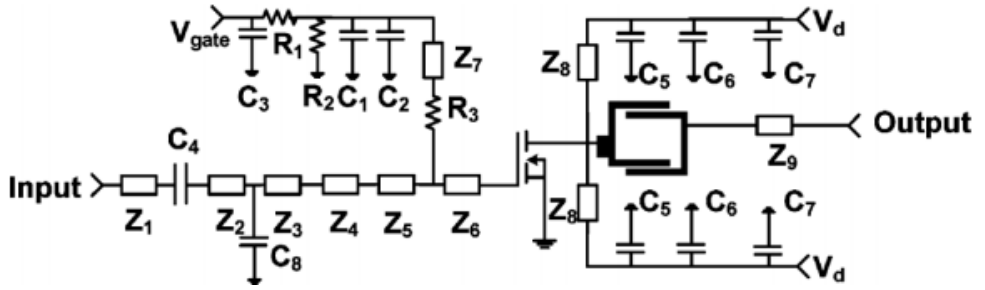

(a)

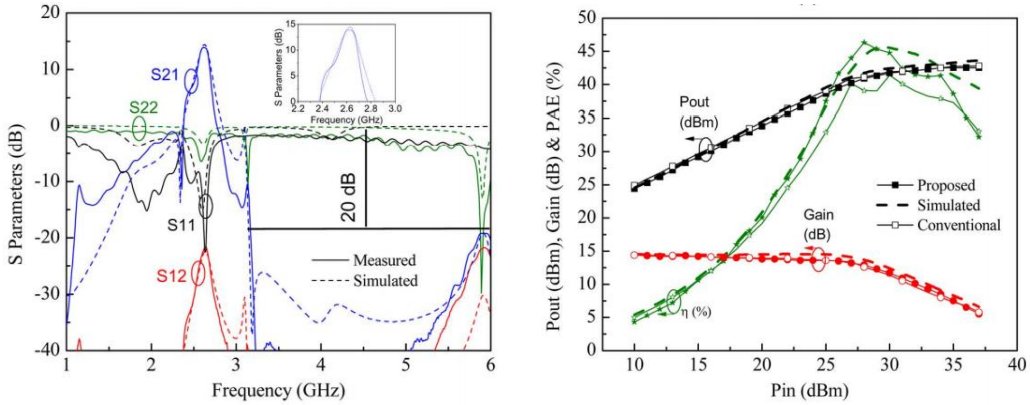

(b) (c)

Figure 1.12. Co-design of filter and power amplifier in [28].

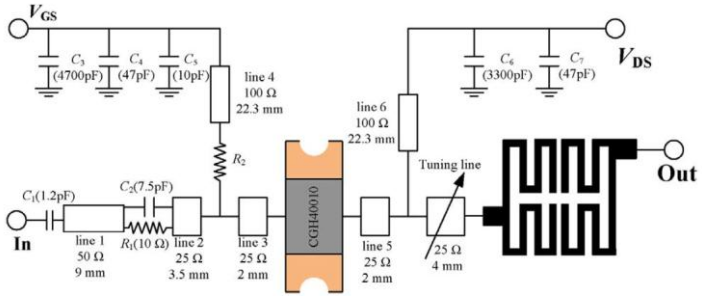

(a)

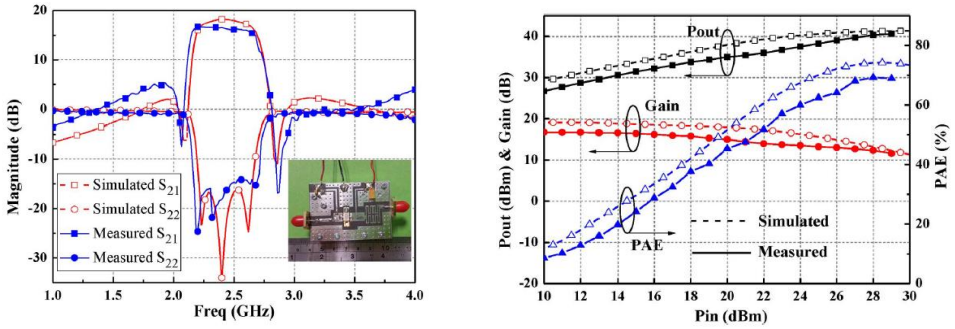

(b) (c)

Figure 1.13. A filtering power amplifier in [29] (a) Schematic; (b) Output power against frequency; (c) Output power, gain, and efficiency against input power.

Moreover, for narrowband applications, high-Q-factor coaxial-resonator-based bandpass filter can be co-designed with a power amplifier [30]. Figure 1.14(a) shows the schematic of the filtering power amplifier. In this design, the impedance conversion function of the filter is realized by controlling the elements in the coupling matrix, so as to meet the optimal impedance desired by the transistor. Figure 1.14(b) shows the simulated and measured results. Narrowband filtering responses are achieved and the efficiency within the passband frequency range is higher than 65%. Nevertheless, the presented design theory in [30] is only suitable for the Chebyshev filtering responses. Thus, no transmission zeros can be generated, and its selectivity can be further improved.

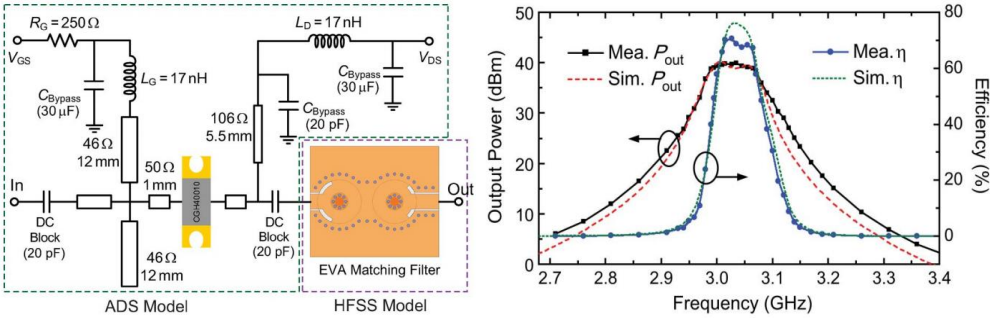

(a) (b)

Figure 1.14. Filtering power amplifier based on coaxial resonators in [30] (a) Schematic; (b) Simulated and measured results.

1.2.1 Passive Multi-Functional Filtering Circuits

Apart from the above-mentioned filtering switches and filtering power amplifiers, some passive multi-functional filtering circuits have also been reported, such as filtering power amplifiers, filtering balun and filtering coupler. The main purpose of designing these passive multi-functional filtering circuits is to reduce the size and loss.

In regards to the filtering power divider, one of the most commonly used methods is to replace the quarter-wavelength ($\lambda_g/4$) transmission lines in the conventional Wilkinson power divider [34]-[36]. For example, by controlling the locations of the

ports in a bandpass filter using open-loop resonators, the filter can realize the impedance conversion from 100 Ω to 50 Ω with the ±90° phase difference [34]. This filter can act as the $\lambda_g/4$ transmission line in the conventional Wilkinson power divider. In this way, a filtering power divider is achieved, as shown in Figure 1.15(a). Simulated and measured results are shown in Figure 1.15(b). As can be seen, good power division and filtering responses are obtained. In [35], by employing two low-pass filters and one bandpass filter, a wide stopband filtering power divider can be designed, as shown in Figure 1.16.

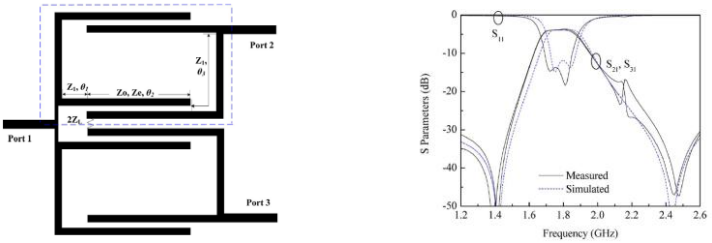

(a) (b)

Figure 1.15. A filtering power divider in [34] (a) Structure; (b) Simulated and measured results.

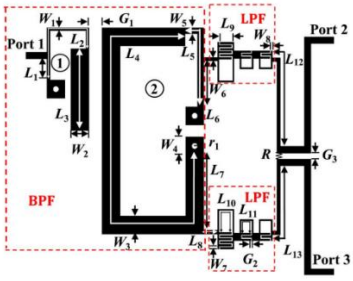

(a)

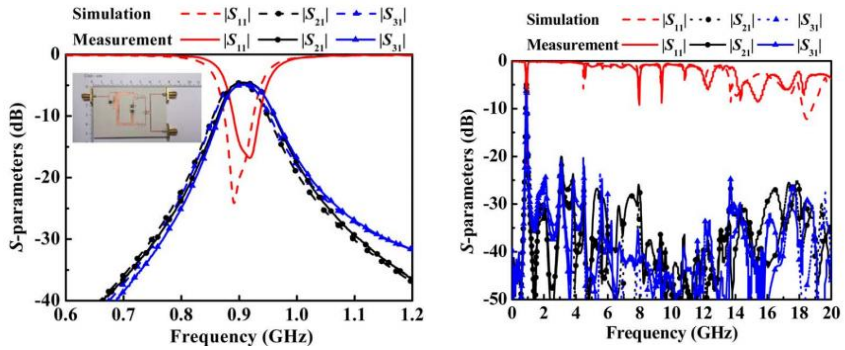

(b) (c)

Figure 1.16. Structure, simulated and measured results of the wide stopband filtering power amplifier [35].

In addition, the filtering power divider can also be realized by loading the filtering structure to the conventional power divider [37], [38]. For example, a power divider with a tunable stopband is proposed in [37] by loading the spurlines with bandstop responses to the Wilkinson power divider. By adding additional resonators to the Wilkinson power divider, a reconfigurable single- and dual-band filtering power divider is presented in [38].

Figure 1.17(a) shows the photograph of the fabricated circuit and Figure 1.17(b) shows the response when it works in the dual-band working state. As can be seen, this circuit realizes good power division and filtering performance. However, the whole structure includes a conventional Wilkinson power divider with multiple resonators, which leads to a large circuit size.

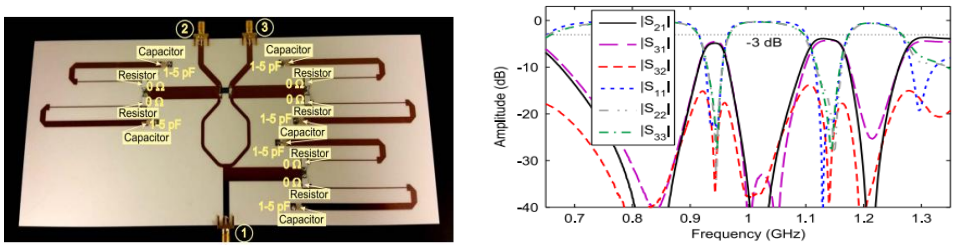

(a) (b)

Figure 1.17. Reconfigurable single- and dual-band filtering power divider [38] (a) Photograph of the fabricated circuit; (b) S parameters when it works in dual-band operation.

Since the relationship between the resonators in a bandpass filter can be described by using the coupling matrix, the coupling matrix can be used to analyze the input impedance of a filter. Thus, by controlling the elements of a coupling matrix, the filter can be designed with different input impedances and then can be employed to design the filtering power dividers. By using this method, a tunable filtering power divider with constant absolute bandwidth is presented in [39], whose circuit structure and topology are shown in Figures 1.18(a) and (b), respectively. When designing this circuit, a coupling matrix is firstly synthesized using filter design theories and then the filtering power divider topology is obtained by

modifying the coupling between the feeding line and the resonator. Figure 1.18(c) shows the simulated and measured S_{21} and S_{31}. As can be seen, good filtering responses with constant absolute bandwidth is achieved when the center frequency is tuning.

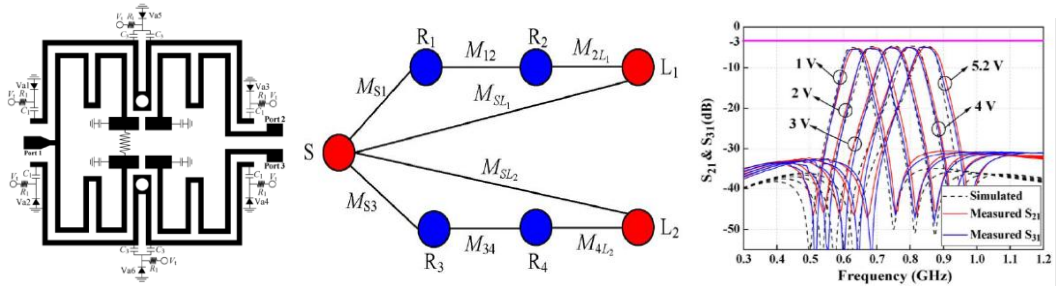

(a) (b) (c)

Figure 1.18. Tunable filtering power divider with constant absolute bandwidth in [39] (a) Circuit structure; (b) Topology; (c) Simulated and measured S_{21} & S_{31}.

Apart from the filtering power divider, multi-functional filtering baluns are also widely reported. In 2007, a dual-band filtering balun is designed by *Prof. K.-L. Wu et al* using stepped impedance coupled lines [40]. By employing three feeding lines coupled with a dual-mode resonator, a single-band balun is proposed by *E.-Y. Jung et al* in [41]. In addition, the hybrid resonators are also used to achieve the filtering balun by *Prof. T. Itoh et al* in [42]. The equivalent circuit of the hybrid resonator is shown in Figure 1.19(a), which consists of a series-connected and a parallel-connected inductors and capacitors. The corresponding microstrip structure is shown in Figure 1.19(b). Figure 1.19(c), (d) and (e) shows the photograph as well as simulated and measured results of the second-order filtering balun. As can be seen, this design has a very compact size, and realizes good filtering responses with good amplitude and phase performance.

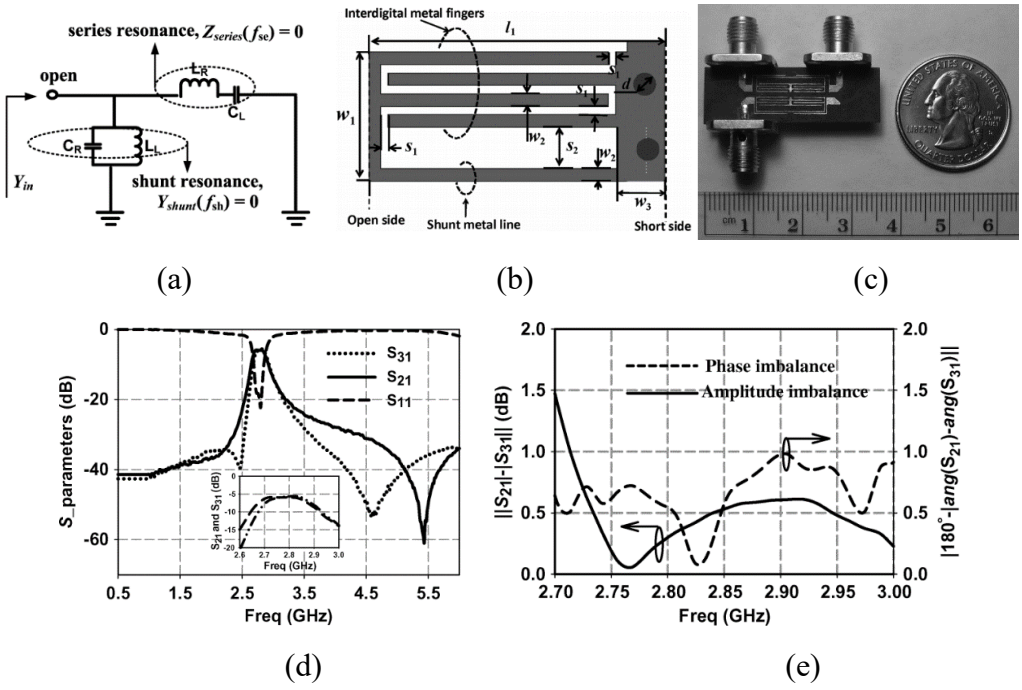

Figure 1.19. Filtering balun based on hybrid resonators [42] (a) Equivalent circuit of the hybrid resonator; (b) Structure of the hybrid resonator; (c) Photograph of the fabricated filtering balun; (d) Measured S parameters; (e) Measured phase and amplitude imbalances.

By using the cross-shaped patch resonators, a filtering balun is proposed by *S. Sun et al* in [43]. Moreover, the coupled substrate integrated waveguide (SIW) cavities are employed by *L.-S. Wu et al* to co-design the filter and balun in [44]. Figure 1.20 shows the structure and experimental results. High-order filtering responses are achieved by using multiple SIW cavities and transmission zeros are generated at two sides of the passband, resulting in high skirt selectivity.

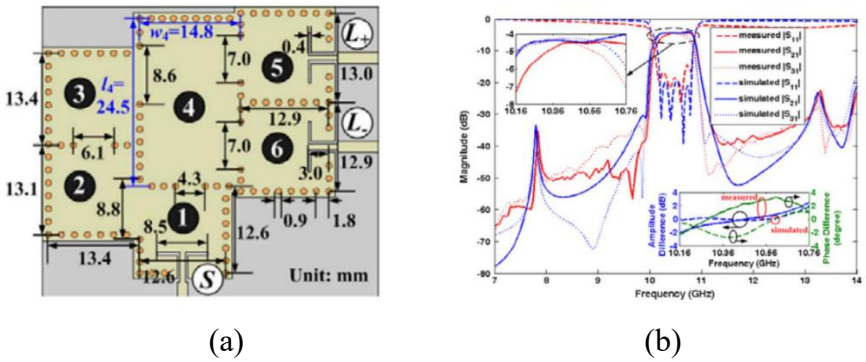

Figure 1.20. SIW-based filtering balun [44] (a) Structure; (b) Experimental results.

As compared to the above-mentioned microstrip resonators, SIW resonators in PCB technology, the multilayer LTCC technique shows the advantage of a more compact size. Some miniaturized LTCC filtering baluns have also been reported [45]-[47]. A commonly used method is to use the lumped-element capacitor and inductor (LC) components in multilayer LTCC structures. Figure 1.21(a) shows the 3-D structure and LC equivalent circuits of an LTCC filtering balun [45]. The design procedures can be summarized as follows. Firstly, the desired filtering responses and 180° phase difference required by a balun circuit can be easily obtained by analyzing the lumped-element LC circuits. Then, the required LC values are obtained to achieve the desired performance by constructing the LTCC structures. Good third-order filtering responses, magnitude balance and 180° phase difference are achieved, as shown in Figures 1.21(b) and (c).

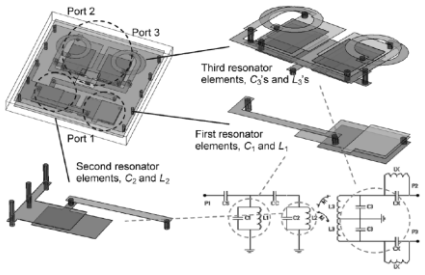

(a)

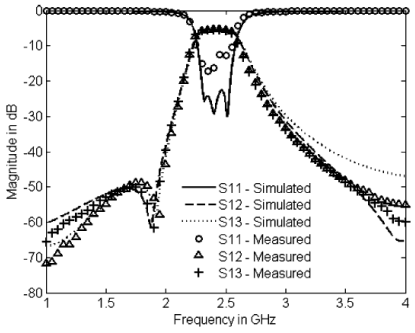

(b)

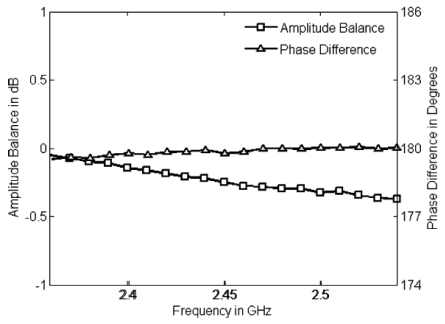

(c)

Figure 1.21. LTCC filtering balun in [45] (a) Structure; (b) S parameters; (c) Amplitude balanced and phase difference.

For the co-design of the filter and balanced circuit, it is usually realized by constructing the differential input and output ports in the filter structure. The desired filtering responses of a balanced filter can be obtained by using the conventional

bandpass filter design theories. Lots of balanced filters have been reported and most of them are presented by using the PCB structures [48]-[50]. For example, in [48], a balanced filter with high common-mode suppression is proposed by *W. Feng et al*. Figure 1.22 shows its circuit structure and experimental results. As can be seen, multiple transmission zeros are generated, which not only realize high selectivity but also achieve wide stopband. The measured common-mode suppression is better than 20 dB over a wide frequency range. By using the multi-mode stub-loaded resonators, *Prof. Y. J. Guo et al* propose dual-band and tri-band balanced filters in [49], which also realize good common-mode suppression, as shown in Figure 1.23.

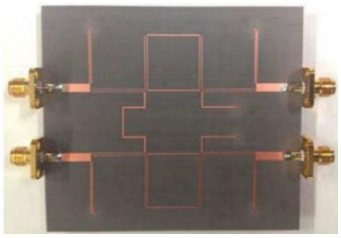

(a)

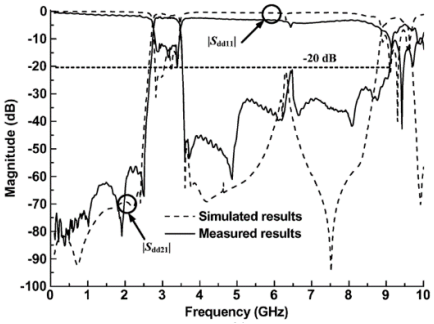

(b)

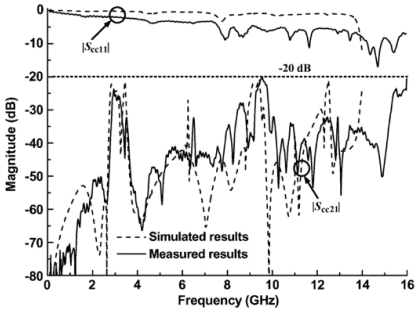

(c)

Figure 1.22. A balanced filter in [48] (a) Photograph; (b) Differential-mode responses; (c) Common-mode responses.

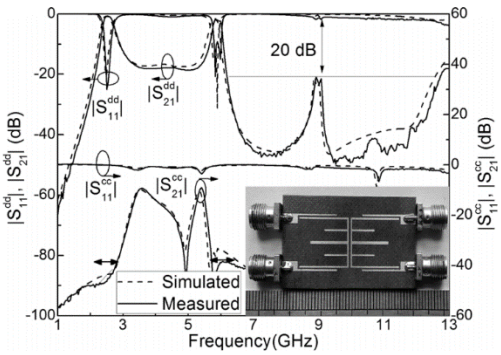

(a)

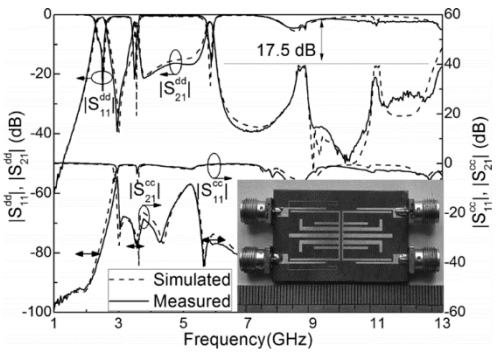

(b)

Figure 1.23. Balanced filters using stub-loaded resonators [49] (a) Dual-band design; (b) Tri-band design.

To meet the narrowband and high power base station applications, dielectric resonators with high Q factor and high power handling capability are employed to design the balanced filters [51]-[53]. For example, a filtering balun is presented by *Prof. J.-X. Chen et al* in [51] by using the electromagnetic (EM) field properties of a DR. After investigating the EM-field distributions of the $TE_{11\delta}$ mode in a rectangular DR, a pair of feeding probes are placed at different positions close to the DR where the EM-fields have opposite directions. In this way, the common-mode signals can be suppressed, which can be utilized to achieve the filtering balun [51]. Figures 1.24(a) and (b) show the circuit structure and experimental results. As can be seen, the circuit realizes not only good narrowband filtering responses but also high common-mode suppression of 50 dB. However, since the circuit is designed using single-mode DRs, it suffers from large size.

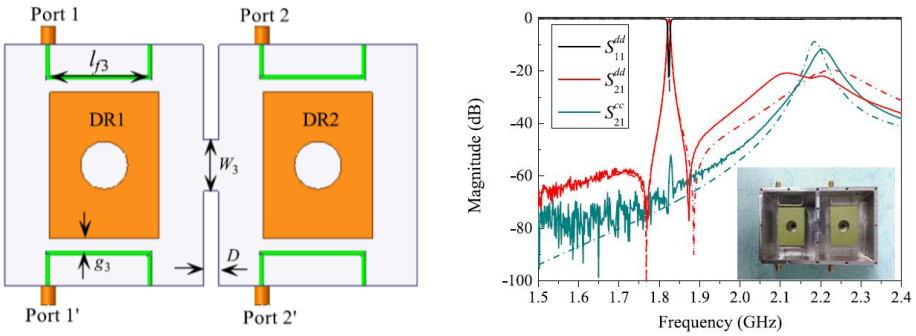

(a) (b)

Figure 1.24. Balanced filter based on $TE_{11\delta}$ mode DRs in [51] (a) Circuit structure; (b) Simulated and measured results.

The coupler is an important circuit in radio frequency (RF) front ends and the co-designs of the filter and coupler have also been reported [54]-[58]. The above-mentioned design methods for the passive multi-functional filtering circuits can also be used to realize the filtering couplers. In [54], *K.-X. Wang et al* propose miniaturized bandpass filters using microstrip transmission lines and lumped capacitors, and then use them to replace the $\lambda_g/4$ and $3\lambda_g/4$ transmission lines in the classic rat-race coupler. A filtering rat-race coupler is realized with the structure shown in Figure 1.25(a). The simulated and measured results are shown in Figure 1.25(b), where the rat-race coupler performance is achieved with wide stopband filtering responses. By using four $\lambda_g/4$ resonators and four $\lambda_g/2$ resonators, a quadrature coupler is proposed in [55]. Moreover, tunable filtering rat-race coupler

can be realized using the half-mode SIW cavities [56], as shown in Figure 1.26(a). In this design, the negative and positive coupling coefficients are used to replace the functions of $\lambda_g/4$ and $3\lambda_g/4$ transmission lines, respectively. Then, the function of the coupler is fused with the filter. Experimental results are shown in Figures 1.26(b) and (c). Good bandpass responses and high isolation between port 1 and 4 are maintained when the passband is tuning.

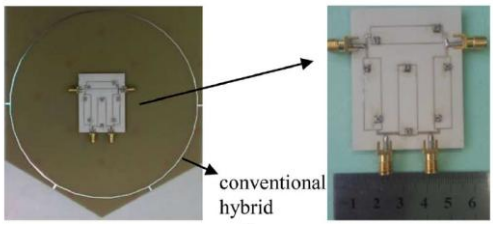

(a)

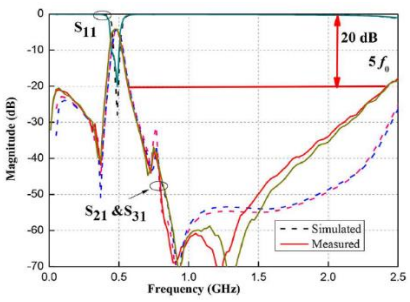

(b)

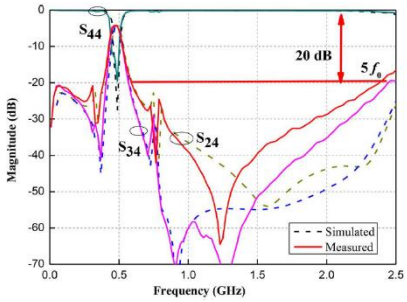

(c)

Figure 1.25. Filtering rat-race coupler in [54] (a) Photograph; (b) S_{11}, S_{21} & S_{31}; (c) S_{44}, S_{34} & S_{24}.

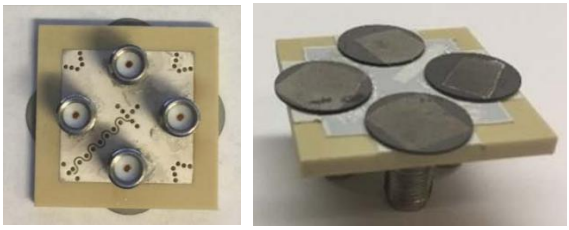

(a)

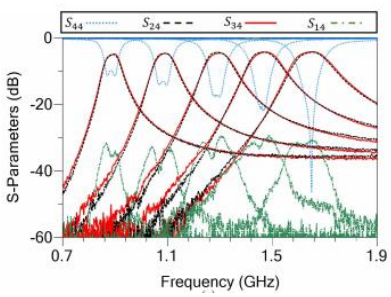

(b)

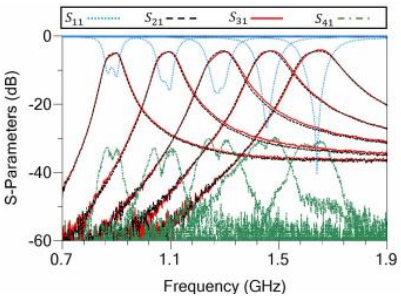

(c)

Figure 1.26. Tunable filtering rat-race coupler based on half-mode SIW cavities [56] (a) photograph; (b) S_{44}, S_{24}, S_{34} & S_{13}; (c) S_{11}, S_{21}, S_{31} & S_{41}.

To design the filtering coupler, dielectric resonators (DRs) can also be used [59], [60]. In [59], the 90º and -90º phase shifts can be obtained by constructing different coupling structures between DRs, such as the coupling using coupling irises and metal probes. With this characteristic, the function fusion of filter and coupler can be achieved. Figure 1.27(a) shows the photograph of the fabricated filtering coupler using this method. The DR-based structure has a very high Q factor whereas the whole circuit consists of four DRs and thus suffers from a large circuit size and a heavy weight. The simulated and measured results are shown in Figure 1.27(b). As can be seen, filtering responses are integrated into the coupler. However, it seems the circuit performance is not good. The port matching, amplitude balance, and selectivity need to be further improved.

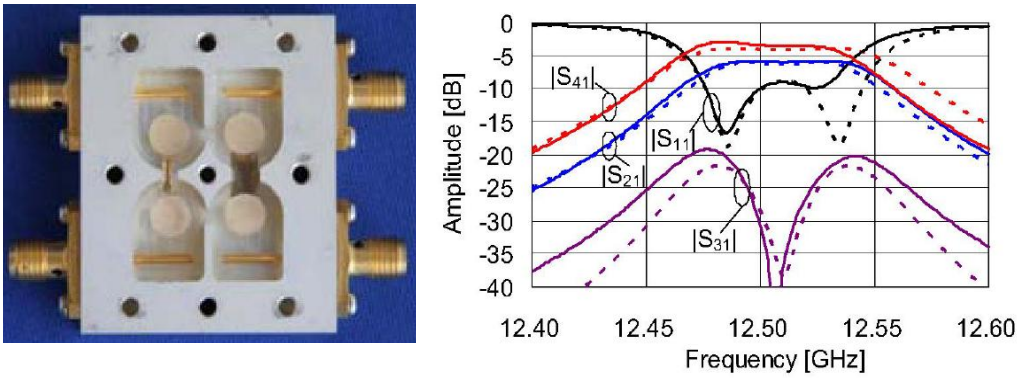

(a) (b)

Figure 1.27. Filtering coupler based on DRs in [59] (a) Photograph of the fabricated circuit; (b) Simulated and measured results.

Apart from the above-mentioned design, the passive multi-functional diplexers and multiplexers are also widely designed. A popular method is to use multiple sets of bandpass filters with different operating frequencies to construct the diplexers or multiplexers [61]-[63], whereas multiple sets of bandpass filters often occupy large circuit size. For size reduction, common multi-mode resonators can be used to place several single-mode resonators [64]-[66]. However, it is a challenge to realize high isolation for a common-resonator-based diplexer or multiplexer.

1.3 Thesis Motivation and Organization

Based on the above literature reviews, although co-designs or fusion designs of the filter and active circuits have been presented, most of the circuit performance needs to be improved and it still lacks design theories for the active filtering circuits. For the filtering switches, most of the designs are based on the PCB process, which is difficult to further reduce the size. A few works are proposed using LTCC technology with miniaturization, whereas the circuit performance is not so good. Moreover, because of the low Q factor, the reported filtering switches based on PCB and LTCC techniques are not applicable to narrowband base station applications. For filtering power amplifiers, one of the useful ways to realize high efficiency is to employ high-Q filter structures, especially in narrowband applications. However, there are only a few reported filtering power amplifiers using high-Q resonators, which can be further researched in this thesis.

As for passive multi-functional filtering circuits, the designs using PCB processes are very difficult to further reduce the circuit size because of their planar structures. Moreover, due to the Q factor limitation, it is also difficult to improve circuit performance. There are a few reported passive multi-functional filtering circuits using multilayer LTCC technology. Very compact size can be achieved, but most of them are designed by constructing the lumped LC elements which are time-consuming. To solve this problem, the designs using distributed elements may be a good solution. For the reported passive filtering circuits using high-Q DRs, most of the designs have the problem of large circuit size and the circuit performance needs to be improved.

In order to meet the requirements of miniaturization and low power consumption of wireless systems as well as to solve the existing problems of the reported active and passive multi-functional filtering circuits, co-designs of filters and active/passive circuits using LTCC and high-Q DRs/coaxial resonators are proposed. This thesis is organized as follows.

Chapter 1 is the Introduction Section. The research background and significance are introduced firstly. Then, literature reviews about the co-designs of filters and active/passive circuits are given. Based on the literature reviews, the research content and necessity of this thesis are presented.

Chapter 2 presents the multi-functional filtering circuits which are aimed to improve the overall efficiency of the power amplifier, switch and bandpass filter in wireless systems. Firstly, a method for designing single-band and dual-band filtering switches based on LTCC technology is proposed to reduce the ON-state loss and improve isolation. Secondly, for narrowband base station applications, low-loss and high-isolation single-pole single-throw (SPST) and single-pole double-throw (SPDT) filtering switches are designed using high-Q DRs. Thirdly, to realize the high-efficiency power amplifier with bandpass responses, a DR filter with cross coupling is co-design with a class-F power amplifier.

Chapter 3 presents the passive multi-functional filtering circuits to reduce size and loss. Firstly, an LTCC filtering balun is realized based on conventional Marchand balun with a simple structure. Then, tunable bandpass filters are proposed with a wide tuning range and constant absolute bandwidth using high-Q coaxial resonators. Thirdly, by constructing a quad-mode DR, a filtering rat-race coupling is designed with a single-cavity configuration, which can greatly reduce the circuit size.

Chapter 4 presents the dual-channel or multi-channel filtering circuits which are extended from the active and passive multi-functional filtering circuits in Chapters 2 and 3. Two or more filtering circuits with the same performance are integrated as one circuit for realizing high integration and miniaturization. Firstly, a dual-channel filter is designed using quad-mode DR, and it is co-designed with a Doherty power amplifier with two inputs and two outputs, realizing high integration and high efficiency. Then, to integrate more filter channels, several multi-channel filters are presented using triple-mode DRs. To further reduce the size and loss, two multi-

functional balanced filters or balun filters are also co-designed as one dual-channel balanced filter or balun filter.

Chapter 5 summarizes the content and significance of this thesis, and also provides the recommended future works.

Chapter 2 Active Multi-Functional Filtering Circuits

2.1 Introduction

In radio frequency (RF) front ends of wireless systems, the switch and bandpass filter are generally connected with the power amplifier, as shown in Figure 2.1. The power consumption of these three circuits is usually high. Thus, it is significant to improve the overall efficiency of these three circuits. On one hand, since the output power of the power amplifier is high, the total loss of the filter and switch has a great impact on the overall efficiency of these three circuits. By using the single functional circuit design method, the total loss in the filter and switch is the sum of their losses, which is generally high and thus drops the efficiency of the system. Moreover, due to the parasitic effect, the isolation of a switch is often lower than 40 dB. Although using more switches in cascade can improve the isolation, the insertion loss would become higher. On the other hand, an impedance mismatch often exists when the power amplifier is cascaded with the filter, and the additional transmission line for connection between them leads to additional circuit loss. These cause efficiency degradation. Accordingly, by using the single-functional circuit design methods, it is difficult to improve the overall efficiency of the power amplifier, switch, and filter.

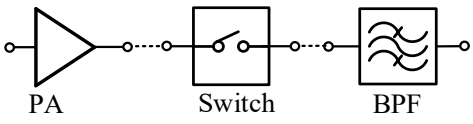

Figure 2.1. Schematic of the cascaded power amplifier, switch and filter.

2.2 Proposed Methods for Co-Design and Function-Fusion of Filters and Active Circuits

To solve the above problems, research on co-design and function-fusion of filters

and active circuits is conducted in this thesis, so as to improve the overall efficiency of the power amplifier, switch, and filter, including the function-fusion of the filter and switch, and the co-design of the filter and power amplifier.

For the function-fusion of the filter and switch, the design method of filtering switches based on coupling control is proposed in this thesis. In conventional single-functional circuit designs, the filter and switch are independently designed and then cascaded using 50-Ω transmission lines, which suffers from high on-state loss and low off-state isolation. In this thesis, the relationship between the coupling matrix and S_{21} can be firstly analyzed as

$$S_{21} = -2j[A^{-1}]_{N+2,1} \tag{2.1}$$

$$[A] = -j[R] + \Omega[W] + [M] \tag{2.2}$$

$$\Omega = \frac{\omega_0}{\Delta\omega} \cdot \left(\frac{\omega}{\omega_0} - \frac{\omega_0}{\omega}\right) \tag{2.3}$$

where $[M]$ is the coupling matrix, $[R]$ is a diagonal matrix, Ω is the normalized frequency and matrix $[W]$ is expressed as: $[W]_{1,1} = [W]_{N+2,N+2} = 0$, otherwise $[W]_{ij} = 1$. Then, by controlling the coupling coefficients in the filter structure, the desired on- and off-state responses can be obtained, for example, the electric and magnetic coupling coefficients (k_e and k_m) can be controlled by the electric- and magnetic-field (E- and H-field) distributions based on the following equations:

$$k_e = \frac{\iiint \varepsilon \vec{E_1} \cdot \vec{E_2} dv}{\sqrt{\iiint \varepsilon \left|\vec{E_1}\right|^2 dv \times \iiint \varepsilon \left|\vec{E_2}\right|^2 dv}} \tag{2.4}$$

$$k_m = \frac{\iiint \mu \vec{H_1} \cdot \vec{H_2} dv}{\sqrt{\iiint \mu \left|\vec{H_1}\right|^2 dv \times \iiint \mu \left|\vec{H_2}\right|^2 dv}} \tag{2.5}$$

where $\vec{E}$ and $\vec{H}$ represent the vectors of E- and H-fields, respectively, and v is the volume. Base on these theories, the method for the function-fusion of the filter and switch is proposed to design the filtering switch.

Figure 2.2 shows the schematic of the proposed function-fusion method of the filter and switch. The loss of the proposed filtering switch is almost the same as a conventional bandpass filter and thus the loss of an individual switch is eliminated.

Moreover, the off-state is realized by controlling the coupling coefficient and the isolation is improved. Based on this proposed method, single- and dual-band LTCC filtering switches are proposed with a compact size. To meet the requirements of narrowband base station applications, the circuit topologies of SPST and SPDT filtering switches based on high-Q dielectric resonators are proposed.

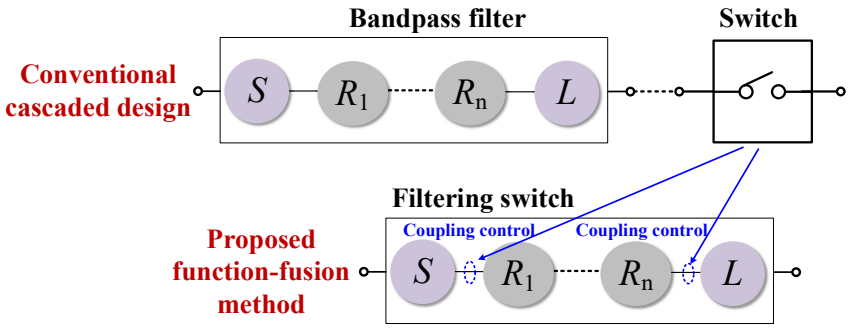

Figure 2.2. Schematic of the proposed function-fusion method of the filter and switch.

For the co-design of the filter and power amplifier, a novel design method is proposed, which can improve their total efficiency by utilizing the complementary performance of the filter and power amplifier, and also reducing the redundant sections and connection structures. Figure 2.3 shows the schematic of the proposed method for the co-design of the filter and power amplifier. In conventional cascaded design, a power amplifier consists of the input matching network, transistor, and output matching network. The output port of the power amplifier is connected to the filter through the 50-Ω transmission line, which has the problem of impedance mismatching and causes efficiency degradation.

To solve this problem, a filtering impedance conversion method based on the coupling matrix is developed. Firstly, based on the coupling matrix, the input impedance of the filter can be analyzed, for example, the input impedance of a filter with source-load coupling can be expressed as:

$$Z_{in1} = \frac{M_{12}^2}{(M_{2L}M_{S1} - M_{12}M_{SL})^2} . \tag{2.6}$$

Then, by controlling the elements of the coupling matrix, such as M_{S1}, M_{12}, and M_{2L}, the high-selectivity dielectric resonator filter can realize the impedance conversion function. By using this filter to take place the output matching network of the power amplifier, connection transmission lines and the individual filter in conventional cascaded design, the circuit architecture is simplified, as shown in Figure 2.3. In this way, the impedance mismatching problem is avoided, and the output matching network in the power amplifier design as well as the connection structures are eliminated, which improve the overall efficiency of the filter and power amplifier.

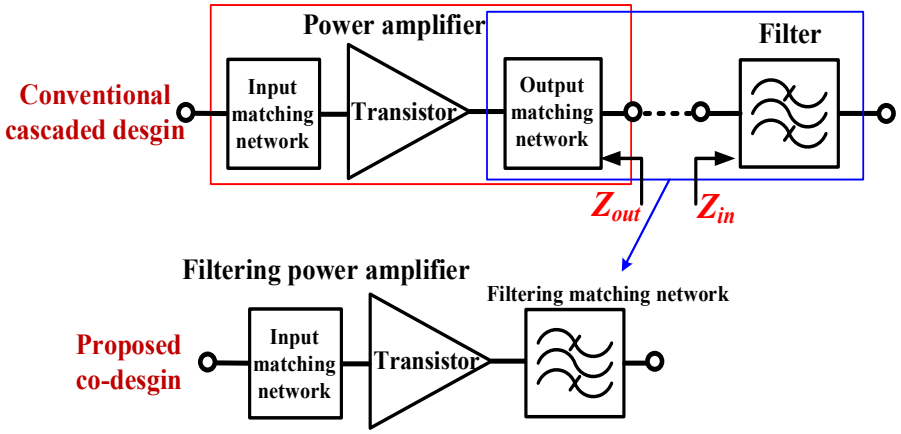

Figure 2.3. Schematic of the co-design method of filter and power amplifier.

2.3 Single- and Dual-Band LTCC Filtering Switch

In order to reduce ON-state insertion loss and improve OFF-state isolation of the filter and switch, lots of methods have been proposed to design filtering switches. For example, the high-isolation filtering switches in [16] and [17] are designed by employing the switchable connected-coupling lines and switchable delay lines, respectively. However, the signals pass through the PIN diodes in the ON-state, which introduces extra insertion loss. In [18], [19], PIN diodes are utilized to change the resonance frequencies of the resonators. In this way, high-order BPFs are needed to obtain high isolation.

Apart from the single-band designs mentioned above [16]-[19], dual-band and multi-band filtering switches have also been studied. In [67], [68], dual-band

filtering switches are realized by using PIN diodes to alter the effective length of the resonators. However, they work at only one operating band at a time and also the PIN diodes introduce additional loss. The independently controlled multiband filtering switches can be achieved by using multiple sets of BPFs, whereas they occupy large circuit area [69], [70]. The multi-mode resonators can be utilized to design the compact dual-band filtering switches [21], [71], but the isolation performance should be improved. Moreover, the filtering switch can also be designed using varactors [72].

Since the filtering switches in [16]-[19], [21], [67]-[72] are realized based on planar printed circuit board (PCB) technology, it is very difficult to further reduce the circuit size. The multilayer LTCC technique, featuring great circuit size reduction and design flexibility, is popularly used to fabricate miniaturized components, such as the LTCC filters [73]-[76] and balun filters [77], [78]. However, there are only a few filtering switches realized in LTCC and the circuit performance of the reported LTCC filtering switch needs to be enhanced [24].

In this thesis, single- and dual-band filtering switches based on coupling control are proposed. PIN diodes are placed in the feeding structures to enable the switch function. When the switch is in ON-state, the PIN diodes are turned off. Thus, signals don’t pass through the PIN diodes and this will not introduce extra loss. Coupling matrices are firstly synthesized to guide the ON-state bandpass responses realization. And then they are manipulated based on filter design theory to reduce the signal transmission between two ports and thus high OFF-state isolation is realized based on the coupling control. Theoretical analysis of the ON- and OFF-state coupling matrices is carried out. Then, a single- and a dual-band filtering switches are implemented using LTCC techniques. The design procedures are given and the results are presented.

2.3.1 Coupling Matrix Analysis for the Filtering Switch in the ON- and OFF-States

The proposed filtering switches can perform dual functions. When they are in ON-state, the circuits are the same as conventional BPFs. Therefore, coupling matrices can be utilized to guide the implementation. For OFF-states, some elements in the ON-state coupling matrix are modified to obtain the OFF-state coupling matrix, which results in suppressed RF signal transmission between the two ports or high isolation. Herein, the theoretical analysis is conducted based on the coupling matrix.

In this design, a second-order Chebyshev filter topology is chosen as a design example to study ON- and OFF-state responses within a narrow frequency range around the passband (less than 20% fractional bandwidth). It should be noted that high-order schemes with complex topology can also be utilized. To realize the desired ON-state bandpass responses, the normalized low-pass prototype responses are analyzed. The return loss is set to be better than 15 dB. According to the method proposed in [79] where "N×N" coupling matrix synthesis method is presented for Chebyshev filters, the normalized coupling matrix can be synthesized as

$$M_{N+2,ON} = \begin{array}{c} \\ S \\ 1 \\ 2 \\ L \end{array} \begin{array}{c} \begin{array}{cccc} S & 1 & 2 & L \end{array} \\ \begin{bmatrix} 0 & -1.0369 & 0 & 0 \\ -1.0369 & 0 & 1.2868 & 0 \\ 0 & 1.2868 & 0 & -1.0369 \\ 0 & 0 & -1.0369 & 0 \end{bmatrix} \end{array} \tag{2.7}$$

According to the equations (2.1)-(2.3), the magnitude of S_{21} ($|S_{21}|$) against the normalized low-pass frequency is studied. For the synthesized coupling matrix (2.7), M_{S2} (M_{2S}), M_{SL} (M_{LS}), and M_{1L} (M_{L1}) are equal to zero. Thus, $|S_{21}|$ is determined by M_{S1} (M_{1S}), M_{2L} (M_{L2}), and M_{12} (M_{21}), which is studied in three cases.

1) The change of M_{S1} (M_{1S}) is studied with other elements in matrix (2.7) fixed. $|S_{21}|$ is the function of M_{S1} and the normalized frequency Ω. Figure 2.4(a) shows the $|S_{21}|$ against Ω with different M_{S1}. As can be observed, when M_{S1} is closer to zero,

the higher isolation can be achieved. Since the matrix (2.7) is symmetric, the result of changing M_{2L} is the same as that of changing M_{S1}.

2) Then, $|S_{21}|$ with different M_{12} (M_{21}) is calculated based on (2.1), with the results shown in Figure 2.4(b). As observed, high isolation can also be obtained by modifying M_{12} close to zero.

3) The impact of changing both M_{S1} and M_{2L} is studied and the calculated results are shown in Figure 2.4(c). When both M_{S1} and M_{2L} are smaller than 0.01, the in-band isolation can be better than 40 dB. Besides, the simultaneous change of M_{12} and M_{S1} (or M_{SL}) can also lead to high isolation levels. For example, more than 40 dB isolation can be achieved by applying a large M_{S1} with a small M_{12}, as shown in Figure 2.4(d).

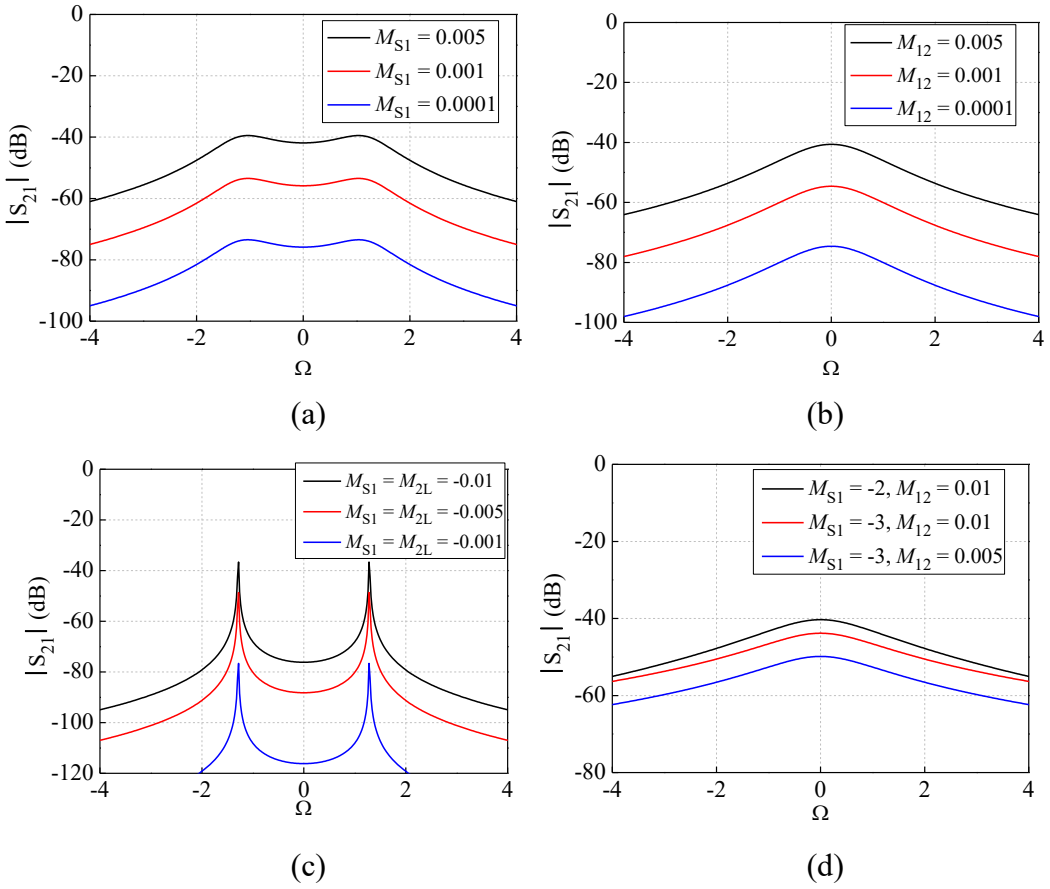

Figure 2.4. Calculated responses of the coupling matrices with different (a) M_{S1}; (b) M_{12}; (c) M_{S1} and M_{2L}; (d) M_{S1} and M_{12}.

As can be seen from Figures 2.4(a)-(d), it is easier to obtain high isolation by simultaneously changing two elements than modifying only one element. In the latter case, the element is required to be very small and thus difficult for circuit realization. In order to realize the high isolation with design flexibility and easy realization, both M_{S1} and M_{2L} are chosen to be controlled, which can be realized by embedding the PIN diodes in feeding lines. To obtain more than 40 dB isolation, the M_{S1} and M_{2L} in (1) are modified to form the OFF-state coupling matrix, which is expressed as as

$$M_{N+2,OFF} = \begin{array}{c} \\ S \\ 1 \\ 2 \\ L \end{array} \begin{array}{c} \begin{array}{cccc} S & 1 & 2 & L \end{array} \\ \begin{bmatrix} 0 & -0.005 & 0 & 0 \\ -0.005 & 0 & 1.2868 & 0 \\ 0 & 1.2868 & 0 & -0.005 \\ 0 & 0 & -0.005 & 0 \end{bmatrix} \end{array} \tag{2.8}$$

Based on the ON- and OFF-state coupling matrices, LTCC multilayer structures are employed to realize a single- and a dual-band filtering switches, as presented below.

2.3.2 Single-Band LTCC Filtering Switch

2.3.2.1 Circuit Configuration

Figure 2.5(a) shows the schematic or equivalent circuit of the proposed LTCC filtering switch. The whole circuit consists of two coupled half-wavelength resonators and two feeding lines. This design can employ either asymmetric or symmetric feeding lines, as enclosed in the blue dashed lines, which will be discussed later. Switch circuitries, as enclosed in the red dashed circles, are connected to the feeding lines to enable the switching function. Figure 2.5(b) illustrates the 3-dimensional (3-D) structure, which consists of twelve metal layers and eleven ceramic sheets. Two half-wavelength resonators (in color green and blue) are folded on the layers 2, 5, 6, 7, 8 and 10 to reduce circuit size. The feeding lines (in red and pink), located on the layers 3, 6, 10 and 12, are utilized to provide broadside coupling to the resonators. Vias are utilized to connect the circuits on

different layers, which go through the holes on layers 4, 9, and 11. The switch circuitries, including the capacitors (*C*), PIN diodes and resistors (*R*), are placed on the top of the whole circuit on layer 12 for easy realization.

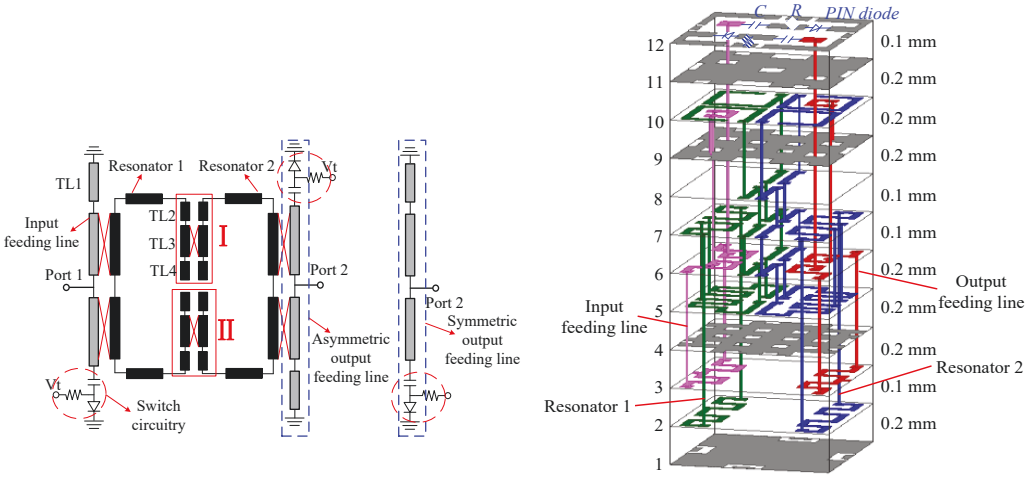

(a) (b)

Figure 2.5. Single-band LTCC filtering switch (a) Schematic; (b) 3-D structure.

2.3.2.2 Analysis of the ON-State Responses

When the PIN diodes in Figure 2.5(a) are turned off, the ends of the feeding lines connected with the switch circuitries are equivalent to be open. Thus, the filtering switch is equivalent to a BPF and the classical filter synthesis method can be adopted. It is designed with the center frequency of 1.4 GHz and fractional bandwidth (*FBW*) of 12%. Using the matrix (1), the ON-state coupling coefficient $k_{s,on}$ and external quality factor $Q_{es,on}$ can be calculated by

$$k_{12} = FBW \times M_{12} \tag{2.9}$$

$$Q_e = \frac{1}{FBW \times M_{S1}^2} \tag{2.10}$$

They are calculated as: $k_{s,on}$ = 0.154, $Q_{es,on}$ = 7.75. Then the circuit structures are constituted to realize $k_{s,on}$ and $Q_{es,on}$. The desired $k_{s,on}$ and $Q_{es,on}$ can be easily obtained by controlling the gaps or distances between the resonators and that between the resonators and feeding lines, respectively.

In the coupling matrix synthesis, a Chebyshev filter topology is chosen to realize the filtering responses within a narrow frequency range around the passband. Thus, no transmission zero is generated around the passband by this filter prototype, which is demonstrated by the synthesized results in Figure 2.4. It is noted that the desired $Q_{es,on}$ for the passband can be realized by using either the symmetric or asymmetric output feeding lines enclosed in the dashed blue line in Figure 2.5(a). Without introducing cross coupling, a transmission zero (TZ_1) can be generated when the asymmetric output feeding line is utilized, as shown in Figure 2.6(a) (solid line).

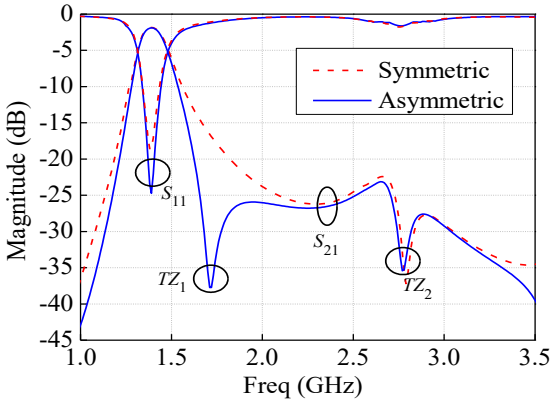

(a)

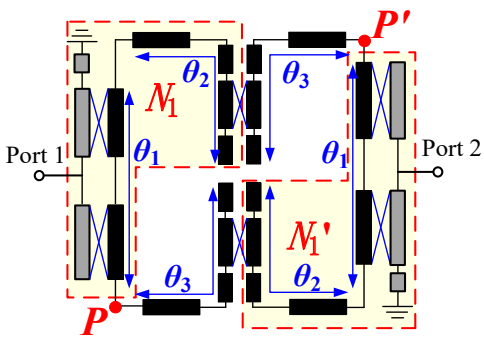

(b)

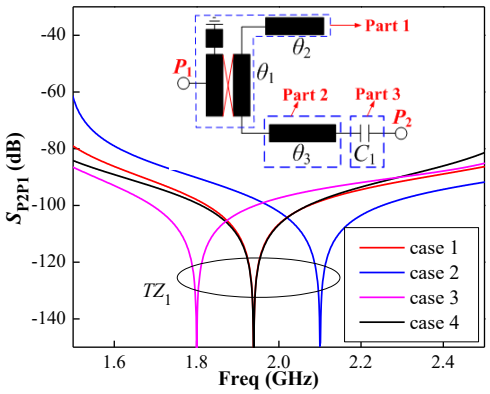

(c)

Figure 2.6. (a) Simulated ON-state responses of the LTCC filtering Switches; (b) Equivalent circuit in the ON-state with asymmetric feeding structure; (c) Simulated results of a feeding line and a resonator: case 1: $\theta_1 = 80$, $\theta_2 = 50$, $\theta_3 = 50$; case 2: $\theta_1 = 80$, $\theta_2 = 40$, $\theta_3 = 50$; case 3: $\theta_1 = 90$, $\theta_2 = 50$, $\theta_3 = 50$; case 4: $\theta_1 = 80$, $\theta_2 = 50$, $\theta_3 = 60$, unit: degree with respect to f_0.

At the frequency of TZ_1 (f_{TZ1}), the resonant mode and transmission states are different from those at the passband frequency and the Chebyshev prototype is no longer applicable. The schematic of the equivalent circuit at f_{TZ1} is shown in Figure 2.6(b). Figure 2.6(c) plots the transmission characteristic from P_1 to P_2 of half the circuit as illustrated in the inset in Figure 2.6(c), in which the small capacitor C_1 represents the coupling region close to the two open ends. As can be seen, the TZ_1 is generated. When θ_1 or θ_2 increases, TZ_1 moves downward lower frequency and θ_3 has no impact on TZ_1. Therefore, Part 1 in the inset of Figure 2.6(c), which corresponds to the part N_1 in Figure 2.6(b), features bandstop responses. Since signals at f_{TZ1} cannot be transmitted from port 1 to P and from P' to port 2, the TZ_1 is generated. In contrast, if the symmetric structure is used, the signals at f_{TZ1} can be transmitted from port 1 to N_1, then coupled to N_1' and delivered to port 2. In this case, the TZ_1 cannot be generated. Therefore, the asymmetric feeding structure is employed in this design to enhance the skirt selectivity.

It is noted that the other transmission zero (TZ_2) is generated at 2.78 GHz, which is due to the coupling structure between two resonators as enclosed in the red real lines (regions I and II) in Figure 2.5(a). The mechanism for realizing the transmission zero at the desired frequency f_z is analyzed as follows. Figure 2.7 shows the structure in one of the regions. Two transmission lines with open ends have the quarter-wavelength electric length at f_z. If the coupling between the two lines is not very strong, the normalized voltage and current distributions can be derived based on the transmission line theory, which are also shown in Figure 2.7 and can be approximately expressed as [80]

$$V(x) = \sin(\beta x) \tag{2.11}$$

$$I(x) = \cos(\beta x) \tag{2.12}$$

where β is the propagation constant. The coupling region is at the center part of these two transmission lines from A to B in Figure 2.7.

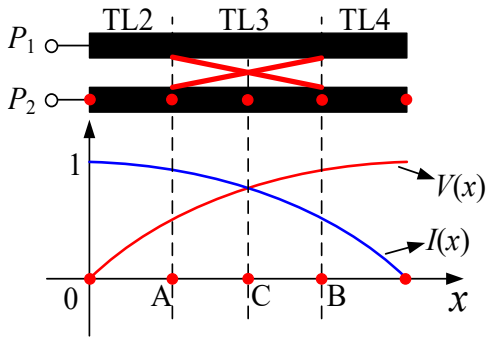

Figure 2.7. Coupling structure between two coupled resonators and its voltage distribution.

The electric and magnetic coupling coefficients can be defined on the basis of the ratio of coupled energy to stored energy by using equations (2.4) and (2.5) [81]. For a quarter-wavelength open-ended transmission line, the stored electric and magnetic energy is the same, namely, the denominators in (2.4) and (2.5) are the same. Since the voltage and current can replace the corresponding electric and magnetic fields to evaluate the coupling coefficients, (2.4) and (2.5) can also be expressed as

$$k_e = P \times \int_A^B |V(x)|^2 \, dx = P \times \int_A^B |\sin(\beta x)|^2 \, dx \tag{2.13}$$

$$k_m = P \times \int_A^B |I(x)|^2 \, dx = P \times \int_A^B |\cos(\beta x)|^2 \, dx \tag{2.14}$$

where P is constant. Accordingly, the overall coupling strength can be expressed as

$$|k'| = ||k_e'| - |k_m'|| = P \times \left| \int_A^B |\sin(\beta x)|^2 \, dx - \int_A^B |\cos(\beta x)|^2 \, dx \right| \tag{2.15}$$

As shown in Figure 2.7, point C is at the middle point of the coupled line and points A and B are symmetric with respect to C. According to (14), $|k'|$ is calculated as zero. Thus, the signal at f_z cannot pass through the regions I and II and consequently cannot be delivered from port 1 to port 2. As a result, a transmission zero (TZ_2) is generated at f_z.

2.3.2.3 Analysis of the OFF-State Responses

The OFF-state responses are also studied based on the coupling matrix. Comparing the ON- and OFF-state coupling matrices in (2.7) and (2.8), M_{S1} and M_{2L} are changed from 1.0369 to 0.005 and the other elements are kept unaltered. In other words, we need only make the coupling between the feeding lines and resonators close to zero in the OFF-state to ensure high isolation. This is realized by turning on the PIN diodes in the feeding lines. In this case, the switch circuitry enclosed in the red dashed lines can be equivalent to the ground. The parasitic capacitance of the PIN diodes increases the effective length of the feeding line. Thus, a transmission line (TL1 in Figure 2.5(a)) is added to the other end of the feeding line to make the whole feeding line nearly symmetric with respect to the port. In this way, the desired coupling can be realized as analyzed as follows.

The equivalent OFF-state feeding structure is shown in Figure 2.8. The coupling region is from *M* to *N* and the whole circuit is symmetric. Based on the transmission line theory, the voltage distribution on the feeding line and half-wavelength resonator can be illustrated in Figure 2.8. The voltage can replace the electric field to evaluate the coupling strength between the feeding line and resonator, which is expressed as

$$k' = p \times \frac{\int V_R(x) V_F(x) dx}{\sqrt{\int |V_R(x)|^2 dx} \sqrt{\int |V_F(x)|^2 dx}} \tag{2.16}$$

where V_R, V_F denote the voltage distribution on the resonator and feeding line, respectively, p is constant. As observed from Figure 2.8, within the coupling region from *M* to *N*, the voltage on the feeding line $V_F(x)$ is even and that on the resonator $V_R(x)$ is odd. According to equation (2.16), the resultant coupling strength is zero. However, in the implemented LTCC circuit, it is impossible to realize exactly symmetrical configuration and thus the coupling coefficient may be slightly different from zero which deteriorates the isolation. It is noted that the simultaneous

change of two elements in the coupling matrix can release the zero coupling requirements, as analyzed in Section II. Consequently, both M_{S1} and M_{2L} are changed by adding the switch circuitries to the input and output feeding lines for achieving higher isolation.

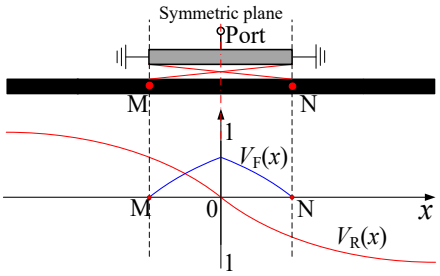

Figure 2.8. Simplified OFF-state schematic of the feeding structure and the voltage distribution.

2.3.2.4 Experiment and Comparison

For verifying the proposed concept, a single-band filtering switch is implemented using the LTCC process. The Ferro A6-M substrate is used with a dielectric constant of 5.9 and a loss tangent of 0.002. In this multilayer circuit realization, discontinuity and mutual coupling are quite common. Therefore, a parameter sweep and optimization are performed. For example, the length of the resonator is swept to obtain the desired center frequency and the length of TL1 is optimized for high isolation, et al. The final circuit with the test PCB board is shown in Figure 2.9. And the photograph is shown inset of Figure 2.10(b). It has a compact circuit size of 4.4 mm × 4.2 mm × 2 mm or 0.050 λ_g × 0.048 λ_g × 0.023 λ_g, where λ_g is the guided wavelength at the center frequency of the passband.

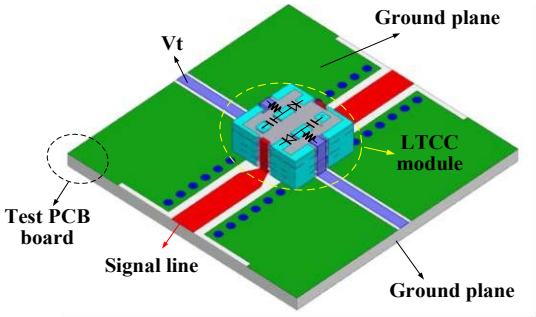

Figure 2.9. A 3-D view of the proposed LTCC filtering switch with a test PCB board.

The simulations and measurements are accomplished by using high-frequency structure simulator (HFSS) and Agilent 8753ES network analyzer, respectively. Figure 2.10 shows the simulated and measured results. In the ON-state, the passband is measured at 1.4 GHz with a 3-dB bandwidth of 12%. The insertion loss at the center frequency is 2.33 dB and the return loss is better than 20 dB. Two transmission zeros appear at the frequencies of 1.75 GHz and 2.87 GHz, which help to enhance the skit selectivity and suppress the harmonic. More than 22 dB rejection levels are realized from 1.67 GHz to 3.5 GHz. In the OFF-state, the isolation is better than 47 dB within the passband and more than 39 dB from 1 GHz to 2 GHz.

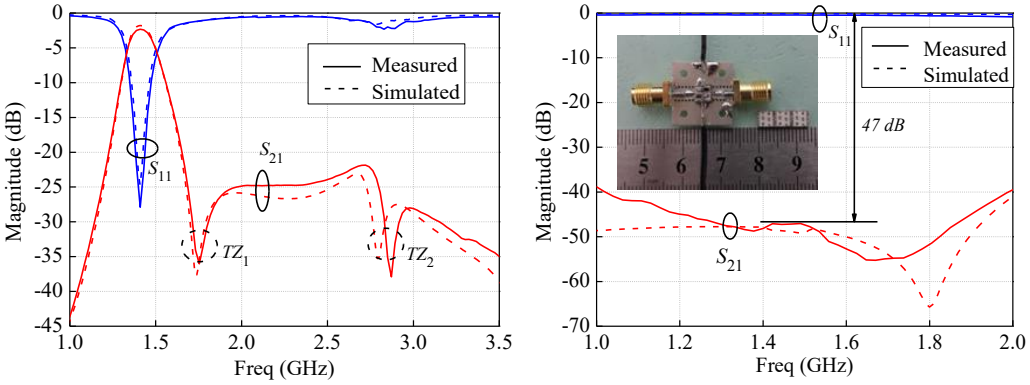

(a) (b)

Figure 2.10. Simulated and measured results of the single-band LTCC filtering switch; (a) ON-state; (b) OFF-state.

Table 2.1 shows the comparison with some LTCC filters [75], [76] and switch products from companies of Skyworks and RFMD [82], [83]. It is assumed that when the LTCC filter and switch are cascaded, the total insertion loss is the sum of the filter loss and switch loss. And the OFF-state isolation is the sum of the filter loss and switch isolation. It can be observed that the insertion loss of this work only includes the LTCC filter loss, which is much lower than the cascaded LTCC filter and switch. Meanwhile, the isolation in our work is 47 dB, which is much higher than that of cascaded one of about 35.4 dB. For the external quality factor (Q_e), it is the same as LTCC filter designs because signals in the ON-state do not pass

through the PIN diodes embedded in the feeding lines. Thus, the coupling between the feeding line and resonator is the same as that in LTCC filters [75], [76]. Also, the PIN diodes do not affect the unloaded quality factor (Q_u) in the proposed design and thus it is almost the same as those in [75], [76]. As for the circuit size, the proposed design is comparable to the LTCC filters without the switch function.

Table 2.1 Comparison With LTCC Filters and Switches

Ref.	Component	IL (ON)	FBW (ON)	Isolation (OFF)	Q_u	Q_e	Size (λ_g^3)
[75]	LTCC filter	2.5 dB	10.8 %	-	37	8.61	0.054×0.045×0.013
[76]	LTCC filter	2.4 dB	12.5 %	-	33	7.44	0.058×0.058×0.01
[82]	Switch	0.7 dB	-	31 dB	-	-	-
[83]	Switch	0.65 dB	-	33 dB	-	-	-
[76] + [83]	LTCC Filter + Switch	3.05 dB	12.5 %	35.4 dB	-	-	> 0.058×0.058×0.01
This work	Filtering switch	2.33 dB	12 %	47 dB	35	7.75	0.05×0.048×0.023

2.3.3 Dual-Band LTCC Filtering Switch

Based on the single-band filtering switch, a dual-band one is further studied and implemented using LTCC techniques. In the ON-state, it is equivalent to a dual-band BPF which has sufficient degrees of freedom to adjust the Q_e and k within two passbands. Thus, the center frequencies and bandwidths of two passbands can be individually controlled. Meanwhile, high OFF-state isolation is realized within two passbands by satisfying the requirement of the OFF-state coupling matrix.

2.3.3.1 Circuit Configuration

Figures 2.11(a) and (b) show the schematic (equivalent circuit) and the 3-D structure of the proposed dual-band LTCC filtering switch, which is similar to the

single-band one shown in Figure 2.5. The main difference is that the dual-band one uses additional T-shape stubs located at the center of the resonators. An open stub TL2' is added to the center of the feeding line, which is coupled to the T-shape stub. Four quasi-lumped capacitors (*C*') are symmetrically placed between the feeding lines and resonators, which are realized by two-layer coupled patches. The input and output feeding lines are asymmetrically placed to generate a transmission zero between the two passbands.

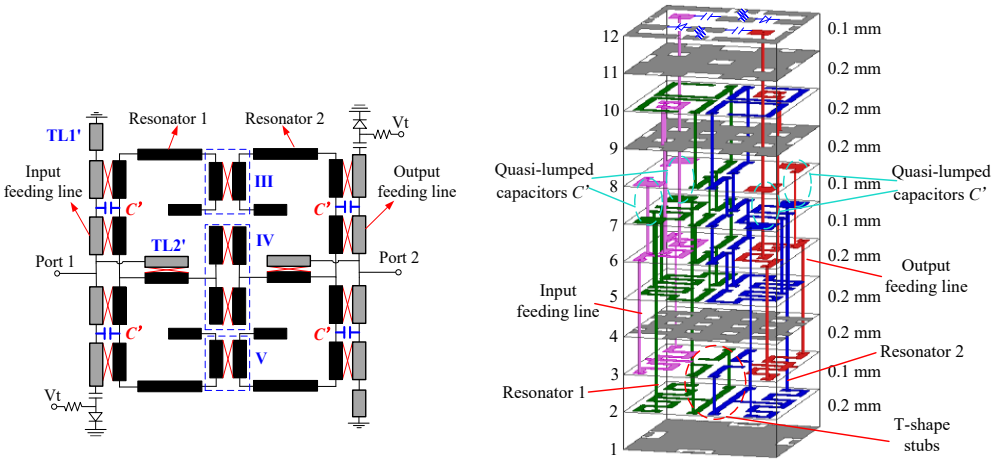

(a) (b)

Figure 2.11. Dual-band LTCC filtering switch; (a) Schematic; (b) 3-D structure.

2.3.3.2 Analysis of the ON-state Responses

When the PIN diodes are turned off, the circuit is equivalent to a BPF with independently controlled dual passbands. As for the passband frequencies, they are determined by the stub- loaded resonator as shown in Figure 2.12(a). It consists of a main transmission line and a T-sharp centrally-loaded stub, where Y_{m1}, Y_{m2}, Y_{m3}, and θ_{m1}, θ_{m2}, θ_{m3} denote the characteristic admittances and electric lengths, respectively. Since the structure is symmetric, even- and odd-mode analysis is adopted to characterize it. Figures 2.12(b) and (c) show the even- and odd- mode equivalent circuits, respectively. To simplify the analysis, it is assumed that $Y_{m1} = Y_{m2} = 0.5\ Y_{m2}$, and the even- and odd-mode resonance frequencies can be calculated as [12]

$$f_{even} = \frac{nc}{2(L_{m1} + L_{m2} + L_{m3})\sqrt{\varepsilon_{eff}}} \tag{2.17}$$

$$f_{odd} = \frac{(2n-1)c}{4L_{m1}\sqrt{\varepsilon_{eff}}} \tag{2.18}$$

where n = 1, 2, 3…, ε_{eff} is the effective dielectric constant of the substrate. From (2.17) and (2.18), it can be observed the odd-mode equivalent circuit is utilized as a quarter-wavelength resonator at f_{odd}, while the even-mode equivalent circuit is regarded as a half-wavelength resonator at f_{even}. The f_{odd} is only controlled by L_{m1}. Thus, the length of L_{m2} and L_{m3} can be utilized to obtain the desired f_{even} without impact on the f_{odd}. Accordingly, by using the f_{odd} and f_{even} to form two passbands, the center frequencies can be controlled individually. Also, by studying the voltage distribution of the half-wavelength even-mode equivalent circuit, it is found that there is a voltage null at the center, as shown in Figure 2.12(d). Capacitors C' are designed at the voltage null at f_{even} of the resonators, which will be discussed later.

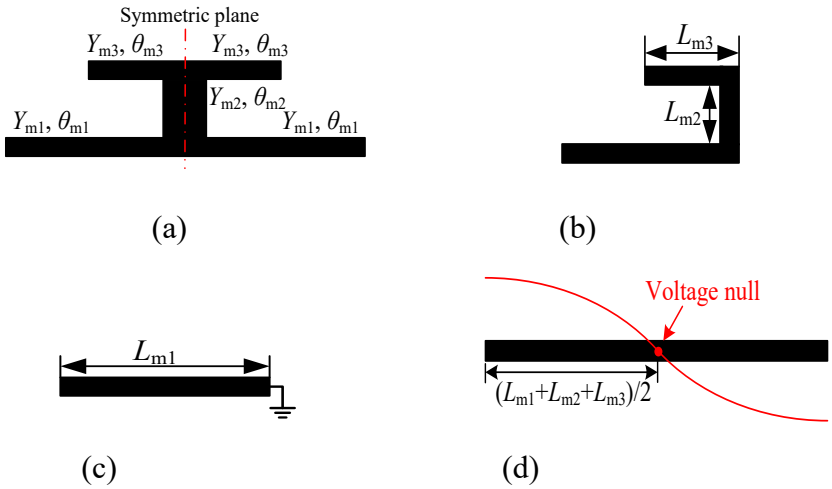

Figure 2.12. (a) The structure of the stub-loaded resonator; (b) Even-mode equivalent circuit; (c) Odd-mode equivalent circuit; (d) voltage distribution of the even-mode circuit.

Besides the passband frequencies, the bandwidth of the first passband is centered at 1.4 GHz with the *FBW* of 12%, while the second passband is centered at 2.45

GHz with the *FBW* of 7%. According to equations (2.7), (2.9) and (2.10), the desired ON-state k and Q_e at the first and second passbands can be calculated as: $k_{1,on} = 0.154$, $Q_{e1,on} = 7.75$; $k_{2,on} = 0.09$, $Q_{e2,on} = 13.3$. These required parameters can be realized as follows.

In order to realize the desired $k_{1,on}$, $k_{2,on}$, three coupling regions are selected, as shown in Figure 2.11(a). In region III and V, parts of the main transmission lines are coupled. In region IV, parts of the center-loaded T-sharp stubs are coupled to each other. From the mode analysis, it is known that the transmission lines in region IV are parts of the even-mode equivalent circuit and can be ignored for the odd-mode circuit. Thus, they only influence the $k_{2,on}$. While regions III and V are parts of both the even- and odd-mode circuits, they have an impact on both the $k_{1,on}$ and $k_{2,on}$. Accordingly, we can first determine the coupling region III and V to realize the required $k_{1,on}$. And then coupling region IV is utilized to tune the $k_{2,on}$ without altering $k_{1,on}$. As a result, the required $k_{1,on}$ and $k_{2,on}$ are realized.

As for the $Q_{e1,on}$ and $Q_{e2,on}$, they can be realized by introducing the novel feeding structures including four quasi-lumped capacitors C'. We obtain the $Q_{e2,on}$ at first and then realize the desired $Q_{e1,on}$ with very slight impact on $Q_{e2,on}$. The gaps or the distances between the feeding lines and resonators, which have an impact on both the $Q_{e1,on}$ and $Q_{e2,on}$, are adjusted to obtain the desired $Q_{e2,on}$ firstly. Since the quasi-lumped capacitors C' are located at the voltage null of the resonator at f_{even} as illustrated in Figure 2.12(d), the value of C' has a slight influence on $Q_{e2,on}$. Thus, they can be tuned to change the $Q_{e1,on}$ with $Q_{e2,on}$ almost unchanged. Then, fine-tuning of $Q_{e1,on}$ and $Q_{e2,on}$ is performed. In this way, both the desired $Q_{e1,on}$ and $Q_{e2,on}$ are realized. In fact, there are enough degrees of freedom when two parameters (the gaps and the quasi-lumped capacitors C') are used to realize two targets ($Q_{e1,on}$ and $Q_{e2,on}$). It is noted that the quasi-lumped capacitors C' are realized by the quasi-lumped elements which can be introduced in the multilayer LTCC circuits and are difficult to be formed in planar PCB circuits.

Based on the above analysis, the bandwidths and frequencies of the dual-band filtering switch can be controlled separately. Figure 2.13 shows the simulated responses. It can be seen that the bandwidth and frequency of the upper passband can be changed with the lower passband unaltered. Moreover, the lower passband can also be controlled. Thus, we can first obtain the desired lower passband responses and then adjust the design parameters to achieve required upper passband responses. In this way, the desired responses of the two passbands can be obtained.

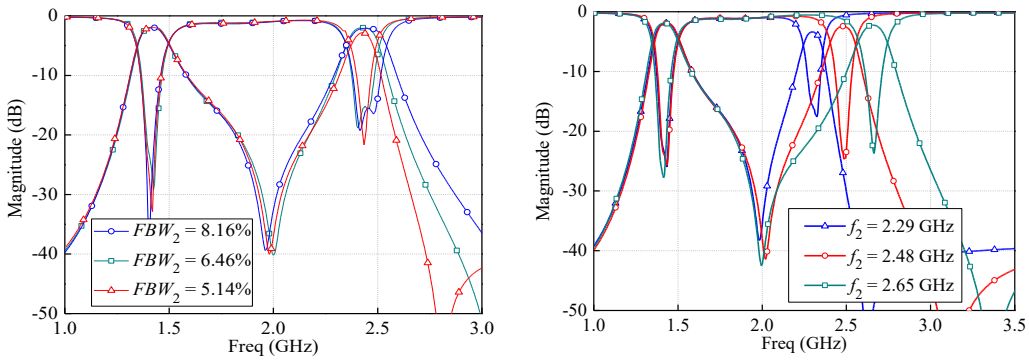

(a) (b)

Figure 2.13. Simulated responses of the dual-band filtering switch (a) with different upper passband bandwidths; (b) with different upper passband frequencies.

2.3.3.3 Analysis of the OFF-state Responses

When the PIN diode is ON, the dual-band filtering switch is in the OFF-state. The coupling between the feeding lines and resonators should be controlled to meet the M_{S1} and M_{2L} in the OFF-state coupling matrix at two passbands. One end of the feeding line, which connects to the switch circuitry, is equivalent to be short. The capacitor effect of the PIN diodes can be compensated by adding TL1'. Thus, the feeding lines are nearly symmetric. Figure 2.14(a) shows the equivalent OFF-state schematic.

When the filtering switch is working at f_{odd}, the T-shape stub can be ignored based on the mode analysis. The voltage distributions on the feeding line $V_{F,odd}(x)$ and the resonator $V_{R,odd}(x)$ are shown in Figure 2.14(b), where $V_{F,odd}(x)$ is even and $V_{R,odd}(x)$ is odd. Thus, the coupling strength determined by $V_{F,odd}(x)$ and $V_{R,odd}(x)$

can be calculated as zero at f_{odd} according to the equation (2.16). Meanwhile, since the feeding line is nearly symmetric, the voltage on the quasi-lumped elements C' is also nearly even, the coupling caused by the symmetric C' is close to zero when $V_{R,\,odd}(x)$ is odd. Thus, the overall coupling between the feeding lines and resonators is close to zero at f_{odd}, which satisfies the M_{S1} and M_{2L} in matrix (2.8) at f_{odd}.

When the filtering switch is working at f_{even}, the voltage distributions on the feeding line and the resonator are shown in Figure 2.14(c), where $V_{RL,even}(x)$, $V_{RS,even}(x)$ and $V_{FL,even}(x)$, $V_{FS,even}(x)$ denote the voltage on the main line and stubs of the resonator and feeding line, respectively. The coupling region includes the region from D to E, E to F, F to G and H to I. The quasi-lumped capacitors C' are located at point E and F which are the voltage null at f_{even} of the resonator. Thus, C' will have no influence on the Q_e at f_{even} ($Q_{e2,off}$). From D to E, the voltages on the feeding line and the resonator are both positive, namely

$$V_{FL,even}^{DE}(x) > 0 \tag{2.19}$$

$$V_{RL,even}^{DE}(x) > 0 \tag{2.20}$$

According to the equation (2.16), the coupling strength at this region at f_{even} is positive, namely $k_{even}^{DE} > 0$.

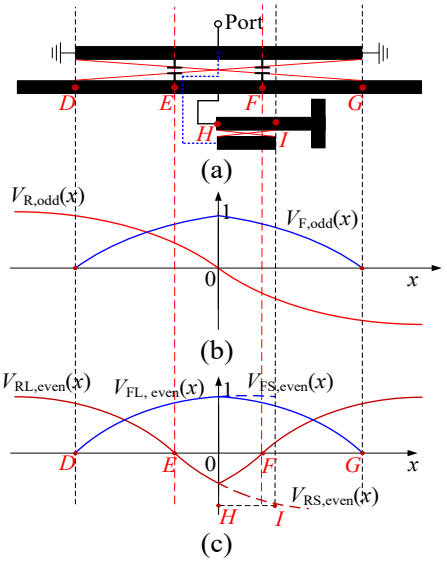

Figure 2.14. (a) The equivalent OFF-state schematic; (b) The voltage distribution at f_{odd}; (c) The voltage distribution at f_{even}.

Similarly, the coupling strength at the regions from *E* to *F*, *F* to *G* and *H* to *I* can be calculated as $k_{even}^{EF} < 0$, $k_{even}^{FG} > 0$ and $k_{even}^{HI} < 0$. Based on this, the overall coupling strength at f_{even} can be expressed as

$$k_{even} = (|k_{even}^{DE}| + |k_{even}^{FG}|) - (|k_{even}^{EF}| + |k_{even}^{HI}|) \tag{2.21}$$

To realize the high OFF-state isolation, k_{even} should be close to zero as indicated by matrix (2.8). According to (2.21), we can first determine the coupling region from *D* to *G*, namely, the strengths of k_{even}^{DE}, k_{even}^{EF} and k_{even}^{FG} are determined. Then, the coupling region *H* to *I* can be tuned to obtain the desired k_{even}^{HI} for making k_{even} close to zero. Accordingly, the required M_{S1} and M_{2L} in matrix (2.8) are realized.

It is noted that in the miniaturized multilayer LTCC circuit, it is very difficult to realize exactly symmetrical configuration. Thus, it is impossible to make coupling to be zero, which deteriorates the isolation. Thus, the same as the single-band design, both M_{S1} and M_{2L} are changed by adding the switch circuitries to the input and output feeding lines for achieving higher isolation.

2.3.3.4 Experiment

The dual-band filtering switch is constituted in the multilayer LTCC structure, as shown in Figure 2.11(b). The circuit size is the same as the single-band one. Seeing from the outside of the LTCC packages, the dual-band filtering switch is the same as the single-band one. The photograph of the fabricated dual-band LTCC filtering switch is the same as the single-band one shown in Figure 2.10(b).

Figure 2.15 shows the simulated and measured results of the dual-band LTCC filtering switch. In the ON-state, the measured passbands are centered at 1.44 GHz and 2.45 GHz with the 3-dB bandwidth of 11.7% and 6.7%, respectively. Since the FBW of the upper passband is narrower and the unloaded *Q* factors at the two frequencies are nearly the same, the insertion loss of the upper passband (2.9 dB) is higher than that of the lower passband (2.26 dB). The return losses are better than 18 dB at two passbands. A transmission zero is located at 2 GHz, which enhances

the skirt selectivity of the two passbands. In the OFF-state, the isolations are better than 40 dB within the two passbands. Meanwhile, the wideband isolation from 1 GHz to 4 GHz is realized higher than 35 dB.

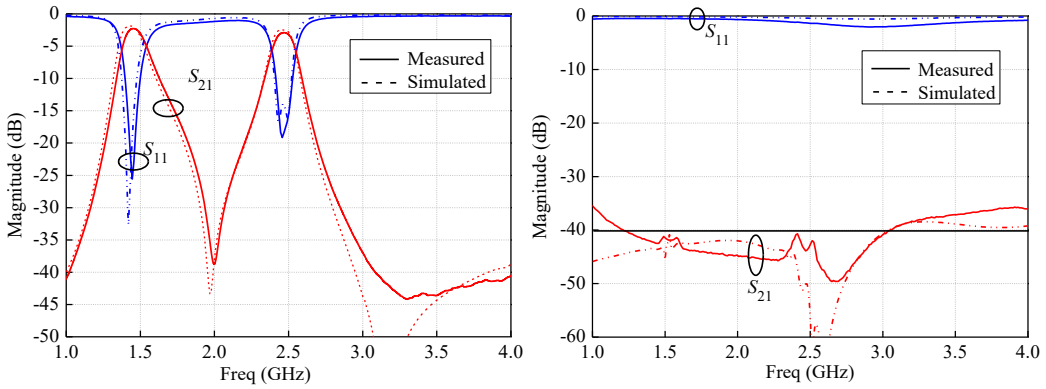

Figure 2.15. Simulated and measured results of the dual-band LTCC filtering switch; (a) ON-state; (b) OFF-state.

2.3.4 Comparison

Table 2.2 shows the comparison with some other filtering switches. In [16] and [17], high isolation is realized by embedding the switchable structures between the resonators or putting them in the output port. However, in the ON-state, the signals pass through the PIN diodes, which introduces extra loss. Comparing to the single-band filtering switches in [19] and [22], the single-band design in our work employs lower-order filters but achieve higher isolation. For the dual-band designs, high isolation of the lower passband is achieved in [67], but the PIN diodes also increase the ON-state insertion loss of the first passband. Meanwhile, the isolation of the second passband is only 25 dB. In [21], the isolation in the two passbands is only 25 and 20 dB, while those in our work are both better than 40 dB. In [72], varactors are utilized to design the switched tunable filters with a wide frequency tuning range. However, in the ON-state, signals go through the varactors which introduce extra loss. Also, the electric coupling as well as magnetic coupling are

not zero, while the total coupling is zero due to the out-of-phase characteristic of electric and magnetic coupling. Thus, this method is not applicable in some cases. For instance, it is difficult to cancel out electric and magnetic coupling in dual-band filtering switches based on dual-mode resonators. Moreover, the work in [72] employs several varactors and thus it is difficult to be realized in LTCC due to limited circuit area. As compared to the other circuits realized in PCB, the LTCC circuits in our design exhibit some advantages. Firstly, by using the LTCC multilayer structure, the circuits are folded horizontally and vertically on different layers, resulting in great size reduction. Secondly, the multilayer structure features more design flexibility. It is convenient to realize multiple coupling regions and quasi-lumped elements. Besides, the broadside coupling realized by the multilayer structure can provide stronger coupling. Thus, the coupling strength can be controlled with a wide range.

Table 2.2 Comparison With Some Other Filtering Switches

Ref.	Band	Filter orders	Additional loss (ON)	Isolation (OFF)	Fabricated process
[16]	Single	2	Yes	44	PCB
[17]	Single	4	Yes	48	PCB
[19]	Single	4	NO	35	PCB
[22]	Single	3	NO	40	PCB
[21]	Dual	2	Yes	45/25	PCB
[67]	Dual	2	NO	25/20	PCB
[72]	Single/Tunable	3	Yes	40	PCB
This work	Single	2	NO	47	LTCC
	Dual	2	NO	40/40	LTCC

Additional loss means that the signals pass through the PIN diodes when the filtering switch is in the ON state and the PIN diodes cause extra loss.

2.4 SPST and SPDT Filtering Switches Based on $TE_{11\delta}$-Mode Dielectric Resonators

In the above section, filtering switches are proposed using LTCC technology, which have very compact sizes and the insertion losses can be reduced as compared to the classical cascaded design. Due to the Q factor and power handling capability limitation, the above LTCC filtering switches and the reported PCB designs cannot be used in some narrowband applications, for example, the fractional bandwidth is smaller than 2%. Otherwise, the insertion losses would be very high. The high-Q dielectric resonators (DRs) can not only be used to obtain low insertion loss under narrowband applications but also have high power handling capability, which have widely employed in base station and satellite applications. Lots of microwave circuits have been designed using DRs, such as filters, diplexers, filtering baluns and so on. For example, in [84], a compact in-line filter is presented with pseudoelliptic responses by employing the mixed TE_{101} cavity mode and $TE_{01\delta}$ dielectric mode. Based on the multi-mode DRs, BPFs and diplexers are designed with compact size [85]-[87]. Besides, electromagnetic (EM) field properties of DRs can be analyzed to realize different phase shifts between the metal probe and DRs. Then, balanced/balun BPFs can be designed by using DRs with narrow FBW and low loss conveniently. Nevertheless, due to the 3-D metallic structures, it seems difficult to embed the PIN diodes or transistors into the DR filters. So far, the DR filter and switch are existed in the wireless system based on cascaded design. The filtering switches based on DRs have not been reported.

In this thesis, the DR filters are co-designed with switches to realize single-pole single-throw (SPST) and single-pole double-throw (SPDT) filtering switches. The electromagnetic (EM) fields of the DR, non-resonance node (NRN) and feeding line are firstly studied for guiding the circuit realization. The ON- and OFF-states are controlled by PIN diodes mounted on PCBs which are embedded in the metal

cavity. A DR-based filtering SPST switch is implemented by adding PIN diodes to the feeding lines. In the ON-state, the PIN diodes are turned off and signals do not pass through them. Consequently, the PIN diodes do not introduce extra loss and reduce power handling capability. In the OFF-state, the isolation is realized by manipulating the filtering structure rather than turning off the diode or transistor in classical switches and it is thus significantly enhanced. To expand the applications, two DR-based filtering SPDT switches are also implemented. Novel methods for generating transmission zeros are utilized and the results are presented.

2.4.1 Analysis of Two Types of Coupling Schemes

The ON- and OFF-states of the proposed filtering switches are realized by using two types of coupling schemes (Types I and II) which consist of a DR and a T-shape metal probe. In the ON-state, the Type I coupling scheme is used to obtain the desired bandpass responses, while Type II is employed for realizing high isolation in the OFF-state. The two coupling schemes corresponding to the two states are analyzed by studying the EM field distributions of the DR and T-shape metal probe, which is addressed below.

2.4.1.1 EM Fields of the Rectangular DR

In the proposed filtering switches, rectangular DRs are employed with a 3-dimension (3-D) view shown in Figure 2.16. The A, B, and L are the length, width, and height, respectively. There are lots of modes resonating at different frequencies. Due to the regular distribution of EM fields, the $TE_{mn(s+\delta)}$ and $TM_{mn(s+\delta)}$ are most popularly used, where m, n, and s are the numbers of the half wave inside of the DR along the x, y and z directions, and $0 < \delta < 1$ [51]. Generally, when a small ratio $L/(A+B)$ is chosen, the dominant mode of the rectangular DR is the $TE_{11\delta}$ mode [51], which is used in the proposed designs. For the $TE_{mn(s+\delta)}$ mode, the EM fields can be calculated by the Hybrid Magnetic Wall Method based on Helmholtz Equation and boundary conditions as follows [51]

$$\begin{cases} E_x = -\dfrac{j\omega\mu_0}{k^2+\gamma_z^2}\dfrac{\partial H_z}{\partial y}, \quad E_y = \dfrac{j\omega\mu_0}{k^2+\gamma_z^2}\dfrac{\partial H_z}{\partial x}, \\ H_x = \dfrac{1}{k^2+\gamma_z^2}\dfrac{\partial^2 H_z}{\partial x \partial z}, \quad H_y = \dfrac{1}{k^2+\gamma_z^2}\dfrac{\partial^2 H_z}{\partial y \partial z}, \end{cases}$$

$$H_z = \begin{cases} A_1 \sin k_x x \cdot \sin k_y y \cdot \sin\left(k_z z + \varphi\right) & 0 \le z \le L \\ A_2 \sin k_x x \cdot \sin k_y y \cdot e^{-\alpha_z (z-L)} & z \ge L \\ A_3 \sin k_x x \cdot \sin k_y y \cdot e^{\alpha_z z} & z \le 0 \end{cases} \tag{2.22}$$

where

$$k_x^2 + k_y^2 + k_z^2 = \varepsilon_r k_0^2 \qquad 0 \le z \le L$$

$$k_x^2 + k_y^2 + \alpha_z^2 = k_0^2 \qquad z \ge L \,\&\, z \le 0$$

$$k_x = m\pi/A, \quad k_y = n\pi/B, \quad k_z = \left(s+\delta\right)\pi/L$$

$$\varphi = \frac{\pi}{2} - \tan^{-1}\left(\frac{\alpha_z}{k_z}\right)$$

where k is wave number at operation frequency, γ_z is the propagation constant along the z-direction, μ_0 is the permeability in vacuum, and ε_r is the relative permittivity of the DR.

According to equation (2.22), the EM fields of the DR at $TE_{11\delta}$ mode are illustrated in Figure 2.17. From the EM fields in the x-y plane shown in Figures 2.17(a) and (b), it can be observed that the electric field (E-field) is out-of-phase with respect to the center plane S_1-S_1', where red arrows represent the strongest density. Figures 2.17(c) and (d) illustrate the magnetic field (H-field) at the plane of $z = L/2$, where the H-field is perpendicular to this plane and symmetric with respect to the center plane S_1-S_1'.

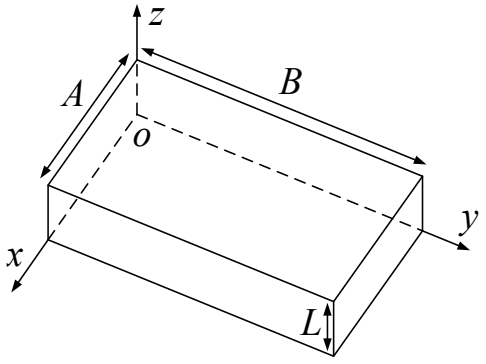

Figure 2.16. A 3-D view of a typical rectangular DR.

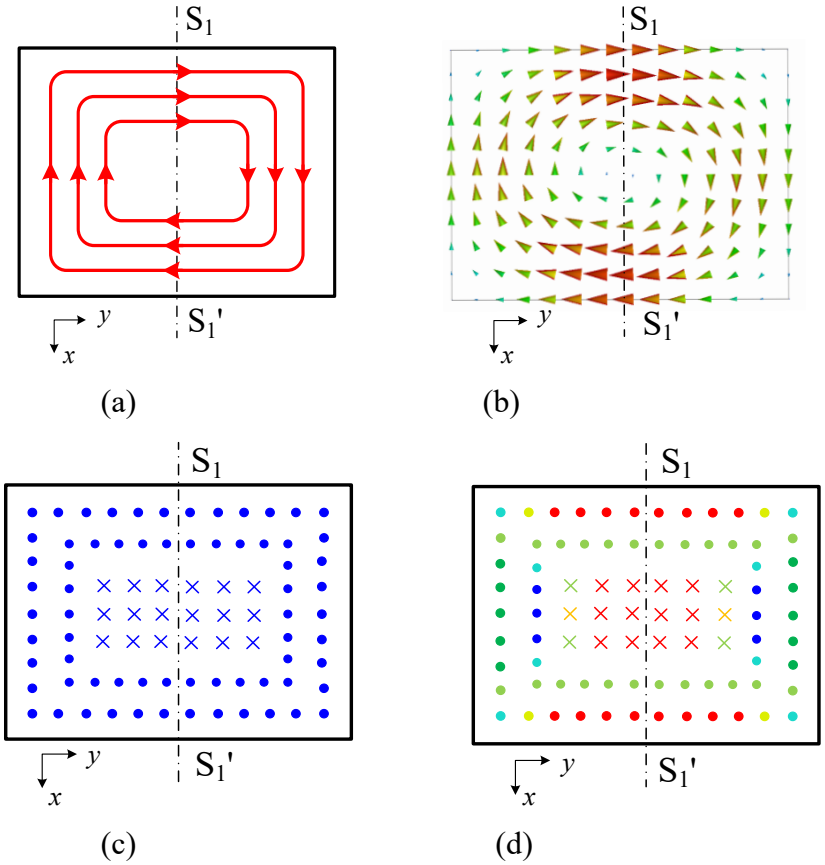

Figure 2.17. EM field distributions of the $TE_{11\delta}$-mode rectangular DR (a) Vector of E-field in the *x*-*y* plane; (b) Magnitude of E-field in the *x*-*y* plane; (c) Vector of H-field in the plane of z = *L*/2; (d) Magnitude of H-field in the plane of z = *L*/2.

2.4.1.2 EM Fields of the T-Shape Metal Probe

To design the desired coupling schemes for the ON- and OFF-states, a T-shape metal probe is utilized as the feeding line or NRN, which is placed in the metal cavity, as shown in Figure 18(a). The T-shape probe consists of two branch lines with the main line at the center. One end of the branch lines is short-circuited, while the other is short- or open-circuited, leading to different states of the filtering switch. When signals are transmitted in the branch lines, the transmission mode is similar to that in the coaxial line. According to the transmission line theory, the normalized voltage and current distributions on the two branch lines (I_1/U_1 and I_2/U_2) are expressed as

1) With two short ends:

$$\begin{cases} I_1 = I_L \cos(\beta(y+l)), U_1 = jI_L Z_C \sin(\beta(y+l)), & y<0 \\ I_2 = I_L \cos(\beta(y-l)), U_2 = jI_L Z_C \sin(\beta(y-l)), & y>0 \end{cases} \tag{2.23}$$

2) With one short end and one open end:

$$\begin{cases} I_1 = I_L \cos(\beta(y+l)), U_1 = jI_L Z_C \sin(\beta(y+l)), & y<0 \\ I_2 = I_L \cos(\beta(y+l)), U_2 = jI_L Z_C \sin(\beta(y+l)), & y>0 \end{cases} \tag{2.24}$$

where I_L is the current at the short end of the metal probe, Z_c and β denote the characteristic impedance and propagation constant, respectively.

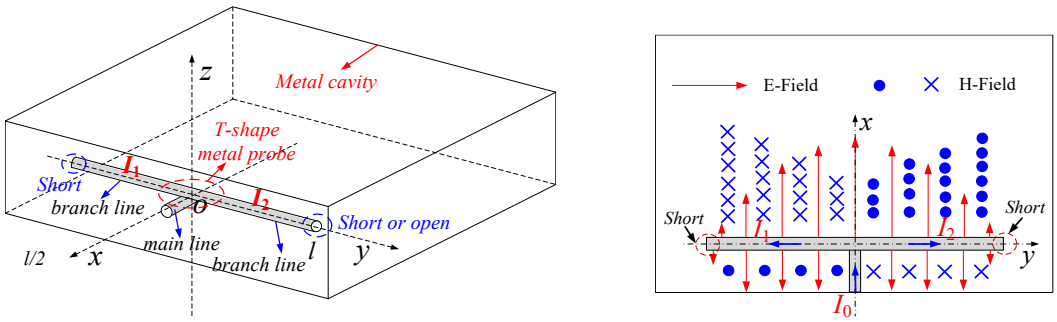

(a) (b)

Figure 2.18. (a) The structure of the metal probe in the metal cavity; (b) E- and H-fields of the metal probe with two short-circuited branches.

According to the voltage and current equations (2.23) and (2.24), the EM fields can be studied. For easy analysis, the effect of main line on the EM field distribution is ignored because of the short electric length. Figure 2.18(b) shows the EM fields at the *x*-*y* plane when two branch lines are short. It can be observed that the E-field is symmetric with respect to the *x*-axis. As for the H-field, it is out-of-phase at two sides of the *x*-axis. When one of the branch lines is short-circuited and the other is open-circuited, the current and voltage at two sides of S_1-S_1' are asymmetric. Thus, both E- and H-fields are asymmetric.

2.4.1.3 Coupling Scheme Analysis

The ON- and OFF-states of the proposed DR filtering switches are realized by using two different coupling schemes, namely, Type I and Type II. Figure 2.19(a) shows the Type I coupling scheme between a rectangular DR and the T-shape metal probe. The branch lines of the metal probe with two short ends are coupled to the DR, which is symmetric with respect to the center plane in Figure 2.19(a). The coupling coefficient (k) between the DR and metal probe is studied, which can be expressed by the electric and magnetic coupling coefficients (k_e and k_m) as

$$k = k_e - k_m \tag{2.25}$$

The k_e and k_m in (2.25) can be defined on the basis of the ratio of coupled energy to stored energy by using equations (2.4) and (2.5).

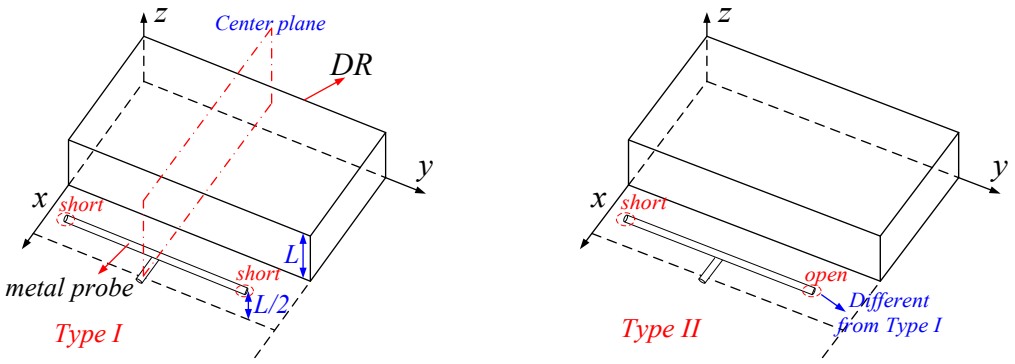

Figure 2.19. The proposed coupling schemes (a) Type I; (b) Type II.

For easy analysis, parts of the H-fields at the coupling regions in the plane of z = $L/2$ are shown in Figure 2.20(a). Based on the analysis in section II-A and B, the H-field of the DR is symmetric with respect to the center plane. As for the H-field of the metal probe, it is out-of-phase at two sides of the center plane. Thus, the k_m of Type I (k_{m1}) is zero according to (2.5), namely, $k_{m1} = 0$. The E-field is shown in Figure 2.20(b). The E-field of the metal probe is symmetric with respect to the center plane. However, the E-field of the DR at the x-axis is out-of-phase at two

sides of the center plane. Thus, from equation (2.4), k_e for Type I (k_{e1}) is zero, namely, $k_{e1} = 0$. Accordingly, k_1 is equal to zero from (2.25), namely, $k_1 = k_{e1} - k_{m1} = 0$.

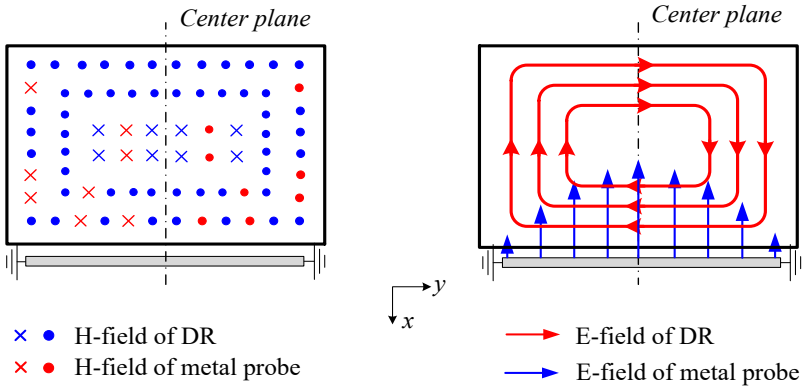

(a) (b)

Figure 2.20. EM fields for the Type I coupling scheme; (a) H-filed; (b) E-filed.

Figure 2.19(b) shows the structure of the Type II coupling scheme where one end of branch lines is short-circuited and the other end is open-circuited. Similar to Type I, the k of Type II (k_2) can also be analyzed. It has been discussed in section II-B that when the metal probe is asymmetric, the E-field and H-field of the metal probe are asymmetric. According to the EM fields of the DR and the equations (2.4)-(2.5), it can be known that k_2 is not zero, namely, $k_2 \neq 0$. The value of k_2 can be controlled by the distance between the DR and metal probe in Type II.

2.4.2 DR-Based SPST Filtering Switch

Based on the analysis in Section 2.3.1, a narrow-band fourth-order DR filtering SPST switch is designed with the 3-D view structure shown in Figure 2.21. It consists of a metallic cavity, four rectangular DRs (DR_1-DR_4) and input and output feeding lines. A hole is dug at the center of the DR to separate the $TE_{11\delta}$ and $TM_{11\delta}$ modes. Tuning disks are installed above the DRs for resonant frequency tuning. To enable the integration of switch circuitries including the capacitors (C), PIN diode

and resistor (R), PCBs are embedded in the metallic cavity, as shown in Figure 2.21. The input and output feeding lines are composed of the T-shape metal probes. One end of the feeding line is connected to the metallic cavity and grounded, while the other end is connected to the switch circuitry on the PCB. The inter-stage coupling is realized by the windows between the cavities. A metal probe is placed between DR_1 and DR_4 to provide electric cross coupling.

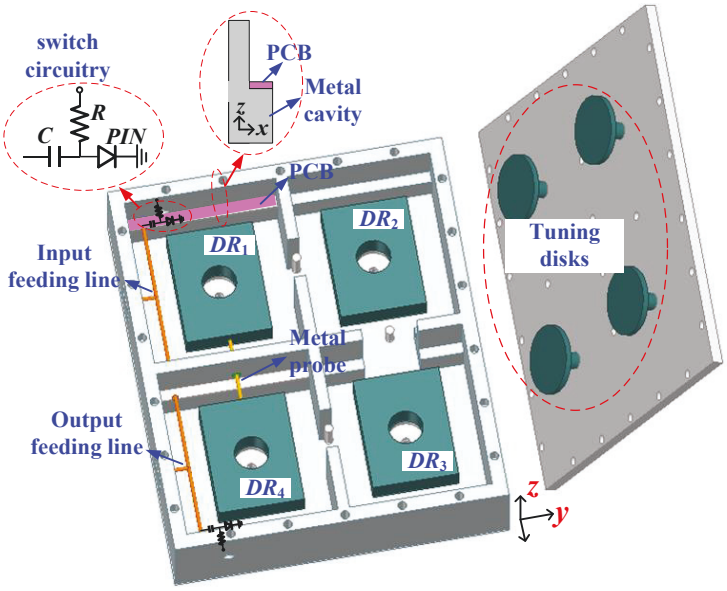

Figure 2.21. A 3-D view of the fourth-order DR filtering switch.

2.4.2.1 Analysis of OFF-State

When the PIN diodes in Figure 2.21 are turned on, the DR filtering SPST switch is in the OFF-state, as analyzed below. Figure 2.22(a) shows the equivalent circuit of the feeding line. One end of the feeding line is connected to the metallic cavity and this end is short-circuited. The other end connected by the switch circuitry is regarded as short-circuited because the PIN diodes are turned on. It should be noted that there exists a capacitance effect introduced by the switch circuitry, which increases the effective length of the feeding line. For this reason, the other end of the feeding line, which is connected to the metallic cavity, is slightly extended to compensate the capacitance effect. Accordingly, the feeding line with two short

ends is nearly symmetric with respect to the center plane. Thus, the coupling between the input (output) feeding line and DR_1 (DR_4) is the same as that of Type I. Based on the analysis in Section 2.3.1.3, the coupling strength is zero. Accordingly, signals at $TE_{11\delta}$ cannot be delivered from port 1 to port 2, resulting in high OFF-state isolation.

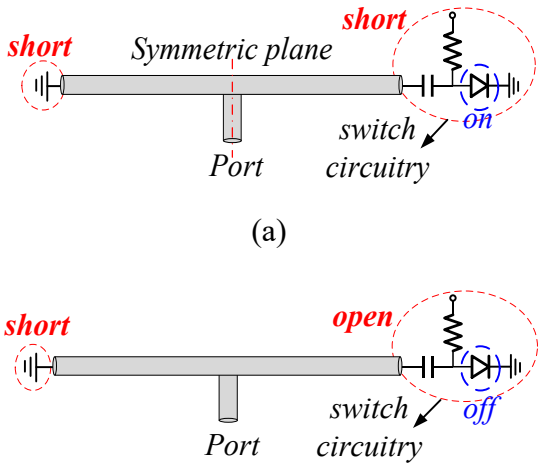

Figure 2.22. Equivalent circuits of the feeding in the (a) OFF-state; (b) ON-state.

2.4.2.2 Analysis of ON-state

When the PIN diodes in Figure 2.21 are turned off, the DR-based SPST filtering switch is in the ON-state. The end of the feeding line connected by the switch circuitry is open-circuited, while the other end connected to the metallic cavity is short-circuited, as shown in Figure 2.22(b). Since no signals pass through the switch circuitries, the filtering switch is the same as a BPF. Thus, the power handling capability is the same as a dielectric filter. Moreover, the classical filter synthesis method can be adopted as presented below.

Since the feeding line with open and short ends is asymmetric, the coupling between the input (output) feeding line and DR_1 (DR_4) is the same as that of Type II. Thus, the coupling strength between the feeding lines and DRs can be controlled to obtain the desired input and output external quality factors. In this design, the

passband is centered at 1.832 GHz with the fractional bandwidth (*FBW*) of 0.65%. The return loss is set to be better than 20 dB. Two transmission zeros are appointed at 1.8 GHz and 1.865 GHz. Based on the structure in Figure 2.9, the N+2 order coupling matrix is synthesized as [79]

$$M_{N+2}=\begin{bmatrix} 0 & 1.0343 & 0 & 0 & 0 & 0 \\ 1.0343 & 0 & -0.9083 & 0 & 0.0117 & 0 \\ 0 & -0.9083 & 0 & -0.7046 & 0 & 0 \\ 0 & 0 & -0.7046 & -0.0001 & -0.9083 & 0 \\ 0 & 0.0117 & 0 & -0.9083 & 0 & 1.0343 \\ 0 & 0 & 0 & 0 & 1.0343 & 0 \end{bmatrix} \tag{2.26}$$

The desired coupling coefficient k and external quality factor Q_e can be calculated by using equations (2.9) and (2.10). Hence the parameters can be calculated as follows: $k_{12} = k_{34} = 0.0059$, $k_{23} = 0.0046$, $k_{14} = 0.0000765$, $Q_e = 143.8$. Consequently, the design parameters of the DR filtering SPST switch can be determined following the classical filter design theory.

2.4.2.3 Experiment

Based on the mechanism discussed above, the proposed DR SPST filtering switch is implemented. Figure 2.21 shows the 3-D structure. The substrate of DRs has a dielectric constant of 36.5. The PIN diodes used in the design are SMP 1302-085LF from Skyworks. The photograph of the proposed filtering switch is shown in Figure 2.23. The size is 13 × 11.5 cm^2 (0.79 × 0.70 λ_g^2).

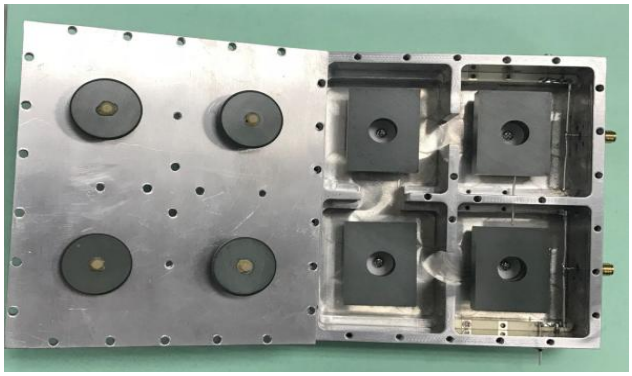

Figure 2.23. Photograph of the fabricated DR-based SPST filtering switch.

The simulation and measurement are carried out by using the high frequency structure simulator (HFSS) and Agilent 8753ES network analyzer, respectively. Good agreement between the theoretical, simulated and measured ON-state responses is observed in Figure 2.24(a). The measured passband is centered at 1.832 GHz with the 3-dB FBW of 0.64 %. The insertion loss at the center frequency is less than 1 dB and the return loss is better than 20 dB. The unloaded Q-factor of the resonator is around 2500. The out-of-band rejection levels are more than 68 dB. Two transmission zeros appear at 1.8 and 1.865 GHz, which greatly enhance the skirt selectively. In the ON-state power handling capability measurement, the reverse bias voltage of 65V is applied to the PIN diodes. It is noted that the overall voltage on the PIN diodes is the superposition of the voltages of the bias and signals. If low (or no) reverse bias voltage is applied, the overall voltage may be higher than the threshold one and thus the diodes will be turned on. Therefore, the high reverse bias voltage is used to ensure that the PIN diodes are off and consequently to improve the power handling capability. In the OFF-state, the isolation is better than 53 dB within the measured frequency range from 1.7 GHz to 1.95 GHz, as shown in Figure 2.24(b). Good performance of the low ON-state loss, high power handling capability and high OFF-state isolation verifies the proposed idea.

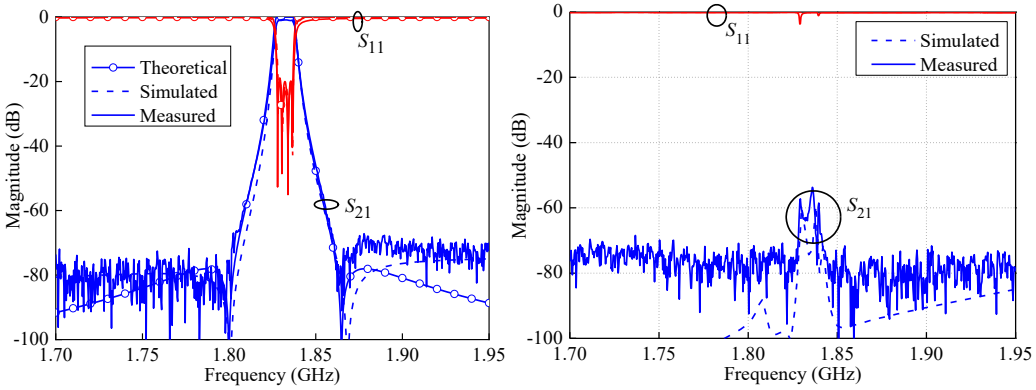

(a) (b)

Figure 2.24. Simulated and measured results (a) In the ON-state; (b) In the OFF-state.

2.4.3 Two-Cavity DR-Based SPDT Filtering Switch

2.4.3.1 Circuit Configuration

Based on the above DR-based SPST filtering switch, a two-cavity SPDT filtering switch is also proposed. Figure 2.25(a) shows the 3-D configuration of the proposed SPDT filtering switch. It consists of a metallic cavity, two DRs (R_1 and R_2), input feeding lines (P1) and two output feeding lines (P2 and P3), where P2 and P3 are both coupled to R_2. One end of each output feeding line is connected to the switch circuitries including the PIN diodes (PIN1 or PIN2), inductors and capacitors (C_1 or C_2), while the other end connects to the capacitors (C_3 or C_4). The topology is shown in Figure 2.25(b). By controlling the PIN1 and PIN2, the circuit works in two states, namely, State 1 and State 2.

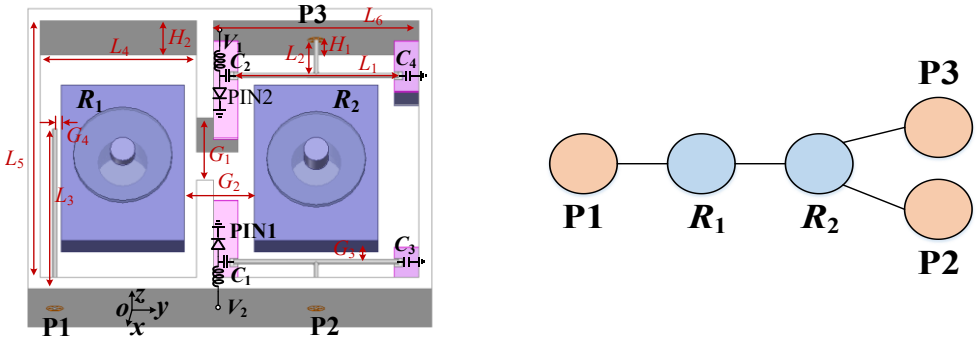

(a) (b)

Figure 2.25. Two-cavity DR-based SPDT filtering switch (a) 3-D structure; (b) Topology.

2.4.3.2 Analysis of the Working Mechanism

When PIN1 is turned on and PIN2 is turned off, the filtering SPDT switch is in State 1, namely, signals at the operating band can be transmitted from P1 to P3 while P2 is isolated. The detailed analysis is addressed as follows. When PIN1 is turned on, one end of the output feeding line P2 that connects to the switch circuitry is approximate to short-circuit, because signals can pass through the switch circuitry

(C_1 and PIN1) to the ground. The other end of P2, which connects to C_3, is also equivalent to a short-circuit when C_3 is chosen with a large capacitance. In this case, P2 can be regarded as a symmetric structure with two short ends. The structure of P2 and R_2 is the same as the Type I coupling scheme. Thus, both the electric and magnetic coupling coefficients (k_e and k_m) R_2 and P2 can be calculated as zero, namely, $k_e = k_m = 0$. Thus, the total coefficient $k = k_e + k_m$ is also zero. Accordingly, it can be concluded that the signals cannot be transmitted from P1 to P2 in State 1, resulting in isolated performance.

Since PIN2 is turned off in State 1, P3 is not symmetric. The structure of P3 and R_2 is the same as the Type II coupling scheme and thus the coupling coefficient between R_2 and P3 is non-zero, which can be tuned to meet the requirement of a BPF. Since the signals do not pass through PIN2, the circuit from P1 to P3 is the same as conventional BPF. Hence, the BPF design method can be utilized. In this design, the Butterworth response is adopted. The lumped element values of the second-order prototype filter are selected to be: $g_0 = 1$, $g_1 = 1.4142$, $g_2 = 1.4142$, $g_3 = 1$. The passband is required to be centered at 1.86 GHz with the FBW of 1.15%. The desired coupling coefficient k and external quality factor Q_e can be calculated $Q_e = 130$, $k = 0.0081$. Consequently, the DR-based structure is constructed to meet these two values and good bandpass responses can be obtained.

In State 2, PIN1 is turned off and PIN2 is turned on. Similar to the above analysis for State 1, it can be known that P3 can be isolated from P1 and P2, while the circuit from P1 to P2 exhibits good bandpass responses. In conclusion, by turning on or off PIN1 and PIN2, the signals at the operating passband can be transmitted from P1 to P2 or P3, featuring good performance of SPDT filtering switch.

2.4.3.3 Experiment

For demonstration, the two-cavity DR-based SPDT filtering switch is implemented. The design parameters are given as follows (all in mm): $L_1 = 40$, L_2

= 7.85, L_3 = 45, L_4 = 38, L_5 = 66, L_6 = 50, G_1 = 8, G_2 = 16.5, G_3 = 3.85, G_4 = 2.5, H_1 = 13, H_2 = 30. The capacitances of C_1 to C_4 are determined as: C_1 = C_2 = 7 pF, C_3 = C_4 = 15 pF. The dielectric material (ε_r = 36.5, tan σ = 0.00015) is from the Jiangsu Jiang Jia Electronics Co., Ltd in Jiangsu, China. The diodes used in this design are implemented with Skyworks SMP 1302-085LF PIN diodes. The photograph of the fabricated filtering SPDT switch is shown in Figure 2.26.

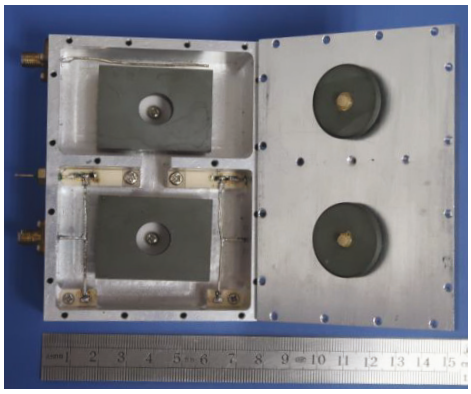

Figure 2.26. Photograph of the fabricated two-cavity DR-based SPDT filtering switch.

The measured results are obtained by using the Agilent E5071C network analyzer, which show good agreement with the simulated one, as shown in Figure 2.27. In State 1, the measured S_{31} is centered at 1.861 GHz with the 3-dB FBW of 1.16%.The return loss is better than 20 dB and the insertion loss is 0.51 dB at the center frequency, featuring good bandpass responses and low loss. Within the 15-dB return loss bandwidth, the difference between maximum and minimum insertion losses is small than 0.15 dB. The measured isolation between P1 and P2 is better than 40 dB at the center frequency and 32 dB within the frequency range from 1.5 to 2.2 GHz. The discrepancy between simulated and measured S_{23} is found in Figures 2.27(a) and (b). It is mainly due to the fabrication errors of the length of the output feeding lines. In State 2, the measured results are almost the same as that in State 1, as shown in Figure 2.27(b), due to the symmetric circuit structure of P2 and P3.The switch time is smaller than 1μs.

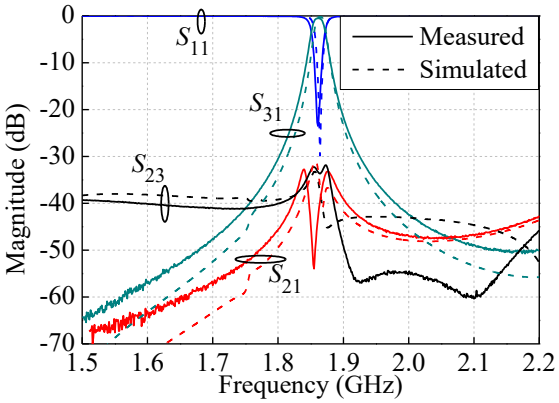

(a)

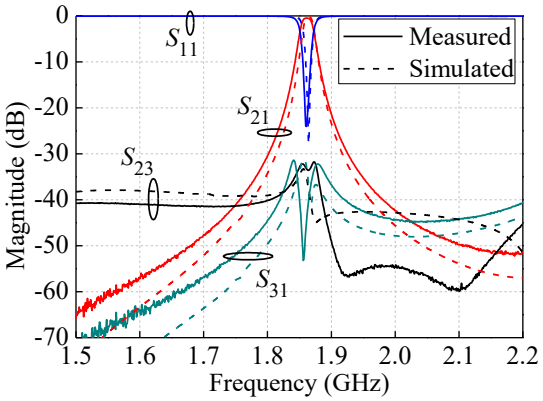

(b)

Figure 2.27. Simulated and measured results (a) In State 1; (b) In State 2.

2.4.4 Three-Cavity DR-Based SPDT Filtering Switch

For the above-proposed two-cavity SPDT filtering switch, there are no transmission zeros near the passband. In order to generate transmission zeros at two sides of the passband to enhance the selectivity, a three-cavity DR-based SPDT filtering switch is proposed. Figure 2.28(a) shows its 3-D structure. It consists of a metallic cavity, three DRs (DR_5-DR_7), two T-shape NRNs (NRN_1 and NRN_2) and three feeding lines (S, L_1, and L_2). Each NRN is placed between two DRs. The branch lines of NRNs are coupled to DR_5 and the main line is coupled to DR_6 or DR_7. PCBs are embedded in the metallic cavity to integrate switch circuitries which are connected to the branch lines of NRNs. The paralleled inductor (L_{DC}) and

capacitor (C_g) are connected to the NRNs. The capacitor is used to compensate the capacitance effect of switch circuitry and the inductor provides the ground for the bias circuit of the PIN diode. Figure 2.28(b) shows the topology of the SPDT DR filtering switch. Cross coupling exists between the feeding lines and NRNs. By using the common S and DR_5, the total circuit can be divided into two filters, namely, Filter 1 and Filter 2, as enclosed in the red and blue dash lines, respectively. By controlling the PIN diodes in NRN_1 and NRN_2, the circuit can work in two states, namely, State 1 (Filter 1 is ON and Filter 2 is OFF) and State 2 (Filter 1 is OFF and Filter 2 is ON).

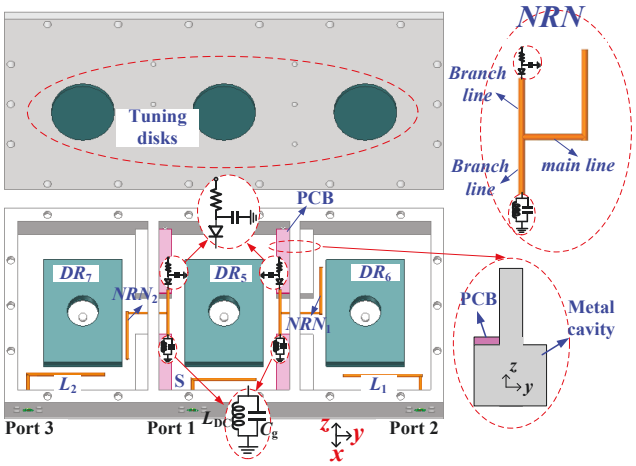

(a)

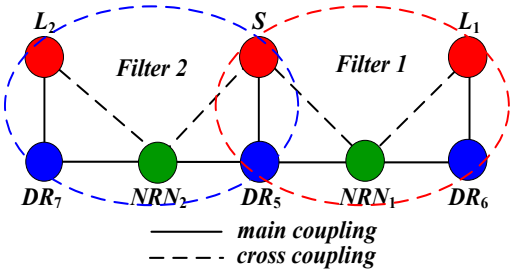

(b)

Figure 2.28. Structure of the SPDT DR filtering switch, (a) 3-D view; (b) Topology.

2.4.4.1 Analysis of State 1: Filter 1 is ON and Filter 2 is OFF

When the PIN diode in NRN_2 is turned on and that in NRN_1 is turned off, the filtering SPDT switch is in state 1, namely, Filter 1 is ON and Filter 2 is OFF. The mechanism is detailed below.

Filter 2 is analyzed firstly. The inductors L_{DC} for providing a DC path can be ignored at the operating frequency. In this case, when the PIN diode in NRN_2 is on, the ends of two branch lines in NRN_2 are shorted to the ground. Thus, the branch lines of NRN_2 are symmetric. Based on the analysis in section II-C, the coupling between DR_5 and NRN_2 is the same as that of *Type I*. The resultant coupling coefficient is zero. Meanwhile, the cross coupling between S and NRN_2 is very weak. Therefore, signals cannot be transferred from S to L_2. Thus, Filter 2 is OFF and high isolation from S to L_2 and from L_1 to L_2 can be obtained.

Since Filter 2 is OFF, it can be ignored. Then, the equivalent structure shown in Figure 2.29(a) includes only Filter 1. When the PIN diode in NRN_1 is off, the ends of the two branch lines in NRN_1 are open-circuited and short-circuited. Thus, NRN_1 is the same as that of *Type II* in section II-C. The coupling between NRN_1 and DR_5 is non-zero and can be controlled. In this case, Filter 1 is the same as the conventional BPF with the topology shown in Figure 2.29(b). Desired passband responses can be realized by using the filter design theory. Due to the cross coupling between S and NRN_1 as well as between NRN_1 and L_1, two transmission zeros can be generated with the mechanism analyzed below.

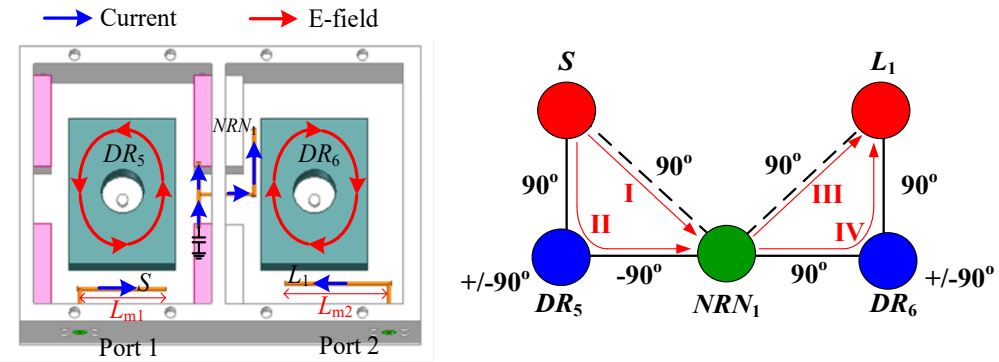

Figure 2.29. (a) The circuit structure of Filter 1; (b) Topology of Filter 1.

In the analysis of transmission zeros, the phase shift generated by the electric and magnetic coupling can be considered as 90° and -90°, respectively. As shown in

Figure 2.29(a), the input feeding line (*S*) with the open end provides electric coupling to the DR_1. Thus, the phase shift from *S* to DR_5 is 90°. Two branch lines in NRN_1 with open and short ends are coupled to DR_5. Because the short end induces a strong magnetic field, the coupling between DR_5 and NRN_1 is magnetic coupling, namely, the phase shift from DR_5 to NRN_1 is -90°. Similarly, the phase shifts from *S* to NRN_1, NRN_1 to DR_6, DR_6 to L_1 and NRN_1 to L_1 are all analyzed to be 90°. For the DR_5 and DR_6, they induce 0° phase shift at the resonant frequency. However, they are equivalent to the capacitor and inductor at the frequencies lower and higher than the passband, which provides 90° and -90° phase shifts, respectively.

Based on the above analysis, the phase relationship can be shown in Figure 2.29(b). There are two transmission paths from *S* to NRN_1, namely, Path I and Path II. At the frequency higher than the passband, the phase shift of each path can be expressed as

$$Path\ I:\ 90^{o} \tag{2.27}$$

$$Path\ II:\ 90^{o}+(-90^{o})+(-90^{o})=-90^{o} \tag{2.28}$$

As indicated by (2.27) and (2.28), the signals transmitted from Path I and Path II are out-of-phase. If their magnitudes are the same at a specific frequency, signals from the two paths can cancel out each other, resulting in a transmission zero. Similarly, the phase shifts at the frequency lower than the passband from Path I and Path II are found to be 90°. Thus, no transmission zero can be generated. As for the circuit structure NRN_1, DR_6 and L_1, it is found that a transmission zero can be generated at the frequency lower than the passband. Thus, for Filter 1, two transmission zeros can be generated at both sides of the passband, which enhance the roll-off rate.

For demonstration, simulations are carried out and the results are shown in Figure 2.30. It is observed that two transmission zeros (TZ_1 and TZ_2) appear at both the passband edges, which verifies the analysis. For further validation, the length of the

input feeding line (L_{m1}) is changed, which alters the coupling strength between S and DR_5 and that between S and L_1. Figure 2.30(a) shows that L_{m1} only has an impact on the location of TZ_2. Besides, Figure 2.30(b) shows the length of the output feeding line (L_{m2}) can alter the location of TZ_1 with TZ_2 fixed. Accordingly, it can be concluded that TZ_1 and TZ_2 are generated by the cross coupling from the NRN to the source and load.

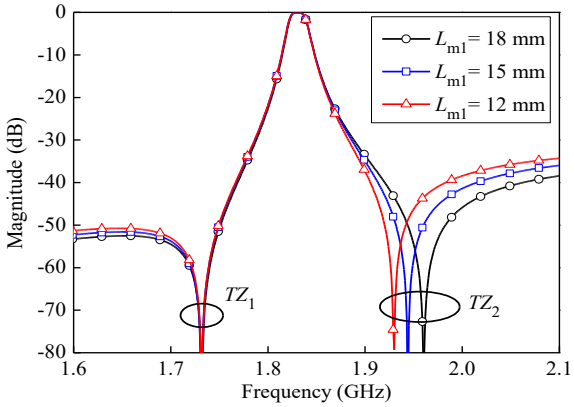

(a)

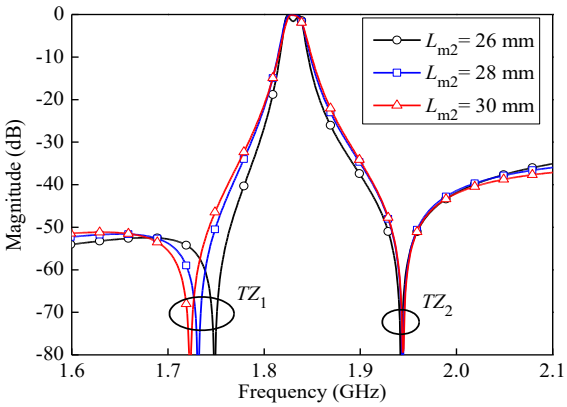

(b)

Figure 2.30. Simulated S_{21} of Filter 1 (a) with different TZ_2; (b) with different TZ_1.

2.4.4.2 Analysis of State 2: Filter 1 is OFF and Filter 2 is ON

When the PIN diode in NRN_1 is on and that in NRN_2 is off, the filtering SPDT switch is in State 2, namely, Filter 1 is OFF and Filter 2 is ON. Similar to State 1, high isolation between S and L_1 as well as L_1 and L_2 is realized. And Filter 2 is the same as the conventional BPF. Its structure is shown in Figure 2.31. The desired

bandpass responses can be realized by the filter design theory. Similar to the Filter 1 in State 1, cross coupling from *NRN* to source and load is also used in Filter 2 to generate transmission zeros for skirt selectivity enhancement.

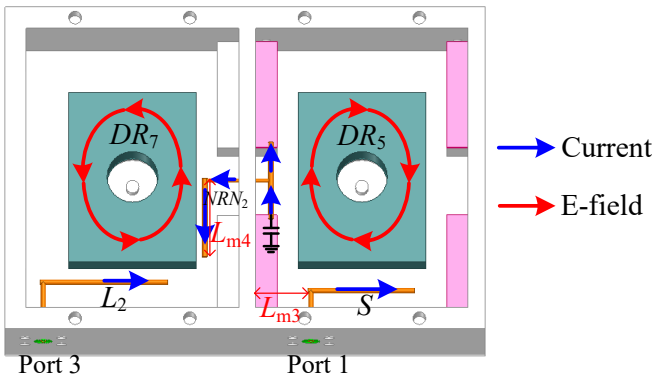

Figure 2.31. The circuit structure of Filter 2.

For analyzing the transmission zeros, the phase shift characteristic in Filter 2 is also discussed. A coupling scheme is presented in Figure 2.32(a). The current on probe 1 and the E-field generated by the DR are in-phase. It is known that the coupling between the DR and probe 1 is electric coupling and thus the phase shift is 90°. However, the current on probe 2 and the E-field in DR are out-of-phase. The coupling between probe 2 and the DR is also electric coupling, but there exists extra 180° phase shift caused by the out-of-phase field distribution. Thus, the total phase shift should be expressed as -90° (or 270°). Based on this, the topology of Filter 2 with the phase shift characteristic is shown in Figure 2.32(b). By employing the same analysis method as State 1, it can be known that two transmission zeros close to the passband can be generated by the cross coupling from *S* to NRN_2 and NRN_2 to L_2. For demonstration, simulations of Filter 2 with different coupling strength are carried out with the results shown in Figure 2.33. The two transmission zeros can be found at both sides of the passband. Meanwhile, by controlling the coupling strength in the structures from *S* to NRN_2 (or NRN_2 to L_2), the location of the TZ_1' (or TZ_2') can be changed with the other fixed, which verifies the analysis.

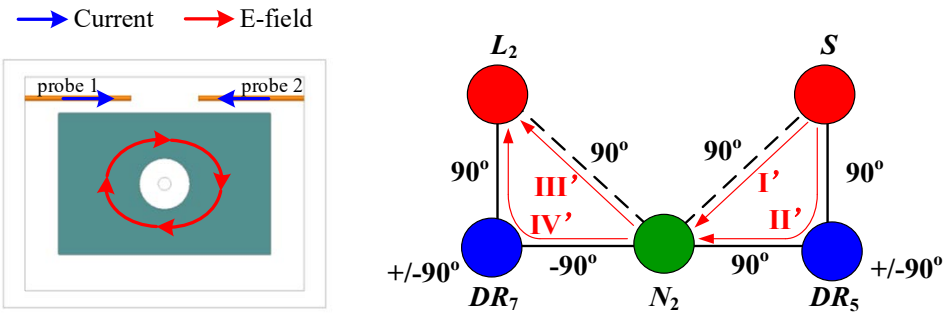

(a) (b)

Figure 2.32. (a) Two types coupling between probe and DR; (b) Topology of Filter 2 with the phase shift characteristic.

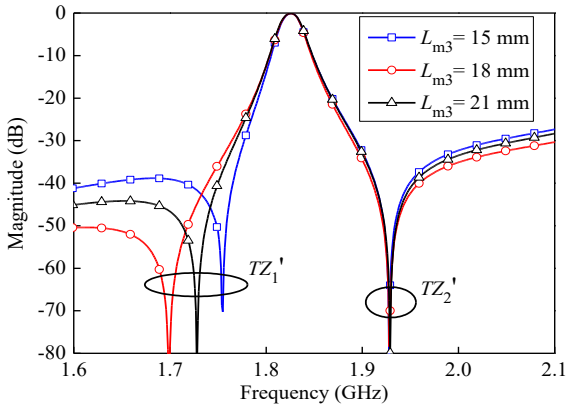

(a)

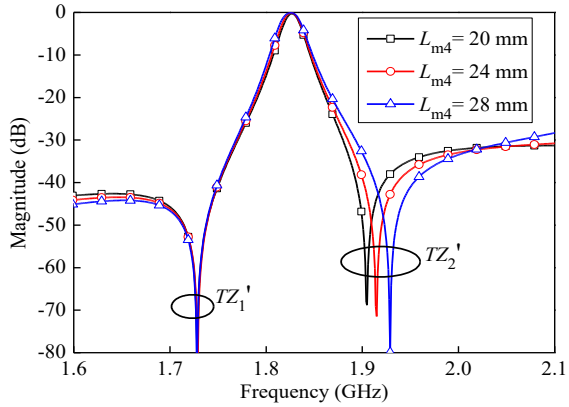

(b)

Figure 2.33. Simulated S_{21} of Filter 2 (a) with different TZ_2; (b) with different TZ_1.

2.4.4.3 Experiment

For verifying the proposed concept, the three-cavity DR-based SPDT filtering

switch is implemented. The fabricated photograph is shown in Figure 2.34. The fabricated SPDT filtering switch has a size of 17.5 × 7.5 cm^2 (1.06 × 0.46 λ_g^2). The simulated and measured results are shown in Figure 2.35, which exhibit good agreement.

When Filter 1 is ON and Filter 2 is OFF, Filter 1 exhibits good filtering responses while Filter 2 is highly isolated. As shown in Figure 2.35(a). The measured passband of Filter 1 is centered at 1.831 GHz with the 3-dB *FBW* of 1.28%. The return loss is better than 25 dB and the insertion loss is 0.39 dB at the center frequency of the passband. Two transmission zeros appear at 1.73 and 1.937 GHz, which greatly enhance the skirt selectivity. As for Filter 2 in OFF-state, the suppression levels are better than 45 dB between port 1 and port 3 (S_{31}) within the frequency range from 1.6 to 2.1 GHz. Meanwhile, isolation between port 2 and port 3 (S_{32}) is higher than 47 dB. The input P_{1dB} is larger than 49 dBm.

When Filter 1 is OFF and Filter 2 is ON, Filter 1 shows high isolation performance and filter 2 exhibits good filtering responses, as shown in Figure 2.35(b). The measured passband of filter 2 is centered at 1.831 GHz with the 3-dB *FBW* of 1.3%. The return loss is better than 20 dB and the in-band insertion loss is 0.4 dB. Two transmission zeros are generated at 1.718 and 1.95 GHz, resulting in high skirt selectivity. For the isolation between port 2 and port 1 or 3, S_{21} and S_{23} are better than 45 and 47 dB, respectively, within the frequency range from 1.6 to 2.1 GHz.

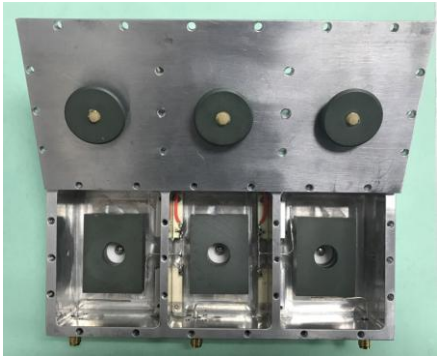

Figure 2.34. Photograph of the fabricated three-cavity DR-based SPDT filtering switch.

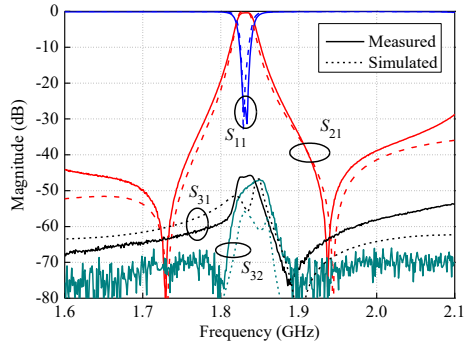

(a)

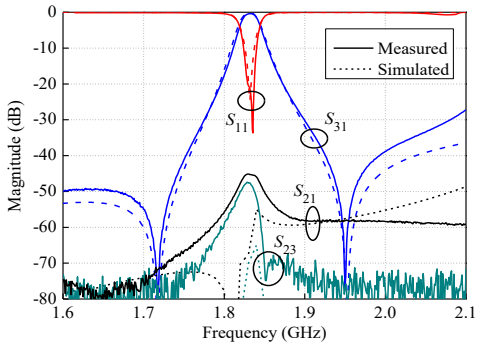

(b)

Figure 2.35. Simulated and measured results (a) State 1; (b) State 2.

2.4.5 Comparison

Table 2.3 tabulates the comparison with the DR filters [88], [89], filtering switches [16]-[18], [22] and the switch products from companies of Skyworks, RFMD, Mini-Circuits and Analog [90]-[96]. It can be rationally assumed that when the DR filter and switch are cascaded, the total insertion loss is the sum of the filter loss and switch loss, and the OFF-state isolation is the sum of the filter loss and switch isolation. From [88]-[91], the cascaded DR filter and SPST switch have the lowest insertion loss of 1.1 dB with an *FBW* of 1.6% and the highest isolation around 36 dB. For the proposed SPST DR filtering switch, it has the insertion loss of 1 dB with the *FBW* of 0.64 %. It should be noted that if our work is designed with the same *FBW* as the cascaded one, the insertion loss will be much smaller. Meanwhile, the OFF-state isolation in our DR SPST filtering switch is 53 dB, which is 17 dB higher than that of the cascaded one. Comparing to the cascaded DR filter and SPDT switches, the proposed SPDT DR filtering switch also has the lower ON-

state insertion loss and higher OFF-state isolation. For the filtering switches fabricated on PCB in [16]-[18], [22], they are compact in size. Unfortunately, their performance is limited by the unloaded quality factor of microstrip resonators and thus unsuitable for the narrow-band systems. Compared to the PCB filtering SPST in [16] and [17], the proposed filtering SPST has not only smaller ON-state loss but also higher OFF-state isolation and roll-off rate. In [18], high isolation of 47 dB is obtained. Nevertheless, the ON-state loss of 3.6 dB is much higher than the 0.4 dB loss in the proposed design. In [22], a relative low-loss and high-isolation filtering SPDT switch is realized by PCB. However, the proposed filtering SPDT switch still exhibits better performance in terms of ON-state loss and OFF-state isolation. What's more, the measured P_{1dB} of the presented DR filtering switches is larger than the switch products [90]-[94] and the PCB filtering switches [17], [22]. This indicates that the presented DR filtering switches can be used in high-power systems.

As for the MEMS switches in [95], [96], although the ON-state insertion losses are low, they still contribute to the overall loss of the cascaded switch and BPF. In contrast, in the proposed design, the losses caused by the PIN diodes are eliminated and the overall loss of the proposed filtering switches is equivalent to the filter loss. Moreover, the presented filtering switches exhibit higher isolation than the MEMS switches in [95], [96]. As for the switching time of the proposed filtering switches, it is comparable to those of the switches using PHEMT GaAs diodes in [91], [92], [94] and it is lower than those of the MEMS switches in [95], [96]. In sum, the proposed DR filtering switches feature lower ON-state insertion loss, higher power handling capability and higher OFF-state isolation. Furthermore, a sharp roll-off rate and high out-of-band rejection are also achieved due to the transmission zeros generated at both sides of the passband.

Table 2.3 Comparison With Some DR Filters, Filtering Switches and Switches

Ref.	Type	f (GHz)	IL (dB)	ISO (dB)	3-dB FBW	Filtering responses	P_{1dB} (dBm)	Technique
[88]	DR	1.86	0.5	-	>1.6%	Yes	-	DR+Cavity
[89]	DR	2.172	1.15	-	>0.7%	Yes	-	DR+Cavity
[90]	SPST	0.01-2.5	1.5	30	-	No	> 19	Coaxial
[91]	SPST	0.5-4	0.6	35	-	No	31	pHEMT GaAs
Cascaded [88], [91]	SPST	1.86	1.1	36	1.6 %	Yes	-	-
[92]	SPDT	0.1-6	0.5	38	-	No	32	pHEMT GaAs
[93]	SPDT	0.005-6.5	0.4	29	-	No	40	pHEMT GaAs
[94]	SPDT	0.5-6.5	0.6	27	-	No	37	pHEMT GaAs
Cascaded [88],[92]	SPDT	1.86	1	38	1.6 %	Yes	-	-
[16]	SPST	0.9	~3	44	9 %	Yes	-	PCB
[17]	SPST	1.5	1.8	48	12.8 %	Yes	23	PCB
[18]	SPDT	1.49	3.6	47	5 %	Yes	-	PCB
[22]	SPDT	1	0.97	40	10 %	Yes	> 40	PCB
[95]	SP4T	0-14	0.26	24	-	No	36	MEMS
[96]	SP4T	0-13	0.45	24	-	No	36	MEMS
This work	SPST	1.832	1	53	0.64 %	Yes	49	DR+Cavity
	SPDT	1.861	0.5	40	1.16%	Yes	49	DR+Cavity
	SPDT	1.831	0.4	45	1.3 %	Yes	49	DR+Cavity

2.5 High-Efficiency Filter-Integrated Class-F Power Amplifier Based on Dielectric Resonator

Power amplifiers (PAs) and filters are key components in radio frequency (RF) transceivers. Recently, the co-design of PAs and filters has drawn much attention. In [25]-[27], the compact microstrip resonant cell (CMRC), notched-band ultra-wideband bandpass filter (BPF) and lowpass filter (LPF) are utilized to optimize the harmonics in class-F PAs. Unfortunately, bandpass responses are not integrated. In [29], the microstrip BPF with more than 20% fractional bandwidth (FBW) is utilized as the output matching network (OMN) of the PA to obtain good filtering responses. The hybrid cavity-microstrip filter is employed in class-F PA in [31]. With the microstrip feeding structure, the resultant FBW is 11%.

With the development of wireless systems, the frequency spectrum becomes crowded and some spectrum bandwidths available for certain applications are very narrow, such as the 1880 to 1900 MHz for the TDD system. This puts forward strict requirement on narrowband BPFs. Due to the *Q*-factor limitation, the BPFs in [29], [31] cannot be used in narrowband applications. Otherwise, the insertion loss of BPFs would be high and will degrade the PA efficiency. To solve this problem, the high-*Q* evanescent-mode cavity resonators are utilized to design the narrow-band filtering PA with high efficiency [32]. Besides evanescent-mode cavity resonators, dielectric resonators (DRs) also feature high-*Q* factor [97]. However, there is no reported filter-integrated PA using DRs.

In this thesis, a high-efficiency filter-integrated class-F PA using DRs is presented. By modifying the elements in the coupling matrix, the DR filter with cross-coupling can be designed with different source impedances and fixed load impedance, which can function as the OMN of the class-F PA. Two transmission zeros (TZs) are generated near the passband, resulting in high skirt selectivity. Moreover, due to the high *Q*-factor of DRs, the presented PA can realize high efficiency with narrow FBW. For validation, a DR filter-integrated PA is implemented. Simulated and measured results are presented.

2.5.1 Analysis of DR Filter with Impedance Conversion

In this work, the DR filter is designed with different input impedances for acting as the OMN of the class-F PA. Figure 2.36 shows the schematic of the DR filter. It consists of a metal cavity, input, and output feeding lines (*S* and *L*) as well as two DRs (DR_1 and DR_2). The input feeding line is welded on the printed circuit board (PCB) to facilitate the integration with the PA circuit, while the output feeding line is connected to the SMA connector. The topology can be shown as Figure 2.36(c) and the coupling matrix is expressed as

$$M = \begin{bmatrix} 0 & M_{S1} & M_{S2} & M_{SL} \\ M_{1S} & M_{11} & M_{12} & M_{1L} \\ M_{2S} & M_{21} & M_{22} & M_{2L} \\ M_{LS} & M_{L1} & M_{L2} & 0 \end{bmatrix} . \tag{2.29}$$

With this matrix, the input external quality factor (Q_e) by the DR filter can be calculated as equation (2.29), where i = 1, 2, or L.

$$Q_{ei} = \frac{1}{M_{Si}^2 \times FBW} \tag{2.30}$$

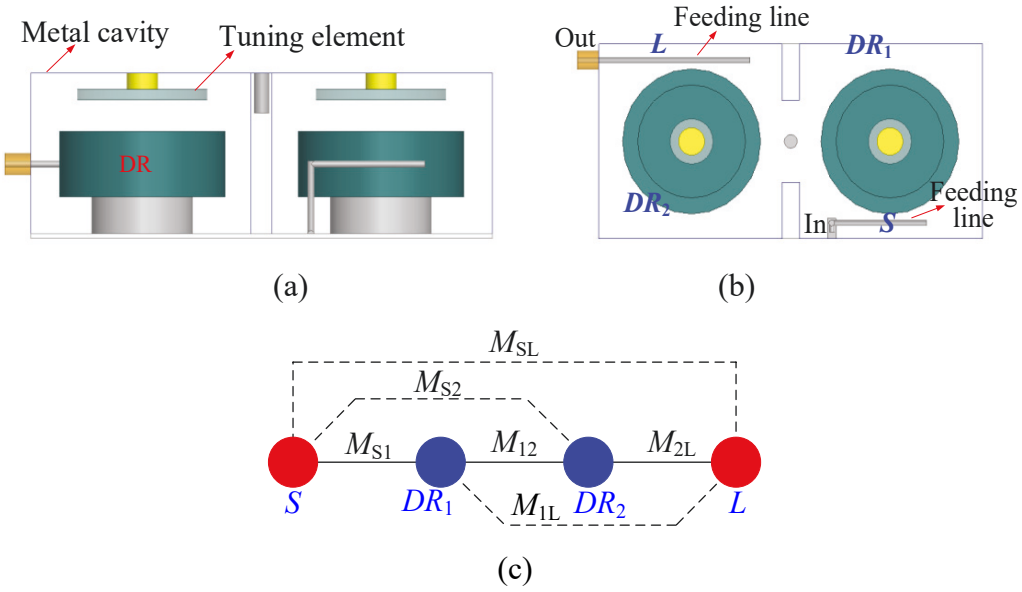

Figure 2.36. Structure of the DR filter (a) front view; (b) top view; (c) topology.

In this design, the DR filter is utilized to convert a real impedance to 50 Ω and the mechanism is addressed as follows. Firstly, the coupling matrix is considered with the same source and load impedance, which can be obtained by the synthesis theory in [79]. Then the source impedance is modified with the load impedance fixed to realize the impedance conversion. It is assumed the desired normalized real source impedance is R_{in}. Since the Q_e is proportional to R_{in}, according to (2.30), the M_{Si} can be modified to obtain the desired R_{in} as

$$M_{Si}^{'} = \frac{M_{Si}}{\sqrt{R_{in}}} . \tag{2.31}$$

Other parameters in matrix (2.29) are kept unaltered. By using this method, the coupling matrix of the DR filter with impedance conversion function can be conveniently realized.

It is noted that the proposed method is different from those in [29], [31], [32] and features more design freedom. In [29] and [32], the coupling matrices only can be used in the topology with no cross coupling. In [31], the TZs only can be located at the symmetric frequencies with respect to the passband. Otherwise, the non-zero M_{S2}, M_{1L}, $M_{11,}$ and M_{22} make the input impedance equations ((3) and (4) in [31]) complex, which make it very difficult or even impossible to modify the elements in coupling matrix to realize complex impedance conversion.

2.5.2 Filter-Integrated Class-F PA Design

Figure 2.37 shows the schematic of the filter-integrated class-F PA. The transistor GaN HEMT CGH40010F from Cree is used as the power device. C_1 and C_3 are utilized for DC block and as parts of the impedance matching network. C_2 and R_1 enhance the stability around passband, while R_2 increases the out-of-band stability. Six bypass capacitors (C_4-C_9) are used for decoupling. TL_2, TL_5, $TL_{6,}$ and TL_{10} act as the pads of the lumped elements and the transistor. TL_4 and TL_7 with around quarter-wavelength ($\lambda_g/4$) electrical lengths are used to bias the transistor. As for the input matching, it is realized by a series and paralleled transmission lines (TL_1 and TL_3).

As a class-F PA, the ideal even- and odd-order harmonics impedance at the intrinsic transistor train node should be zero and infinite, respectively. In this design, TL_6-TL_9 fulfill the requirement, as analyzed below. At first, the package of the transistor is not considered. TL_9, with the $\lambda_g/4$ electrical length at the third harmonic (f_{3rd}), manipulates the third harmonic impedance as zero at node A. In this way, the DR filter does not affect the third harmonic impedance, because it is short-circuited by TL_9 at f_{3rd}. And then, TL_8 with the same length as TL_9 converts the zero

impedance to infinite at node *B*. TL_7, with the $\lambda_g/4$ electrical length at the operating frequency (f_0), cooperates with C_7-C_9 to realize shorted circuit for the second harmonic (f_{2nd}) at node *B*. It should be noted that the DR filter does not affect the second harmonic impedance, because node *B* is short-circuited. Accordingly, the required harmonic impedances are realized at node *B*. However, the TL_6 for pad has small electrical length and the parasitics due to the transistor package exist. Fine-tuning is performed to meet the impedance requirement at the intrinsic transistor drain node.

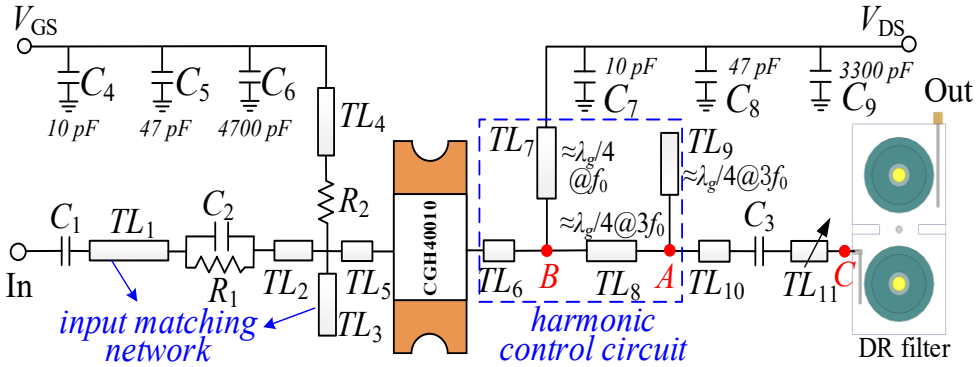

Figure 2.37. Schematic of the presented filter-integrated class-F PA.

To realize the output matching, a tuning line TL_{11} is used to transform the desired complex load impedance to a real one. Then, the DR filter converts the real impedance to 50 Ω, as addressed below. Firstly, the general Chebyshev response is selected for the presented DR filter. As a design example, the passband is at 1.88 GHz with 0.6% 20-dB equi-ripple return loss. Two TZs are pointed at 1.75 and 2.03 GHz. The normalized coupling matrix can be synthesized as follows [79]

$$M = \begin{bmatrix} 0 & 1.2223 & -0.0026 & 0.0041 \\ 1.2223 & -0.0139 & -1.6589 & 0.0083 \\ -0.0026 & -1.6589 & 0.0153 & 1.2222 \\ 0.0041 & 0.0083 & 1.2222 & 0 \end{bmatrix} \tag{2.32}$$

By using the load-pull simulation in Keysight Advanced Design System (ADS) at the reference plane of *C* in Figure 2.37, the highest efficiency appears at 25 Ω. Thus,

the input impedance of the DR filter is determined as 25 Ω and normalized by 50-Ω system as $\overline{R}$ = 0.5. Based on (2.31), the M_{S1}, M_{S2}, and M_{SL} in (2.32) are reduced by a factor of $\sqrt{0.5}$ as 1.7286, -0.0037 and 0.0058, respectively. Accordingly, the DR filter for output matching can be designed based on the elements in the modified coupling matrix. Figure 3.38 shows the simulated and synthesized responses of the DR filter with source and load impedances of 25 Ω and 50 Ω, respectively. As seen, good impedance matching is realized, which verifies the proposed idea.

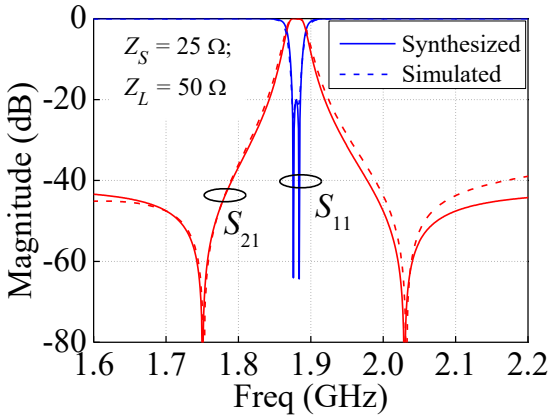

Figure 2.38. Synthesized and simulated results of the DR matching filter.

2.5.3 Experiment and Comparison

For demonstration, the filter-integrated class-F PA is implemented. The dielectric material (ε_r = 38, tan δ = 0.0002) is from the Jiangsu Jiang Jia Electronics Co., Ltd in Jiangsu, China. The output matching DR filter and other circuits fabricated on the printed circuit board (PCB) substrate (ε_r = 2.2, h = 0.508 mm, tan δ = 0.0009) are enclosed in the metal cavity and separated by a metal wall, as shown in Figure 2.39. The metal parts also function as a heat sink for the transistor. The DR filter is simulated by HFSS and the S-parameters are imported to ADS for co-simulation. The simulated impedances at f_{2nd} and f_{3rd} as well as the voltage and current distribution at the drain are shown in Figure 2.40. As observed, the impedance at f_{2nd} and f_{3rd} are close to the short- and open-circuited ones, respectively, while the simulated voltage and current waveforms look like a square one and a half-sin one, indicating the class-F operation.

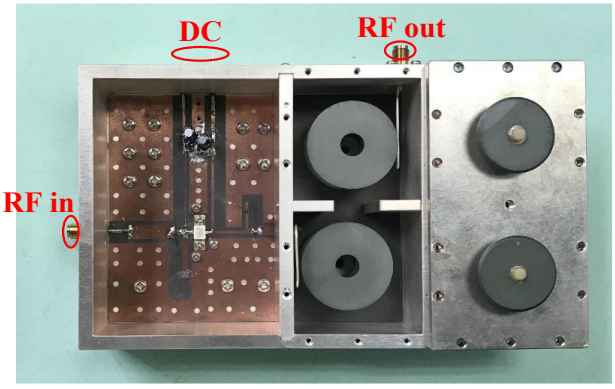

Figure 2.39. Photograph of the filter-integrated class-F PA.

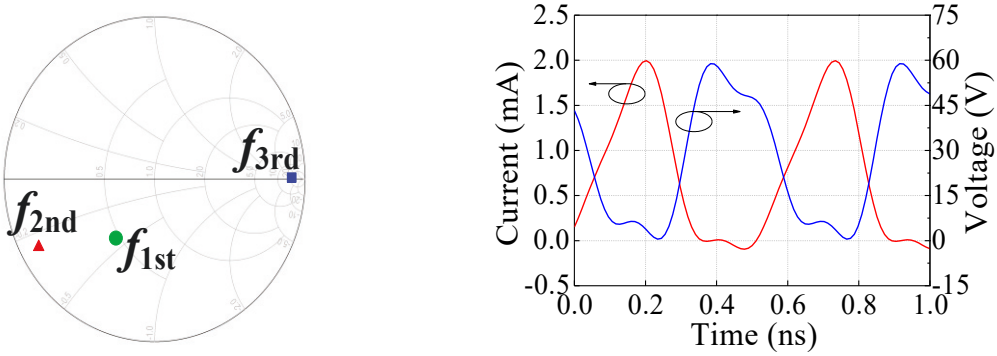

(a) (b)

Figure 2.40. (a) Harmonic impedance; (b) voltage and current waveform at the drain.

The small-signal responses measured by Agilent 5071C network analyzer are shown in Figure 2.41. The passband is centered at 1.88 GHz with a small-signal gain of 18.3 dB and 3-dB FBW of 2.3%. The input return loss is better than 15 dB. Due to the fabrication tolerance and the inaccuracy of the transistor model used in the ADS simulation, it is observed from S_{22} that there is only one transmission pole. However, it still features good output matching of better than 15 dB. Two TZs are generated at 1.745 and 2.023 GHz, which exhibits high skirt selectivity.

Figure 2.42(a) shows the output power (P_{out}) and power added efficiency (PAE) at the input power (P_{in}) of 28 dBm. The P_{out} is larger than 40 dBm within the passband from 1.865 to 1.89 GHz, with the maximum one of 41.06 dBm. At the center frequency, the measured maximum PAE is 70.7%. Figure 42(b) shows the output power over a wide frequency range when P_{in} = 28 dBm at 1.88 GHz. As seen,

the second and the third harmonics are suppressed. Figure 2.43 shows the measured P_{out}, gain, PAE and drain efficiency at 1.88 GHz with different P_{in}. The highest efficiency is 75.8%, featuring high efficiency.

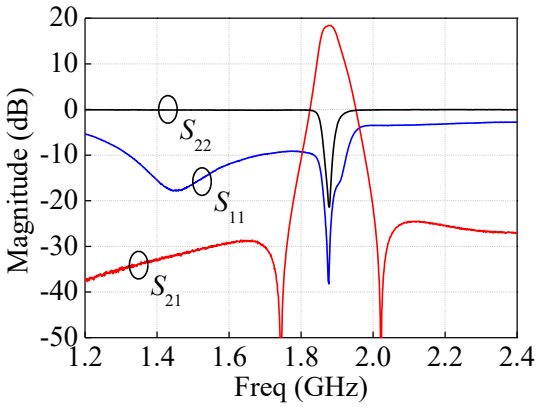

Figure 2.41. Measured S-parameters of the presented filter-integrated class-F PA.

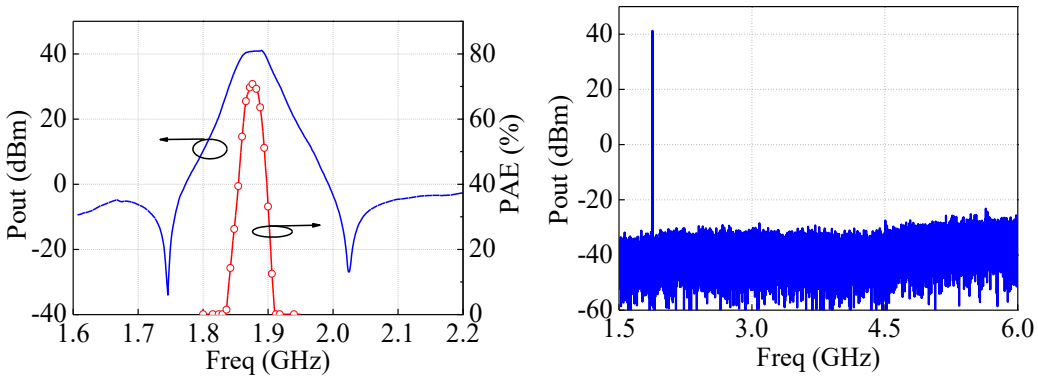

Figure 2.42. (a) Measured P_{out} and PAE versus frequency; (b) Pout over a wide frequency range.

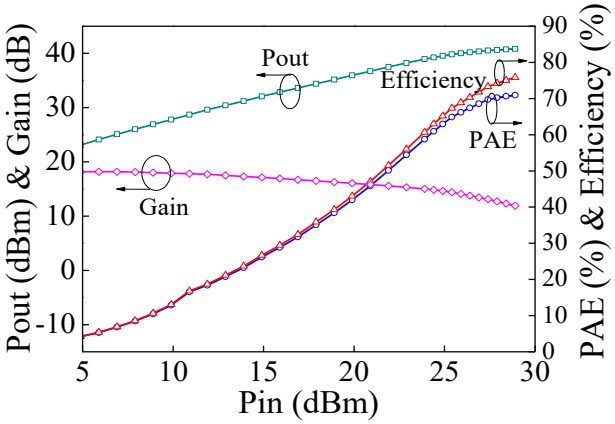

Figure 2.43. Measured output power P_{out}, gain, PAE and drain efficiency.

Table 2.4 tabulates the comparison with some other works. In [25], high efficiency of 74% is obtained whereas it does not realize filtering responses. In [29] and [31], the FBWs are larger than 10% whereas the PAEs are similar to that in our design. It should be noted that in BPF designs, the narrower FBW leads to higher insertion loss and thus the overall efficiency degrades. If the FBWs in [29] and [31] are the same as that in this work, the PAE will be lower than that of our design. As compared with [32], our design generates two transmission zeros near the passband and also realize narrower FBW but higher PAE.

Table 2.4 Comparison of Various Filter-Integrated PAs

Ref.	Filter type	TZs	Transistor	PAE (%)	Filtering	3dB FBW
[25]	Microstrip LPF	0	GaAs	74	No	-
[29]	Microstrip BPF	2	GaN	69.8	Yes	> 20%
[31]	Microstrip-cavity BPF	2	GaN	70.9	Yes	11%
[32]	Cavity BPF	0	GaN	68	Yes	>3 %
This work	DR BPF	2	GaN	70.7	Yes	2.3%

2.6 Conclusions

In order to improve the overall efficiency of the power amplifier, switch, and filter, the filter has been co-designed with a power amplifier and switch. Firstly, miniaturized single- and dual-band filtering switches have been presented using multilayer LTCC structures. Since the signals do not pass through the PIN diodes in the ON-state, the losses of the proposed filtering switches are the same as conventional filters. As compared to the cascaded filter and switch, the losses have been reduced. In the OFF-state, high isolation has been obtained by controlling the coupling between the feeding line and the resonator to be close to zero. Moreover, for narrowband and high-power base station applications, SPST and SPDT filtering switches have been proposed using high-Q DRs. Compared to other reported

filtering switches, the proposed designs show the advantages of low loss, high isolation, and high power handling capability. What's more, to avoid the efficiency degradation by the impedance mismatching of cascaded power amplifier and filter, the DR filter has been co-designed with a class-F power amplifier. By modifying the elements in a coupling matrix, the DR filter with cross coupling has been designed with impedance conversion function and utilized as the output matching network of a class-F power amplifier. Two transmission zeros are generated at two sides of the passband, realizing high selectivity. As compared to other reported filter-integrated power amplifiers, the proposed design shows high efficiency and high selectivity, which is suitable for base station applications.

Chapter 3 Passive Multi-Functional Filtering Circuits

3.1 Introduction

There are lots of passive circuits in RF front ends of wireless systems, such as filters, power dividers, balun, balanced circuits, couplers and so on. Among them, the filter is an essential circuit, which is demanded in most of the wireless systems. Generally, filters are cascaded with other passive circuits in wireless systems, occupying large circuit sizes. In some wireless systems, the size of passive circuits may be larger than 70% of the whole system. It is of great significance to reduce the sizes of the passive circuits so as to reduce the overall size of the whole system. However, for single-functional passive circuit design, a smaller circuit size generally leads to a lower Q factor, resulting in a higher insertion loss. Thus, it is very difficult to further reduce the size as the circuit performance should be guaranteed. In order to meet the trend of the miniaturized wireless devices, new theories and new design methods should be developed for passive circuits.

3.2 Proposed Methods for Co-Design and Function-Fusion of Filters and Other Passive Circuits

To solve the above problems, novel methods for the co-design and function-fusion of filters and other passive circuits are proposed in this thesis to design the multi-functional filtering circuits, including the filtering balun, diplexer and filtering rat-race coupler, which can reduce the size and loss of the passive circuits in wireless systems.

For the design of filtering balun, the working mechanism and transmission function of a balun circuit are firstly analyzed. Then, a design method for the function-fusion of the filter and balun circuit is proposed where the function of the

balun circuit is constructed in the filter structure to fuse these to circuit functions. Figure 3.1 shows the schematic of the proposed method for the fusion of the filter and balun circuit. In conventional cascaded design, a balun circuit includes the impedance conversion structure with the 180° phase difference between two output ports. The whole cascaded structure suffers from large size and the insertion loss is usually high. In the proposed function-fusion design method, the condition for the desired 180° phase difference between two output ports can be expressed as

$$\frac{T_{even}(1-\Gamma_{odd})}{2-(\Gamma_{even}+\Gamma_{odd})}=0. \tag{3.1}$$

where Γ_{even} and Γ_{odd} are the reflection coefficients of the even- and odd-mode equivalent circuits, respectively, and T_{even} is the transmission coefficient of the even-mode equivalent circuit. This equation can be easily achieved by only setting the coupling coefficients at the two branches to be opposite is the proposed method, as shown in Figure 3.1. The impedance conversion function in a conventional balun circuit can be realized by reducing the coupling coefficients with a factor of $\sqrt{2}$. Based on this method, a filtering balun is proposed with a simple structure, which can reduce the size and loss. Moreover, the multilayer LTCC structure is used to further reduce the size in this thesis.

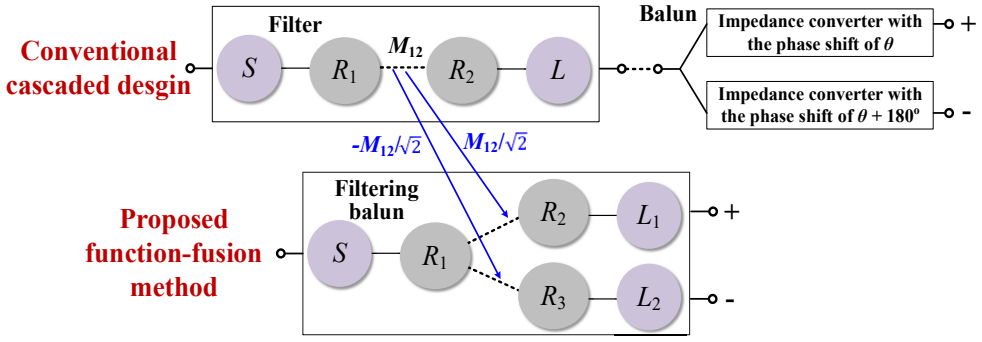

Figure 3.1. Schematic of the proposed function-fusion method for the filter and balun circuit.

In the design of a passive multi-functional filtering circuit, the method for designing miniaturized diplexer is also proposed. Based on the requirements of a

diplexer, two out-of-band rejection methods are proposed for two filters using a common dual-mode resonator. Then, a topology for the high-isolation diplexer is presented, which simplifies the diplexer structure and improve the isolation. Figure 3.2 shows the schematic of the diplexer. In conventional designs, two filter channels are connected by using a T junction, resulting in a large size. In the proposed design, a dual-mode resonator is used, which can replace the T junction and single-mode resonators to reduce the size.

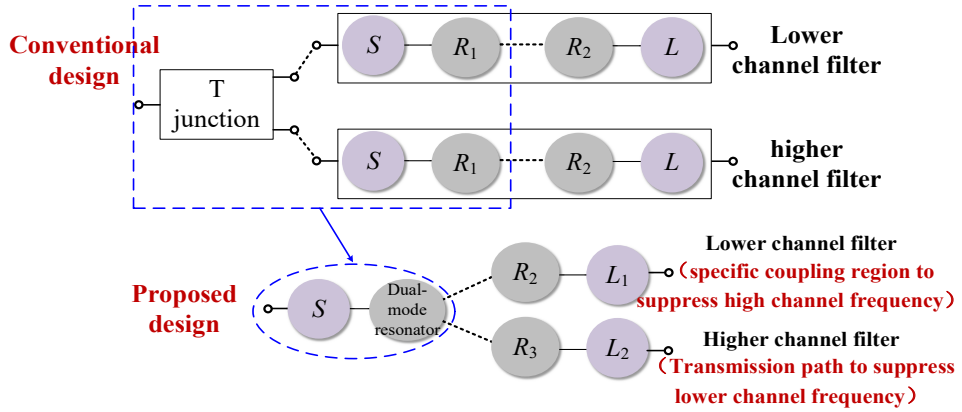

Figure 3.2. Schematic of the proposed diplexer.

In this design, two methods are proposed to improve the isolation for a diplexer using a common resonator. The first one is to construct a transmission path based on the transmission line theories, whose transmission coefficient can be expressed as

$$S_{12} = \frac{2}{A_{11} + A_{12}/Z_0 + A_{21}Z_0 + A_{22}} = \frac{N}{D}$$
$$N = 2Z_0Z_1Z_2\omega C\cos(\theta_1)\cos(\theta_3) \tag{3.2}$$

where A_{11}, A_{12}, A_{21}, and A_{22} are the elements of the [ABCD] matrix of the transmission path, N and D are the numerator and denominator of S_{12}, respectively. By solving $N = 0$, a transmission zero can be generated by the higher channel filter at the lower channel frequency to realize high suppression. The second method is to select a specific coupling region by analyzing the coupling coefficient of the coupled line. For example, using the following equation,

$$|k'| = |k_e'| - |k_m'| = P \times \left| \int_A^B |\sin(\beta x)|^2 \, dx - \int_A^B |\cos(\beta x)|^2 \, dx \right| \tag{3.3}$$

the coupling coefficient of the lower channel filter at the higher channel frequency can be analyzed as zero, which can also generate a transmission zero to realize high out-of-band rejection. Thus, when we combine these two channel filters based on the common dual-mode resonator, the diplexer can realize high isolation with a simple structure. LTCC technology is used to further reduce the size in this thesis.

For the function fusion of filter and coupler, a method for designing the filtering rat-race coupler based on the EM-field properties of the dielectric resonator is proposed. Figure 3.3 shows the schematic of the proposed function-fusion method for filter and rat-race coupler. In conventional cascaded design, one rat-race coupler and two filters are needed to realize the filtering rat-race coupler, resulting in large size and high insertion loss. In the proposed function-fusion method, a high-*Q*-factor quad-mode dielectric resonator is constructed firstly, which can realize the filtering responses. Then, the function of the rat-race coupler is realized in the filter structure. As shown in Figure 3.3, four ports are coupled to the dielectric resonator. By using the EM-field properties of the dielectric resonator, the phase shifts from P1 to P2 and P3 are the same, while the phase shifts from P4 to P2 and P3 have a difference of 180°. Thus, the rat-race coupler function is fused into the filter structure, realizing a high-Q filtering rat-race coupler. Only one dielectric resonator in a metallic cavity is used to realize the second-order filtering rat-race coupler performance, which has a very compact size.

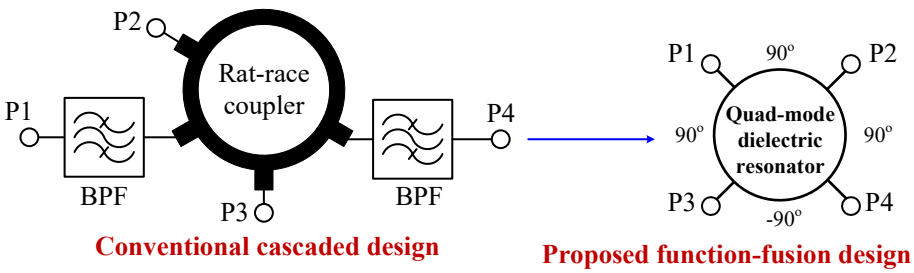

Figure 3.3. Schematic of the proposed function-fusion method of the filter and rat-race coupler.

3.3 Compact LTCC Balun With Bandpass Response Based on Marchand Balun

As one of the most important functional passive devices in RF front-ends, the balun is commonly used [98]. A lot of techniques and structures have been proposed to design baluns. In many cases, a balun needs to be cascaded with a filter and they can be integrated to obtain a compact size and low insertion loss. Accordingly, various balun filters have been investigated.

In order to realize the more compact devices, the multi-layer structures are popularly used [45], [47], [99]-[102]. The multilayer PCB balun filter with independently controllable dual passbands is proposed in [99]. In [100], a balun bandpass filter is presented based on multilayer substrate integrated waveguide (SIW) power divider. To further reduce the size, low temperature co-fired ceramic (LTCC) technology is used. In [45], the extracted-pole technique is utilized to obtain the LTCC balun filter with a complex load, which is desired in many applications. By constructing miniaturized resonators using the LTCC multilayer structure, the filtering baluns can be designed with a very compact size [47], [101]. In [102], an LTCC balun filter is designed by applying a vertical split-ring resonator. However, the phase imbalance performance needs to be improved.

In this thesis, a compact balun with filtering responses based on a Marchand balun is presented. The circuit consists of one half-wavelength and two quarter-wavelength resonators as well as three feeding lines. As compared to a Marchand balun, only three feeding lines are added and the size is compact. Moreover, all the lines are folded horizontally and vertically in the LTCC multi-layer structure and the size is further reduced. The out-of-phase characteristic at the two open ends of the half-wavelength resonator is utilized to obtain the out-of-phase outputs. The coupling matrix is synthesized for realizing the required filtering responses. For demonstration, an experimental LTCC balun filter is implemented.

3.3.1 Analysis of the LTCC Balun Filter

3.3.1.1 Circuit Configuration

Figure 3.4 shows the 3-dimensional structure of the proposed LTCC balun filter. It consists of eleven metal layers and ten ceramic sheets. The metal layers include three main parts: three resonators, three feeding lines as well as the ground. The half-wavelength resonator is folded on layers 7 and 9 to miniaturize the circuit size, while the two quarter-wavelength resonators are located on the layers 3, 4 and 10. Three feeding lines are located on layers 2 and 6. They are used to not only provide broadside coupling to the resonators but also generate the source-load coupling for skirt selectivity improvement. Vias are utilized to connect the circuits on different layers, which go through the holes in layers 5 and 8. The ground planes are plotted on layers 1, 5, 8 and 11.

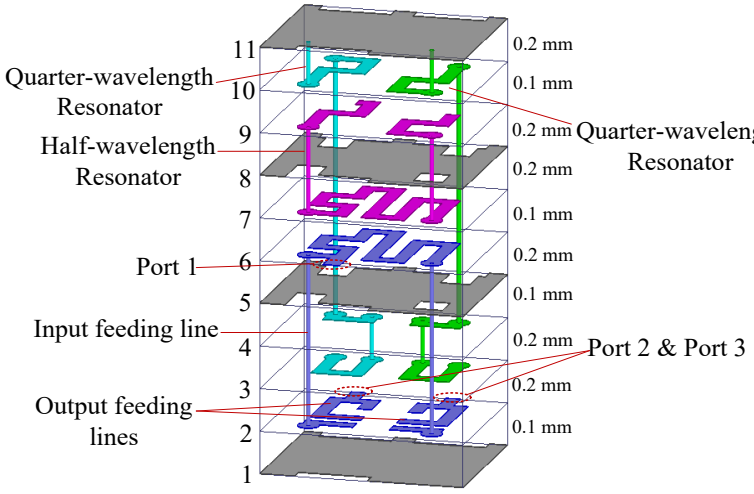

Figure 3.4. 3-dimensional structure of the proposed LTCC BPF.

3.3.1.2 Analysis of Phase Characteristic

As shown in Figure 3.5(a), the conventional Marchand balun consists of one half-wavelength and two quarter-wavelength transmission lines. It is symmetrical and even- and odd-mode analysis is applied to analyze it. Figures. 3.5(b) and (c) illustrate the even- and odd-mode equivalent circuits, respectively. In order to satisfy the ideal balun-type characteristics of the 180^{o} phase difference, the

condition of equation (3.1) should be satisfied [76]. As shown in Figure 3.5(b), the even-mode equivalent circuit features transmission stop for all frequencies [80]. Thus, $T_{even} = 0$, and condition (3.1) is satisfied. Consequently, the ideal balun-type characteristic of the 180° phase difference is realized.

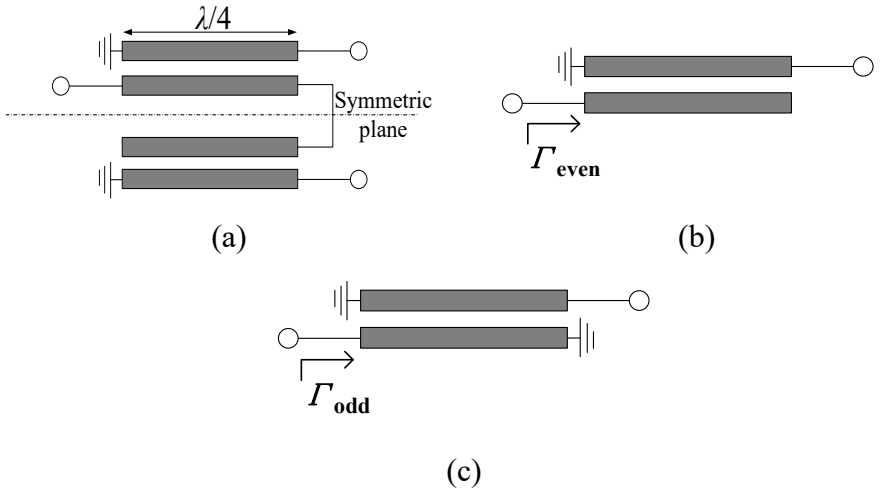

Figure 3.5. (a) Conventional Marchand balun; (b) Even-mode equivalent circuit; (c) Odd-mode equivalent circuit.

3.3.1.3 Analysis of Filtering Response

Apart from the above-mentioned phase characteristic, filtering responses are also desired in this design. To enable the balun with filtering responses, the half- and quarter-wavelength transmission lines in Marchand balun are used as the resonators and three feeding lines are added as input and outputs, as shown in Figure 3.6. It can be observed that the coupling between the quarter- wavelength resonators and two output ports is the same. Thus, the 180° phase difference realized by the half-wavelength resonator can be kept.

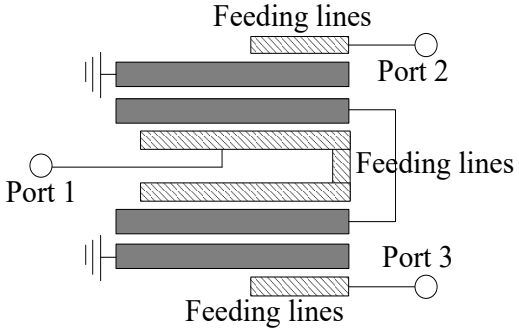

Figure 3.6. Structure of balun with filtering responses.

Figure 3.7(a) shows the topology of the proposed LTCC balun filter. R_1-R_3 represent the three resonators and S, L_1 and L_2 denote the three feeding lines. Since the circuit is symmetrical, we can analyze the circuit from port 1 to port 2 (or port 3) to characterize the overall circuit. The circuit from port 1 to port 2 is equivalent to a two-port second-order filter. Its topology is shown in Figure 3.7(b). Therefore, the coupling matrix of this second-order filter can be expressed as

$$M = \begin{bmatrix} 0 & M_{S1} & M_{S2} & M_{SL} \\ M_{1S} & M_{11} & M_{12} & 0 \\ M_{2S} & M_{21} & M_{22} & M_{2L} \\ M_{LS} & 0 & M_{L2} & 0 \end{bmatrix} \tag{3.4}$$

Firstly, the coupling matrix (3.4) with the same input and output impedance is considered, and the value of the elements can be obtained by the synthesis theory [79]. Then the source impedance of this filtering network should be modified to meet the source impedance of the whole circuit. According to the topology shown in Figures 3.7(a) and (b), it can be found that the value of $M_{12}(M_{21})$, $M_{SL}(M_{LS})$, and $M_{S2}(M_{2S})$ should be reduced by a factor of $\sqrt{2}$ whereas other parameters are kept unaltered. Accordingly, the 3-port coupling matrix is obtained for design guidance and the balun with filtering responses can be conveniently realized.

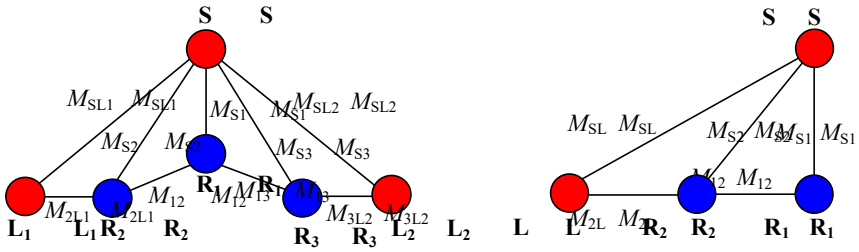

(a) (b)

Figure 3.7. (a) Proposed topology of the filtering balun; (c) Topology of the network from port 1 to port 2.

3.3.2 Circuit Design, Experiment and Comparison

3.3.2.1 Design Procedures

Based on the above analysis, a compact LTCC balun filter is designed by the following procedures:

Firstly, based on the required specifications, the coupling matrix can be obtained. The required passband in this design is centered at 5.55 GHz with 3-dB bandwidth (*FBW*) of 14%. Two transmission zeros are appointed at 3.6 and 6.6 GHz to reject the unwanted signal from the WiMAX band and enhance the selectivity. The coupling matrix is synthesized as

$$M = \begin{bmatrix} 0 & 1.1909 & -0.2182 & 0.0291 \\ 1.1909 & -0.3162 & -1.6238 & 0 \\ -0.2182 & -1.6238 & 0.2785 & 1.2131 \\ 0.0291 & 0 & 1.2132 & 0 \end{bmatrix} \tag{3.5}$$

Secondly, to obtain the 3-port coupling matrix, the $M_{12}(M_{21})$, $M_{SL}(M_{LS})$, and $M_{S2}(M_{2S})$ are reduced by a factor of $\sqrt{2}$ while the M_{S1} and M_{2L} are unchanged, which can be obtained from comparing Figures 3.7(a) and (b). The required external quality factors (Q_e) and coupling coefficient (k) can be calculated by equations (2.9) and (2.10). Thus, the mainly desired parameters can be calculated as follows: $k_{12} = k_{13} = 0.161$, $Q_{ein} = 5$, $Q_{eout} = 4.9$. It is noted that the Q_{ein} and Q_{eout} are maintained unchanged since the value of M_{S1} and M_{2L} in the 2-port and 3-port matrices are the same.

Thirdly, the proposed LTCC balun filter circuit is constituted to obtain the required Q_e and k. In order to obtain the initial values, Q_e and k can be extracted from the simulation results by following the method in [81]. Then the circuit structure can be determined according to the extracted results.

Finally, since the circuit is designed in the LTCC multilayer structure and loading effect exists, fine-tuning is performed.

3.3.2.2 Experiment

Based on the above design process, an LTCC balun filter is fabricated and the detail layouts are shown in Figure 3.8. The ceramic sheets have a dielectric constant of 5.9 and a loss tangent of 0.002. The dimensions are determined as follows (all in mm): L_1=2.8, L_2=2.3, L_3=0.35, L_4=45, L_5=0.7, L_6=0.5, L_7=1.07, L_8=0.9, L_9=0.22,

L_{10}=0.35, L_{11}=0.55, L_{12}=1.6, L_{13}=0.85, L_{14}=0.6, L_{15}=0.3, L_{16}=0.65, L_{17}=0.4, L_{18}=0.6, g_1=0.17, d_1=0.3, W_1=0.2, W_2=1, W_3=0.5, W_4=0.65. The core circuit size is 2 mm × 1.7 mm × 1.6 mm or 0.089 λ_g × 0.076 λ_g × 0.071 λ_g, where λ_g is the guided wavelength at the operating frequency. The overall circuit size including the package is 2.8 mm × 2.3 mm × 2 mm. The photograph of the fabricated LTCC balun filter with a test board is shown in the inset of Figure 3.9(a).

The simulation and measurement are carried out by HFSS and 8753 network analyzer, respectively. Good agreement between synthesized, simulated and measured results is observed in Figure 3.9(b). The measured passband is centered at 5.5 GHz with a 3-dB bandwidth of 14.8%. The insertion losses at the center frequency are 3+1.76 and 3+1.85 dB, respectively, with the amplitude imbalance of less than 0.1 dB and the return loss is better than 15 dB. Two transmission zeros appear at the frequencies of 3.6 and 6.6 GHz, which help enhance the selectivity. The phase difference between the two output ports is from 175° to 183° and the maximum magnitude imbalance within the whole 3-dB passband is less than 0.6 dB, as shown in Figure 3.9(c).

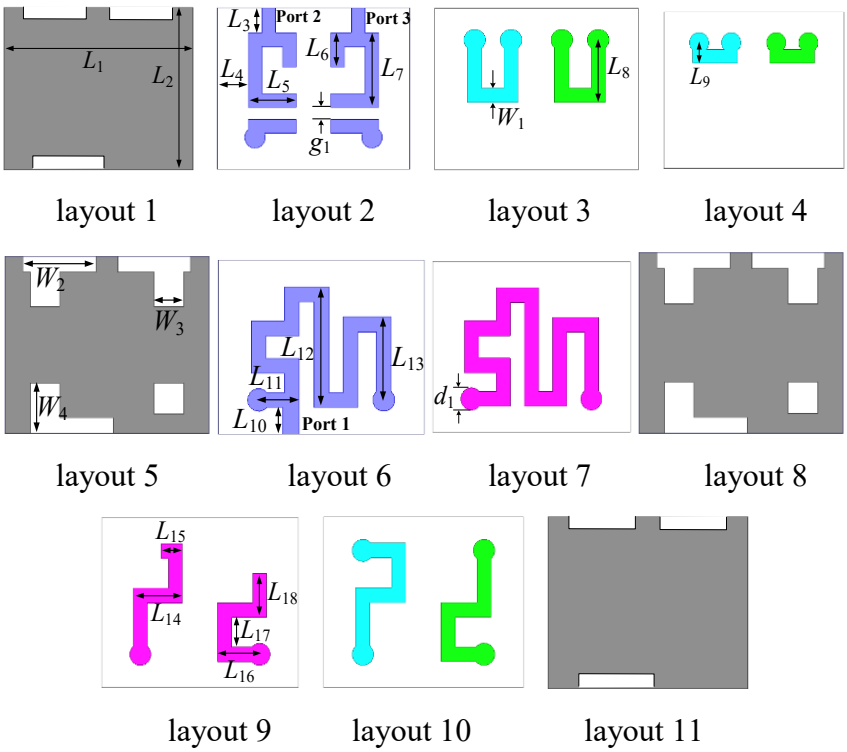

Figure 3.8. Detail layouts of the proposed LTCC balun filter.

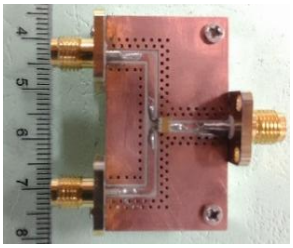

(a)

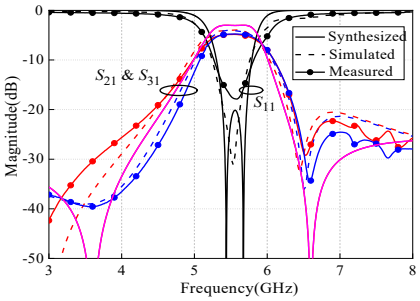

(b)

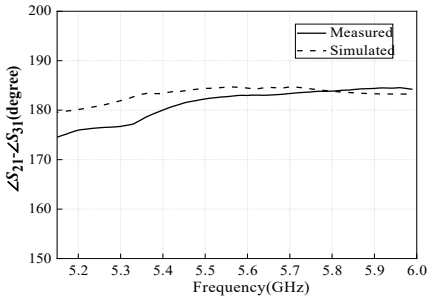

(c)

Figure 3.9. (a) Photograph of the fabricated circuit with test PCB-board; (b) Synthesis, simulated and measured S_{11}, S_{21} & S_{31}; (c) Simulated and measured phase difference.

3.3.2.3 Comparison

The proposed design is compared with some other LTCC balun filters as tabulated in Table 3.1. Our design is realized based on Marchand balun, whereas others are based on resonators. Moreover, in [45], [47], [101], the LC lumped elements are utilized to constitute the balun filters with compact size. However, it is difficult to accurately model the lumped inductors and capacitors in high-frequency ranges and thus time-consuming optimization is needed. In our work, the distributed transmission lines are employed and the coupling matrix is given to guide the design. The required responses can be conveniently obtained by realizing the elements in the coupling matrix. In [102], distributed resonators were also introduced. However, it costs a larger circuit area and suffers from a larger phase imbalance. As for the height, it is determined by the fabricated process. In [102] and our design, there are 8 circuit layers excluding the ground planes. However, the thickness of each ceramic sheet is equal to the times of 100 μm in our design and equal to the times of 23 μm in [102]. Thus, the height of our design is larger than that in [102]. It is noted that if the thicknesses of each sheet in the two designs are the same, the height is nearly the same.

Table 3.1 Comparison With Some Other LTCC Balun Filters

Ref.	Basic	Design method	Mag. (dB)/ phase (deg) imbalance	Electrical size (λ_g^3)	Circuit layers	Sheet thickness (μm)
[45]	Resonator	Lumped	0.3/1.0	0.103×0.091×0.018	~9	91
[47]	Resonator	Lumped	1.8/6.2	0.099×0.065×0.041	12	23
	Resonator	Lumped	1.1/3.2	0.099×0.050×0.035	10	23
[101]	Resonator	Lumped	0.4/3.5	0.066×0.042×0.042	>10	-
[102]	Resonator	Distributed	0.6/12.5	0.124×0.074×0.037	8	23
This work	Marchand balun	Distributed	0.6/5	0.089×0.076×0.071	8	100

3.4 Compact High-Isolation LTCC Diplexer Using Common Stub-Loaded Resonator with Controllable Frequencies and Bandwidths

Diplexers are essential components in radio frequency (RF) transceivers to separate input signals into two output ports, or vice versa. With the stringent requirements in modern communication systems, a diplexer with compact size, simple structure, lightweight, high isolation, high channel rejection level and lost cost is always in demand.

To design diplexers with high isolation, there are two popular solutions. The first one is to use high-quality-factor waveguides and cavity/dielectric resonators [103]-[105]. This method is widely used in based station applications, but the large size and heavyweight of waveguide and cavity/dielectric components make them unsuitable for miniaturized systems. The other method is to design two independent filters on the printed circuit boards (PCBs) and then use T-junctions to combine them [63], [106]-[110]. In this way, it is very convenient to control the performance of each channel. However, in these designs [63], [106]-[110], the T-junction combiners and the independently-designed two filters cost extra circuit size. In

order to reduce the size, common resonators operating at two frequencies are used to replace several resonators and matching (or combining) networks in diplexers [64]-[66], [111], [112]. However, isolation and the control of each channel filter (eg, channel frequencies and bandwidths) are problematic issues.

The above diplexers [63]-[66], [106]-[112] employ planar PCB structures and it is difficult to further reduce the circuit size. To solve this problem, multilayer structures are utilized. For example, the diplexers can be fabricated in multilayer PCB substrates [113], [114]. Owing to the design flexibility, the low temperature co-fired ceramic (LTCC) technology is widely used in miniaturized components [115]-[119]. In [115], a compact LTCC diplexer is realized based on transmission lines whereas the roll-off rate needs to be improved. By introducing the filters with transmission zeros located at the lower and higher passband edges, an LTCC diplexer with two close channels is realized [116]. Besides, the SIW in LTCC is presented in [117] for millimeter-wave diplexer applications.

In this thesis, a compact high-isolation LTCC diplexer with controllable frequencies and bandwidths is presented. A common resonator is used for the two channels and thus, only three resonators are needed to form the two second-order channel filters, resulting in simple structure and miniaturization. The common resonator consists of a main transmission line and an open stub loaded at the line center, which is called as the stub-loaded resonator. By making full use of the inherent features of the stub-loaded resonator, a novel transmission path is utilized to simultaneously realize the higher-channel filter and prevent the signal at the lower frequency band. Meanwhile, a specific coupling region is used to not only realize the coupling strength required by lower channel filter but also generate a transmission zero at the higher-band frequency (f_H). By using these two methods, high isolation can be obtained. The design method for manipulating the external quality factors and coupling coefficients at the two passbands are also proposed to control the bandwidths. Moreover, the center frequencies of the two channel filters

can be adjusted individually. The design theory and the circuit realization in LTCC are presented. The simulated and measured results are shown to verify the proposed idea.

3.4.1 Analysis of LTCC Diplexer

Figure 3.10 shows the schematic of the proposed LTCC diplexer. It consists of one common resonator operating at the lower and higher channel frequencies (f_L and f_H) and two half-wavelength resonators (R_1) and (R_2). Three ports (Port 1, 2 and 3) are tap- connected to three resonators. A capacitor (C') is placed between port 1 and the common resonator. The common resonator and R_1 are utilized to form the higher channel filter, while the common resonator and R_2 are used to design the lower channel filter. For diplexers using common resonators, it is a key issue for each channel filter to suppress signals at the frequency of the other filter to ensure high isolation. In this design, a transmission path is utilized in the higher channel filter to generate a transmission zero at the frequency of the lower channel filter, as addressed in Section 3.3.1.1. Meanwhile, a specific coupling region is introduced in the lower channel filter to produce a transmission zero at higher channel filter frequency, as presented in 3.3.1.2. Then, the two channel filters are combined to realize the proposed diplexer with high isolation, as described in Section 3.3.1.3.

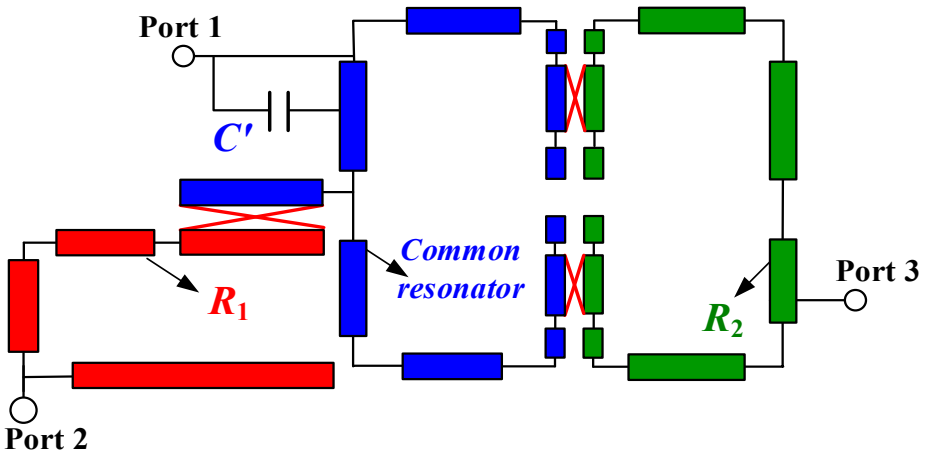

Figure 3.10. Schematic of the presented LTCC diplexer.

3.4.1.1 Analysis of Higher Channel Filter

For the higher channel filter, a transmission path is analyzed and utilized to generate a transmission zero at f_L. To analyze the transmission path, the common stub-loaded resonator is firstly introduced, as shown in Figure 3.11(a). It consists of a main transmission line and a centrally-loaded open stub, where Y_{m1}, θ_{m1}, Y_{m2}, and θ_{m2} denote the characteristic admittances and electric lengths of the main transmission line and open stub, respectively, and L_{m1} and L_{m2} are the physical lengths. Figures. 3.11(b) and (c) show its odd- and even-mode equivalent circuits, respectively. To simplify the analysis, it is assumed that $Y_{m2} = 2Y_{m1}$. Then, odd- and even-mode resonance frequencies can be calculated as [120]

$$f_{odd} = \frac{(2n-1)c}{2L_{m1}\sqrt{\varepsilon_{eff}}} \tag{3.6}$$

$$f_{even} = \frac{nc}{(L_{m1}+2L_{m2})\sqrt{\varepsilon_{eff}}} \tag{3.7}$$

where n = 1, 2, 3, …, c is the speed of light in free space, and ε_{eff} denotes the effective dielectric constant of the substrate. It can be observed the length of the open stub (L_{m2}) has no impact on f_{odd}. Thus, f_{odd} can be firstly determined by L_{m1}, and then L_{m2} is altered to meet the required f_{even} with f_{odd} fixed. In this design, the modes at f_{odd} and f_{even} are employed to form the two passbands at f_L = 3.5 GHz and f_H = 5.5 GHz, respectively.

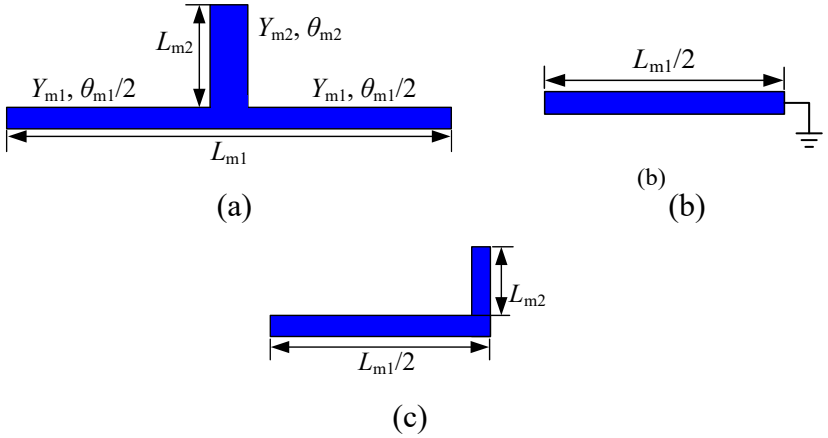

Figure 3.11. (a) Structure of the common resonator; (b) Odd-mode equivalent circuit; (c) Even-mode equivalent circuit.

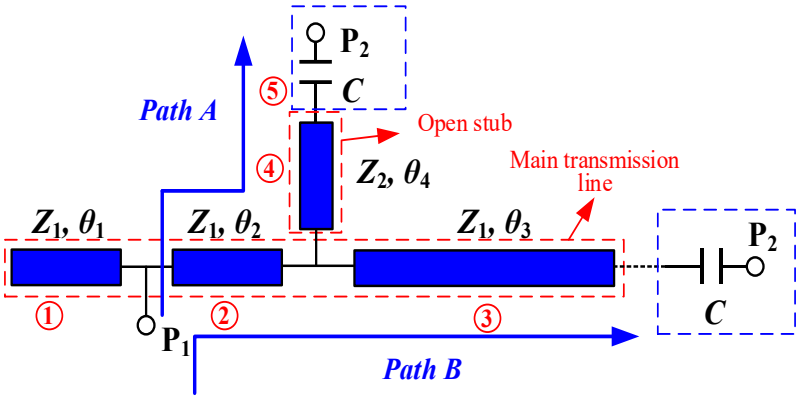

Figure 3.12. The transmission paths on the common resonator.

Based on the resonance property of the common resonator, the transmission path can be determined. Since the open stub is not part of the odd-mode circuit, the signal at f_{odd} cannot be transmitted to the open stub, namely, it can prevent the signal transmission at f_{odd}. For verification, two ports (P_1 and P_2) are added to the common resonator, as illustrated in Figure 3.12. P_1 is tap-connected to the main transmission line. P_2 is connected to the open end of the centrally-loaded stub through a series capacitor C which provides weak coupling between P_2 and the open stub. The proposed transmission path is illustrated as Path A in Figure 3.12, which is divided into five parts, where Z_1, Z_2, and θ_1-θ_4 represent the characteristic impedance and electrical lengths, respectively. The [ABCD] matrix of each part is calculated as

$$A_1 = \begin{bmatrix} 1 & 0 \\ j\frac{1}{Z_1}\tan(\theta_1) & 1 \end{bmatrix} \tag{3.8}$$

$$A_2 = \begin{bmatrix} \cos(\theta_2) & jZ_1\sin(\theta_2) \\ j\frac{1}{Z_1}\sin(\theta_2) & \cos(\theta_2) \end{bmatrix} \tag{3.9}$$

$$A_3 = \begin{bmatrix} 1 & 0 \\ j\frac{1}{Z_1}\tan(\theta_3) & 1 \end{bmatrix} \tag{3.10}$$

$$A_4 = \begin{bmatrix} \cos(\theta_4) & jZ_2\sin(\theta_4) \\ j\frac{1}{Z_2}\sin(\theta_4) & \cos(\theta_4) \end{bmatrix} \tag{3.11}$$

$$A_5 = \begin{bmatrix} 1 & \dfrac{1}{j\omega C} \\ 0 & 1 \end{bmatrix} \tag{3.12}$$

The overall [ABCD] matrix is expressed as

$$A = A_1 \times A_2 \times A_3 \times A_4 \times A_5 \tag{3.13}$$

Then, the S_{21} can be calculated as equation (3.2). Based on the desired passbands at f_L = 3.5 GHz and f_H = 5.5 GHz, initial parameters are chosen as follows: $\theta_1 + \theta_2 = \theta_3 = \pi/2$, $\theta_4 = 0.14\pi$, $Z_1 = 2Z_2 = 60\ \Omega$, $C = 0.001$ pF, where $\theta_1 - \theta_4$ are counted with respect to 3.5 GHz. With these parameters, the S_{12} at 3.5 GHz is calculated to be zero. Moreover, the wideband responses of Path A can be calculated by using (3.2), as illustrated in Figure 3.13. Also, the other transmission path (Path B in Figure 3.12) is given, where P_2 and the series capacitor C are connected to the main line of the common resonator. The corresponding S_{12} are shown in Figure 3.13 for comparison. As observed, by using the Path A, the mode at f_H = 5.5 GHz is kept whereas that at f_L = 3.5 GHz is suppressed due to the transmission zero. This transmission characteristic is suitable for the higher channel filter design.

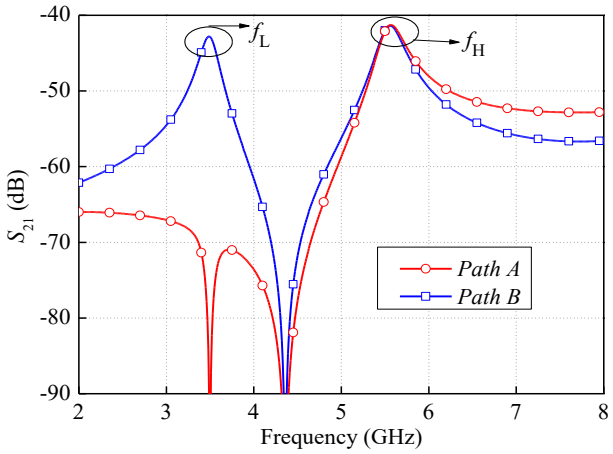

Figure 3.13. Calculated S_{21} of Path A and Path B under weak coupling.

Based on Path A, the higher channel filter is designed, as shown in Figure 3.14. A half-wavelength resonator (R_1) is coupled to the center stub of the common resonator. The coupling corresponds to the capacitor C in Figure 3.12. It has been

analyzed that a transmission zero can be generated at f_L. Meanwhile, in this structure, the input and output external quality factors (Q_{eiH} and Q_{eoH}) as well as the coupling coefficient (k_H) can be easily controlled by the location of two ports and the coupling strength between the common resonator and R_1, respectively. Hence, the desired higher channel responses can be obtained, as plotted in Figure 3.15. As observed, a passband is realized at 5.5 GHz and a transmission zero is located at the lower channel frequency 3.5 GHz with around 50 dB rejection levels. With these features, the desired higher channel filter is realized.

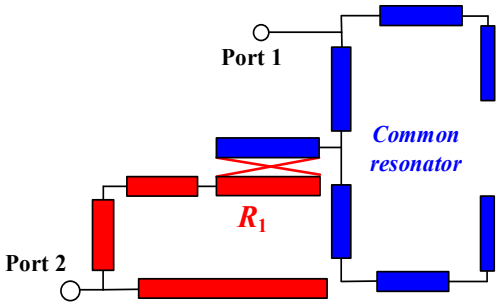

Figure 3.14. Schematic of the higher channel filter.

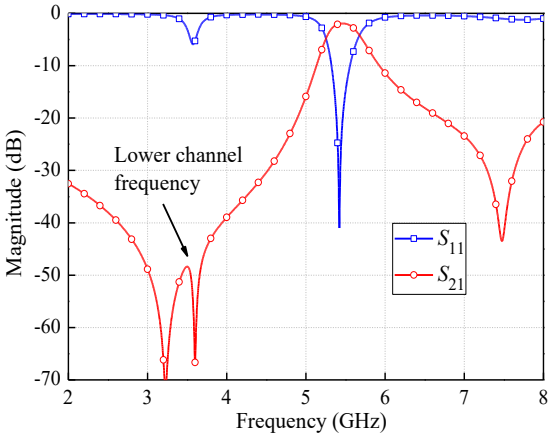

Figure 3.15. Simulated result of the higher channel filter.

3.4.1.2 Analysis of Lower Channel Filter

For the lower channel filter of a diplexer, it should have a high rejection level at the higher channel frequency (f_H). Herein, a coupling structure is introduced in the lower channel filter to generate a transmission zero at f_H, as presented below.

Figure 3.16(a) shows the schematic of the coupling structure. It consists of two open-ended transmission lines with quarter-wavelength electric length at f_H. The center parts of the two transmission lines are coupled to each other. Based on the transmission line theory, the normalized voltage and current distributions can be expressed as follows and illustrated in Figure 3.16(a) [80]

$$V(x) = \sin(\beta x) \tag{3.14}$$

$$I(x) = \cos(\beta x) \tag{3.15}$$

where β is the propagation constant. The electric and magnetic coupling coefficients can be defined on the basis of the ratio of coupled energy to stored energy by using equations (2.4) and (2.5).

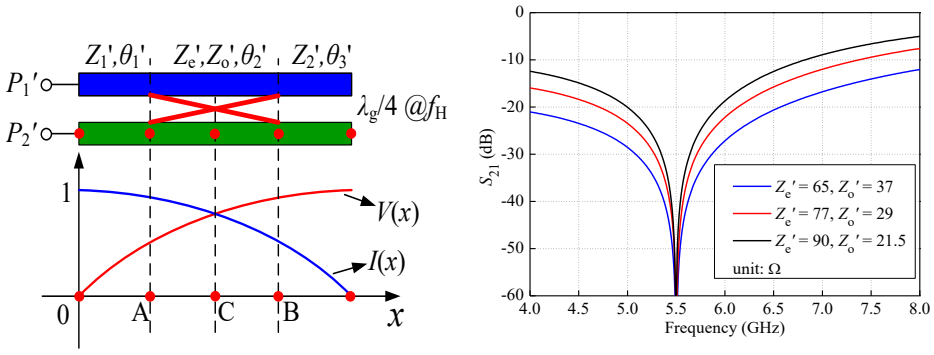

(a) (b)

Figure 3.16. (a)The coupling structure for generating a transmission zero at f_H; (b) simulated responses of the coupling structure.

For a quarter-wavelength open-end transmission line, the stored electric and magnetic energy is the same. Thus, the denominators in (2.4) and (2.5) are the same. The voltage and current can replace the corresponding electric and magnetic fields to evaluate the coupling coefficients, which can be expressed as

$$k_e' = P \times \int_A^B |V(x)|^2 \, dx = P \times \int_A^B |\sin(\beta x)|^2 \, dx \tag{3.16}$$

$$k_m' = P \times \int_A^B |I(x)|^2 \, dx = P \times \int_A^B |\cos(\beta x)|^2 \, dx \tag{3.17}$$

where P is constant. Accordingly, the overall coupling strength can be expressed as equation (3.3). Using this simplified equation (3.3), the coupling coefficient can be

evaluated. As shown in Figure 3.16(a), point C is at the middle point of the coupled line and points A and B are symmetric with respect to C. According to equation (3.3), $|k'|$ is calculated as zero. Thus, the signal at f_H cannot pass through this coupling region. Consequently, a transmission zero is generated. For verification, the coupling structure in Figure 3.16(a) is simulated by ADS and some parameters are chosen as follows: $Z_1' = Z_2' = 50\ \Omega$, $\theta_1' = \theta_2' = \theta_3' = 30^o$, where θ_1'-θ_3' are counted with respect to f_H (5.5 GHz). Figure 3.16(b) shows the simulated responses. It can be seen that a transmission zero is generated at f_H, which agrees with the analysis. Furthermore, it is noted that the transmission zero can be fixed when different Z_e' and Z_o' are selected, which can be utilized to control coupling strength at the lower channel filter frequency without impact on the transmission zero.

By using this coupling structure, the lower channel filter is designed with the schematic shown in Figure 3.17(a). It is comprised of a common resonator and a half-wavelength resonator (R_2) whose coupling sections (I and II) are the same as that of Figure 3.16(a). Port 1 and port 3 are tap-connected to the resonators. It is noted that the tap position of port 1 affects the input quality factor (Q_{ei}) at f_L and f_H. To increase the degree of freedom for controlling the external factor at port 1, a capacitor (C') is added between port 1 and the common resonator. Figure 3.17(b) shows the normalized voltage distribution at f_H. As seen, there are two voltage nulls at f_H. The capacitor is added to one null so that the effect on the Q_{ein} at f_H is very slight and can be nearly ignored.

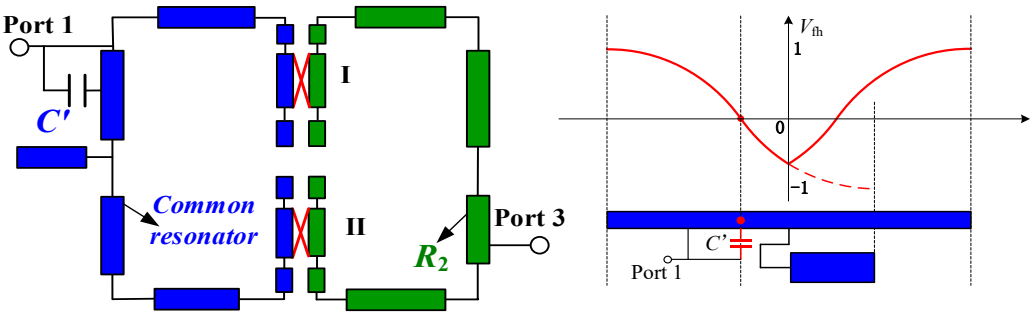

(a) (b)

Figure 3.17. (a) Schematic of the lower channel filter; (b) voltage distribution of the common resonator at f_H.

In order to realize the desired lower channel filter responses, it is necessary to study the coupling coefficient (k_L) and the input and output external quality factors (Q_{eiL} and Q_{eoL}). As shown in Figure 3.17(a), the desired k_L can be obtained by the coupling strength in regions I and II. For the Q_{eiL}, it is determined by the location of port 1 and the capacitor C'. In the higher channel filter design presented in section II-A, the location of port 1 is utilized to realize the Q_{eiH}. Thus, it is unchanged while designing the lower channel filter. Since the capacitor C' is placed at the voltage null of the common resonator at f_H, the influence on the coupling between the port 1 and the common resonator is slight. Accordingly, it is altered to realize the desired Q_{eiL} with a slight impact on Q_{eiH}. As for the Q_{eoL}, it can be controlled by the location of port 3. Consequently, passband responses of the desired lower channel filter can be obtained. Besides, a transmission zero at f_H can be generated by the coupling section I and II to enhance the out-of-band performance, which has been analyzed before. Accordingly, the desired lower channel filter responses are obtained. It is seen from the simulated results in Figure 3.18 that a transmission zero is generated at (f_H) and a high rejection level of around 46 dB is achieved within the higher passband frequencies, which can meet the requirement of the lower channel filter.

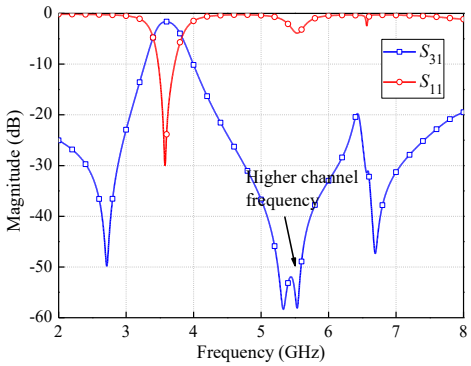

Figure 3.18. Simulated responses of the lower channel filter.

3.4.1.3 Analysis of Diplexer

Based on the above analysis, a diplexer is designed by combining the lower and higher channel filters, as shown in Figure 3.10. For a diplexer, the isolation between two output ports (S_{23}) is a significant design target. In the proposed design, high

isolation at the two passbands can be obtained, as analyzed below. Firstly, the R_1 is coupled to the center stub of the common resonator. As analyzed in Section 3.3.1.1, the signal at the lower passband frequency (f_L) cannot be transmitted to the center stub. Thus, the signal at f_{odd} from port 2 cannot pass through the open stub to the main line of the common resonator, or vice versa, resulting in high isolation. Secondly, the coupling region (I and II) between the common resonator and R_2 is the same as that in the lower channel filter design, which has been analyzed in Section 3.3.1.2. It is known that a transmission zero at the higher passband frequency (f_H) can be generated by these coupling sections because the electric and magnetic coupling at f_H is canceled. Accordingly, it can be known that from port 2 to port 3, both the signals at f_L and f_H cannot be transmitted. Thus, high isolation within the passbands of two channel filters can be realized. For demonstration, the simulated S_{23} is shown in Figure 3.19. As seen, the isolation levels within the two passbands are better than 48 dB, which verifies the analysis.

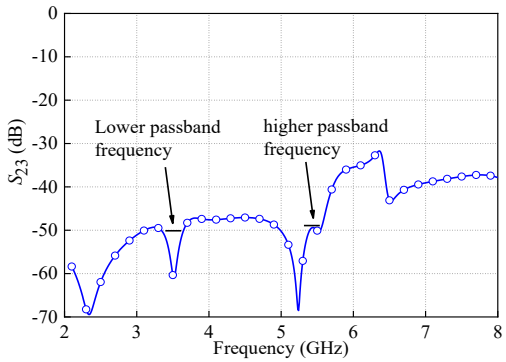

Figure 3.19. Simulated S_{23} of the presented diplexer.

3.4.2 Design of LTCC Diplexer

Based on the above analysis, the diplexer is realized using the LTCC process. The Ferro A6-M substrate is used with a dielectric constant of 5.9 and a loss tangent of 0.002. Figure 3.20 shows the 3-D structure of the presented LTCC diplexer. The whole circuit is composed of eighteen metal layers and seventeen ceramic sheets with the thicknesses shown in Figure 3.20. In the middle parts (in blue), the common resonator is folded vertically and horizontally on layers 6, 8, 9, 10 and 12

for size reduction. A half-wavelength resonator (R_2 in green) for the lower channel filter is placed above the common resonator on layers 14, 16 and 17. Two metal patches are placed between the common resonator and R_2 to control the coupling coefficient of the lower channel filter at layer 13. The other half-wavelength resonator (R_1 in red) for the higher channel filter is located on layers 2, 4 and 6. The metal patch in layer 5 is used for adjusting the coupling coefficient of the higher channel filter. Vias are utilized to connect circuits on different layers. The capacitor C' in Figure 3.18(a) is realized by introducing the quasi-lumped capacitor between layers 8 and 9. The ground planes are plotted on layers 1, 3, 7, 11, 15 and 18. The squares are etched on layers 3, 7, 11 and 15 for solid adhesion of two ceramic sheets to enhance the reliability. Due to the design flexibility of the multilayer LTCC structure, the bandwidths and frequencies of the two passbands can be controlled separately, as analyzed below.

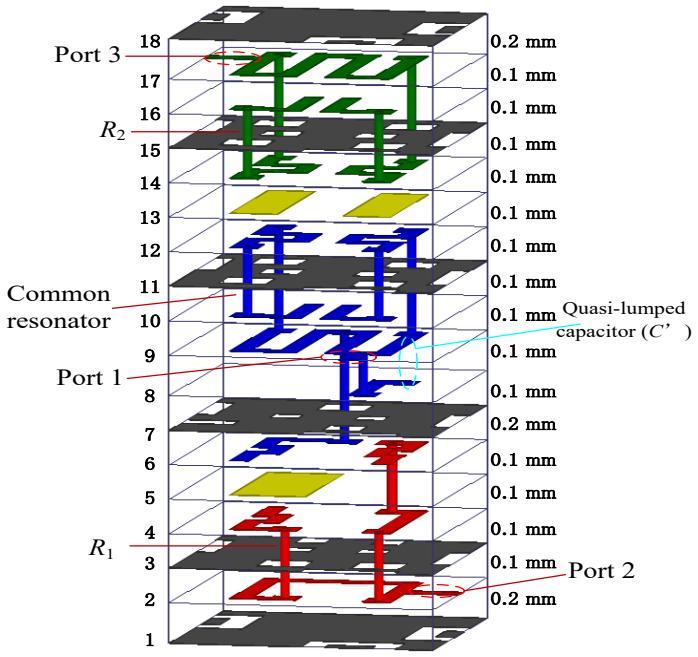

Figure 3.20. 3-D structure of the presented LTCC diplexer.

To obtain the desired bandwidths of the two passbands, the external quality factor Q_e and coupling coefficient k should be controlled. Here, Q_e is discussed firstly. According to the analysis of the higher and lower channel filters, it can be known

that Q_{eiH} and Q_{eiL} can be obtained by changing the location of port 1 and the value of capacitor C'. In the LTCC structure, the location of port 1 is firstly determined to obtain the Q_{eiH}. Then, the quasi-lumped capacitor C' as shown in Figure 3.20 is tuned to realize the Q_{eiL}. As for Q_{eoH} and Q_{eoL}, they can be realized by controlling the locations of port 2 and port 3. Accordingly, the required Q_es can be realized.

For the coupling coefficients (k_H and k_L), they are obtained by introducing the special multi-layer coupling structures in the LTCC circuit. The k_H is analyzed firstly. Figure 3.21(a) shows the LTCC structure of the coupling region from layer 3 to layer 7. Parts of resonators are placed on layer 4 and layer 6. Layers 3 and 7 are the ground planes. A metal patch, which provides the electric coupling to the common resonator (C_{r2}) and R_1 (C_{r1}), are plotted on layer 5. C_{r3} represents the coupling between the two resonators. Meanwhile, there are two equivalent capacitors C_{g1} and C_{g2}, which are formed by the patch and two ground planes. The equivalent circuit is illustrated in Figure 3.21(b). The capacitance of the parallel plate capacitor can be expressed as

$$C = \frac{\varepsilon S}{d} \tag{3.18}$$

where ε is a constant, S means the coupling area and d denotes the distance between the two plates. In the proposed design, the size of the metal patch is changed to control the coupling coefficient. As seen, if the area of metal patch is much larger than part of the common resonator and R_1 in layers 4 and 6, when the patch size increases, C_{r1}, $C_{r2,}$ and C_{r3} nearly keep unaltered. However, it can be noted that the values of C_{g1} and C_{g2} increase when the size of the patches is larger. As shown in Figure 3.21(b), when the values of C_{r1}, C_{r2}, and C_{r3} are kept unchanged, C_{g1} and C_{g2} can be tuned to change the total coupling strength. Thus, the size of the patch can be utilized to control the value of k_H. Similarly, the k_L can also be controlled by introducing patches between the common resonator and R_2, as shown in Figure 3.20(layer 13). Thus, k_H and k_L are realized.

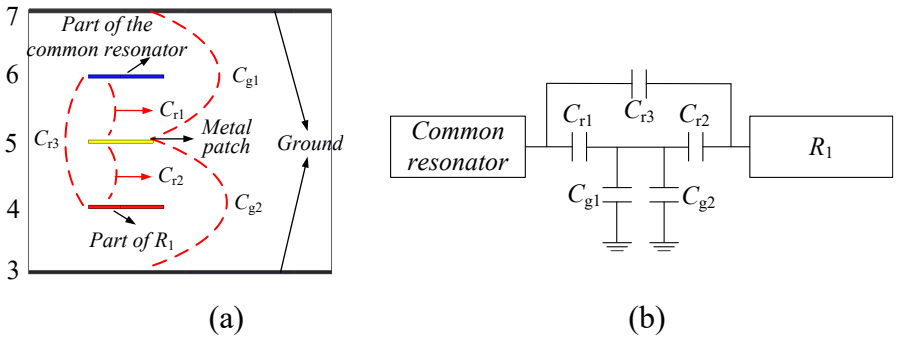

(a) (b)

Figure 3.21. (a) LTCC structure of the coupling region from layer 3 to layer 7; (b) Equivalent circuit of the coupling region.

Based on the above analysis, it is known that the Q_e and k of the two channel filters can be realized separately. Thus, the bandwidths can be realized individually. For demonstration, LTCC diplexers with different bandwidths are simulated and results are shown in Figures 3.22(a). It can be found that the bandwidth of one passband can be altered with almost no influence on the other one.

Apart from the bandwidths, the center frequencies of the two passbands can also be controlled individually. It is due to the use of the stub-loaded common resonator and two separated resonators. As indicated by equation (3.4) and (3.5), the even- and odd-mode resonance frequencies can be controlled individually. The transmission zero, generated by the coupling region between R_2 and common resonator, can be moved as f_H is changed to ensure high rejection levels at the higher passband. Meanwhile, for the higher channel filter, the signal at the lower passband is suppressed by a specific transmission path. Thus, when the diplexers are designed with different center frequencies, a high rejection level can also be realized. Figure 3.22(b) shows the simulated responses. It can be seen that the higher channel frequency can be changed with the lower passband frequency fixed, which verifies the proposed idea.

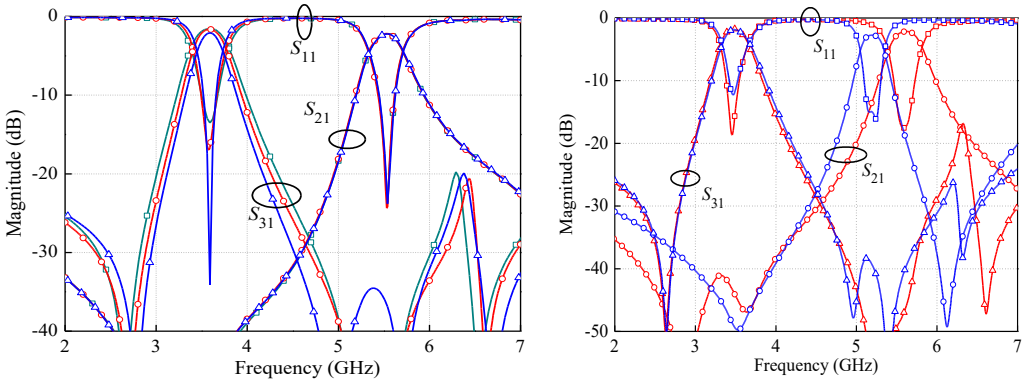

(a) (b)

Figure 3.22. Simulated results of the LTCC diplexer (a) with different lower passband bandwidths; (b) with different passband frequencies.

3.4.3 Experiment and Comparison

For verifying the proposed concept, the LTCC diplexer is implemented. The design procedure is listed as follows.

Step 1: Based on the desired lower and higher passband frequencies, the dimensions of the common resonator are determined by equations (3.6) and (3.7). R_1 and R_2 are half-wavelength resonators, whose dimensions can also be calculated.

Step 2: For the implemented diplexer, the *FBWs* of the two passbands are chosen as 11% and 9%. Then, the desired Q_e (Q_{eiL}, Q_{eoL}, Q_{eiH}, and Q_{eoH}) and k (k_L and k_H) of the two passbands can be calculated by

$$Q_e = \frac{g_0 g_1}{FBW} \tag{3.19}$$

$$k = \frac{FBW}{\sqrt{g_1 g_2}} \tag{3.20}$$

where g_0, g_1... are the lumped element values of the second-order prototype filter: $g_0 = 1$, $g_1 = 1.4029$, $g_2 = 0.7071$ and $g_3 = 1.9841$.

Step 3. The main transmission line of the common resonator and R_1 are coupled to meet the k_L. It should be noted that the coupling region is selected to generate a transmission zero at f_H according to the analysis in 3.3.1.2. The centrally-loaded

open stub of the common resonator is coupled to R_2 to realize the k_H.

Step 4. The locations of the port 1, 2 and 3 are controlled to realize the Q_{eiH}, Q_{eoH}, and Q_{eoL}, respectively. The quasi-lumped capacitor between port 1 and the common resonator is controlled to obtain the Q_{eiL}.

Step 5. Fine-tuning is performed to ensure performance.

Following the design procedure, a LTCC diplexer is fabricated and the 3-D configuration is shown in Figure 3.20. Figure 3.23 shows the layout of the metal layers. The parameters are determined as follows (all in mm): $L_1 = 2.8$, $L_2 = 2.7$, $L_3 = 0.55$, $L_4 = 0.35$, $L_5 = 1.28$, $L_6 = 0.4$, $L_7 = 1.7$, $L_8 = 0.47$, $L_9 = 0.4$, $L_{10} = 1.6$, $L_{11} = 0.7$, $L_{12} = 0.5$, $L_{13} = 0.4$, $L_{14} = 0.4$, $L_{15} = 1$, $L_{16} = 0.3$, $L_{17} = 0.7$, $L_{18} = 2.25$, $L_{19} = 0.95$, $L_{20} = 0.7$, $L_{21} = 0.5$, $L_{22} = 1.29$, $d_1 = 0.15$, $W_1 = 0.2$, $W_2 = 0.3$. The core circuit size is 1.9 mm × 1.7 mm × 2 mm or 0.054 λ_g × 0.048 λ_g × 0.057 λ_g, where λ_g is the guided wavelength at the lower channel frequency. The overall circuit size including the package is 2.8 mm × 2.7 mm × 2 mm. Figures 3.24(a) and (b) show the 3-D view and photograph of the proposed LTCC diplexer with test PCB board.

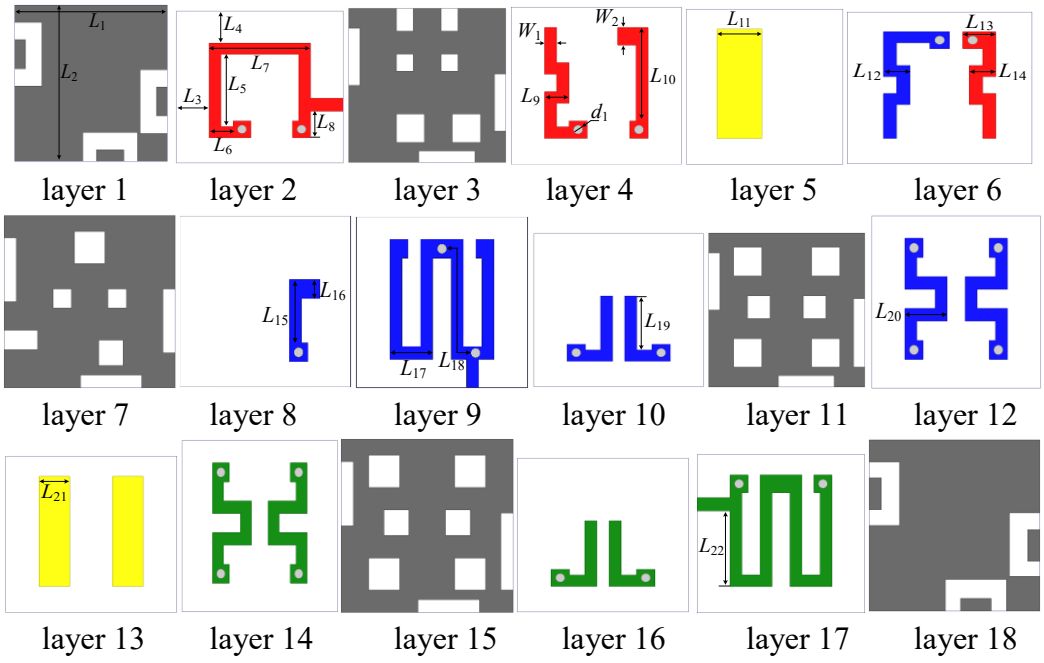

Figure 3.23. Layouts of the proposed LTCC diplexer.

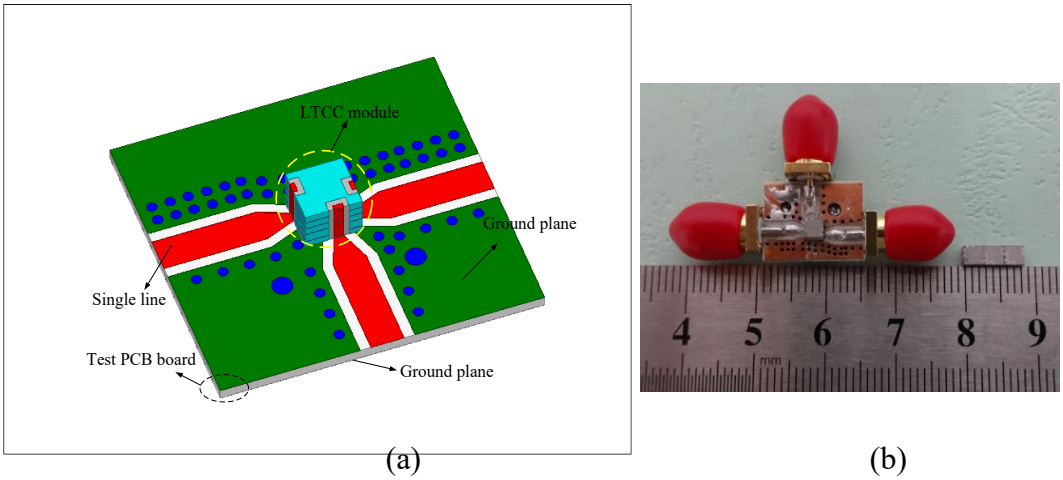

(a) (b)

Figure 3.24. (a) A 3-D view of the LTCC diplexer with test PCB board; (b) Photograph of the fabricated LTCC diplexer.

The simulation and measurement are carried out by using high frequency structure simulator (HFSS) and Agilent 8753ES network analyzer, respectively. Good agreement between the simulated and measured results is observed in Figure 3.25. The measured two passbands are centered at 3.55 and 5.55 GHz with the 3-dB bandwidth of 11.5% and 8.6%. The insertion losses are 1.74 and 2.37 dB at the two center frequencies, while the return losses at both two passbands are better than 15 dB. The measured isolation within the two passband frequencies is better than 40 dB and 45 dB. Meanwhile, the better than 36-dB isolation is measured from 2 GHz to 8 GHz.

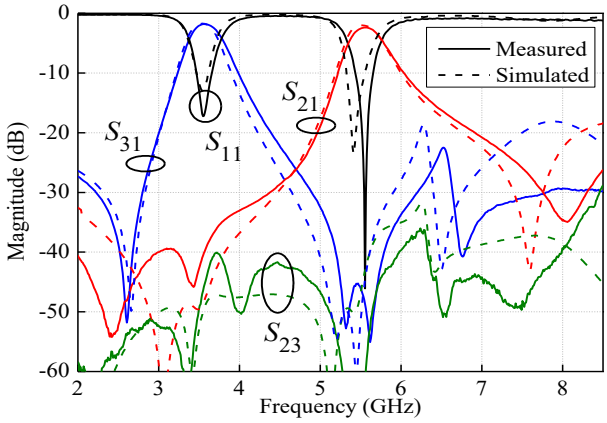

Figure 3.25. Simulated and measured results of the LTCC diplexer.

Table 3.2 tabulates the comparison with some PCB diplexers [64], [65], [105],

[107], [113] and LTCC ones [115]-[117]. In [105] and [107], T-junctions are utilized as combining circuits and two channel filters are designed separately, which cost extra circuit size. In our design, a common resonator is used and thus only three resonators are needed and the matching/combining circuits are avoided. Meanwhile, the isolation in our design is better than 40 dB while that in [105] and [107] is less than 30 dB. Comparing to the diplexer in [64], [113], the bandwidths and frequencies of the two channel filters in our work are controllable. What's more, the single-layer PCB structure is utilized to fabricate the diplexers in [64], [105] and [107], which are difficult to reduce the circuit size. In [113], multilayer PCB is employed for size reduction. However, isolation is less than 30 dB. In [115]-[117], diplexers are fabricated using LTCC techniques. The multilayer structures make the diplexer components able to be designed within a very compact size. Nevertheless, the isolation in these works is less than 35 dB. In sum, the proposed LTCC diplexer features compact size, high isolation as well as controllable frequencies and bandwidths.

Table 3.2 Comparison With Some Other Diplexers

Ref.	f_L/f_H (GHz)	Resonators	Isolation (dB)	Bandwidth control	Frequency control	Fabricated process
[105]	1.8 / 2.45	4	30/25	Yes	Yes	PCB
[107]	3.65 / 5.2	4	25/25	Yes	Yes	PCB
[64]	1.95 / 2.14	3	44/36	No	No	PCB
[65]	1.95 / 2.14	3	40/35	No	No	PCB
[113]	1.03 / 1.37	-	27/22.5	Yes	Yes	PCB
[115]	0.92 / 1.8	-	>20/20	Yes	Yes	LTCC
[116]	1.9 / 2.45	4	30/30	Yes	Yes	LTCC
[117]	40 / 50	2	33/24	Yes	No	LTCC
This work	3.55 / 5.55	3	40/45	Yes	Yes	LTCC

3.5 Filtering Rat-Race Coupler Based on Quad-Mode Dielectric Resonator

Couplers and bandpass filters (BPFs) are key components in many radio frequency (RF) front-ends of wireless communication systems [121]-[125]. Generally, they are cascaded, such as the rat-race coupler and BPFs shown in Figure 3.3. Two BPFs are needed to integrate bandpass responses to one rat-race coupler, occupying large circuit areas. The inter-stage mismatch may exist and thus cause performance degradation. Moreover, the total loss including the losses of rat-race coupler and BPF is usually high.

To overcome these problems, many efforts are conducted to integrate the rat-race coupler and BPF as a multifunctional filtering rat-race coupler with the schematic shown in Figure 3.3 [54], [57], [126]-[130]. In [54], a compact wide-stopband filtering rat-race coupler is designed by using four $\pm K$ inverters with bandpass functions that replace the one or three quarter-wavelength transmission lines in classical rat-race coupler. In [126], quarter- and half-wavelength microstrip resonators are used to construct the rat-race coupler with bandpass responses. By using four stub-loaded stepped-impedance resonators, a dual passband 180^{o} hybrid is realized [127]. Based on the low-temperature co-fired ceramic (LTCC) techniques, the multilayer filtering rat-race couplers are designed with a very compact size [57], [128]. Nevertheless, the above multifunctional designs [54], [57], [126]-[130] suffer from the low Q factor, which are not suitable for narrow-band applications, such as the fractional bandwidth (FBW) less than 2%. Otherwise, the insertion loss would be high.

Due to the high Q factor, dielectric resonator (DR) and cavity are popularly employed in narrow-band specifications [131]. Apart from the BPFs, diplexers and balance/balun BPFs, the filtering couplers have also been developed using DRs. In [59], a Ku- band bandpass 180^{o} directional coupler is designed using four $TE_{01\delta}$-

mode DRs. Narrow bandwidth is obtained with low loss whereas the quad-cavity configuration suffers from large size and heavyweight. By utilizing a single cavity with a cross-shaped dual-mode DR, the four-port filtering rat-race coupler is constructed with miniaturized size [60]. However, this coupler features the first-order bandpass responses where the out-of-band roll-off rate performance is not so good, resulting in poor skirt selectivity.

In this thesis, filtering rat-race couplers are designed using the quad-mode DR. Due to the high *Q* factor, the proposed couplers are realized with a low loss under narrow-bandwidth specification. By utilizing one quad-mode DR and four feeding probes, a single-cavity configuration is achieved with compact size. In order to construct a quad-mode DR, resonant frequencies of a rectangular DR is firstly investigated and then EM-field properties at two resonant mode pairs are studied. Inherent in-phase and out-of-phase characteristics of EM fields in the DR are utilized to obtain the desired 0° and 180° phase differences of the rat-race coupler topology. By properly arranging the four feeding probes, a single-cavity coupler configuration is constructed, featuring compact size. The detailed design method is given. For verification, a filtering rat-race coupler using rectangular DR is fabricated and measured, showing the good performance of filtering responses, amplitude balance as well as the 0^{o} and 180^{o} phase differences. Moreover, for further verifying the proposed design method, the other filtering rat-race coupler is implemented based on cylindrical DR with an improved *Q* factor. Comparison with other filtering couplers indicates that proposed designs exhibit the advantages of compact size, high *Q* factor, and good filtering responses.

3.5.1 Filtering Rat-Race Coupler Based on Quad-Mode Rectangular DR

3.5.1.1 Analysis of Rectangular Quad-Mode DR and Rat-Race Coupler Schematic

In the proposed filtering rat-race coupler, a quad-mode rectangular DR is

employed with the 3-D view shown in Figure 3.26(a). The DR is placed at the center of a cuboid metallic cavity. Its top and bottom surfaces are connected to the metal walls of the cavity. In other words, the rectangular DR is designed as short-circuited at two ends. a, b and h are the length, width, and height of the DR, respectively, while A, B, H are those of the metal cavity. To generate the orthogonal resonant modes with the same frequency, a and b are selected with the same dimension, namely, $a = b$. In order to investigate the resonant frequencies of this DR, some initial dimensions are chosen as follows (all in mm): $a = b = 10$, $A = B = 25$, $h = H = 13$. The substrate of DR has a dielectric constant of 36.5. Solving by the eigenmode solution type in high frequency structure simulator (HFSS), resonant frequencies of the DR versus h (a and b are unaltered) are illustrated in Figure 3.26(b). Here, we use M1-M4 to represent the lowest modes. Among them, both M2 pair and M3 pair are the orthogonal mode pairs. As can be observed in Figure 3.26(b), when h is around 14 mm, M2 pair and M3 pair resonate at the same frequency. Thus, by selecting the values of a, b and h within a proper range, this DR can be used as a quad-mode resonator.

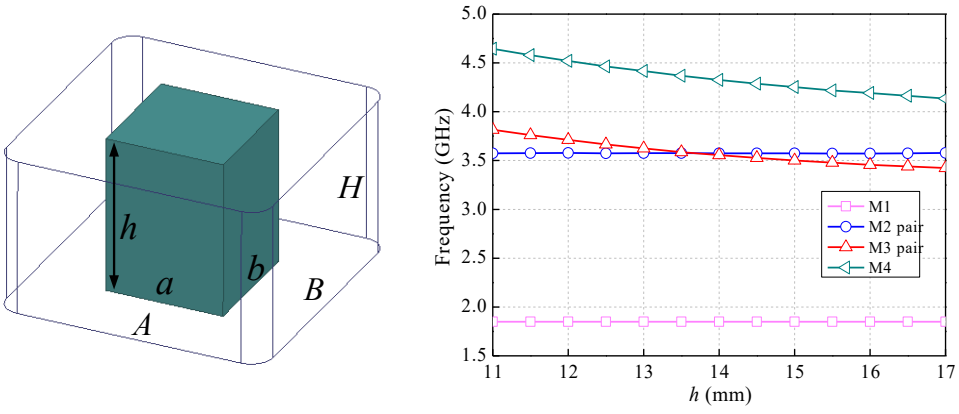

(a) (b)

Figure 3.26. Quad-mode rectangular DR (a) 3-D structure; (b) Resonant frequencies versus h.

In order to employ the quad-mode DR to construct a filtering rat-race coupler, the EM-field properties of the two mode pairs are studied. Figure 3.27 shows the

EM-field distributions of the DR at M2 pair and M3 pair. As seen, both the M2 pair and M3 pair are orthogonal pairs. The E-fields of M2 pair are extended between the top and bottom walls, while that of the M3 pair form two half circles. As seen from E-fields in Figure 3.27, M2 and M3 pairs do not coincide with each other at the middle plane $z = h / 2$. Hence, four tuning probes, which placed at the plane $z = h / 2$ of the cavity as shown in Figure 3.28, can be utilized to theoretically fine-tune the M2 and M3 pairs independently. Taking into account the resonant frequency study of the DR in Figure 3.26, it has enough design freedom to obtain arbitrary desired resonant frequencies of this quad-mode DR. And it is utilized to construct a filtering rat-race coupler.

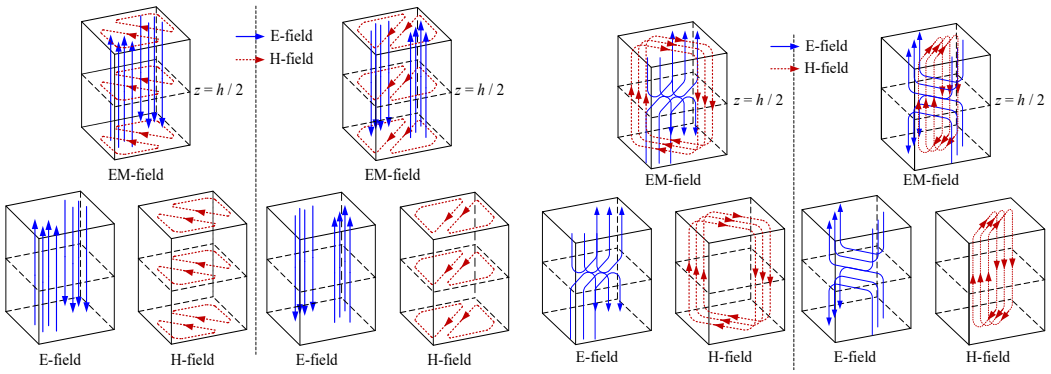

Figure 3.27. EM-field distributions of the quad-mode DR at (a) M2 pair; (b) M3 pair.

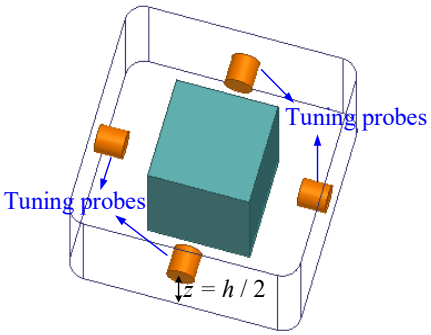

Figure 3.28. The quad-mode rectangular DR with four tuning probes.

For a four-port rat-race coupler configuration, when signals are injected from port 1, the output signals from ports 2 and 3 are in-phase. If port 4 is excited, the

out-of-phase responses are obtained in ports 2 and 3. Hence, the schematic can be depicted as Figure 3.29 (a), where the phase shifts from port 1 to ports 2 and 3 should be the same, while those from port 4 to ports 2 and 3 are required to exhibit the difference of 180°. For easy analysis of the amplitude and phase characteristics, the schematic is divided into two sections, including an in-phase power divider and an out-of-phase power divider, as shown in Figures 3.29(b) and (c), respectively. To construct the 3-D single-cavity structure to fulfill the whole schematics in Figure 3.29(a), the in-phase and out-of-phase power dividers with the schematic in Figures 3.29(b) and (c) based on DR are firstly designed. Then, the two power dividers are combined as a rat-race coupler. The detailed analyses are addressed below.

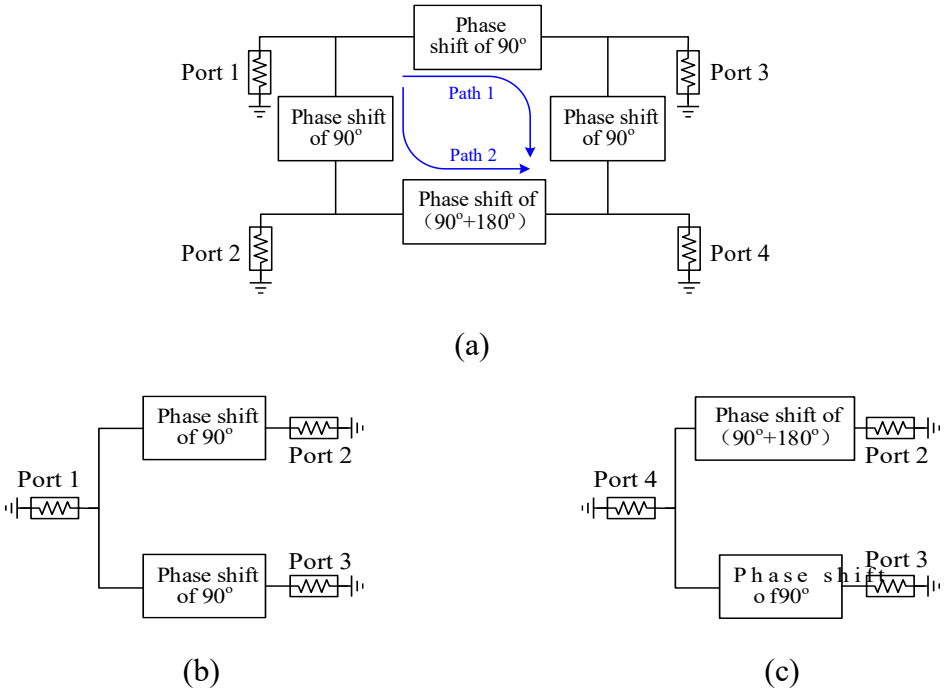

Figure 3.29. (a) Schematic of a rat-race coupler; (b) Schematic of an in-phase power divider; (c) Schematic of an out-of-phase power divider.

3.5.1.2 Analysis of the In-Phase Filtering Power Divider

Figure 3.30 shows the 3-D configuration of the in-phase power divider. It consists of a quad-mode rectangular DR and three feeding probes. The three feeding probes are arranged close to the DR for inputs and outputs, where ports 1-3 are defined as

illustrated in Figure 3.30. Among them, port 1 is extended from the top metal wall to the center, while ports 2 and 3 are extended from the bottom metal wall. Port 1 is placed at the center plane between ports 2 and 3 so as to separate the input signals to ports 2 and 3 equally. The whole 3-D structure is symmetric.

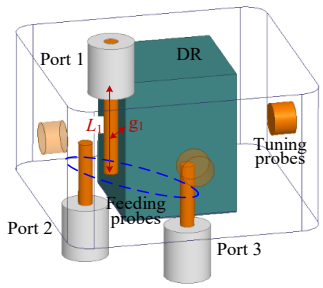

Figure 3.30. 3-D structure of the in-phase filtering power divider.

When signals are injected from port 1, the quad-mode rectangular DR can be excited. According to the analysis in Section II, the EM-field distributions of the DR at the two resonant pairs and feeding probes can be illustrated in Figure 3.31. Here, to show each mode clearly, we use M2' and M2" to represent the M2 pair, while the M3' and M3" are the M3 pair. To obtain good filtering responses, electric and magnetic coupling coefficients (k_e and k_m) between the DR and feeding probes are studied, which can be calculated on the basis of the ratio of coupling energy to stored energy by using equations (2.4) and (2.5).

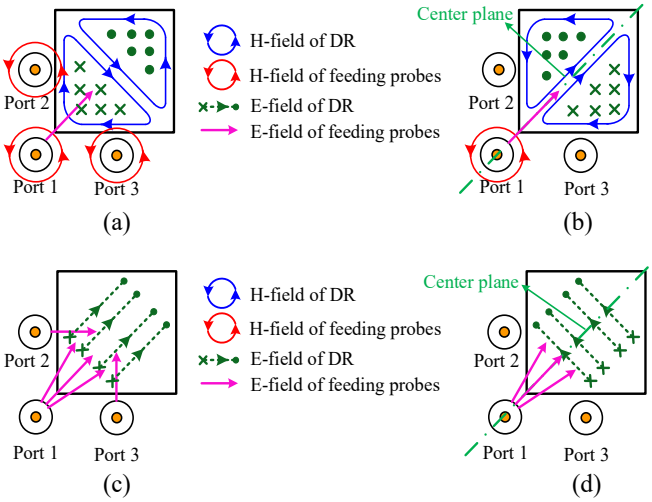

Figure 3.31. Top-view of EM-field distributions of the DR and feeding probes at (a)

M2' mode; (b) M2" mode; (c) M3' mode; (d) M3" mode.

From Figures 3.31(a) and (b), k_e between the feeding probes and DR at M2 pair can be calculated as zero based on equation (2.4) because the E-fields of feeding probes and DR are perpendicular to each other. However, at M2' mode, the feeding probes and DR can be coupled to each other through the magnetic coupling, as shown in Figure 3.31(a). In Figure 3.31(b), the H-field of the DR at M2" mode is symmetric at two sides of the center plane, while that of the port 1 is out-of-phase. According to equation (2.5), the k_m between DR and port 1 is calculated as zero. In conclusion, when the DR resonates at M2 pair, signals can only be transmitted to ports 2 and 3 through M2' mode. Similar to that in Figures 3.31(a) and (b), the coupling between feeding probes and DR at M3 pair in Figures 3.31(c) and (d) can also be analyzed. It is found that the coupling coefficient between port 1 and DR at M3" mode is nearly zero. As shown in Figure 3.31(d), the E-field of DR at two sides of the center plane is out-of-phase while that of port 1 is symmetric and thus the coupling between them is zero based on equation (2.4). As for the magnetic coupling, it is very weak and thus can be ignored. Since port 1 is closed to ports 2 and 3, weak source-load coupling exists.

Based on the above-mentioned analysis, the topology of in-phase power divider is obtained as Figure 3.32(a). As seen, the whole topology is symmetric. Hence, the half circuit with the topology shown in Figure 3.32(b) can be analyzed to characterize the overall circuit. It is equivalent to a second-order BPF. The coupling matrix of this second-order filter can be expressed as

$$M_{N+2} = \begin{array}{c} \\ S \\ 1 \\ 2 \\ L \end{array} \begin{array}{c} \begin{array}{cccc} S & 1 & 2 & L \end{array} \\ \begin{bmatrix} 0 & M_{S1} & M_{S2} & M_{SL} \\ M_{1S} & M_{11} & 0 & M_{1L} \\ M_{2S} & 0 & M_{22} & M_{2L} \\ M_{LS} & M_{L1} & M_{L2} & 0 \end{bmatrix} \end{array}. \tag{3.21}$$

As a design example, the desired passband is centered at 3.49 GHz with the 1.6% fractional bandwidth (FBW) of 20-dB equal-ripple return loss. Two transmission zeros are appointed at the frequencies of 3.15 and 4.1 GHz. Based on the advanced

coupling matrix synthesis method in [79], the initial coupling matrix with the same normalized input and output impedance can be synthesized as

$$M_{N+2} = \begin{array}{c} \\ S \\ 1 \\ 2 \\ L \end{array} \begin{array}{c} \begin{array}{cccc} S & 1 & 2 & L \end{array} \\ \begin{bmatrix} 0 & 0.8413 & -0.8826 & 0.0096 \\ 0.8413 & 1.6654 & 0 & -0.8411 \\ -0.8826 & 0 & -1.6525 & -0.8824 \\ 0.0096 & -0.8411 & -0.8824 & 0 \end{bmatrix} \end{array}. \tag{3.22}$$

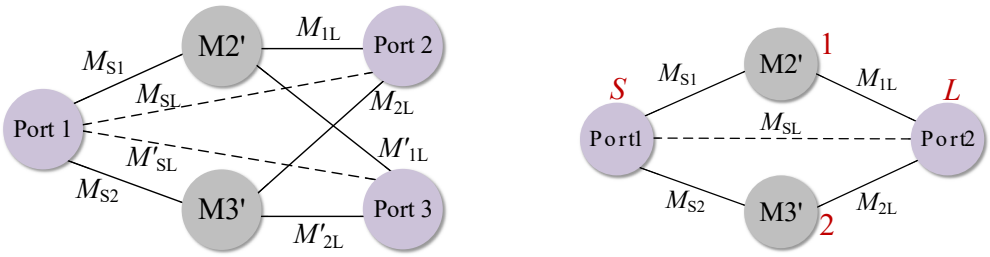

(a) (b)

Figure 3.32. (a) The topology of the in-phase power divider; (b) Topology of the half in-phase power divider.

Comparing to the topologies of an in-phase power divider and second-order BPF in Figures 3.32(a) and (b), it can be found that the in-phase power divider is realized by adding port 3 to the second-order BPF through the coupling expressed as M'_{1L}, M'_{2L}, and M'_{SL}. According to the filter design theory, some elements M_{1L} (M_{L1}), M_{2L} (M_{L2}) and M_{SL} (M_{LS}) in matrix (3.22) should be reduced by a factor of $\sqrt{2}$ to meet the requirement of input port matching of the in-phase power divider [45], which is expressed as equation (3.23), where $i = S, 1, 2$.

$$M_{iL,\text{modified}} = \frac{M_{iL}}{\sqrt{2}} \tag{3.23}$$

Other elements in matrix (3.22) are unaltered. The desired input and output external quality factor Q_{ei} at the center frequency (f_0) can be calculated by (3.24), where $i = 1, 2$.

$$Q_{ei} = \frac{1}{FBW \times M_{Si}^2 (or\ M_{iL}^2)} \tag{3.24}$$

The resonant frequency of the resonator corresponding to the non-zero M_{ii} is given by

$$f_i = f_0 \times \left| \sqrt{1+\left(\frac{M_{ii} \times FBW}{2}\right)^2} - \left(\frac{M_{ii} \times FBW}{2}\right) \right|. \tag{3.25}$$

After determining the above parameters, the 3-D structure of in-phase power divider is constructed to obtain the desired responses. Firstly, based on the resonant frequency study in Figure 3.26, the resonant frequencies of M2 pair and M3 pair are adjusted by the dimensions of the DR and tuning probes to meet the desired values of f_i. Then, Q_{ei} is realized by controlling the coupling between feeding probes and DR.

Figure 3.33(a) and (b) illustrate the extracted Q_{e1} and Q_{e2} against the length of the feeding probe (L_1) as well as the gap between the DR and feeding probe (g_1). From these two figures, it is known that the desired Q_{e1} and Q_{e2} can be obtained by optimizing the values of L_1 and g_1. The source-load coupling M_{SL} is achieved by the weak coupling between the input and output feeding probes. Consequently, the in-phase filtering power divider responses can be obtained. Figure 3.34(a) shows the theoretical and simulated results, which exhibit good bandpass responses and equal power division. Since the whole structure is symmetric, ports 2 and 3 have a good phase imbalance of less than ± 2°, as shown in Figure 3.34(b).

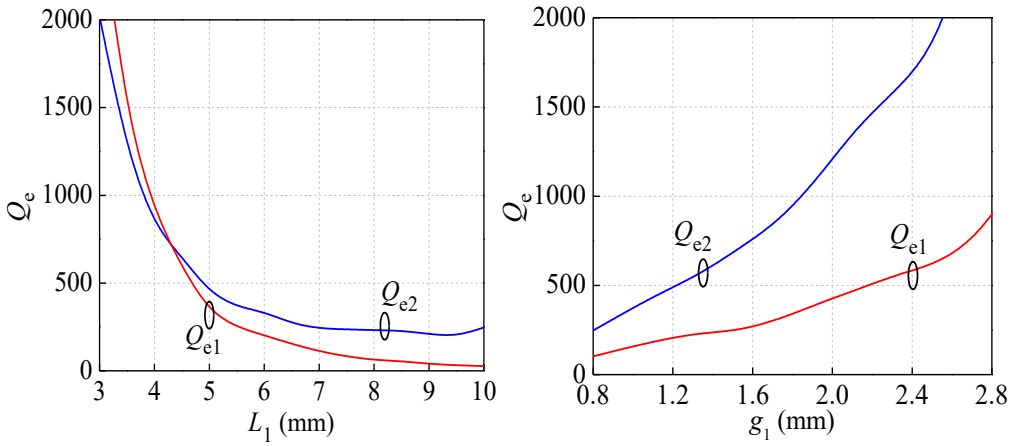

(a) (b)

Figure 3.33. Extracted Q_{e1} and Q_{e2} (a) against L_1; (b) against g_1.

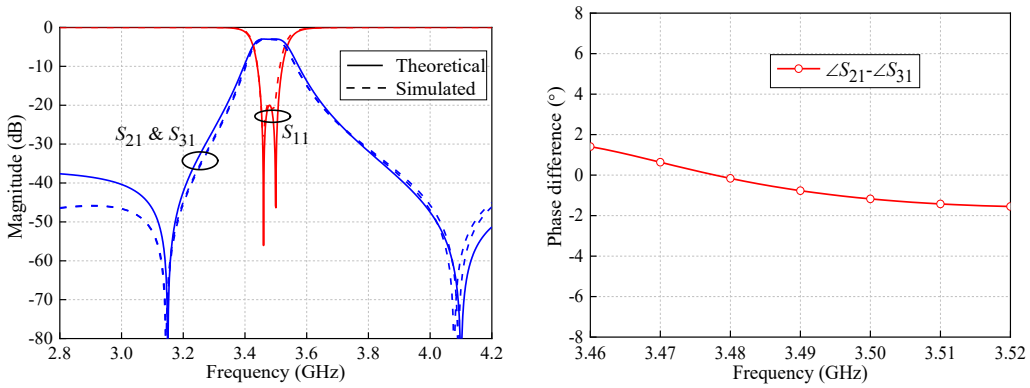

(a) (b)

Figure 3.34. (a) Theoretical and simulated results of the in-phase power divider; (b) Simulated phase difference between S_{21} and S_{31}.

3.5.1.3 Analysis of the Out-of-Phase Filtering Power Divider

Figure 3.35 shows the 3-D configuration of the out-of-phase filtering power divider. As compared to the in-phase power divider, the location of port 4 is different from that of port 1 in Figure 3.30. When the signals are injected from port 4, the EM-field distributions of the DR and feeding probes are shown in Figure 3.36. On the basis of the analysis of in-phase power divider, the topology of the out-of-phase filtering power divider can be easy obtained as Figure 3.37. As can be seen, the topology is similar to that of the in-phase power divider in Figure 3.32(a). Nevertheless, obvious differences can be found when comparing the EM-field distributions of the in-phase and out-of-phase filtering power divider. In Figure 3.31(a) and (c), signals are coupled from DR to ports 2 and 3 with the same phase at M2' and M3' modes. However, by analyzing the EM fields of feeding probes and DR at M2" and M3" modes in the out-of-phase filtering power divider in Figure 3.36(b) and (d), it is found that the EM-field directions of port 2 are opposite to that of port 3. It is because of the inherent in-phase and out-of-phase E-field distributions of the DR. Hence, it can be known that the desired out-of-phase output signals at ports 2 and 3 are obtained.

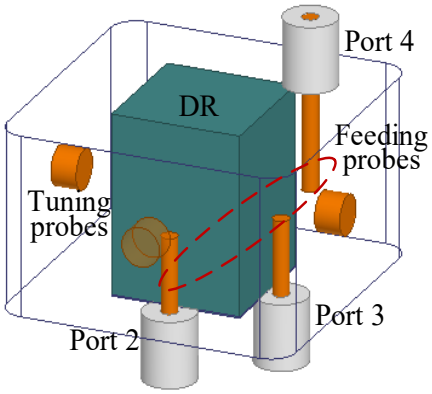

Figure 3.35. 3-D structure of the out-of-phase filtering power divider.

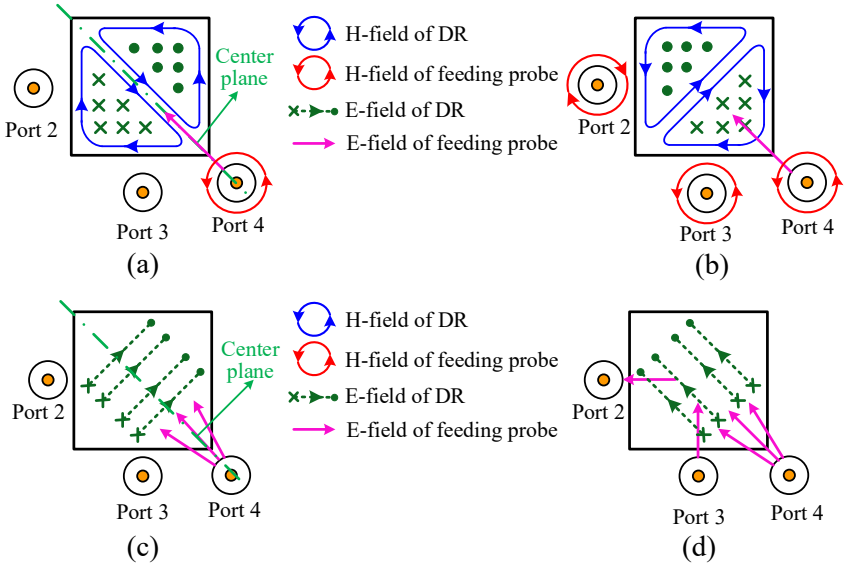

Figure 3.36. Top view of EM-field distributions of the DR and feeding probes in the out-of-phase power divider at (a) M2'; (b) M2"; (c) M3'; (d) M3".

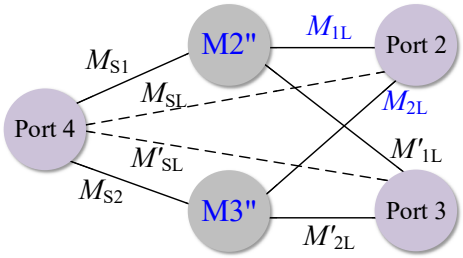

Figure 3.37. The topology of the out-of-phase filtering power divider.

To obtain good filtering responses, the desired values of the external quality factor (Q_{ei}) and resonant frequencies of DR (f_i) can be determined according to the analysis of in-phase power divider. Consequently, the out-of-phase filtering power

divider can be constructed. Figure 3.38 shows the simulated results of the out-of-phase filtering power divider. As can be seen, good filtering responses can be obtained and the phase difference between the two output ports is near 180°, which verifies the proposed idea.

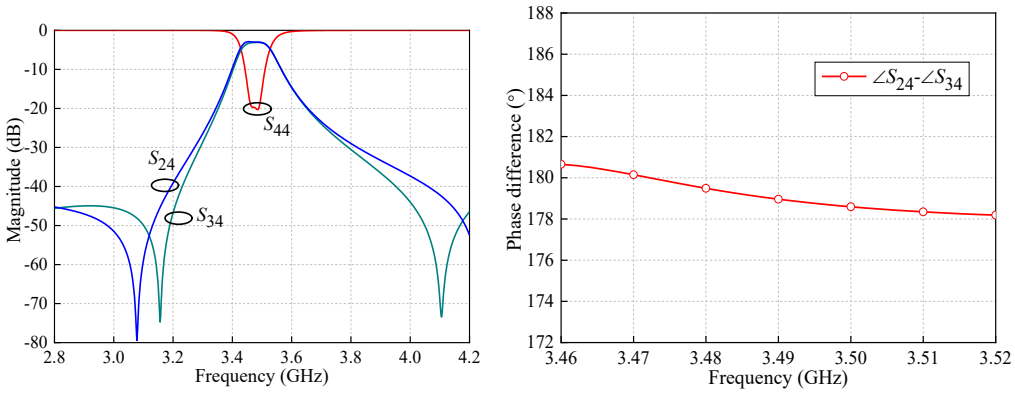

(a) (b)

Figure 3.38. Simulated responses of the out-of-phase filtering power divider (a) S_{24}, S_{34} & S_{44}; (b) Phase difference between two output ports.

3.5.1.4 Analysis of the Filtering Rat-Race Coupler

Based on the above-mentioned analysis, a filtering rat-race coupler is designed by combining the in-phase and out-of-phase power dividers, as shown in Figure 3.39. The whole structure is a single-cavity configuration, featuring compact size.

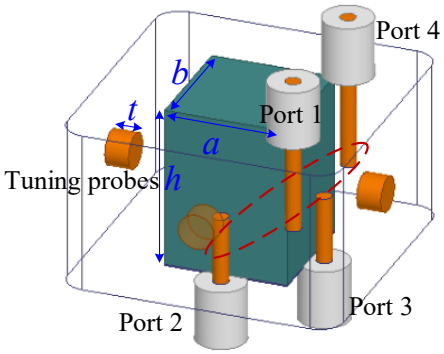

Figure 3.39. 3-D structure of the filtering rat-race coupler using rectangular DR.

As for a rat-race coupler, the isolation between port 1 and port 4 (S_{41}) is a significant design target. From the schematic of the proposed filtering rat-race

coupler in Figure 3.29(a), it is known that the isolation can be obtained, as analyzed below. The signals injected from port 1 are equally coupled to ports 2 and 3, and then transmitted to port 4 with the 180° phase shift. Thus, the signals from port 1 to port 4 through two transmission paths (paths 1 and 2 in Figure 3.29(a)) can be canceled out, resulting in isolation performance. Meanwhile, when the in-phase and out-of-phase power dividers are combined, port matching of ports 2 and 3 can be realized. For demonstration, the simulated S_{22}, S_{33}, and S_{41} are shown in Figure 3.40. As can be seen, good isolation can be realized and the return losses of ports 2 and 3 are better than 18 dB. Thus, a filtering rat-race coupler can be designed.

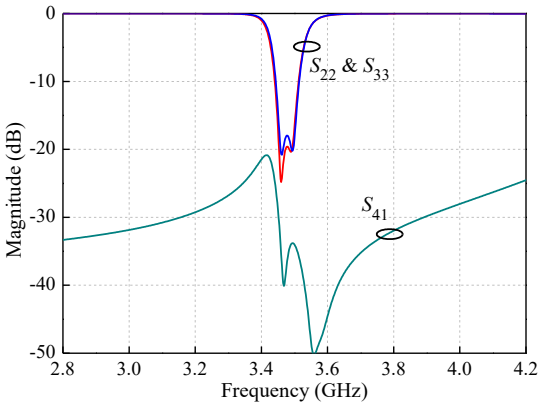

Figure 3.40. Simulated S_{22}, S_{33}, and S_{41} of the rat-race coupler.

It is noted that manufacturing tolerance exists in the implementation, which may affect the responses. To evaluate this issue, the sensitivity of some key parameters is studied. From the resonant frequency analysis of rectangular DR in Figure 3.26, we know that it is crucial to control the ratio of the height (h) and length (a) (or width (b)) of the rectangular DR to realize a quad-mode resonator. Figure 3.41(a) shows the simulated S_{11} and S_{21} of the filtering rat-race coupler with different values of h. As can be seen, if h is fabricated with a tolerance of ± 0.1mm, the bandwidth and return loss (S_{11}) only have slight differences. Moreover, the four tuning probes with the length of t can be utilized for fine-tuning, as shown in Figure 3.41(b). Thus, the responses are not sensitive to the fabrication tolerance and it would be easy to obtain the desired responses.

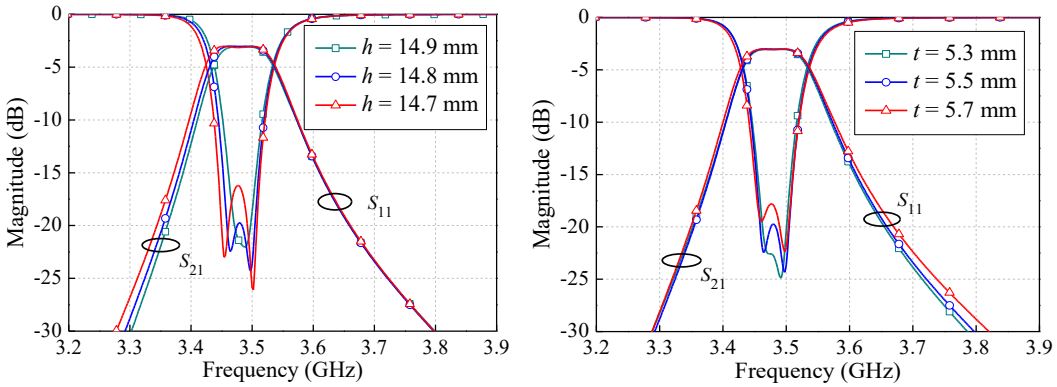

Figure 3.41. Simulated S_{11} and S_{21} (a) versus h; (b) versus t.

3.5.1.5 Experiment

Based on the design method discussed earlier, the proposed filtering rat-race coupler is implemented with the 3-D structure shown in Figure 3.39. The dielectric material is from the Jiangsu Jiangjia Electronics Co. Ltd in Jiangsu, China, with the operating temperature range from -40 to 85 ºC. Within this temperature range, the temperature coefficient of frequency of the DR is smaller than 10 ppm/ºC. It should be noted that the fabrication process is the same as that of traditional DR circuits. Thus, the thermal behaviors of the fabricated DR-based filtering rat-race couplers are similar to that of other reported DR works. The photograph of the fabricated coupler is shown in Figure 3.42. The overall circuit size is 33 × 33 × 22.5 mm^3 (or 0.38 × 0.38 × 0.26 λ_g^3).

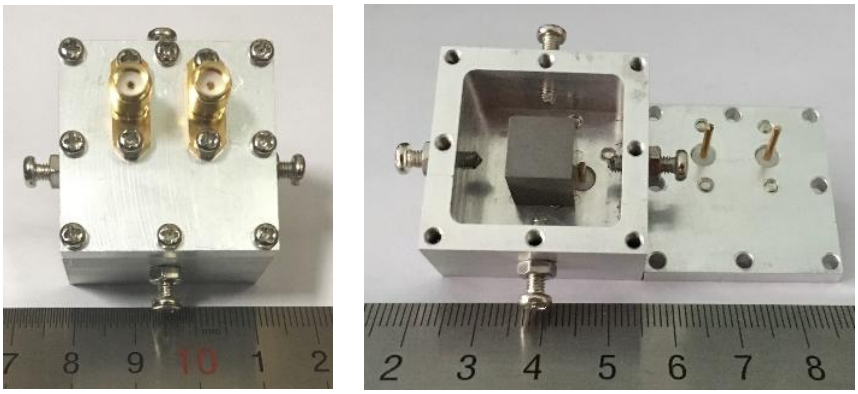

Figure 3.42. Photograph of the fabricated rectangular-DR-based filtering rat-racce coupler.

The simulation is carried out by using HFSS and measurement is accomplished by using Keysight Agilent E5071C network analyzer under the indoor temperature of around 25 ºC. Figure 3.43 shows the simulated and measured results under the in-phase operation. Good agreement can be observed. The measured passband is centered at 3.49 GHz with the 3-dB FBW of 1.7 %. The Q factor is measured as around 1200. It should be noted that there are several sources of loss that may decrease the measured Q factor, such as the losses in aluminum walls and losses of SMA connectors. Two transmission zeros are generated at both sides of the passband, which enhance the skirt selectively. The return loss is better than 15 dB. The insertion losses at the center frequency including the 3-dB equal power division loss are (3 + 0.62) and (3 + 0.7) dB, with the amplitude imbalance of less than 0.1 dB. The phase difference between the two output ports is less than 2.5º, showing good filtering in-phase power division responses.

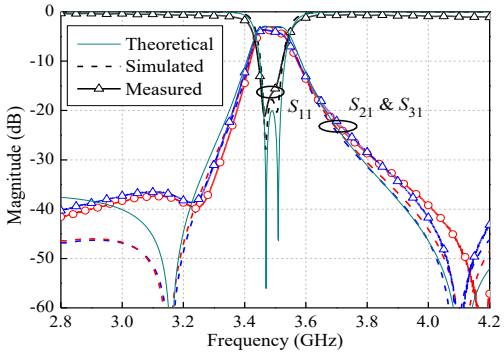

(a)

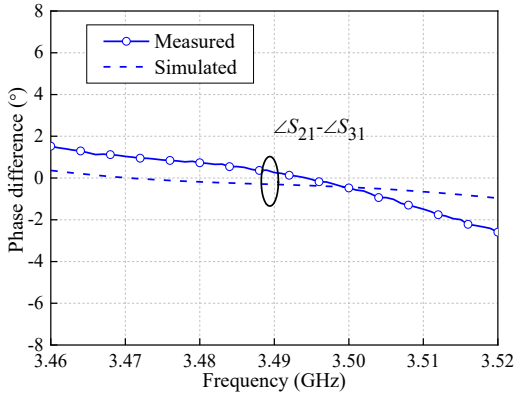

(b)

Figure 3.43. Simulated and measured results under the in-phase operation. (a) S_{11}, S_{21} & S_{31}; (b) Phase difference between the two output ports.

Figure 3.44 shows the simulated and measured results under the out-of-phase operation. The measured magnitude of S_{24} and S_{34} are - (3 + 0.65) dB and - (3 + 0.71) dB at the center frequency, respectively, with the difference of less than 0.1 dB. The in-band return loss is better than 15 dB. The phase difference between ports 2 and 3 is around 180° with a variation of less than 2.5°. Good performance of bandpass filtering responses, equal power division, and 180° phase difference is realized.

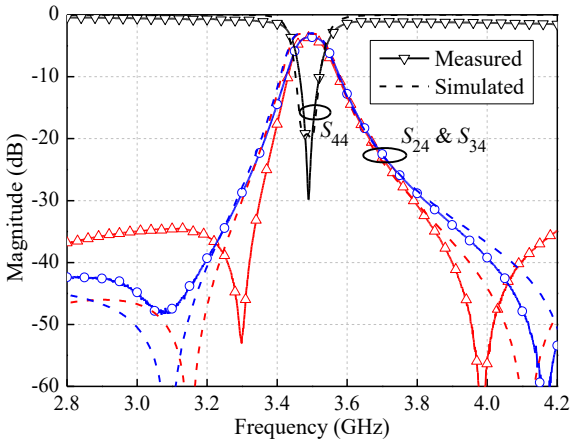

(a)

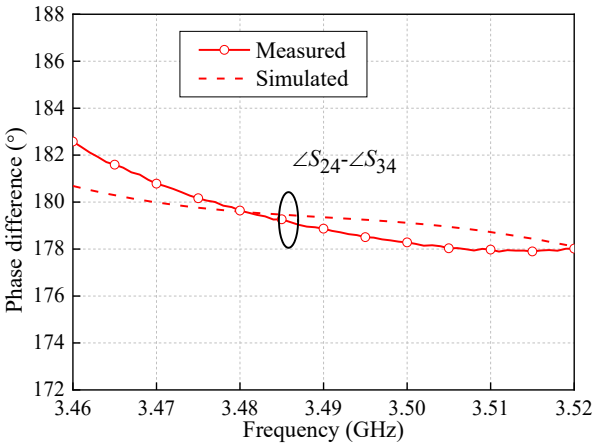

(b)

Figure 3.44. Simulated and measured results under the out-of-phase operation. (a) S_{44}, S_{24} & S_{34}; (b) Phase difference between the two output ports.

Figure 3.45 shows the simulated and measured S_{41}, S_{22} and S_{33}. As seen, the isolation between ports 1 and 4 within the passband is better than 22 dB and the

return losses of two output ports are better than 18 dB, showing high isolation and good output port matching. Moreover, due to the use of high-power DR material and metal cavity, the proposed filtering rat-race coupler with a heat sink can be applied to high-power applications.

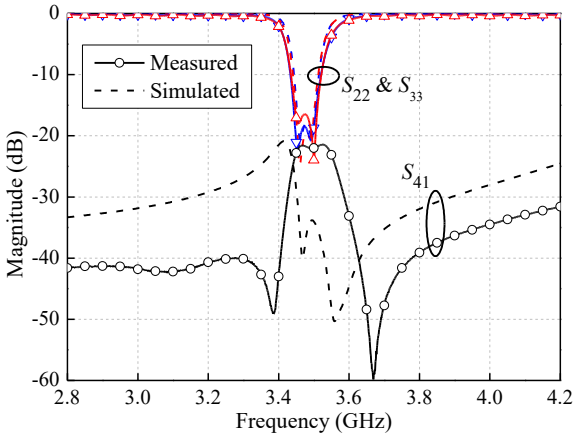

Figure 3.45. Simulated and measured S_{22}, S_{33} & S_{41}.

3.5.2 Filtering Rat-Race Coupler Based on Quad-Mode Cylindrical DR

As presented earlier, a method that using the quad-mode DR to design a compact filtering rat-race coupler with a single-cavity configuration is proposed. The quad-mode rectangular DR is constructed with two short ends and then applied to realize the filtering rat-race coupler. For further verifying the proposed concept, the other quad-mode cylindrical DR is employed to demonstrate this method, which features a higher Q factor comparing to the constructed rectangular DR.

3.5.2.1 Design of the Filtering Rat-Race Coupler

Figure 3.46 shows the 3-D structure of the filtering rat-race coupler. It consists of a cylindrical DR, four feeding probes and the tuning probes. Some of the lower order modes of the DR are the TEH, HEH_{11} pair, HEE_{11} pair, and TME modes. When the ratio of diameter and height of the DR are properly selected, the resonant

modes of HEH_{11} and HEE_{11} pairs are at the same frequency. Thus, this DR can be used as a quad-mode resonator [86]. The tuning probes are placed under and above the DR to separate the TME mode from HEH_{11} and HEE_{11} pairs.

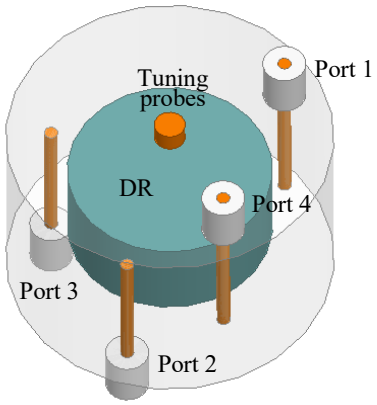

Figure. 46. 3-D structure of the filtering rat-race coupler using cylindrical DR.

When the quad-mode DR is excited, the E-field distributions of the DR and feeding probes at these two resonant pairs are illustrated in Figure 3.47. Here, to show each resonant mode clearly, we use HEH'_{11} and HEH''_{11} to represent the HEH_{11} pair, while the HEE_{11} pair is expressed as HEE'_{11} and HEE''_{11}. Similar to the analysis in Section III, the coupling between DR and feeding probes can be analyzed. For example, when the DR is resonated at HEH'_{11}, ports 1, 2 and 3 can be coupled to the DR while port 4 cannot, as shown in Figure 3.47(a). After analyzing the coupling between DR and feeding probes, it is found that the schematic of this structure the same as that of the rectangular DR-based coupler in Figure 3.29(a). Thus, rat-race coupler performance can be obtained by this structure.

For circuit realization, a 3-D configuration of the filtering rat-race coupler can be constructed following the method in Section 3.4.1. Firstly, the coupling matrix of a second-order BPF is synthesized. Secondly, M_{iL} ($i = S, 1, 2$) is reduced by a factor of $\sqrt{2}$ to fulfill the input impedance requirement of the in-phase power divider and thus the coupling matrix of in-phase operation can be obtained. Thirdly, the desired values of external qualify factor (Q_{ei}) and resonant frequencies (f_i) are calculated by (3.24)-(3.25) and the in-phase power divider can be constructed according to these

values. Fourthly, the out-of-phase power divider is also designed based on the above Q_{ei} and f_i, where the location of port 4 is different from that of port 1 in the in-phase power divider. Finally, the in-phase and out-of-phase power dividers are combined to realize the whole circuit and fine-tuning is performed to obtain excellent filter and rat-race coupler responses.

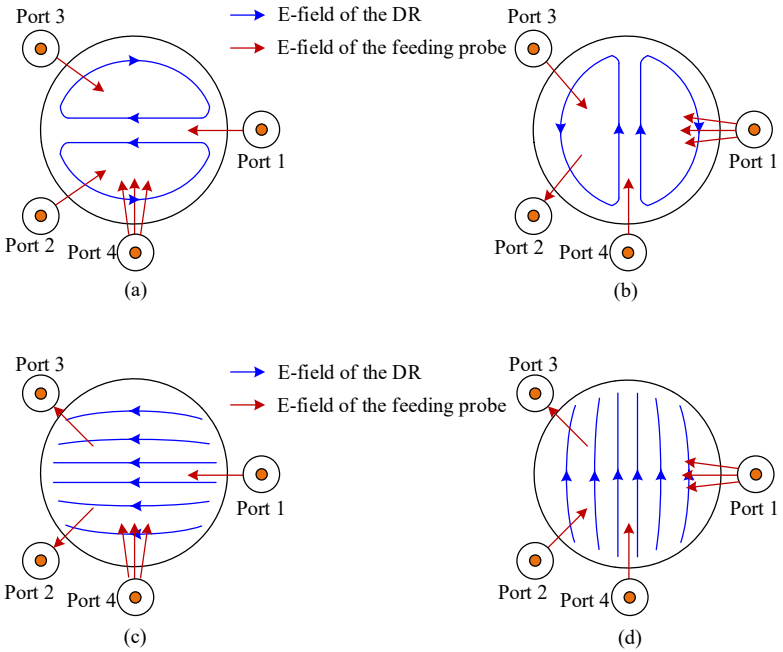

Figure 3.47. E-field distribution of the feeding probes and DR at (a) HEH'$_{11}$; (b) HEH"$_{11}$; (c) HEE'$_{11}$; (d) HEE"$_{11}$.

3.5.2.2 Experiment

The proposed filtering rat-race coupler based on cylindrical DR is also implemented. The photograph of the fabricated coupler is shown in Figure 3.48. The circuit size is 36 × 36 × 28 mm^3 (or 0.42 × 0.42 × 0.32 λ_g^3). Figure 3.49 shows the simulated and measured results under the in-phase operation. The measured passband is centered at 3.51 GHz with the 3-dB FBW of 1.3%. The minimum insertion losses at the two output ports are (3 + 0.36) and (3 + 0.43) dB, with the amplitude imbalance of less than 0.1 dB. The Q factor is measured as around 2500. As compared to the filtering rat-race coupler using rectangular DR presented in Section IV, this present design features a higher Q factor. Three transmission zeros

are generated at 3.21, 3.46 and 3.63 GHz by multiple transmission paths from source (port 1) to the load (port 2 or port 3), including the paths of TME mode, HEH'$_{11}$ mode, HEE'$_{11}$ mode, and source-load coupling, as shown in Figure 3.50. The return loss is better than 17 dB. The phase difference between the two output ports is less than 2°, showing good filtering in-phase power division performance.

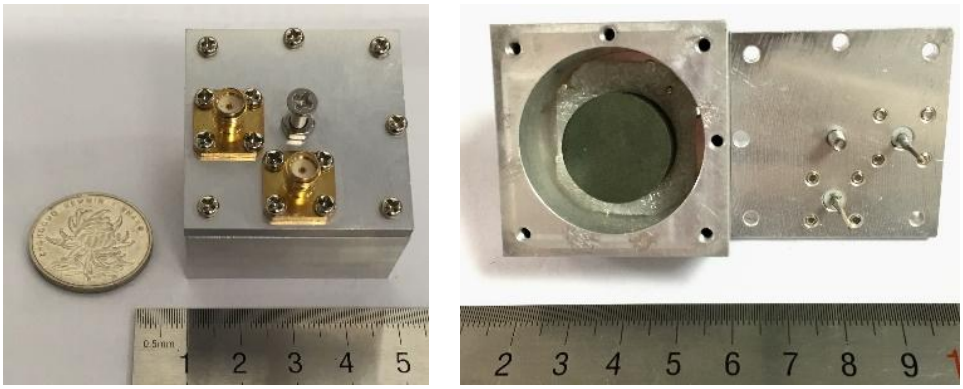

Figure 3.48. Photograph of the filtering rat-race coupler based on cylindrical DR.

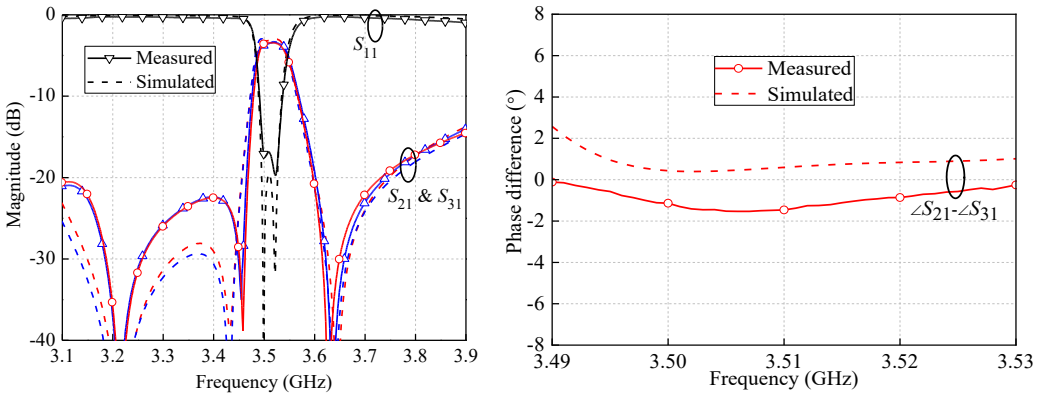

(a) (b)

Figure 3.49. Simulated and measured results under the in-phase operation. (a) S_{11}, S_{21} & S_{31}; (b) Phase difference between the two output ports.

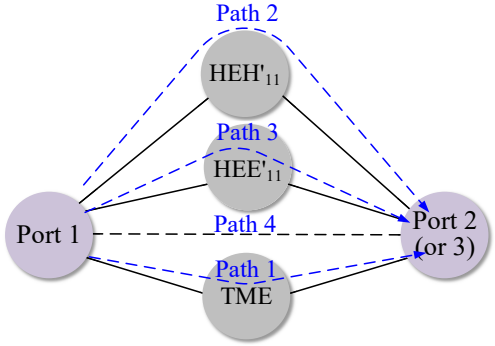

Figure 3.50. Topology from port 1 to port 2 (or port 3).

Figure 3.51 shows the simulated and measured results under the out-of-phase operation. The measured magnitude of S_{24} and S_{34} are - (3 + 0.41) dB and - (3 + 0.37) dB, respectively, with the difference of less than 0.1 dB. The return loss is better than 16 dB. The phase difference between ports 2 and 3 is around 180°. Good performance of bandpass filtering responses, equal power division, and 180° phase difference is realized.

Figure 3.52 shows the simulated and measured S_{41}, S_{22} and S_{33}. As seen, the S_{41} within the passband is smaller than -23 dB and the return losses of two output ports are better than 15 dB, showing high isolation and good output port matching.

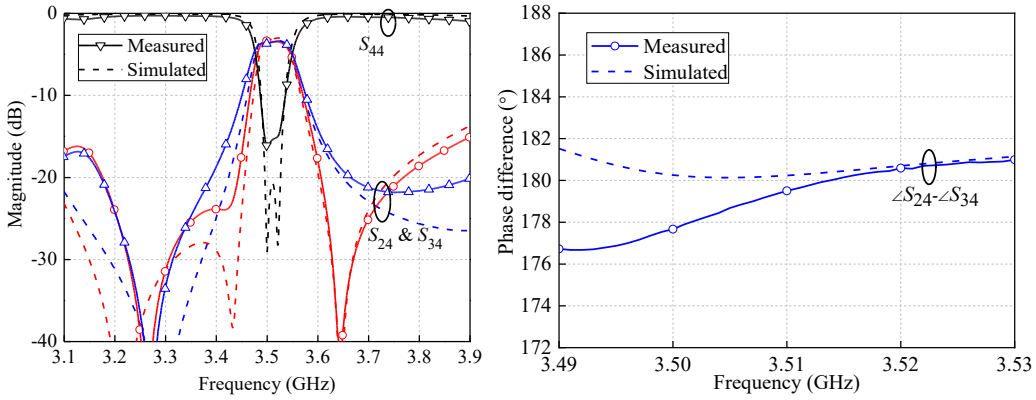

(a) (b)

Figure 3.51. Simulated and measured results under the out-of-phase operation. (a) S_{44}, S_{24} & S_{34}; (b) Phase difference between the two output ports.

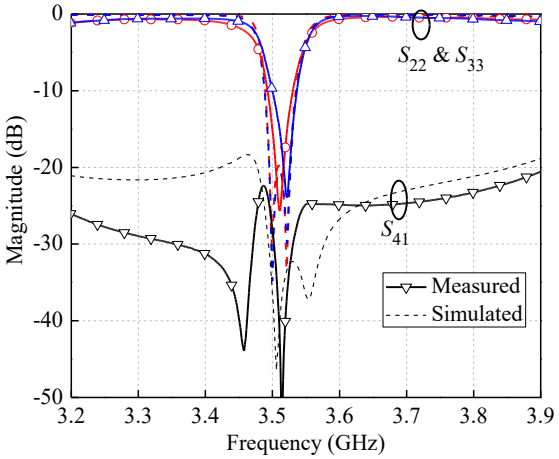

Figure 3.52. Simulated and measured S_{22}, S_{33} & S_{41}.

3.5.3 Comparison

Table 3.3 tabulates the comparison with some other filtering couplers. In [54], the microstrip and LC lumped components realize ± K inverters with filtering functions, which is used to replace the 1/4 or 3/4 λ_g transmission lines in classical rat-race coupler. Very compact size is achieved whereas it is not suitable for high-frequency operations due to the self-resonance of LC lumped components. In [57], [126], [128], [129], good bandpass responses are integrated in the couplers by using coupled resonators in PCB or LTCC techniques. Nevertheless, due to the Q factor limitation, these couplers [54] [57], [126], [128], [129] cannot be designed with narrow bandwidth (FBW less than 2 %). Otherwise, the insertion loss would be very high. Compared to the filtering coupler using high Q factor DRs in [59], only one resonator is employed in the proposed designs while four DRs are needed in [59]. Hence, size and weight can be reduced by using the proposed method. In [60], the filtering coupler is constructed using one DR with the first-order bandpass responses, where the selectively is poor and the bandwidth is difficult to be controlled. For the proposed filtering couplers using high-Q-factor DR, they have low insertion loss under the narrow-bandwidth specification as well as high power handling capability, which is attractive in base station applications.

Table 3.3 Comparison With Some Other Filtering Couplers

Ref.	f_0 (GHz)	FBW (%)	IL (dB)	Resonators	Mag. (dB)/phase (°) imbalance	Techniques
[54]	0.47	13	1.14	8	0.1 / 4.5	PCB+LC
[126]	2.4	10	0.7	4	1 / 2	PCB
[128]	24.1	8.6	2.2	N.A.	0.2 / 6	LTCC
[57]	3.5	14	1.5	4	0.25 / 5	LTCC
[129]	1.284	4.7	1.88	8	0.15 / 2	PCB
[59]	12.5	N.A.	N.A.	4	~2 / 10	DR
[60]	1.94	0.5	N.A.	1	N.A. / 5	DR
This work	3.49	1.7	0.62	1	0.1 / 2.5	DR
	3.51	1.3	0.36	1	0.1 / 3.5	DR

3.6 Conclusions

In wireless systems, filters are generally cascaded with other passive circuits, which have the problems of large circuit size and high insertion loss. To solve these problems, co-designs of filters and other passive circuits have been carried out in this chapter. Firstly, a miniaturized filtering balun is proposed based on LTCC technology. The filtering responses have been integrated into a balun circuit by only adding three feeding lines to a conventional Marchand balun, resulting in a simple structure. Secondly, an LTCC diplexer has been presented. By using a common dual-mode resonator, only three resonators are needed to form the two second-order filtering channels for the diplexer. Moreover, a transmission zero can be generated by one of the filter channels at the passband frequency of the other filter channel, resulting in high isolation. Due to the design freedom of the multilayer LTCC structure, the center frequencies and bandwidths of the two channels can be controlled separately. Thirdly, a method for designing DR-based filtering rat-race couplers has been proposed. By constructing the quad-mode DRs, the second-order filtering rat-race can be designed with a single-cavity configuration. Comparing with other reported designs, the proposed rat-race filtering couplers have shown good performance in terms of filtering responses, amplitude balance as well as 0º and 180º phase differences.

Chapter 4 Dual-/Multi-Channel Filtering Circuits

4.1 Introduction

In Chapters 2 and 3, filters are co-designed with other active and passive circuits, which can reduce the size/loss or improve efficiency. In some wireless systems, several circuits with the same performance may also be desired. For example, in a massive multiple-input multiple-output (MIMO) antenna system, there are lots of filters, power amplifiers and switches [132], as shown in Figure 4.1(a). In base station applications, bandpass filters should have a high Q factor and high power handling capability. By using the conventional metallic cavity or DR structures to construct the massive wireless system, the circuit size would be very large and the weight is heavy. Although there are some miniaturized cavity and DR filters reported in recent years, the size reduction is not obvious due to their 3-D structure. Especially, in massive wireless systems, a large number of filters or filtering circuits would be an obstacle to realize high integration of wireless systems.

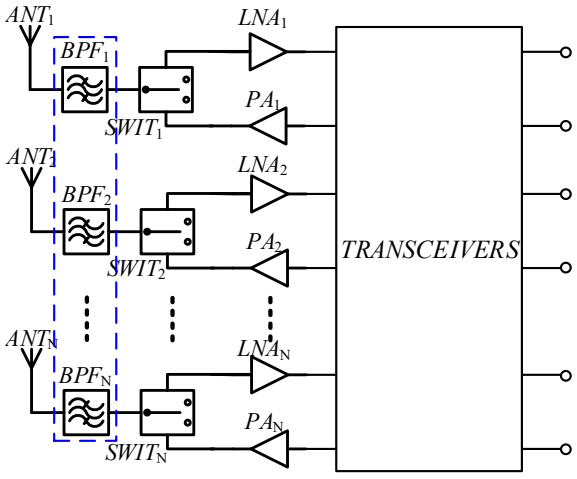

Figure 4.1. Schematic of a massive MIMO system [132].

4.2 Proposed Methods for Dual-/Multi-Channel Filter and Filtering Circuits

To solve the above problems, the methods for integrating multiple filters or filtering circuits with the same performance as one dual- or multi-channel filtering circuits are proposed in this thesis, which can further reduce the size and improve the integration of the whole system.

Figure 4.2 shows the schematic of the dual-channel filter design method, where two filters are integrated as one circuit. By sharing the same resonator and metallic cavity, the size of the proposed dual-channel filter can be greatly reduced as compared to the two individual filters. The mode control mechanism of the dielectric resonator is analyzed, and the grouping excitation method of a multi-mode dielectric resonator is proposed. The feeding structures of one filter channel can only excite the resonant modes for this channel, while those of the other filter can only excite other resonant modes for the other channel. In this case, the coupling coefficient between the two filter channels is zero, and thus high isolation between them can be realized even though they share the same multi-mode resonator and cavity. When using the proposed dual-channel filter to replace the two conventional single-channel filters, the number of the filter in the system can be reduced by half, eg, from 128 to 64. The circuit size can be reduced the integration is improved. Moreover, the proposed dual-channel filter is also co-designed with a two-input two-output Doherty power amplifier, achieving high integration and high efficiency.

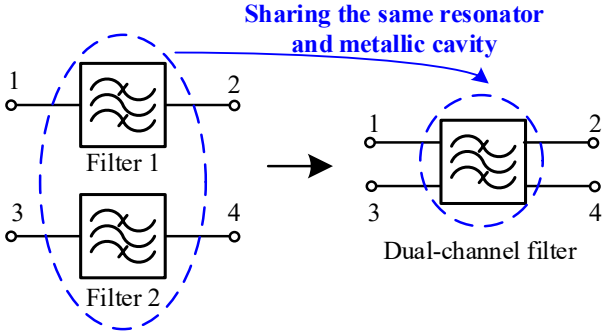

Figure 4.2. Schematic of the proposed dual-channel filter.

For higher integration, more filters can be integrated as one multi-channel filter by sharing the resonators and cavities, as shown in Figure 4.3. The resonant properties of a tri-mode DR are analyzed firstly, and then the grouping coupling method of the tri-mode DRs are proposed. By using the proposed method, any resonant mode of a tri-mode DR can only be coupled with another resonator in a single direction, so that a large number of filters can be integrated as a multi-channel filter without affecting to each other. Thus, the multi-channel filters can be realized, such as the 12-channel filter, 27-channel filter and so on.

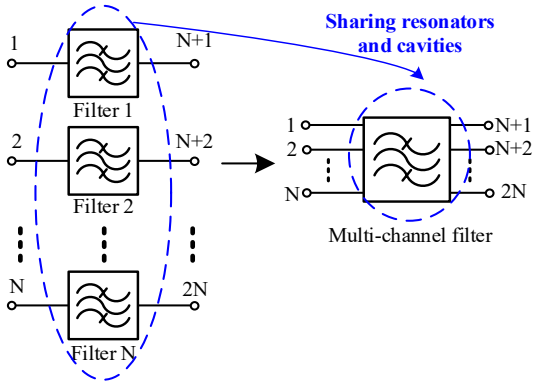

Figure 4.3. Schematic of the proposed multi-channel filter.

Moreover, by using the proposed design methods of the active and passive multi-functional filtering circuits presented in Chapters 2 and 3, the functions of balanced and balun circuits can be fused into the dual-channel filter to realize the dual-channel balanced and balun filters, respectively. The schematics of dual-channel balanced and balun filters are shown in Figures 4.4(a) and (b), respectively. They can be utilized as two balanced or balun filters in wireless systems for high integration.

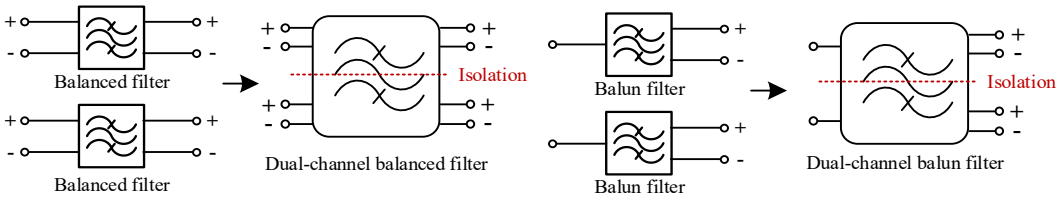

Figure 4.4. (a) Dual-channel balanced filter; (b) Dual-channel balun filter.

4.3 Dual-Channel Filter and Its Co-design with a Two-Input Two-Output Doherty Power Amplifier

Bandpass filters are essential in RF front ends of wireless communication systems. To reduce the size and cost of wireless systems, a lot of research has been conducted to realize the miniaturized BPFs. The most common method to construct the compact BPFs is to use the miniaturized resonators fabricated in the printed circuit board (PCB), such as the multi-mode resonators [120], composite right-/left-handed resonators [121], or folded quarter-wavelength resonator [133]. Due to the advantages of multilayer structures, the low-temperature co-fired ceramic (LTCC) techniques have been widely used. In [134], the BPFs are folded vertically and horizontally in LTCC for compact size. However, the above filters suffer from the low *Q*-factor or low power handling capability.

Due to the high *Q* factor and high power handling capability, the dielectric resonator (DR) and cavity filters are popularly employed in base stations, where low insertion loss is required despite narrow bandwidth specifications [135]. In [136], six coaxial resonators in an inline configuration are used to realize a sixth-order BPF with good filtering responses. The $TE_{01\delta}$-mode DR filters are presented in [137] with controllable transmission zeros. Besides, the cylindrical and rectangular DRs can be utilized to develop balanced/balun BPFs [51]-[53]. In these designs, the single-mode resonators are employed, where the desired filter topology can be realized conveniently. However, the single-mode cavity/DR BPFs usually occupy a large size. To overcome this problem, multi-mode resonators (MMRs) are used, where the number of resonant cavities can be diminished. For example, in [138], the quad-mode BPF is designed using a modified coaxial cavity resonator with compact size and improved *Q*-factor.

Apart from the BPFs, lots of power amplifiers (PAs) are also needed in the 5G massive MIMO system, which are cascaded with the BPFs, as shown in Figure 4.1.

To improve the efficiency and further reduce the size, co-designs of PA and BPF have been developed, which have been discussed in Section 2.5.

In this thesis, different from the previous designs for size reduction, a dual-channel DR filter is presented. The two BPFs are integrated as one dual-channel filter with two input ports and two output ports, with the schematic shown in Figure 4.2. It is realized by sharing a quad-mode DR and a metallic cavity, in which the space between the two separate filters is eliminated. Thus, the circuit size is greatly reduced. Resonant frequencies of the DR are investigated and electromagnetic field properties at HEH_{11} and HEE_{11} resonant pairs are studied. Two of the resonant modes are excited for one filter and other two for the other filter. Although two filters are placed together, high isolation between two filters is obtained because the resonant modes in two filters are orthogonal. By introducing the cross coupling, three transmission zeros are generated at two sides of the passband. Simulated and measured results are presented. The dual-channel filter with the impedance transformation function is also integrated with a two-input two-output Doherty power amplifier for 5G massive MIMO system application.

4.3.1 Dual-Channel Filter Design

Figure 4.5 shows the 3-D structure of the proposed dual-channel DR filter. A cylindrical DR is placed at the center of a cuboid metallic cavity. Four ports placed at four corners of the cavity are coupled to the DR for inputs and outputs. Among them, ports 1 and 2 are used for filter 1, while ports 3 and 4 for filter 2. To obtain good filtering responses, the dual-channel filter is analyzed below. Firstly, the resonant frequencies of the DR at different modes are investigated. Two mode pairs of HEH_{11} and HEE_{11} are selected to form the dual-channel filter, whose E-field distributions are studied. Then, excitation of the two mode pairs is presented for guiding the dual-channel filter realization and the filter topology is analyzed to obtain good bandpass responses.

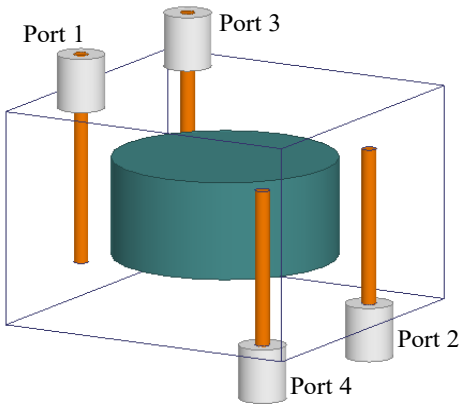

Figure 4.5. 3-D structure of the dual-channel DR filter.

4.3.1.1 Analysis of the Quad-Mode Cylindrical DR

In the proposed dual-channel DR filter, the cylindrical DR is employed with the 3-D view shown in Figure 4.6(a). D and H are the diameter and height of the DR, respectively, while a, b, and c are the length, width, and height of the cubic cavity. When the ratio of D and H (D/H) is selected within a proper range, some of the lower order modes of the DR are the TEH, HEH_{11}, HEE_{11}, and TME modes. To investigate the resonant frequencies of the DR, some initial dimensions are chosen as follows (all in mm): $a = b = 28$, $c = 20$, $D = 20$, $H = 8$. The substrate of the DR has a dielectric constant of 38. Figure 4.6(b) shows the resonant frequencies of the modes versus H (D is unaltered). When H is around 9 mm, the HEH_{11} and HEE_{11} pairs almost resonate at the same frequency. Thus, this DR can be used as a quad-mode resonator.

To study the resonant property, E-field distributions of the DR at HEH_{11} and HEE_{11} orthogonal pairs are shown in Figure 4.7. As can be seen, the E-field of HEH_{11} pair is mainly concentrated in the middle of the resonator, while that of the HEE_{11} pair is mainly concentrated at the top and bottom of the resonator. Thus, the E-fields of these four modes do not coincide with each other. Meanwhile, considering the resonant frequency study in Figure 4.6(b), it is known that the four modes can be theoretically controlled independently, which are utilized to construct the dual-channel filter as addressed below.

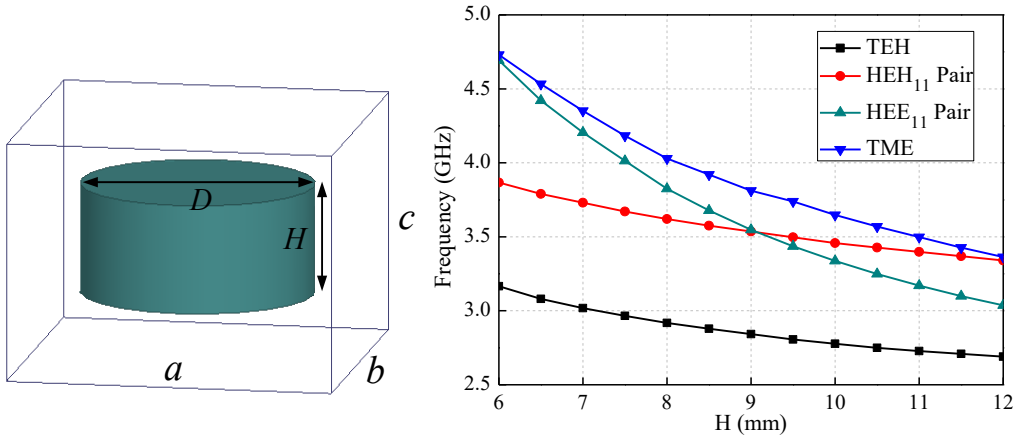

(a) (b)

Figure 4.6. (a) 3-D structure of the cylindrical DR; (b) Resonant frequencies of the modes versus *H*.

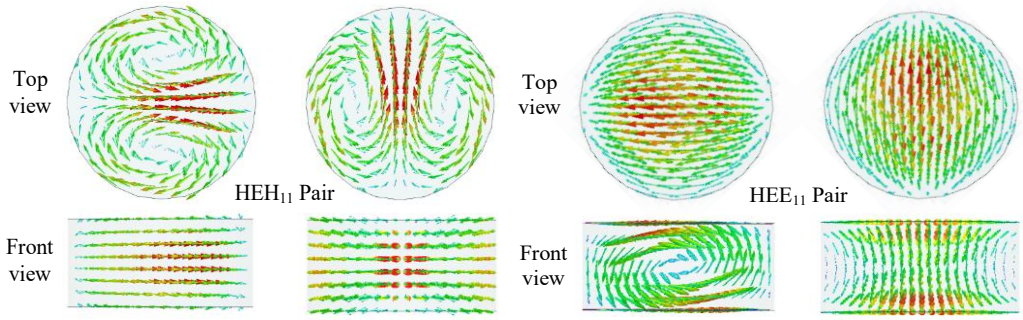

(a) (b)

Figure 4.7. E-field distribution of the DR (a) HEH_{11} pair; (b) HEE_{11} pair.

4.3.1.2 Analysis of Dual-Channel DR Filter

The quad-mode cylindrical DR is used to design the dual-channel filter, as shown in Figure 4.5. Two filters share the common metallic cavity and DR for size reduction, where there is no division plate that used in the conventional two separate filters for blocking the signals between two filters. Hence, one of the significant design targets of the dual-channel filter is the isolation between two filters. To obtain good isolation, the novel design method that used to excite the two mode pairs of HEH_{11} and HEE_{11} is proposed. By properly arranging the input and output feeding probes, two of the modes are excited to form a BPF, while other two are excited for the other BPF. The analysis is detailed as follows.

To study the dual-channel filter, the circuit performance of one channel filter is

firstly analyzed. Figures 4.8(a) and (b) show the 3-D configuration and top view of one channel filter, respectively. Two feeding probes are placed at two corners of the cavity and at 180° from each other, extending from the top and bottom walls of the cavity. When signals are injected into this filter, the E-field distributions of the two feeding probes and DR at HEH_{11} and HEE_{11} pairs are illustrated in Figure 4.9. Here, to show each mode clearly, we use HEH_{11}^{1} and HEH_{11}^{2} to represent the HEH_{11} pair. The HEE_{11}^{1} and HEE_{11}^{2} are the HEE_{11} pair. As can be observed, the E-fields of the two feeding probes are paralleled to that of the HEH_{11}^{1} and HEE_{11}^{1} in Figures 4.9(a) and (c). Thus, the signals can be coupled from the feeding probe to the DR, or vice versa. However, in Figures 4.9(b) and (d), the E-fields of the feeding probes are perpendicular to that of the HEH_{11}^{2} and HEE_{11}^{2}. Therefore, the coupling coefficient between the probes and the DR at HEH_{11}^{2} and HEE_{11}^{2} mode is zero.

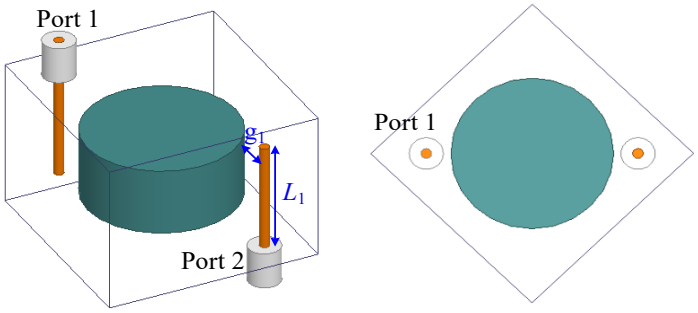

(a) (b)

Figure 4.8. Structure of one channel filter (a) 3-D configuration; (b) top view.

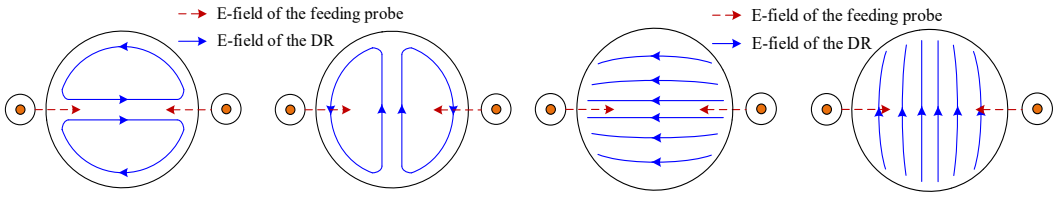

(a) (b)

Figure 4.9. E-field distribution of the two feeding probes and DR (a) HEH_{11}^{1} mode; (b) HEH_{11}^{2} mode; (c) HEE_{11}^{1} mode; (d) HEE_{11}^{2} mode.

Based on the above analysis, it can be concluded that by arranging the feeding probes as shown in Figure 4.8(a), only two modes of the HEH_{11} and HEE_{11} pairs

are excited while the other two modes are not. For verification, simulated S_{21} of the filter in Figure 4.8(a) under weak coupling condition is shown in Figure 4.10. As can be seen, only two modes are excited, showing good agreement with the analysis.

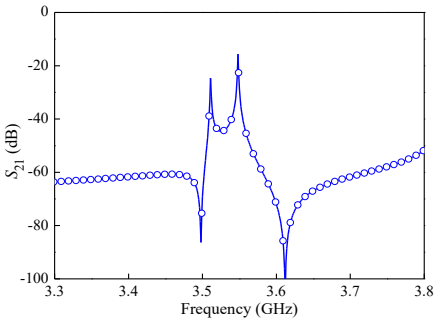

Figure 4.10. Simulated S_{21} of the single-channel filter under weak coupling.

To obtain good filtering responses, the coupling coefficient and external quality factor need to be properly addressed. The topology of the filter in Figure 4.8(a) can be illustrated in Figure 4.11. The corresponding coupling matrix, including the non-resonance nodes of the source (S) and load (L), can be expressed as

$$M_{N+2} = \begin{array}{c} \\ S \\ 1 \\ 2 \\ L \end{array} \begin{array}{c} \begin{array}{cccc} S & 1 & 2 & L \end{array} \\ \begin{bmatrix} 0 & M_{S1} & M_{S2} & M_{SL} \\ M_{1S} & M_{11} & 0 & M_{1L} \\ M_{2S} & 0 & M_{22} & M_{2L} \\ M_{LS} & M_{L1} & M_{L2} & 0 \end{bmatrix} \end{array}. \tag{4.1}$$

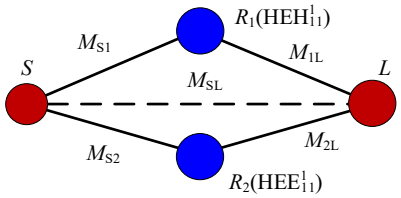

Figure 4.11. The topology of the single-channel filter.

In this design, the desired BPF is centered at 3.525 GHz with 0.5% fractional bandwidth (FBW) of 20-dB equi-ripple return loss. Two transmission zeros are appointed at the frequencies of 3.43 and 3.59 GHz. Since the topology in Figure 4.11 is a doublet structure with extra source-load coupling, two transmission zeros can be generated. Among the four parameters M_{S1}, M_{1L}, M_{S2} and M_{2L}, one should

have a different sign from the other three. Otherwise, a transmission zero would appear within the passband. According to the front view of E-field distributions of the feeding probes and DR at HEH_{11}^{1} and HEE_{11}^{1} modes in Figure 4.12, it is known that M_{S1} and M_{1L} have different signs while M_{S2} and M_{2L} have the same sign, which can fulfill the requirement. Based on the advanced coupling matrix synthesis method in [79], the initial coupling matrix can be synthesized as

$$M_{N+2} = \begin{array}{c} \\ S \\ 1 \\ 2 \\ L \end{array} \begin{array}{c} \begin{array}{cccc} S & 1 & 2 & L \end{array} \\ \begin{bmatrix} 0 & 0.8850 & 0.8182 & 0.0314 \\ 0.8850 & 1.6522 & 0 & -0.8871 \\ 0.8182 & 0 & -1.6678 & 0.8202 \\ 0.0314 & -0.8871 & 0.8202 & 0 \end{bmatrix} \end{array}. \tag{4.2}$$

The desired coupling coefficient $k_{i,j}$ and external quality factor Q_{ei} at the center frequency (f_0) are calculated by using equations (2.9) and (2.10). The resonant frequency of the resonator corresponding to the non-zero M_{ii} can be obtained by using equation (3.25).

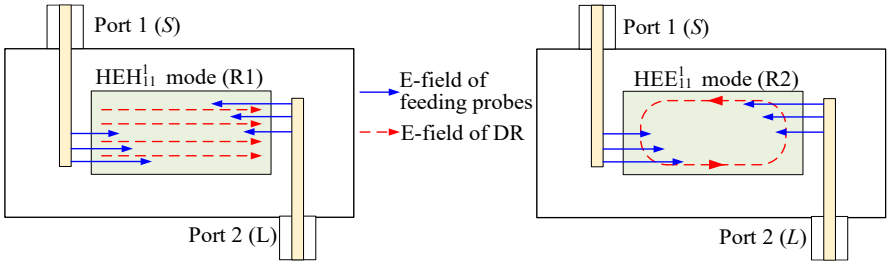

Figure 4.12. E-field distributions of the filter at (a) HEH_{11}^{1} mode; (b) HEE_{11}^{1} mode.

In circuit realization, Q_{e1} and Q_{e2} are important parameters which evaluate the coupling strength between input/output feeding probes and DR at HEH_{11}^{1} and HEE_{11}^{1} modes. Figures 4.13(a) and (b) illustrate the extracted Q_{e1} and Q_{e2} against the length of feeding probe (L_1) as well as the gap between DR and feeding probe (g_1) shown in Figure 4.8(a) (initial values L_1 = 14.5 mm, g_1 = 3 mm). From these two figures, we know that it has enough design freedom to obtain the desired Q_{e1} and Q_{e2} by tuning the values of L_1 and g_1.

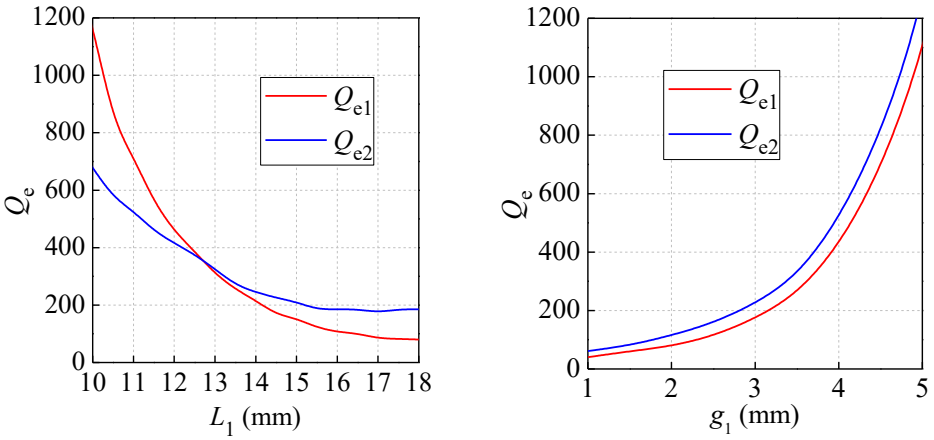

(a) (b)

Figure 4.13. Simulated Q_{e1} and Q_{e2} (a) against L_1; (b) against g_1.

According to the above analysis, the filter shown in Figure 4.8(a) is constructed to obtain the desired filtering responses. Firstly, based on the investigation of the resonant mode in Figure 4.6(b), the resonant frequencies of HEH_{11} and HEE_{11} pairs are controlled by the dimensions of D and H to meet the values of f_i. Then, Q_{ei} is realized by adjusting the values of L_1 and g_1 based on Figures 4.13(a) and (b). The source-load coupling M_{SL} is achieved by the weak coupling between the input and output feeding probes. Since there is no coupling between the HEH_{11} and HEE_{11} modes, the k value is equal to zero. Consequently, the bandpass responses of the filter in Figure 4.8(a) can be obtained. Figure 4.14 shows the simulated results which present good bandpass responses. However, it can be observed that the spurious mode occurs at around 3.83 GHz which is near the passband.

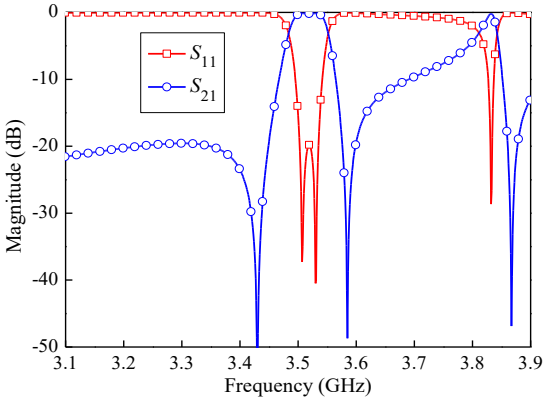

Figure 4.14. Simulated results of the single-channel DR filter.

From Figure 4.6(b), it is known that the spurious mode is formed by the TME mode. Figure 4.15(a) shows the E-field distribution of the TME mode. Comparing to the E-field distributions of the DR at HEH_{11} and HEE_{11} modes in Figure 4.7, it is found that at the center part of the DR, the E-fields at HEH_{11} and HEE_{11} modes are paralleled to the top or bottom surface while that at TME mode is perpendicular. According to this property, two metal screws are placed extending from the top and bottom walls of the cavity, as shown in Figure 4.15(b). Based on the E-field distribution of the DR at TME mode, it is known that there exists the capacitor effect between metal screws and the DR, which decreases the TME mode frequency. However, the E-fields of the DR at HEH_{11} and HEE_{11} modes are perpendicular to metal screws, and thus the coupling between the DR and metal screws is weak. Hence, the impact on the HEH_{11} and HEE_{11} modes are slight. Accordingly, it is possible to separate the TME mode from the HEH_{11} and HEE_{11} modes (passband frequency) by the metal screws. For demonstration, the simulated S_{21} versus the length of the screws (L) are shown in Figure 4.16. As observed, the TME mode can be shifted down to a much lower frequency than the passband when a larger L is chosen. Meanwhile, a transmission (TZ_3) is realized at the upper frequency of the TME mode by the two independent signal paths generated by TME mode and the source-load coupling, which enhances the out-of-band rejection levels. Accordingly, good out-of-band performance of one channel (channel 1) can be obtained.

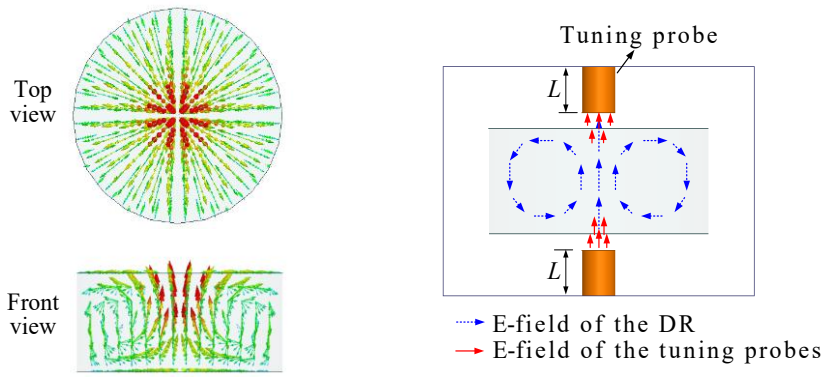

(a) (b)

Figure 4.15. (a) E-field distribution of the DR at TME mode; (b) The DR with tuning probes.

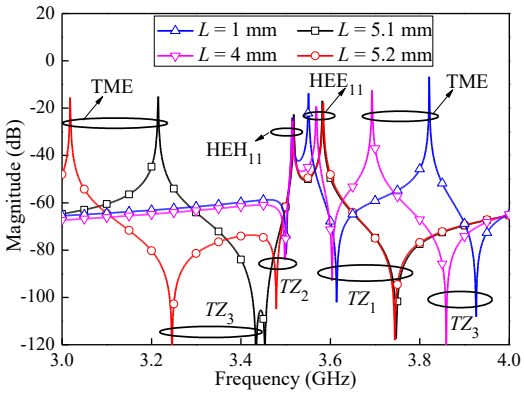

Figure 4.16. Simulated responses of the lower channel filter.

To realize the dual-channel filter, other two feeding probes (ports 3 and 4) are added at the other two corners of the cavity to form the other channel filter (channel 2), as shown in Figure 4.5. Based on the analysis of channel 1, it is known that ports 3 and 4 only excite the HEH_{11}^{2} and HEE_{11}^{2} modes. Thus, the feeding probes of one channel filter do not excite the resonators of the other channel filter. Good isolation between the two channels is realized, as shown in Figure 4.17. Within the passband, simulated isolation is better than 27 dB. Since the circuit structure of the dual-channel filter is symmetric, the channel 2 filter has the same filtering responses as that of channel 1. Hence, the dual-channel filter responses are obtained.

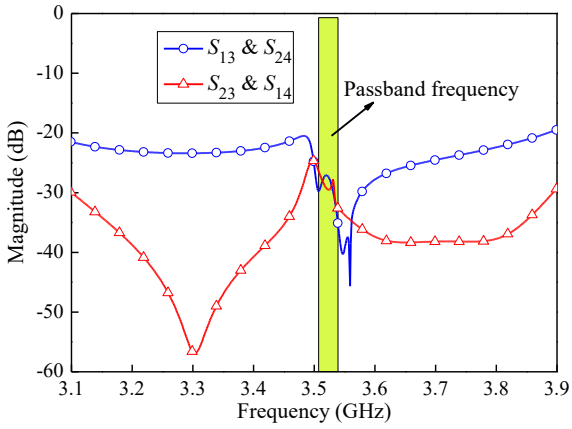

Figure 4.17. Simulated isolation between two channel filers.

4.3.1.3 Experiment and Comparison

Based on the analysis above, the proposed dual-channel filter is implemented. Figure 4.5 shows the 3-D structure. The dielectric material is from the Jiangsu Jiang

Jia Electronics Co. Ltd in Jiangsu, China, with the operating temperature range from -40 to 85 °C. The dimensions are chosen as follows (all in mm): $a = b = 28$, $c = 20$, $D = 20$, $H = 9.1$. In experiment, the foam is utilized as support of the DR, as shown in Figure 4.18(a). The photograph of the fabricated circuit is shown in Figure 4.18(b). The circuit size is $36 \times 36 \times 28$ mm^3 ($0.42 \times 0.42 \times 0.33\ \lambda_g^3$).

The simulation is carried out by using the high-frequency structure simulator (HFSS) and measurement is accomplished by using Keysight E5071C network analyzer under the indoor temperature of 25 ℃. Good agreement between the simulated and measured results is observed in Figure 4.19. The measured passband is centered at 3.525 GHz with the 20-dB return losses of 19 MHz (0.54%) and the insertion loss is 0.32 dB at the center frequency. The corresponding unloaded Q-factor is calculated as around 3000. It should be noted that there are several sources of loss that may decrease the calculated Q factor, such as the losses of the SMA connectors, losses in aluminum walls as well as losses in adhesive between resonator and support. Three transmission zeros appear at 3.15, 3.43 and 3.59 GHz, which greatly enhance the skirt selectivity and out-of-band rejection. The measured isolation between two filter channels at the center frequency is better than 25.3 dB. In theoretical analysis, the two filter channels should have the same filtering responses due to the symmetric circuit structure. However, owing to the fabrication errors, a slight difference in the responses between two filters exists. Nevertheless, the proposed dual-channel filter still features good performance of low insertion loss, high selectivity and high isolation between two channels.

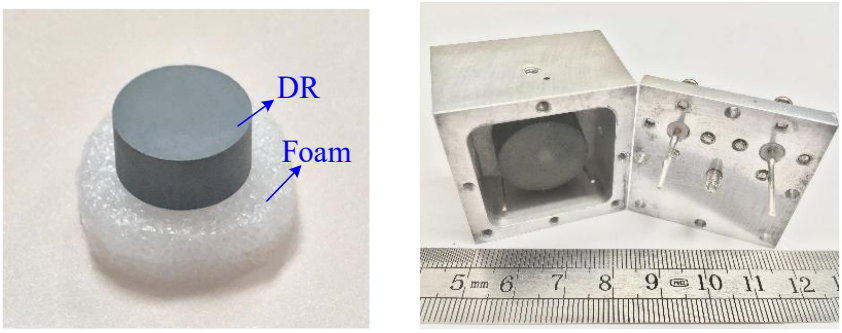

(a) (b)

Figure 4.18. (a) Photograph of the DR using foam as support; (b) Photograph of the fabricated dual-channel filter.

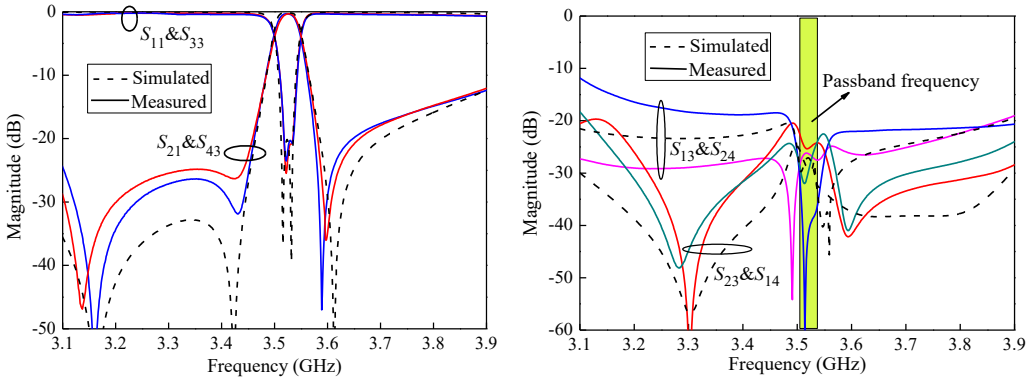

(a) (b)

Figure 4.19. Simulated and measured results of the dual-channel filter (a) S_{11}, S_{21}, S_{33}, and S_{43}; (b) S_{13}, S_{14}, S_{23} & S_{24}.

Table 4.1 tabulates the comparison with other DR BPFs in terms of size and Q-factor. Compared to the BPF designs in [85] and [137], the proposed design has a more compact size. It should be noted that the proposed design integrates two BPFs while those in [85] and [137] are the single-channel filters. Meanwhile, the circuit size of the proposed design is approximate to that in [86] where the BPF is realized with very compact size using quad- mode and dual-mode DRs. As for the Q factor, the proposed design is comparable to the designs in [84], [85] in Table 4.1.

Table 4.1 Comparison With Other DR filters

Ref.	Orders	Cavity Size (λ_g^3)	Q factor
[137]	2	0.59 × 0.28 × ~	N. A.
[84]	4	N.A.	5000 ($TE_{01\delta}$) / 2500 (TE_{101})
[85]	2	0.44 × 0.44 × 0.34	2800
[86]	4	0.29 × 0.29 × 0.37	N. A. (eigen-mode 8200)
This work	2	0.33 × 0.33 × 0.24	3000

4.3.2 Co-Design of Dual-Channel DR Filter and Two-Input Two-Output Doherty Power Amplifier

To demonstrate the application of the dual-channel filter to the MIMO system, it is applied to a two-input two-output (2 × 2) Doherty power amplifier (DPA). In a conventional design, four transistors are required to form the 2 × 2 DPA as each

DPA consists of two sub-amplifiers. To reduce the cost and circuit size, the design procedure of a 2 × 2 DPA is followed by the work presented in [139], where two DPAs share the common carrier power amplifier and thus only three transistors are needed. Figure 4.20 shows the simplified schematic of the 2 × 2 DPA in [139]. The transistor GaN HEMT CGH40010F from Cree is used as the power device. For the input section, two Wilkinson power dividers and a T-junction combiner are used to distribute the identical RF input signals into three sub-amplifiers. Then, these three sub-amplifiers are combined as two output ports with the DPA properties. It is noted that there are two quarter-wavelength transmission lines (TL1 and TL2) placing before the two output ports, which are used to transform 25 Ω impedance to 50 Ω.

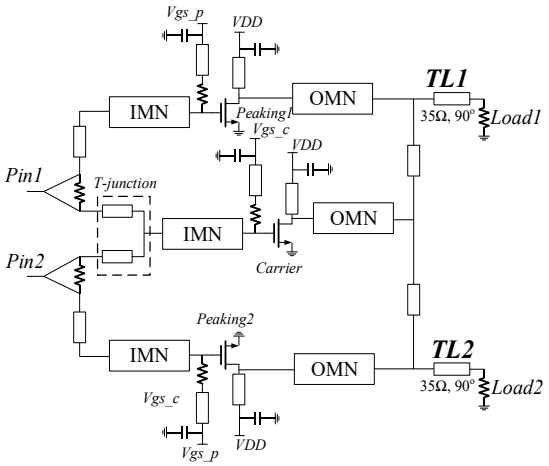

Figure 4.20. Simplified schematic of the compact 2 × 2 DPA.

As shown in the RF front end of the 5G massive MIMO system in Figure 4.1, the power amplifiers are cascaded with the BPFs. It has been demonstrated that the co-design of the power amplifier and BPF can improve the total efficiency and reduce the circuit size of these two components [28]-[32]. Hence, to achieve a 2 × 2 DPA with bandpass responses, the proposed dual-channel filter is integrated with the 2 × 2 DPA. It is realized by using the dual-channel filter to replace the TL1 and TL2 in Figure 4.20. In this way, the two quarter-wavelength transmission lines are eliminated, resulting in simple structure and size reduction. To develop this co-design method, the dual-channel filter should be designed with the real impedance

transformation function from R_{in} = 25 Ω to 50 Ω. Based on the filter design theory, it is known that Q_{ei} is proportional to R_{in} and controlled by the M_{Si} values in the coupling matrix. According to equation (2.10), the M_{Si} (M_{iS}) can be modified to obtain the desired R_{in} as

$$M_{Si}^{'} = \frac{M_{Si}}{\sqrt{R_{in}^{'}}} . \tag{4.3}$$

where R'_{in} = 0.5 is the R_{in} normalized by the 50-Ω system and i = 1, 2, L. Other elements in the coupling matrix (4.2) are kept unaltered. Based on equation (4.3), the desired M'_{Si} values in the modified coupling matrix can be calculated as: M'_{S1} = 1.1599, M'_{S2} = 1.2545, M'_{SL} = 0.0222. The dual-channel filter with the impedance conversion function can be conveniently realized. Figure 4.21 shows the simulated results of the impedance conversion dual-channel filter with different source impedances. As observed, good input port matching is realized when the source impedance is around 25 Ω. Thus, this dual-channel filter can be used as an impedance transformer and replaces the TL1 and TL2 in Figure 4.20 to integrate the filtering responses to the 2 × 2 DPA.

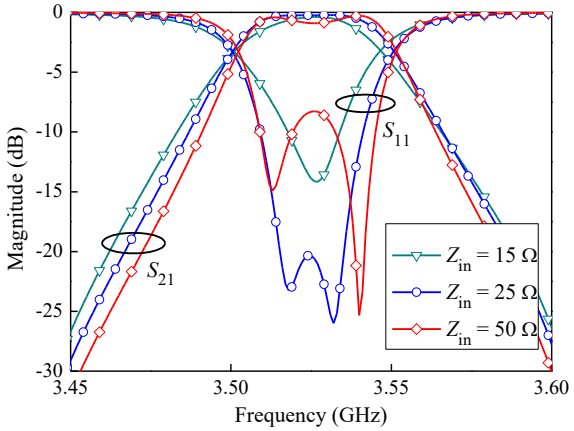

Figure 4.21. The impedance conversion dual-channel filter with different source impedances.

For demonstration, the proposed compact filter-integrated 2 × 2 DPA for the MIMO system application is implemented. The dual-channel matching DR filter

and other circuits fabricated on the printed circuit board (PCB) substrate ($\varepsilon_r = 2.33$, $h = 0.787$ mm, $\tan\delta = 0.0012$) are enclosed in the metal cavity and separated by the metal wall, as shown in Figure 4.22. The metal parts also function as a heat sink for the transistor. The dual-channel DR filter is simulated by HFSS and the S-parameters are imported to the Keysight Advanced Design System (ADS) for co-simulation with the 2 × 2 DPA.

The small-signal responses are measured by the Keysight E5071C network analyzer, as shown in Figure 4.23. The passbands of both channels are centered at 3.53 GHz with the 3-dB FBW of 1.4% and a small-signal gain of 10.5 dB. Due to the use of the dual-channel DR matching filter, the output return losses are better than 15 dB, featuring good output port matching. Three transmission zeros are generated near the passband and at the lower stopband, which exhibits high skirt selectivity and good out-of-band rejection. It is found that discrepancy between the the responses of the two channels exists in Figure 4.23. It may be caused by the device variation of transistors and lumped elements, and the fabrication tolerance.

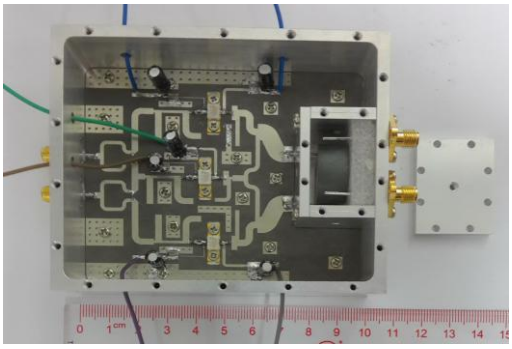

Figure. 4.22. Photograph of the fabricated filter-integrated 2 × 2 DPA.

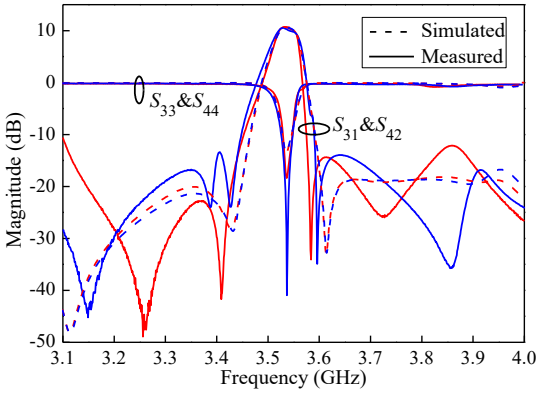

Figure. 4.23. Small-signal responses of the filter-integrated 2 × 2 DPA.

The large-signal responses are measured by the Agilent EXG Vector Signal Generator N51728 and Agilent EXA Signal Analyzer N9010A. Figure 4.24(a) shows the simulated and measured total drain efficiency and gain versus total output power at 3.53 GHz under continuous wave (CW) excitation. The peak total output power is 43.93 dBm with a gain of 8 dB. The simulated and measured drain efficiency is 62% and 61.5% at saturation, respectively. Within the 6 dB back-off power, the drain efficiency is higher than 50%, features high efficiency. Figure 4.24(b) depicts the output power against the frequency. As can be seen, good bandpass responses are realized. Within the passband from 3.52 GHz to 3.54 GHz, the output power of each channel is larger than 40 dBm. Near the passband, two transmission zeros are generated at 3.43 and 3.58 GHz, which greatly enhance the selectivity.

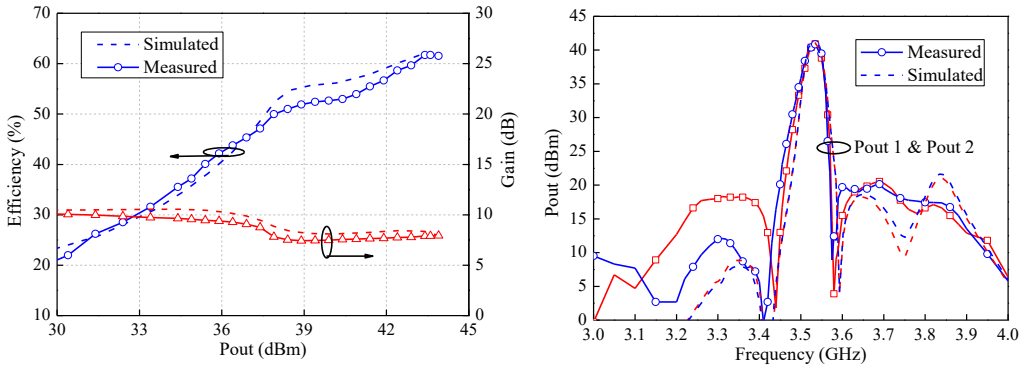

(a) (b)

Figure 4.24. (a) Simulated and measured total drain efficiency and gain versus total output power at 3.53 GHz. (b) Output power versus frequency.

Figure 4.25(a) shows the measured output power and magnitude imbalance between two channels versus the input power (Pin). As can be seen, the power imbalance is smaller than 0.2 dB within a wide input power range. The small discrepancy may be caused by the device variation of transistors or fabrication tolerance. Figure 4.25(b) shows the DC currents of two peaking PAs. It can be observed that the two current curves are close to each other. This is because the circuit is symmetric. All of these measured results show good conformity between

two channels.

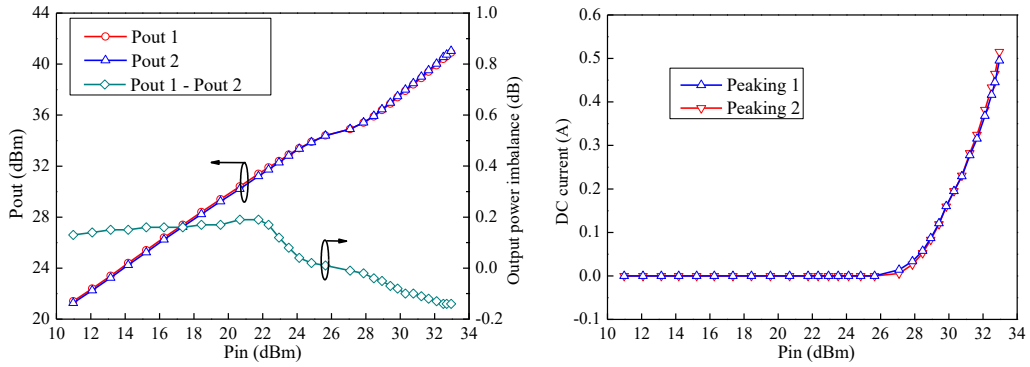

(a) (b)

Figure 4.25. (a) Output power and output power imbalance versus input power; (b) DC currents for the peaking amplifiers.

4.4 Multi-Channel DR Filter

A dual-channel filter is presented in Section 4.3. Two filters are integrated as one circuit by sharing a quad-mode DR, where the two filter channels have good isolation. However, by using the quad-mode DR in Section 4.3, it seems difficult to integrate more channel filters to realize the multi-channel filter for higher integration. To solve this problem, triple-mode DRs are used in this section. A large number of filters can be integrated as one multi-channel filter with multiple inputs and multiple outputs. The schematic is shown in Figure 4.3. Resonant frequencies and electromagnetic (EM) field properties of a cubic DR are analyzed for guiding the circuit realization. Locations of the feeding probes and coupling probes are properly arranged. Then the feeding probes, coupling probes and resonant modes in one filter channel do not couple to those of other channels, resulting in isolation among multiple channels sharing the common DRs. The design method for several circuits with different channels and filter orders is given. For demonstration, a twelve-channel BPF is fabricated and measured. Comparisons between the proposed designs with other reported DR filters are given to show the advantages of the proposed multi-channel BPFs.

4.4.1 Analysis of Triple-Mode Dielectric Resonator

In the proposed multi-channel BPF, a cubic DR with the 3-D structure shown in Figure 4.26 is utilized as the basic resonance cell. Six surfaces of the DR are connected to the metal walls in a metallic cavity and thus are grounded. *a*, *b* and *c* denote the length, height, and width of the DR, respectively.

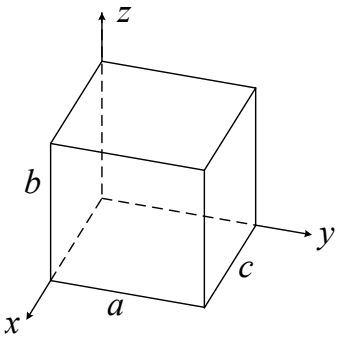

Figure 4.26. 3-D structure of the tri-mode dielectric resonator.

The field configurations inside this DR are either TE or TM mode, which is similar to those of the waveguide [140]. Noticeably, an obvious difference between waveguide and DR is that the waves in the DR are standing waves, instead of traveling waves in waveguides. For guiding the circuit realization, the resonant frequencies of the DR are studied. Based on Maxwell's equations and the corresponding boundary conditions, resonant frequencies of the DR can be analyzed as [140]

$$(f_r)_{mnp}^{TE} = \frac{1}{2\pi\sqrt{\mu\varepsilon}}\sqrt{\left(\frac{m\pi}{a}\right)^2+\left(\frac{n\pi}{b}\right)^2+\left(\frac{p\pi}{c}\right)^2},$$
$$where \begin{cases} m = 0,1,2,... \\ n = 0,1,2,... , and\ m = n \neq 0. \\ p = 1,2,3,... \end{cases} \tag{4.4}$$

$$(f_r)_{mnp}^{TM} = \frac{1}{2\pi\sqrt{\mu\varepsilon}}\sqrt{\left(\frac{m\pi}{a}\right)^2+\left(\frac{n\pi}{b}\right)^2+\left(\frac{p\pi}{c}\right)^2},$$
$$where \begin{cases} m = 1,2,3,... \\ n = 1,2,3,... \\ p = 0,1,2,... \end{cases} \tag{4.5}$$

where $(f_r)^{TE}_{mnp}$ and $(f_r)^{TM}_{mnp}$ denote the resonant frequencies of TE_{mnp} and TM_{mnp}, respectively, m, n, p represent the numbers of half-wave inside the DR along the x-, y-, z-directions.

From equations (4.4) and (4.5), it can be found that when a, b and c have the same values ($a = b = c$), the three fundamental modes of the DR are TE_{101}, TE_{011}, and TM_{110} modes. These three modes have the same resonant frequencies (f_d), which can be expressed as

$$f_d = \frac{1}{\sqrt{2}a\sqrt{\mu\varepsilon}} \tag{4.6}$$

Moreover, when designing the circuit using this DR, by using the eigenmode solution type in the High-Frequency Structure Simulator (HFSS), resonant frequencies of the DR can be easily obtained, as shown in Figure 4.27. Here, the initial dimensions are chosen as follows: $a = b = c = 15$ mm and the DR has the dielectric constant of 38. It can be seen in Figure 4.27 that TE_{101}, TE_{011}, and TM_{110} modes coincide well with each other and the spurious modes (TE_{111} and TM_{111} modes) are about 500 MHz above these modes. Therefore, this DR can be utilized as a tri-mode resonator.

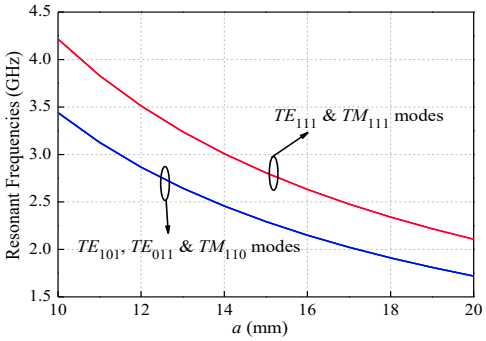

Figure 4.27. Resonant frequencies of the DR versus a. (b and c are kept the same as a when a is changed.)

By using the HFSS software, the electric-filed (E-field) and magnetic-field (H-field) distributions of the DR at TE_{101}, TE_{011} and TM_{110} modes can be simulated as shown in Figures 4.28(a), (b) and (c), respectively. As can be seen, the E-fields of

these three modes are orthogonal to each other. The E-fields of TE_{101} and TE_{011} modes are extended along the ± *x*-direction and ± *y*-direction, respectively, while that of the TM_{110} mode corresponds to the ± *z*-direction. As for the H-field of each mode, it is perpendicular to the E-field, which forms a circle around the E-field.

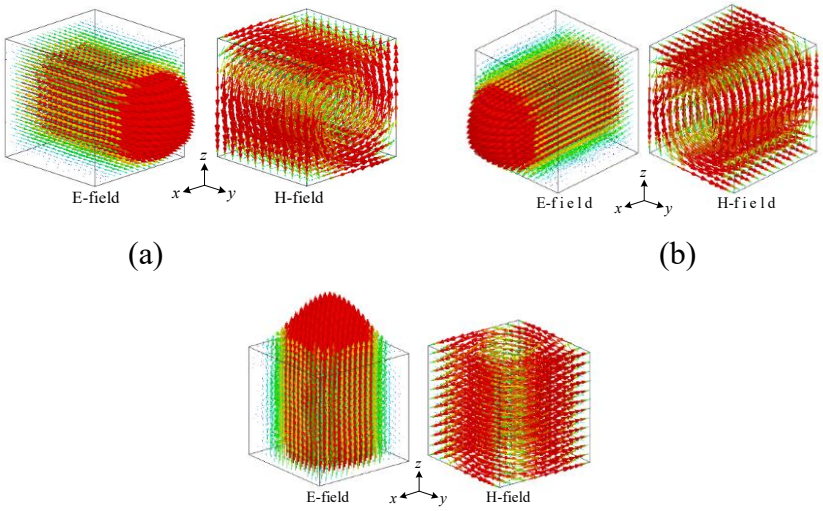

Figure 4.28. EM-field distribution of the DR at (a) TE_{101} mode; (b) TE_{011} mode; (c) TM_{110} mode.

4.4.2 Multi-Channel DR Filter Design

Based on the above-mentioned analysis of the tri-mode DR, multi-channel BPFs are designed. Firstly, by properly arranging the feeding probes, three modes of the DR are excited for different channels without interference with each other. Then, on the basis of this type of excitation, the design method for a 12-channel BPF with second-order Chebyshev filtering responses is proposed. To verify that the presented multi-channel circuit configuration is flexible to be integrated with more filter channels to meet different application scenarios, a 27-channel BPF featuring the third-order filtering responses and a 26-channel BPF integrating 12 second-order, 8 third-order and 6 fourth-order BPFs are designed.

4.4.2.1 Excitation of the Tri-Mode DR

In the proposed multi-channel BPFs, three modes of a single DR are excited for different channels. To obtain high isolation among different channels, signals

should be properly isolated among different modes. To meet this requirement, two feeding probes (ports 1' and 2') are placed at the center of the DR, as shown in Figure 4.29. Here, to excite the DR, three cylindrical holes are elaborately designed at the center of the DR, so that the feeding probes can be inserted into the DR.

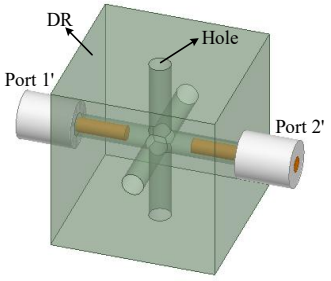

Figure 4.29. 3-D structure of the DR with two feeding probes.

When signals are injected at port 1', EM-field distributions of the feeding probes and the DR at TE_{101}, TE_{011}, and TM_{110} modes are illustrated in Figure 4.30. The electric and magnetic coupling coefficient between feeding probes and the DR can be defined on the basis of the ratio of the coupled energy to the stored energy by using equations (2.4) and (2.5). In Figure 4.30(a), it can be seen that the E-fields of the feeding probes are perpendicular to that of the TE_{101} mode. Based on equation (2.4), the electric coupling coefficient between feeding probes and TE_{101} mode (k_{e1}) can be calculated as zero, namely,

$$k_{e1} = 0. \tag{4.7}$$

However, the H-fields of the feeding probes and TE_{101} mode coincide with each other. Thus, the corresponding magnetic coupling coefficient (k_{m1}) is nonzero according to equation (2.5), namely,

$$k_{m1} \neq 0. \tag{4.8}$$

As a result, the total coupling coefficient between feeding probes and TE_{101} mode (k_1) is nonzero, which is expressed as

$$k_1 = k_{e1} + k_{m1} \neq 0. \tag{4.9}$$

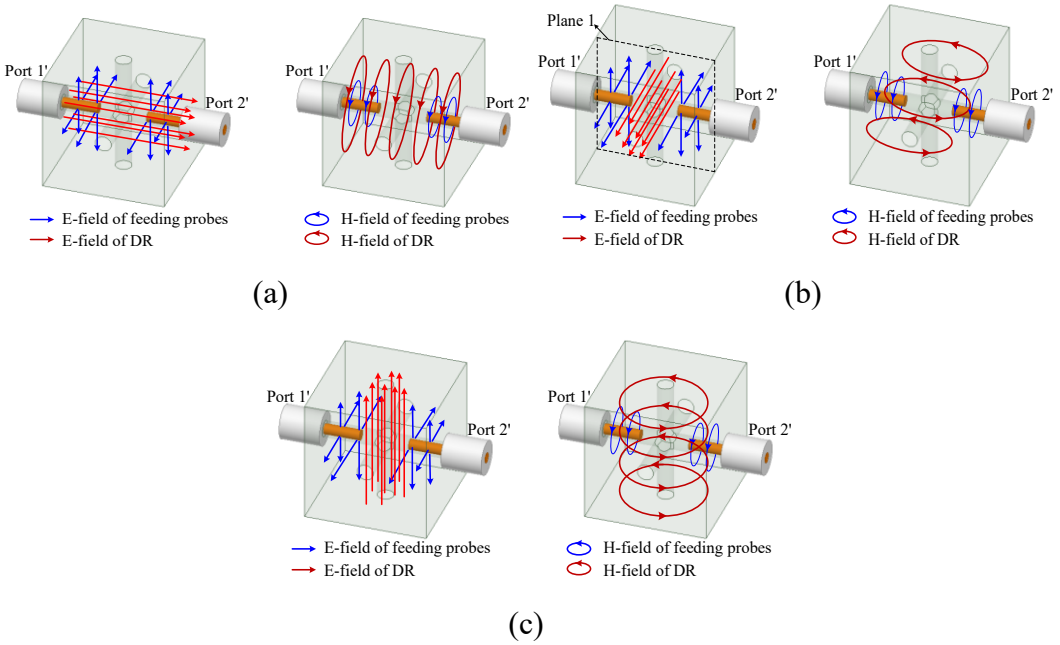

Figure 4.30. EM-field distributions of the DR with two feeding probes at (a) TE_{101} mode; (b) TE_{011} mode; (c) TM_{110} mode.

In Figure 4.30(b), it can be found that the E-fields of the feeding probes are symmetric with respect to the center plane (Plane 1) while that of the TE_{011} mode is out-of-phase. By using equation (2.4), the electric coupling coefficient between feeding probes and TE_{011} mode (k_{e2}) can be analyzed as zero, namely,

$$k_{e2} = 0 . \tag{4.10}$$

Moreover, the H-fields of feeding probes and TE_{011} mode are perpendicular to each other and thus the resultant magnetic coupling coefficient (k_{m2}) is also zero based on equation (2.4), namely,

$$k_{m2} = 0 . \tag{4.11}$$

The total coupling coefficient (k_2) between feeding probes and TE_{011} mode is expressed as

$$k_2 = k_{e2} + k_{m2} = 0 . \tag{4.12}$$

Similar to the TE_{011} mode, the total coupling coefficient between feeding probes

and TM_{110} mode (k_3) can be easy analyzed by the EM-field distribution in Figure 4.30(c) as

$$k_3 = k_{e3} + k_{m3} = 0. \tag{4.13}$$

In summary, for the structure in Figure 4.29, only the TE_{101} mode can be excited by the two feeding probes while the TE_{011} and TM_{110} modes cannot.

Based on the above analysis, a DR with six feeding probes is presented with the structure shown in Figure 4.31(a). Ports 3'-4' and ports 5'-6' are placed at the orthogonal angles of the port 1'-2' and have the same dimensions as ports 1'-2'. Thus, the whole structure is symmetric. According to the EM-field distribution in Figure 4.30, it can be inferred that there are three transmission paths for this structure, including the port 1'-TE_{101} mode-port 2', port 3'-TE_{011} mode-port 4' and port 5'-TM_{110} mode-port 6'. Moreover, due to the orthogonal EM-field distributions, these three transmission paths have no impact on each other. In other words, isolation between them can be achieved. For verification, simulated results of the structure in Figure 4.31 under weak coupling are shown in Figure 4.31(b). Only one mode can be excited by one pair of the feeding probes (ports 1'-2', ports 3'-4' or ports 5'-6') and excellent isolation among them ($S_{3'1'}$, $S_{4'1'}$, $S_{5'1'}$ and $S_{6'1'}$) can be achieved, which verifies the proposed ideas.

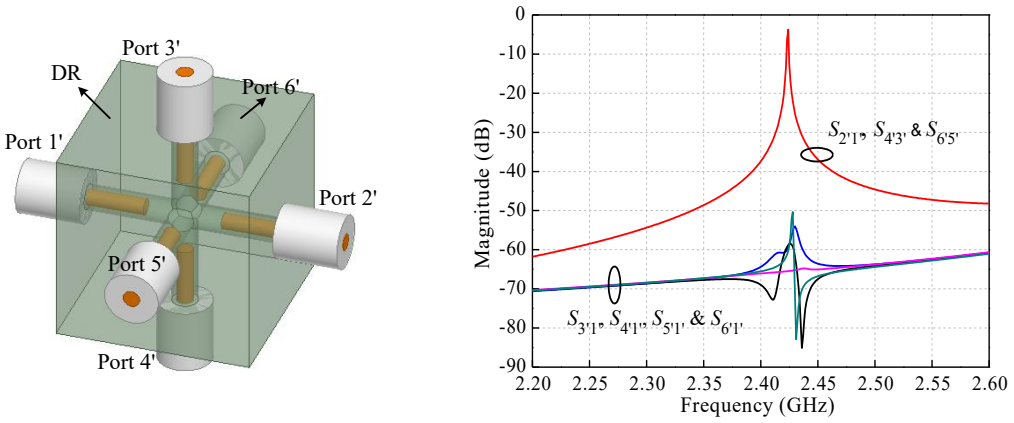

(a) (b)

Figure 4.31. (a) 3-D structure of the DR with six feeding probes. (b) Simulated results of the DR with six feeding probes under weak coupling.

4.4.2.2 Analysis of 12-Channel DR Filter

Based on the structure in Figure 4.31, a 12-channel BPF is designed with the 3-D structure shown in Figure 4.32, which integrates 12 BPFs. It is comprised of eight tri-mode DRs. Twenty four feeding probes (Ports 1-24) are utilized for inputs and outputs and twelve coupling probes (CP1-CP12) are placed among DRs to enable the coupling among the neighboring DRs. The working mechanism is addressed as follows.

According to the analysis in Section 4.3.2.1, when signals are injected from Port 1, it can be known that only the TE_{101} mode of the DR1 can be excited by port 1 while the TE_{011} and TM_{110} modes cannot. Then, the signals can be transmitted to CP1 and coupled to the TE_{101} mode of the DR2. Finally, output signals can be obtained in Port 2. Accordingly, the Port 1, TE_{101} mode of DR1, CP1, TE_{101} mode of DR2 and Port 2 form a transmission path, namely, Path 1. Based on the analysis in Section 4.3.2.1, signals from Path 1 cannot be coupled to other coupling probes (CP2-CP12) and feeding probes (Ports 3-24) due to the orthogonal EM-field distributions of the DRs. Thus, Path 1 in the structure in Figure 4.32 is an independent transmission path. Similarly, from Port 3 to Port 4, there is another independent transmission path (Path 2), so as that from Port 5 to Port 6 (Path 3), Port 7 to Port 8 (Path 4), et al. In total, there are 12 independent transmission paths for the structure in Figure 4.32.

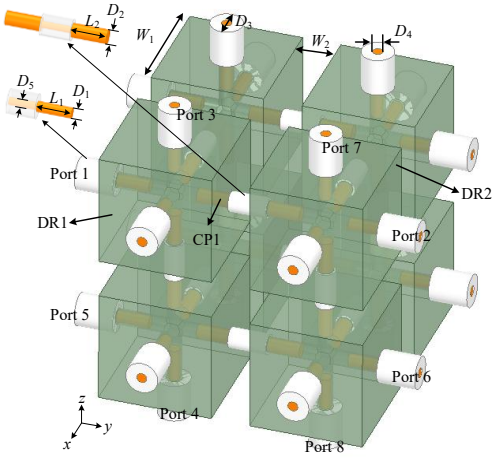

Figure 4.32. 3-D structure of the 12-channel BPF.

For each path, there are two feeding probes and two resonators so that its topology is shown in Figure 4.33. With this topology, Chebyshev BPF responses can be achieved. Thus, the circuit in Figure 4.32 can realize 12 BPFs with the same responses, which is called as a 12-channel BPF. For the realization of bandpass responses for each channel, the conventional BPF design method can be used.

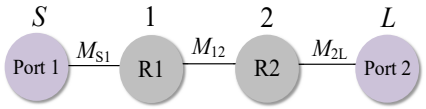

Figure 4.33. The topology of one transmission path of the 12-channel DR filter.

As an example, the BPF is designed with the center frequency of 2.402 GHz, an equal ripple of 0.04321 dB and a 3-dB fractional bandwidth (FBW) of 0.75%. Based on these required responses, the lumped element values of the second-order Chebyshev prototype filter are selected as: $g_0 = 1$, $g_1 = 0.6648$, $g_2 = 0.5445$, $g_3 = 1.2210$. The theoretically desired coupling coefficient k_{12} and external quality factor Q_e at the center frequency (f_0) can be calculated by using equations (3.19) and (3.20). In EM simulation, the coupling coefficient $k_{12,\,ext,}$ and external quality factor $Q_{e,\,ext}$ can be extracted to meet the theoretical values by

$$k_{12,ext} = \frac{f_o^2 - f_e^2}{f_o^2 + f_e^2} \tag{4.14}$$

$$Q_{e,ext} = \frac{f_0}{\Delta f_{\pm 90^0}} \tag{4.15}$$

where f_o and f_e are the odd- and even-mode resonant frequencies, respectively, and $\Delta f_{\pm 90^o}$ is the bandwidth over which the phase shifts $\pm 90^o$ with respect to the absolute phase at f_0. Based on equations (4.14) and (4.15), the $k_{12,\,ext}$ against L_1 and $Q_{e,\,ext}$ against L_2, are obtained as Figures 4.34(a) and (b), respectively. As can be seen, when L_1 increases, $k_{12,\,ext}$ increases, and $Q_{e,\,ext}$ decreases as L_2 increases. Based on these studies, dimensions of the circuit can be tuned to meet the theoretical k_{12} and Q_e values to obtain the desired bandpass responses.

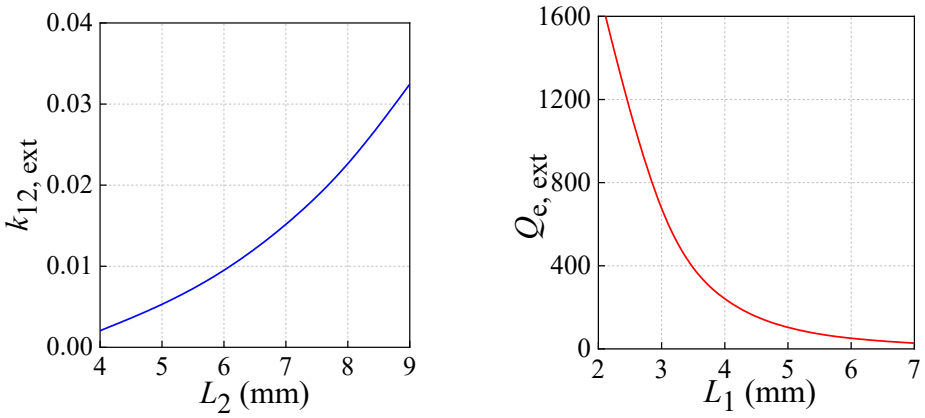

Figure 4.34. (a) $k_{12, ext}$ against L_1; (b) $Q_{e, ext}$ against L_2.

Figure 4.35 shows the simulated results of the 12-channel BPF. It can be seen that each channel exhibits good Chebyshev filtering responses with a 3-dB bandwidth of 0.75%. The in-band isolation among twelve channels is better than 30 dB, which satisfies the requirement of a massive MIMO antenna system. In this design, the isolation can be influenced by the length of the feeding probes (L_1) and coupling probes (L_2). A sensitivity analysis is given as follows. Figures. 36(a) and (b) shows the simulated results (S_{31}) with different values of L_1 and L_2, respectively. In Figure 4.36(a), when L_1 is changed from 4.1 to 4.7 mm, the in-band isolation varies from 27.1 to 33.5 dB. In Figure 4.36(b), the in-band isolation is changed from 34.0 to 26.5 dB when L_2 is adjusted from 5.5 to 6.1 mm.

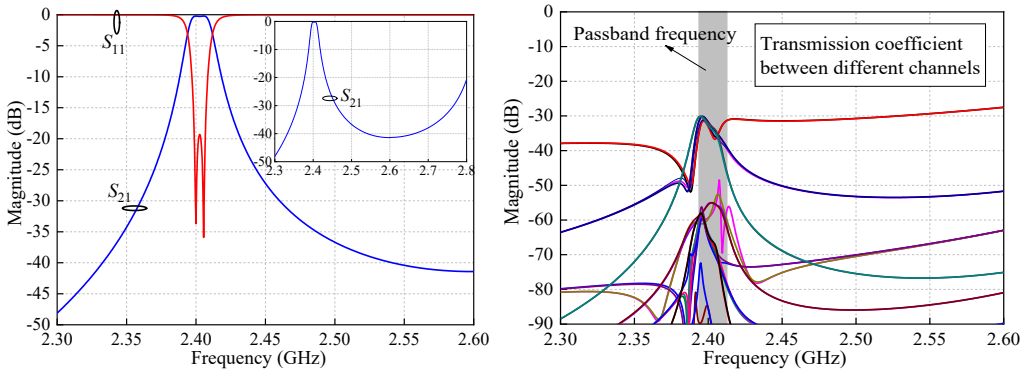

Figure 4.35. Simulated results of the 12-channel BPF (a) S_{11} and S_{21}; (b) Transmission coefficient between channels.

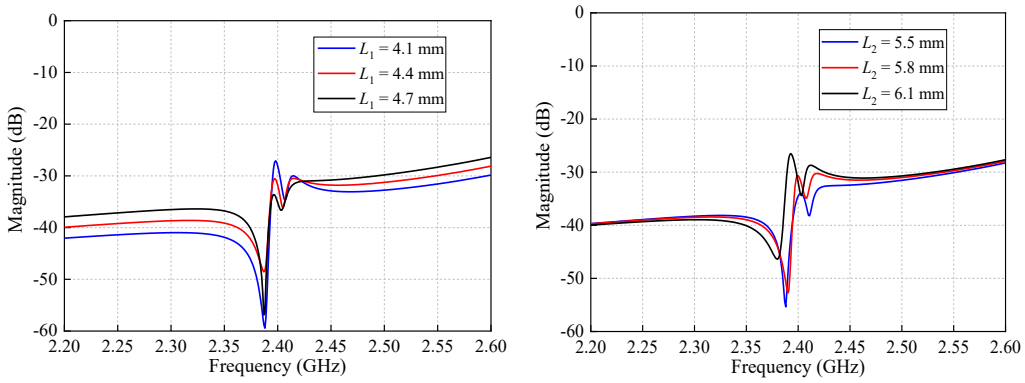

(a) (b)

Figure 4.36. Simulated S_{31} of the proposed 12-channel BPF (a) with different values of L_1; (b) with different values of L_2.

For this proposed design, the coupling coefficient can be adjusted by L_2 and D_2, while the external quality factor can be changed by L_1 and D_1. By controlling these parameters (L_1, D_1, L_2, D_2), wider filter bandwidths can be obtained, as shown in Figure 4.37(a). A wider 3-dB bandwidth of 2.6% is achieved. However, the maximum achievable bandwidth is limited by the desired isolation values, because there is a tradeoff between the filter bandwidth and channel isolation. When the bandwidth increases, the isolations among channels get worse, as shown in Figure 4.37(b). If the isolation among channels is desired to be better than 20 dB, the maximum achievable bandwidth is around 2.6% for this second-order design.

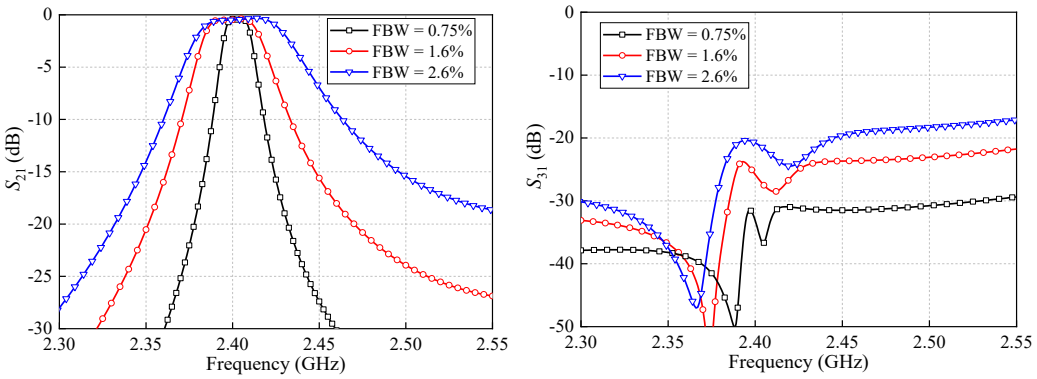

(a) (b)

Figure 4.37. Simulated results of the second-order multi-channel filter with different bandwidth (a) S_{21}; (b) S_{31}.

4.4.2.3 Analysis of Higher-Order Multi-Channel DR Filter

In the above section, a 12-channel BPF featuring second-order filtering responses has been presented with high integration. However, in practical applications, BPFs are often desired with high selectivity and high out-of-band rejection. The twelve-channel BPF with second-order filtering responses may not satisfy this requirement. Moreover, only twelve channels are not sufficient for a massive MIMO antenna system. Thus, a multi-channel BPF with higher-order filtering responses and more channels is in demand.

Figure 4.38 shows the 3-D structure of a multi-channel BPFs, where the number of DRs along the *x*-, *y*- and *z*-axes are all three. The feeding probes and coupling probes are similar to that of the 12-channel BPF. Based on the analysis of the12-channel BPF, it can be easy inferred that this structure integrates 27 BPFs and each BPF features the third-order filtering responses. It should be noted that the proposed circuit configurations are convenient to be extended to realize more higher-order filtering responses by setting more DRs along the *x*-, *y*- and *z*-axes, such as, four, fix or more, which can fulfill the desired specifications of massive channels, higher selectivity, and higher out-of-band rejection.

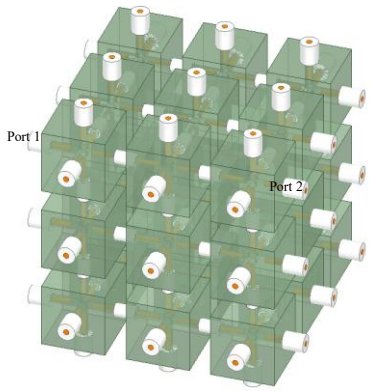

Figure 4.38. 3-D structure of a twenty seven-channel filter with third-order filtering responses.

The design processes of this multi-channel BPF is similar to the 12-channel BPF. Firstly, the resonant frequency of the DR is tuned to meet the passband frequency.

Secondly, the lumped elements of the third-order Chebyshev low-pass prototype filter can be obtained and the desired external quality factors Q_e and coupling coefficient k can be calculated by equations (3.19) and (3.20). Then, dimensions of the coupling probes and feeding probes are determined based on the desired k and Q_e. Finally, fine-tuning is performed to obtain good circuit performance. Figure 4.39 shows the simulated results. As can be seen, each channel has good third-order filtering responses and isolation between channels is better than 29 dB.

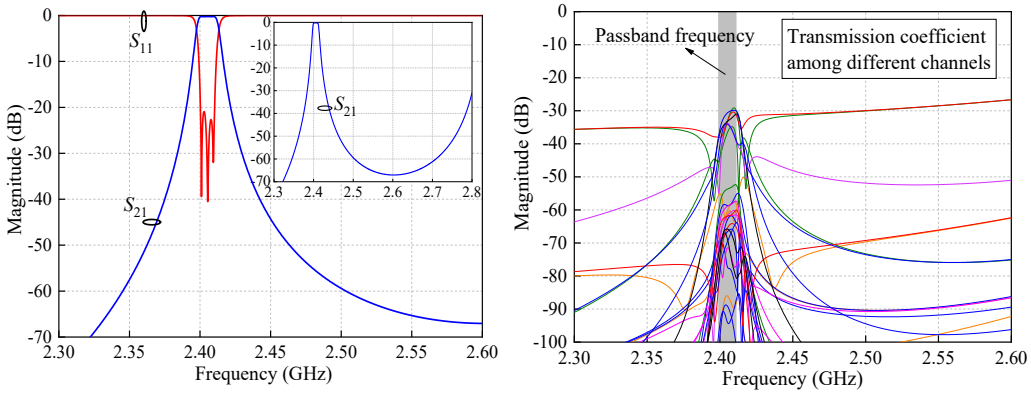

(a) (b)

Figure 4.39. Simulated results (a) S_{11} and S_{21}; (b) Transmission coefficient between channels.

4.4.2.4 Analysis of Multi-Channel DR Filter with Different Filter Orders

The requirements of selectivity and out-of-band rejection in different cases are often different. Thus, the BPFs with different filter orders are also integrated as one multi-channel BPF to meet different specifications. As a design example, a multi-channel BPF integrating the second-order, third-order and fourth-order BPFs are proposed with the structure shown in Figure. 40. The number of DRs along the x-, y- and z-axes are three, four and two, respectively.

The design procedures are similar to that of the multi-channel with second- or third-order filtering responses. Figures 41(a), (b) and (c) show the simulated results of the second-order, third-order and fourth-order channels, respectively. All of the channels exhibit excellent performance, which verifies the proposed ideas.

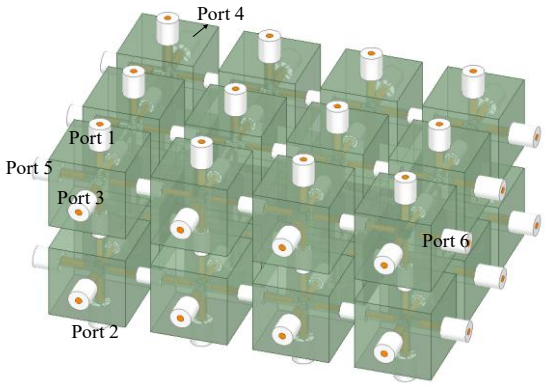

Figure 4.40. 3-D structure of the multi-channel filter second-, third- and fourth-order filtering responses.

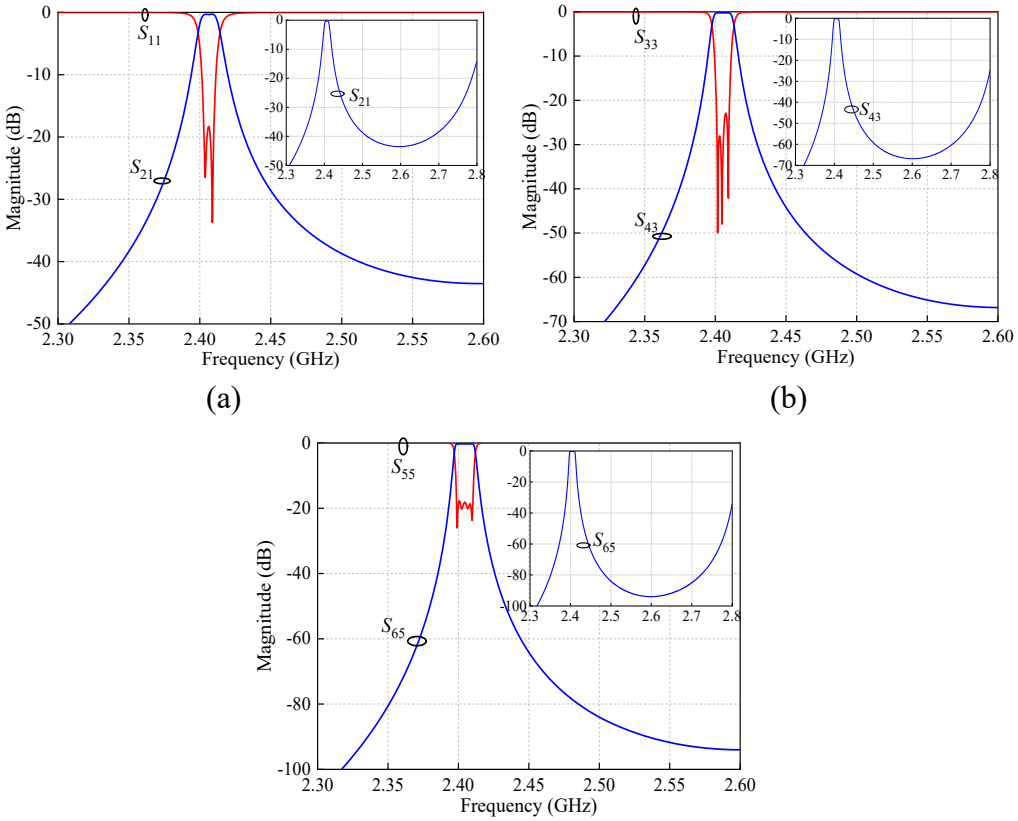

Figure 4.41. Simulated results of BPF with different orders in one multi-channel filter (a) Second-order; (b) Third-order; (c) Fourth-order.

4.4.3 Experiment and Comparison

To demonstrate the proposed concept for multi-channel BPF based on tri-mode DRs, the 12-channel BPF discussed in Section 4.3.3.2 is implemented. The DR is fabricated from the Jiangsu Jiangjia Electronics Co. Ltd., Jiangsu, China, with the

dielectric constant of 38. The dimensions are determined as follows (all in mm): L_1 = 4.42, L_2 = 5.8, W_1 = 15.1, W_2 = 5, D_1 = 0.65, D_2 = 0.47, D_3 = 2.1, D_4 = 0.65, D_5 = 0.65. The photograph of the fabricated 12-channel BPF is shown in Figure 4.42. The implemented circuit has a weight of 0.328 kg. The overall circuit size including the metal cavity is 43.2 × 43.2 × 43.2 mm^3 (0.35 × 0.35 × 0.35 λ_g^3). For this 3-D circuit configuration, RF coaxial cables can be utilized to connect the proposed circuit to other circuits in practical applications, such as antennas, switches, and power amplifiers.

In experiment, metal materials are printed to the surfaces of DR to ensure that the six surfaces are connected to the metal wall and thus grounded. The metal cavity is made by the conventional mechanical processing. When measuring the filter, if discrepancy between the simulated and measured results happen, we can tune the length of the feeding probes and coupling probes until the simulated and measured results agree with each other. The measurement is accomplished by using the Keysight Agilent E5071C network analyzer. Figure 4.43(a) shows the results of one-channel. The measured passband is centered at 2.4 GHz with a return loss of better than 25 dB. The 3-dB FBW is 0.75% and the minimum insertion loss is 1.01 dB. It should be noted that there are several sources that may increase the measured insertion loss, such as the losses in aluminum walls. The measured Q factor is around 2800. The measured responses of other channels are almost the same as that from port 1 to port 2 due to the symmetrical structure. The measured isolation between different channels is better than 24.5 dB, as shown in Figure 4.43(b), which is sufficient for the massive MIMO antenna systems.

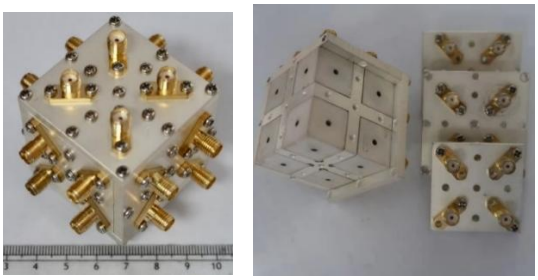

Figure 4.42. Photograph of the fabricated twelve-channel BPF.

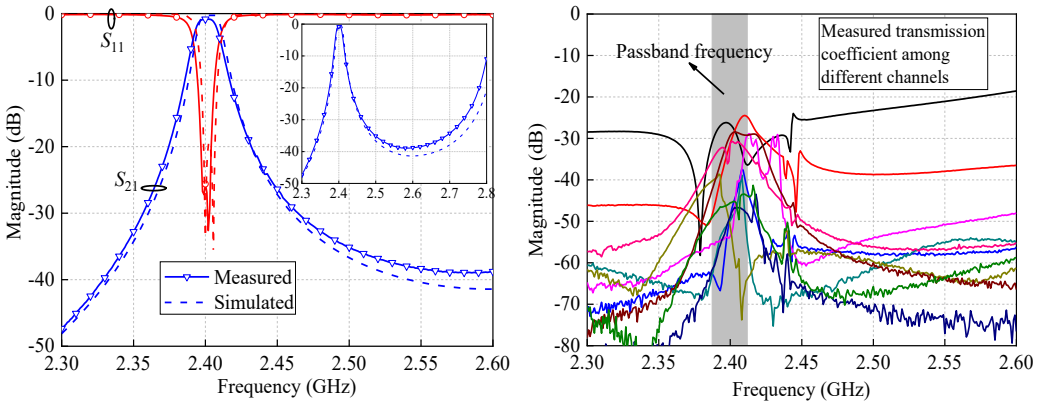

(a) (b)

Figure 4.43. Simulated and measured results of the 12-channel DR filter (a) S_{11} and S_{21}; (b) Transmission coefficient between different channels.

Table 4.2 tabulates the comparison with some other reported DR BPFs. As can be seen, the size of the proposed 12-channel BPF is comparable to the single-channel filter in [85], [86] and [137]. It should be noted that the proposed design integrates twelve BPFs while others only have one or two BPFs. However, if only one or two filters are needed in a wireless system, the use of one proposed multi-channel filter may not reduce the size as compared to the single-channel or dual-channel filters because a lot of filter channels are not in use. By contrast, if a larger number of filters are needed, the proposed designs show the advantage of significant size reduction.

Table 4.2 Comparison With Some Other Couplers

Ref.	Orders	Size (λ_g^3)	Filter channels
[137]	2	0.59 × 0.28 × ~	Single-channel
[85]	2	0.44 × 0.44 × 0.34	Single-channel
[86]	4	0.29 × 0.29 × 0.37	Single-channel
This work	2	0.35 × 0.35 × 0.35	Twelve-channel

4.5 Compact Dual-Channel Balanced Filter and Balun Filter Based on Quad-Mode Dielectric Resonator

In Section 4.3, two filters are integrated as one dual-channel filter by sharing a common quad-mode DR. The circuit is designed with a single-cavity configuration, resulting in a compact size. Moreover, in Section 4.4, by utilizing tri-mode DRs, more filters can be integrated to realize high-integration multi-channel filters. Based on the design methods of the dual- and multi-channel filters in Sections 4.3 and 4.4, dual-channel balanced and balun filters are proposed using quad-mode DR. Two balanced filters or two balun filters are integrated as one dual-channel balanced or balun filter with multiple input ports and multiple output ports, with the schematic shown in Figures 4.4(a) and (b). They are realized by sharing one common quad-mode DR in a metallic cavity, which can eliminate the metal wall and space between two separate circuits, resulting in a significant size reduction. A cylindrical DR with two short ends is firstly studied to construct a quad-mode DR and its electromagnetic (EM) field properties are studied for guiding the circuit realization. By properly arranging the feeding probes, a single-cavity dual-channel balanced filter is constructed. Detailed design methods are given to obtain good filtering responses and high common-mode suppression of each channel as well as high isolation between the two channels. Furthermore, a dual-channel balun filter is implemented based on the proposed dual-channel balanced filter. Comparison with other balanced and balun filters is also given to show the advantages of the proposed designs.

4.5.1 Analysis of the Quad-Mode DR

A circular quad-mode cylindrical DR with two short ends is utilized as the resonance cell of the proposed dual-channel balanced and balun filters. The structure is similar to the rectangular quad-mode DR presented in Section 3.4. Figure 4.44 shows its 3-D structure where a cylindrical DR is placed at the center

of a cylindrical metallic cavity. Two ends of the DR are connected to the top and bottom metal wall of the cavity and thus are short-circuited. D and H are the diameter and height of the metallic cavity, respectively while d and h represent the diameter and height of the DR.

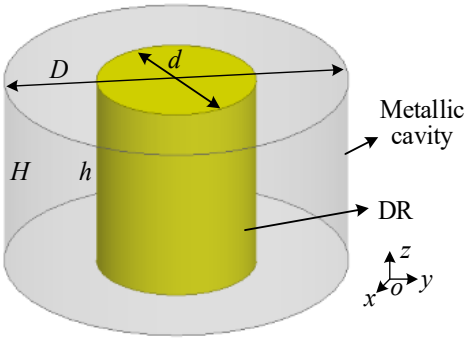

Figure 4.44. 3-D structure of the cylindrical quad-mode DR in a metallic cavity.

To construct the quad-mode DR, resonant frequencies of some lower-order modes of this cylindrical DR are investigated. Initial parameters of the DR and metallic cavity are chosen as follows (all in mm): d = 11.6, h = 13, D = 25.2, H = 13. The substrate of the DR has a dielectric constant of 36.5 and a loss tangent of 0.0002. By using the eigenmode solution, resonant frequencies of the DR at some lower-order modes with different values of h (H is always equal to h) can be obtained as in Figure 4.45(a). Here, we use M1, M2 pair and M3 pair to represent the TM_{01} mode, HEH_{11} pair, and TM_{11} degenerate modes, respectively. From Figure 4.45(a), it can be found that the resonant frequencies of M2 pair and M3 pair are closed to each other. We use these four modes (M2 and M3 pairs) to realize the proposed filtering circuits. In other words, the DR is utilized as a quad-mode resonator.

Figure 4.45(b) shows the simulated resonant frequencies of M2 and M3 pairs with different values of d ($H = h$ = 13 mm and D = 25.2 mm are unaltered). As can be seen, when d is changed from 4 mm to 14 mm, the resonant frequencies of M2 and M3 pairs can be tuned within a wide range from 9 GHz to 3 GHz. Theoretically,

the M2 and M3 pairs can be tuned to arbitrary frequencies by adjusting the values of *H*, *D*, *h* and *d*. However, the limits of the fabrication process exist. The metallic cavity and DR cannot be fabricated with too small dimensions, which limits the tuning range of the center frequency (towards very high frequency).

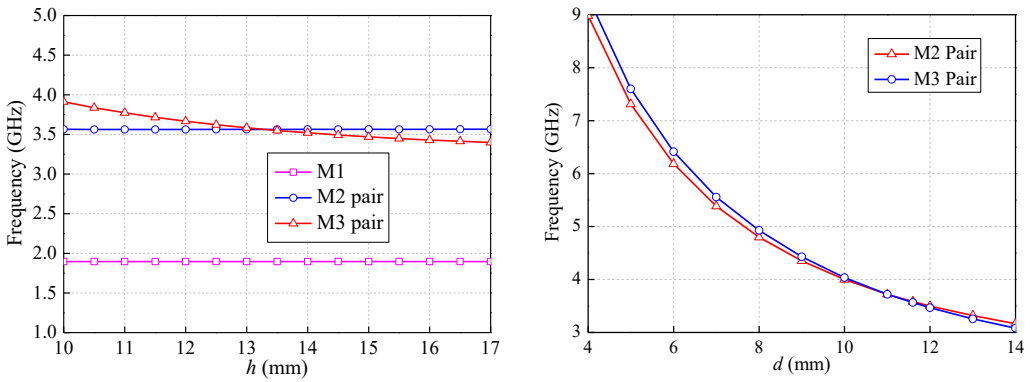

Figure 4.45. Resonant frequencies of the DR with (a) different *h*; (b) different *d*.

EM-field distributions of the quad-mode DR are shown in Figure 4.46. As can be seen, the electric-fields (E-fields) of the M2 pair form two half circles while that of the M3 pair are vertically distributed between the top and bottom metal walls. The magnetic field (H-field) of each mode is perpendicular to the E-field. From the side views of the E-fields of the M2 and M3 pairs in Figure 4.47(a), it can be seen that the E-fields of four modes do not coincide with each other at z = *h* / 2 plane, where the E-field of the M2 pair is parallel to the *xoy* plane, while that of the M3 pair is perpendicular. For these E-field distributions, the four tuning probes made of metallic material at the *z* = *h* / 2 plane in Figure 4.47(b) are coupled to the M2 pair, which can change the resonant frequency of M2 pair. However, the impact on the M3 pair is very slight because tuning probes are placed at the orthogonal angle of the E-fields of the M3 pair. In this case, the resonant frequency of the M2 pair can be changed by the length of the tuning probes (t_1) with almost no influence on the M3 pair, as shown in Figure 4.47(c). Moreover, from the resonant frequency investigation of the DR in Figure 4.45, when *h* is changed, the resonant frequency

of the M2 pair is changed while the M3 pair is unaltered. Thus, the M2 pair and M3 pair can be controlled independently. By fully utilizing the inherent EM-field properties of the DR, the dual-channel balanced and balun filters are designed, as addressed below.

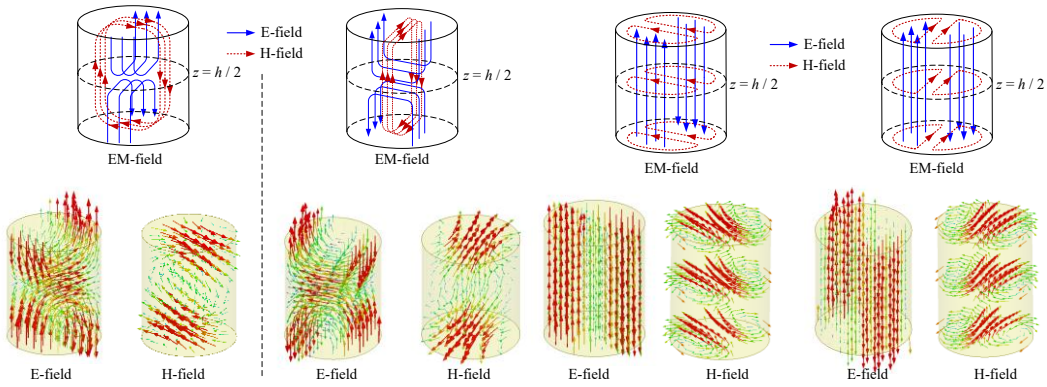

Figure 4.46. EM-field distributions of the quad-mode DR at (a) M2 pair; (b) M3 pair.

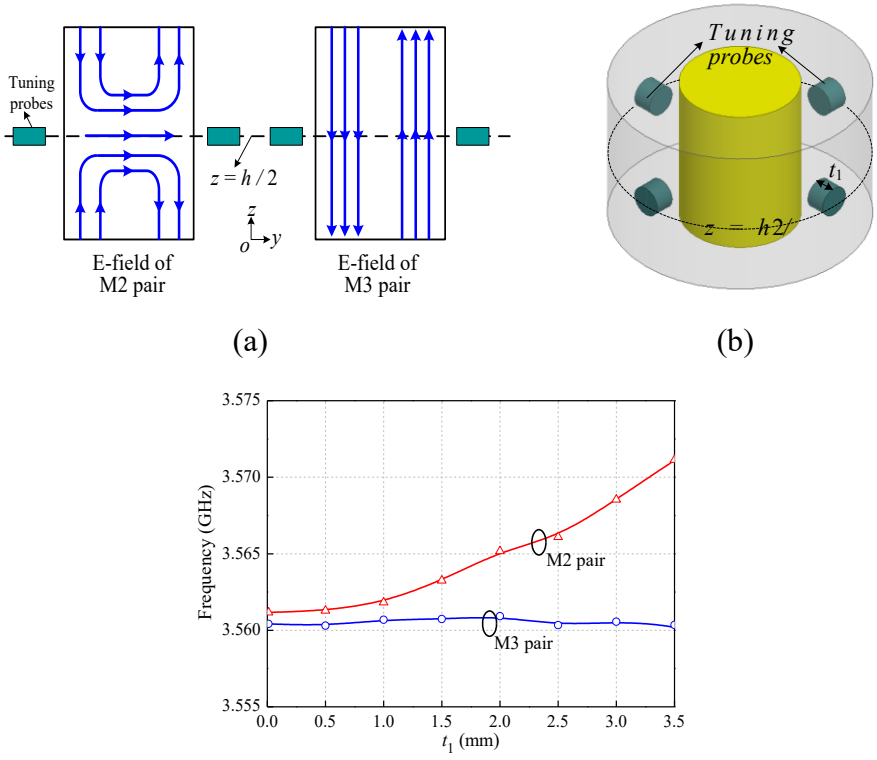

Figure 4.47. (a) Side view of E-field at M2 and M3 modes; (b) DR with four tuning probes at $z = h / 2$ plane; (c) Resonant frequencies of M2 and M3 pairs against t_1.

4.5.2 Dual-Channel Balanced Filter

4.5.2.1 Circuit Configuration

By employing the aforementioned quad-mode DR, a dual-channel balanced filter is proposed with the 3-D structure shown in Figure 4.48. Eight ports, which are defined as ports 1-4 and ports 1'-4', are arranged with the orthogonal angle and coupled to the quad-mode DR for inputs and outputs. Four of them are extended from the top metal wall to the center and the other four are extended from the bottom metal wall. Ports 1, 1', 2 and 2' are used for one channel while ports 3, 3', 4 and 4' are for the other channel. Here, two balanced filters share the common metallic cavity and DR with no space between them. The metal wall that used in two conventional balanced filters for blocking the signals between them is also eliminated, featuring high integration. The operating principle of the proposed dual-channel balanced filter is detailed as follows.

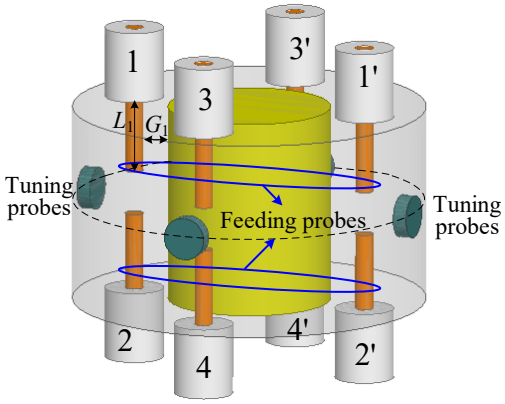

Figure 4.48. 3-D structure of the dual-channel balanced filter.

4.5.2.2 Single-End Excitation of the DR in Single-Channel Filter

In order to construct the proposed dual-channel balanced filter, we firstly introduce a single-channel single-end BPF with the structure shown in Figure 4.49. Two feeding probes are placed at the same side of the quad-mode DR. One is extended from the top metal wall to the center and the other is extended from the bottom metal wall.

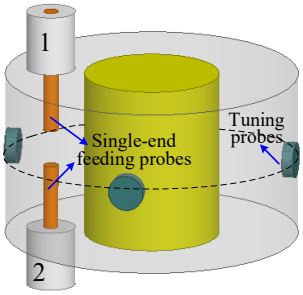

Figure 4.49. Structure of the quad-mode DR with two single-end feeding probes.

According to the analysis of the quad-mode DR, the EM-field distributions of this BPF at the M2 and M3 pairs can be illustrated in Figure 4.50. Here, to describe each mode clearly, we use M2' and M2" to represent the M2 pair while M3' and M3" denote the M3 pair. With the EM-field distributions, the coupling coefficient between the feeding probes and DR at each mode can be studied on the basis of the ratio of the coupling energy to stored energy by using equations (2.4) and (2.5). From Figure 4.50(a), k_e and k_m between the feeding probe and the DR at the M2' mode can be analyzed based on equations (2.4) and (2.5) as non-zero. In Figure 4.50(b), the E-fields of the DR at M2" mode are out-of-phase at two sides of the center plane (Plane 1), while that of feeding probe are in-phase. Thus, the corresponding k_e can be calculated as zero by using equation (2.4). Similarly, k_m in Figure 4.50(b) is also zero due to the in-phase and out-of-phase H-fields of the DR at the M2" mode and the feeding probe. In Figure 4.50(c) and (d), it can be seen that the E-fields of the feeding probes and the DR at the M3 pair are perpendicular to each other. Thus, the corresponding k_e is calculated as zero based on equation (2.4). As for k_m between the feeding probes and the DR at M3' mode, it is analyzed by using (2.5) as non-zero, as shown in Figure 4.50(c). However, in Figure 4.50(d), since the H-field of the DR at the M3" mode is symmetric at two side sides of Plane 1 and that of the feeding probes are out-of-phase, the resultant k_m is zero based on equation (2.5). Accordingly, it can be concluded that when signals are injected from the feeding probes, only the M2' and M3' modes can be excited while M2" and M3" cannot. Here, the phase shift between feeding probes and DR from electric coupling

is positive and that from magnetic coupling is negative. Simulated S_{21} of the single-end filter in Figure 4.49 under weak coupling is shown in Figure 4.51. Only two modes are excited, which verifies the analysis.

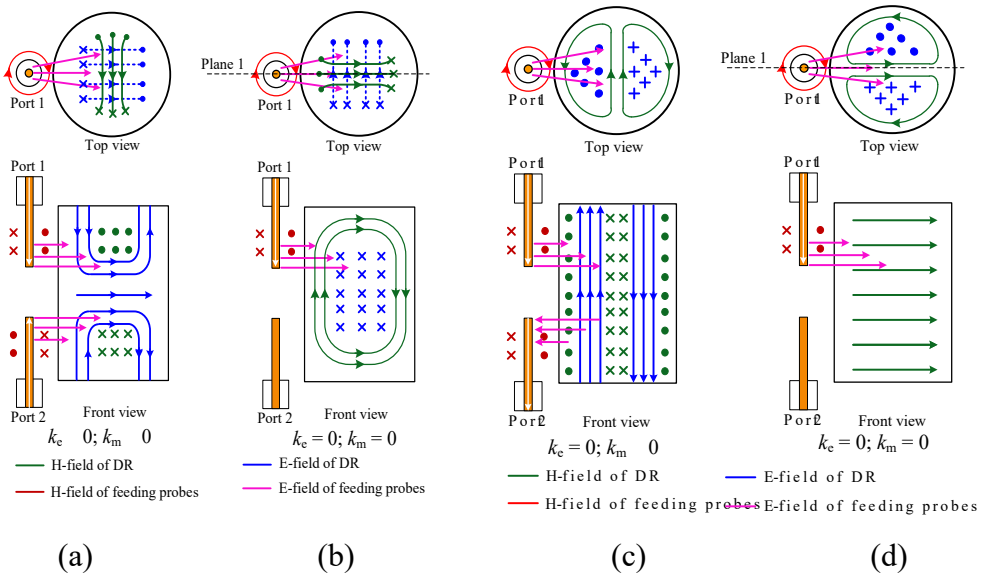

Figure 4.50. EM-field distribution of the DR with single-end feeding probes at (a) M2' mode; (b) M2" mode; (c) M3' mode; (d) M3" mode.

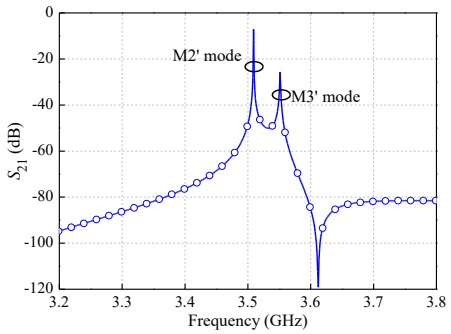

Figure 4.51. Simulated S_{21} of the single-end feeding structure under weak coupling.

4.5.2.3 Design of Single-Channel Balanced Filter

Based on the above single-end filter structure, the other two feeding probes (ports 1' and 2') can be added symmetrically to realize differential feeding schemes to construct a balanced filter, as shown in Figure 4.52. When differential-mode (DM) signals are injected, the currents on a pair of differential feeding probes are in the opposite directions. According to the Ampere's right-hand screw rule, the EM-fields generated by the differential feeding probes are out-of-phase. Figures 4.53(a)

and (b) show the EM-field distributions of feeding probes and DR at M2' mode and M3' mode, respectively. As seen, the EM-field directions of the DR and differential feeding probes at the two sides of the symmetric plane (plane 2) coincide well with each other. Hence, the M2' and M3' modes of the DR can be excited by these differential schemes. On the contrary, if the common-mode (CM) signals are injected, the EM-field directions of DR and the CM feeding probes do not coincide with each other, as shown in Figure 4.53(c) and (d). The coupling coefficient between the CM feeding probes and the M2' mode or M3' mode is calculated as zero based on equations (2.4) and (2.5). Thus, the M2' and M3' modes would not be excited, resulting in CM suppression. Moreover, according to the analysis of the single-end filter in Figure 4.50, it can be inferred that the M2" and M3" modes also cannot be excited by the feeding structure in Figure 4.52, because the coupling coefficient between the feeding probes and the DR at the M2" and M3" modes are still zero.

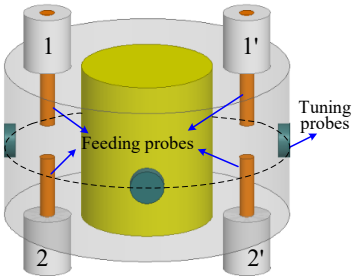

Figure 4.52. 3-D structure of the DR with differential feeding probes.

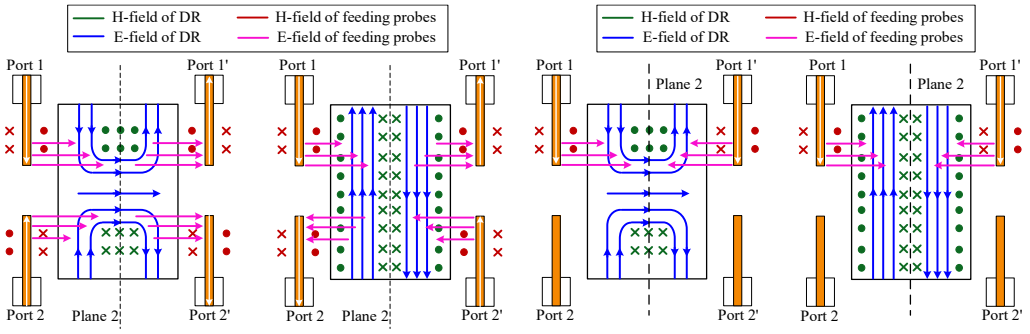

Figure 4.53. EM-field distributions of the quad-mode DR (a) DM excitation at M2' mode; (b) DM excitation at M3' mode; (c) CM excitation at M2' mode; (d) CM excitation at M3' mode.

For verification, simulated results of the structure in Figure 4.52 with DM and CM excitations under weak coupling are shown in Figure 4.54. As can be seen, only two modes of the quad-mode DR are excited by the DM signals and the CM signals are highly suppressed. Accordingly, this structure can be utilized to obtain balanced bandpass responses with high CM suppression.

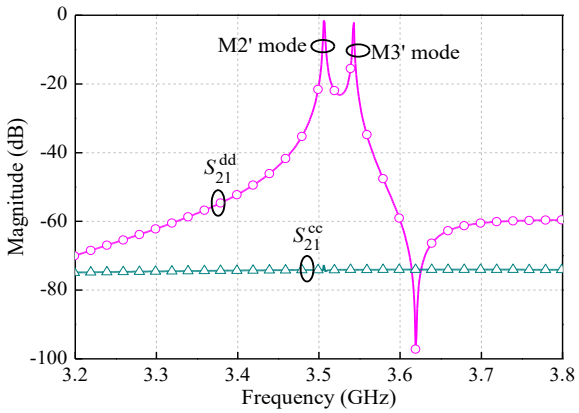

Figure 4.54. Simulated S_{21}^{dd} and S_{21}^{cc} under weak coupling.

From the symmetric and out-of-phase EM-field distributions of M2' and M3' modes in Figure 4.46, the coupling coefficient between M2' and M3' modes can be analyzed as zero based on equations (2.4) and (2.5). Since the differential feeding probes are coupled to both the M2' and M3' modes, the topology of the filter structure in Figure 4.52 can be illustrated as Figure 4.55, where S^{d} and L^{d} denote the input and output differential pairs. Here, the existence of the source-load coupling (M_{SL}) is due to the fact that the open ends of the input and output differential feeding probes are closed to each other.

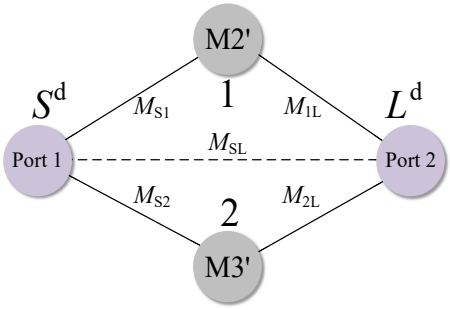

Figure 4.55. The topology of a single-channel balanced filter.

As an example, the balanced filter is designed with a center frequency (f_0) of 3.48 GHz. The 20-dB equal-ripple return loss has a fractional bandwidth (FBW) of 0.6%. Two transmission zeros are appointed at 3.27 and 3.66 GHz. Based on the coupling matrix synthesis method in [79], the initial coupling matrix can be synthesized as

$$M_{N+2} = \begin{array}{c} \\ S^d \\ 1 \\ 2 \\ L^d \end{array} \begin{array}{c} \begin{array}{cccc} S^d & 1 & 2 & L^d \end{array} \\ \begin{bmatrix} 0 & -0.8711 & 0.8548 & -0.0071 \\ -0.8711 & 1.6567 & 0 & -0.8711 \\ 0.8548 & 0 & -1.6619 & -0.8547 \\ -0.0071 & -0.8711 & -0.8547 & 0 \end{bmatrix} \end{array}. \tag{4.16}$$

The desired external quality factor Q_{ei} at f_0 and the resonant frequencies of the resonator corresponding to the non-zero M_{ii} can be calculated by equations (3.24) and (3.25).

After calculating these parameters, the dimensions of the filter structure in Figure 4.52 can be determined to obtain the desired filtering responses. The design processes can be summarized as follows. Firstly, according to the quad-mode DR investigation, the dimensions of the DR and length of the tuning probes are adjusted to meet the values of f_i calculated by equation (3.25). Then, by controlling the length of the feeding probes (L_1) and the gap between feeding probes and DR (G_1), the required external quality factors Q_{ei} calculated by equation (3.24) can be realized. Finally, fine-tuning is performed to obtain good single-channel filtering responses. Figure 4.56(a) shows the calculated responses of matrix (4.16) and the simulated results, which agree well with each other and high CM suppression is obtained. Moreover, from the topology in Figure 4.55, it is known that the bandwidth of the passband can be adjusted by spacing the frequency between the M2' mode and M3' mode (eg, changing the value of h or D). Figure 4.56(b) shows the simulated results, which verifies that the proposed method can be used to design the filter with different bandwidths. Thus, a single-channel balanced filter is realized.

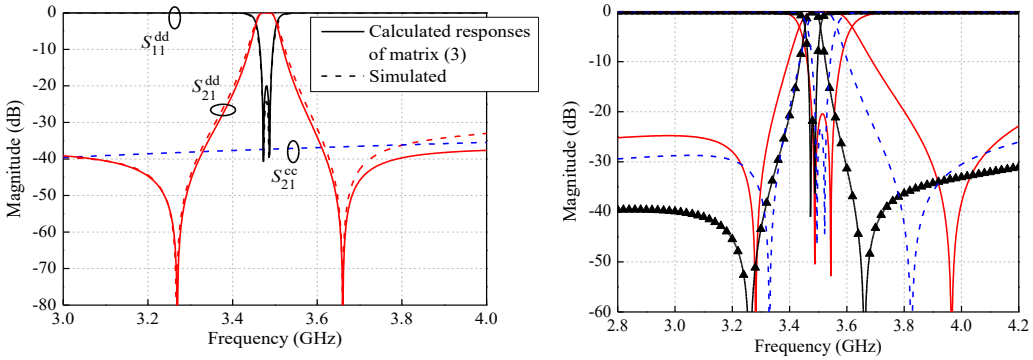

Figure 4.56. (a) Calculated responses of matrix (3) and simulated results of the single-channel balanced filter; (b) Simulated results with different bandwidths.

4.5.2.4 Analysis of Dual-Channel Balanced Filter

On the basis of the above single-channel balanced filter, the other two pairs of the differential feeding probes (ports 3-3' and port 4-4') are added at the orthogonal angle of the original feeding probes (ports 1-1' and ports 2-2') to construct the dual-channel balanced filter, as shown in Figure 4.48. According to the analysis of the single-channel balanced filter in Section III-C, it can be inferred that the differential pairs 3-3' and 4-4' only excite the M2" and M3" modes of the quad-mode DR. Figure 4.57 shows the top view of the EM-field distribution of DR and the feeding probes. Here, the four modes of the quad-mode DR are divided into two sets for two channels, namely, SET1 (M2' and M3' modes) for Channel 1 (ports 1-1' and 2-2') and SET 2 (M2" and M3" modes) for Channel 2 (ports 3-3' and 4-4'). The feeding probes of one channel do not excite the modes of the other channel. Hence, signals cannot be transmitted between the two channels, resulting in good isolation.

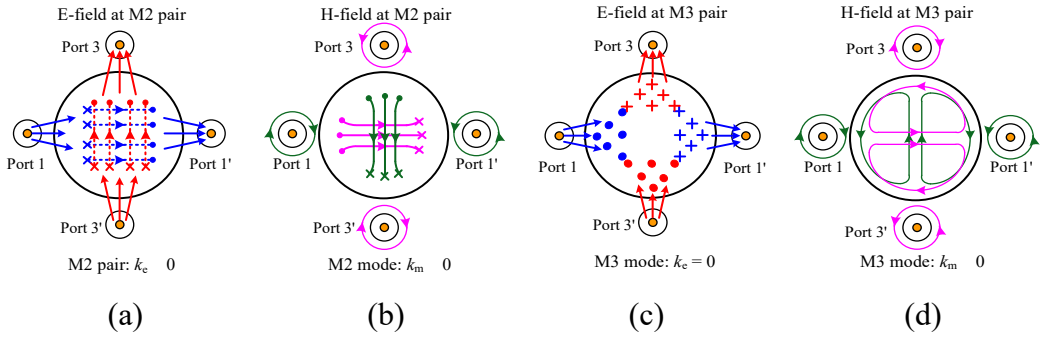

Figure 4.57. Top view of EM-field distributions of DR and the feeding probes.

Figure 4.58 shows the simulated isolation between the two channels. Within the passband, simulated isolation is better than 50 dB. Since the whole structure of the dual-channel balanced filter is symmetric, the two channels have the same balanced filtering responses.

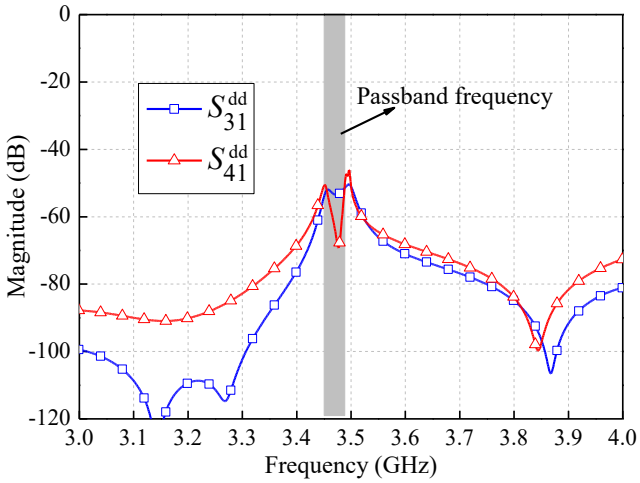

Figure 4.58. Simulated DM isolation between two channels.

When fabricating the circuit, the fabrication errors, such as the size of the metallic cavity, may exist, which would have a slight influence on the circuit performance. To solve this problem, the length of the tuning probes (t) can be adjusted for fine-tuning of the filtering responses, as shown in Figure 4.59. Accordingly, a dual-channel balanced filter can be realized with good performance.

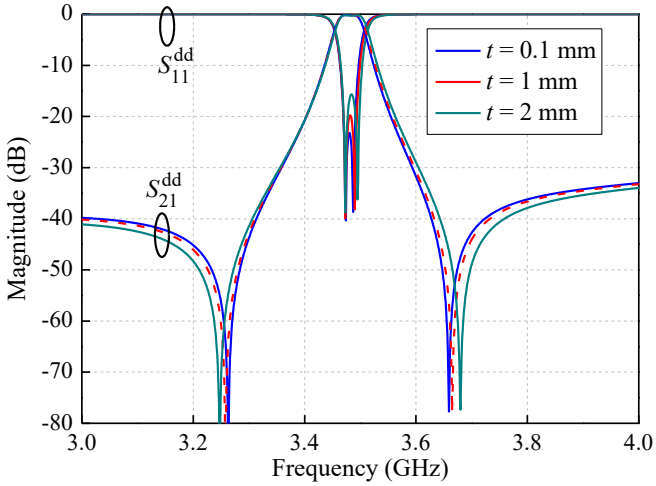

Figure 4.59. Simulated results of the filter with different values of t.

4.5.2.5 Experiment

Based on the above design method, a dual-channel balanced filter using quad-mode DR is implemented. The dielectric material is from Jiangsu Jiang Jia Electronics Co. Ltd in Jiangsu China, with the operating temperature range from -40 ºC to 85 ºC. The dimensions are chosen as follows (all in mm): d = 11.6, h = 13.9, D = 25.2, H = 13.9, L_1 = 5.4, G_1 = 0.4, t_1 = 0.5. The photograph of the fabricated circuit is shown in Figure 4.60. The dual-channel balanced filter housing with a compact size of 25.2 × 25.2 × 13.9 mm^3 (or 0.292 × 0.292 × 0.161 λ_g^3, where λ_g is the wavelength in free space at the operating frequency) is made of aluminum.

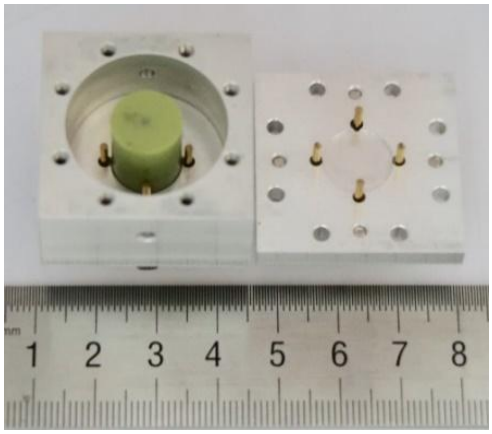

Figure 4.60. Photograph of the fabricated dual-channel balanced filter.

The simulation is carried out by using the solution type of “Terminal” in the EM software High Frequency Structure Simulator (HFSS). The Ports 1-1', Ports 2-2', Ports 3-3' as well as Ports 4-4' are pointed as differential pairs. The measurement is accomplished by using the 4-terminal Keysight E5071C network analyzer. In measurement, four ports of the circuit (eg, ports 1, 1', 2 and 2') are connected to the terminals of the network analyzer, while other four ports are connected by the 50-Ω loads. By using the “balun analysis” function in the network analyzer, the DM and CM responses can be obtained. Figure 4.61 shows the simulated and measured results. Due to the symmetric circuit structure, the two channels have almost the same responses, as shown in Figure 4.61(a). The measured DM passband is

centered at 3.48 GHz. The return loss is better than 15 dB and 3-dB FBW is 1.6%. The measured minimum insertion loss is 0.43 dB, which is a bit higher than the simulated one of 0.2 dB. It is due to the loss in the SMA connectors and the loss in the aluminum wall. The measured Q factor is around 1990. Two transmission zeros are generated at 3.265 and 3.663 GHz, which enhance the skirt selectivity. A spurious band is located at 4.6 GHz, which is away from the passband frequency, as shown in Figure 4.61(b). In Figure 4.61(c), the CM suppression is better than 35 dB within the DM passband. The measured DM and CM isolation between two channels are better than 45 and 36 dB, respectively. In conclusion, the proposed dual-channel balanced filter features good balanced filtering responses of each channel and high isolation between the two channels.

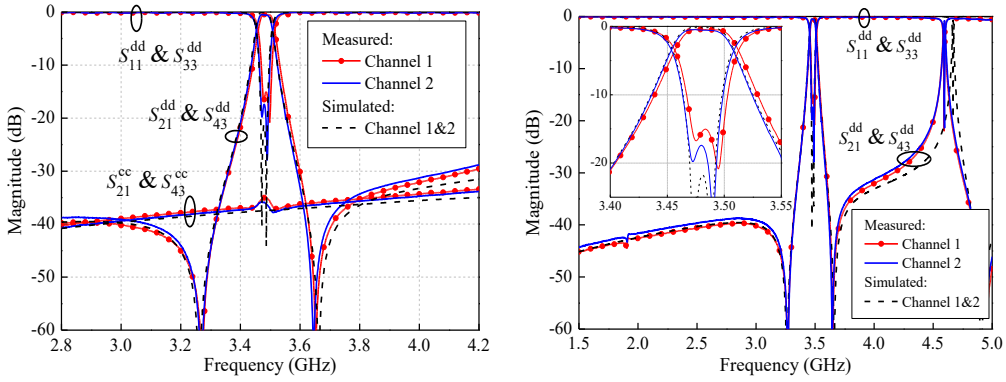

(a) (b)

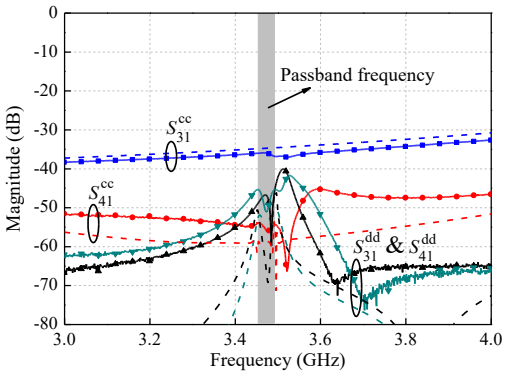

(c)

Figure 4.61. Simulated and measured results (a) Transmission and reflection coefficient for 2.8 to 4.2 GHz; (b) DM responses in a wide frequency range and around the passband; (c) DM and CM isolation between two channels.

4.5.3 Dual-Channel Balun Filter

4.5.3.1 Design of Dual-Channel Balun Filter

As presented earlier, a method for designing the dual-channel balanced filter using the quad-mode DR is proposed and the circuit is implemented with good performance. For further verifying the proposed concept, a dual-channel balun filter is designed based on the above dual-channel balanced filter.

It is known that the balun filter can be realized by replacing one differential pair in the balanced filter with a single-end port. Hence, the design processes of the dual-channel balun filter can be detailed as follows. Firstly, one differential pair of each channel (ports 1-1' and 3-3') in the proposed dual-channel balanced filter is substituted by the single-end feeding probes (ports 5 and 6) to construct the dual-channel balun filter with the schematic shown in Figure 4.62(a). The corresponding 3-D structure is shown in Figure 4.62(b). Secondly, to obtain the desired filtering responses, external quality factors of the single-end ports 5 and 6 ($Qs\ e$) should be equal to that of differential ports 1-1' and 3-3' in the dual-channel balanced filter, while the other parameters are kept unaltered. Thus, the length of the single-end feeding probes (L_2) as well as the gap between the DR and the single-end feeding probes (G_2) are adjusted to meet this requirement. Other dimensions of the structure are kept the same as that of the proposed dual-channel balanced filter. Finally, fine-tuning of the circuit is needed to realize good performance.

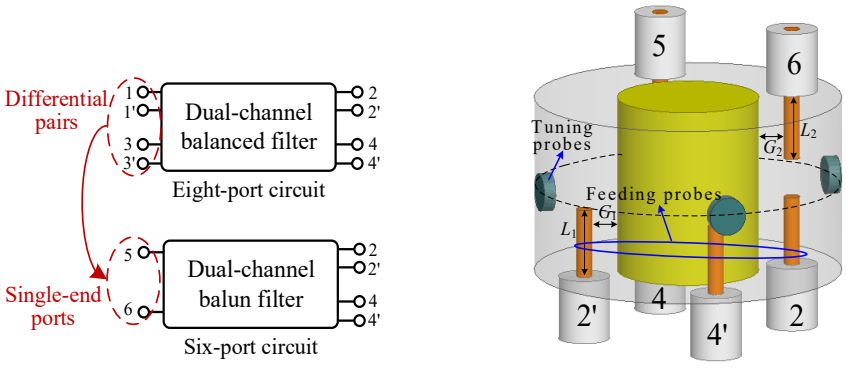

(a) (b)

Figure 4.62. Dual-channel balun filter (a) Schematic; (b) 3-D structure.

As for the isolation between the two channels, it is similar to that of the proposed dual-channel balanced filter. The feeding probes of the two channels are located at the orthogonal angle of each other and thus the feeding probes of one channel do not excite the modes for the other channel. Accordingly, the dual-channel balun filter with high isolation between two channels is realized.

4.5.3.2 Experiment

For demonstration, a dual-channel balun filter is fabricated. The parameters of the single-end feeding probes are given as follows (all in mm): $L_2 = 6.4$, $G_2 = 0.25$. The other dimensions of the circuit are the same as those of the proposed dual-channel balanced filter. Figure 4.63 shows a photograph of the fabricated dual-channel balun filter, which has the same size as that of the proposed dual-channel balanced filter.

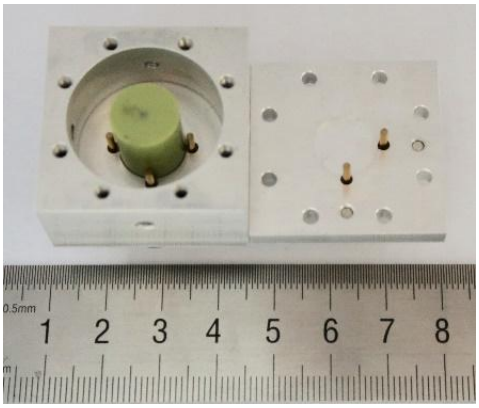

Figure 4.63. Photograph of the fabricated dual-channel balun filter.

Figure 4.64 shows the simulated and measured results, where the responses of the two channels agree well with each other. In Figure 4.64(a), the measured passband is centered at 3.485 GHz with the 3-dB FBW of 1.9 %. The measured return loss is better than 15 dB. The miniaturized insertion losses including the 3-dB equal power division loss are (3 + 0.38) dB and (3 + 0.41) dB. The measured Q factor is around 1940. In Figure 4.64(b), the lower and upper spurious bands are measured at 1.9

GHz and 4.6 GHz, respectively, which are far from the passband frequency. The measured in-band amplitude imbalances of the two channels are less than 0.15 dB and the phase difference between the two output ports of each channel is 180º ± 2º, as shown in Figure 4.64(c), featuring a good amplitude balance and 180º phase difference. In Figure 4.64(d), the measured in-band isolation between ports 5 and 6 is better than 25 dB, while that between ports 5 and 4 (or 4') is better than 32 dB, and that between ports 4 and 2 (or 2') is better than 38 dB, showing high isolation between the two channels.

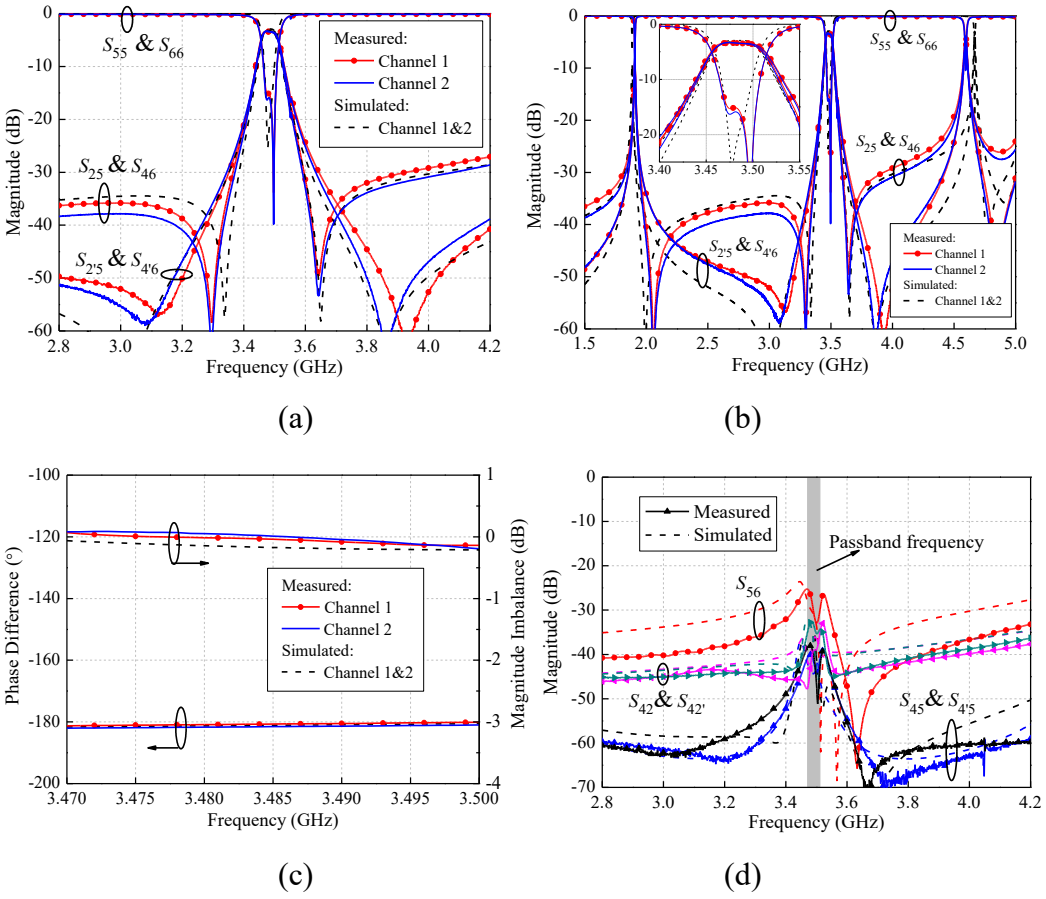

Figure 4.64. Simulated and measured results (a) Transmission and refection coefficient from 2.8 to 4.2 GHz; (b) Transmission and refection coefficient in a wide frequency range and around the passband; (c) Phase difference and magnitude imbalance; (d) Isolation.

4.5.4 Comparison

Table 4.3 tabulates the comparison with some other DR-based balanced and balun filters. In [51] and [141], narrow-band DR-based balanced and balun filters are designed with low losses. However, the ring-shaped and rectangular DRs in these designs function as single-mode DRs, which occupy a larger circuit size as compared to the presented quad-mode DR. In [53], cross-shaped DRs are utilized to construct balanced and balun filters with a size reduction. Nevertheless, the proposed dual-channel balanced and balun filters still exhibit a more compact size. Moreover, it should be noted that the proposed designs integrate two balanced or balun filters while those in [51], [53] and [141] are single-channel designs. Hence, it can be concluded that the proposed dual-channel balanced and balun filters feature a significant size reduction and high integration.

Table 4.3 Comparison With Some Other Balanced and Balun Filters

Ref.	Filter type	3-dB FBW (%)	IL (dB)	NR	Size (λ_g^3)	Techniques
[51]	Balanced	0.32	0.55	2	0.692 × 0.400 × 0.182	DR
[53]	Balanced	1.3	0.8	1	0.267 × 0.267 × 0.315	DR
	Balun	1.3	0.6	1	0.267 × 0.267 × 0.315	DR
[141]	Balun	1.3	0.55	2	0.554 × 0.268 × 0.187	DR
This work	Dual-channel balanced	1.6	0.43	1	0.292 × 0.292 × 0.161	DR
	Dual-channel balun	1.9	0.41	1	0.292 × 0.292 × 0.161	DR

4.6 Conclusions

In order to realize the compact size and high integration for wireless systems, multiple filters or filtering circuits with the same performance have been integrated as one dual-/multi-channel filter or filtering circuit in this chapter. Firstly, a dual-channel filter has been presented, which consists of two filters. By analyzing the EM-field properties of the quad-mode DR and properly arranging the feeding

probes, two of the resonant modes of the DR can be excited for one channel and other two modes are excited for the other channel. Thus, two filtering networks are formed without influence on each other, resulting in high isolation between the two channels. Moreover, the proposed dual-channel filter has also been co-designed with a two-input two-output Doherty power amplifier, achieving high efficiency and high integration. Secondly, by using tri-mode DRs, a large number of filters have been co-designed as a multi-channel filter. The filter orders and the number of filter channels of the proposed multi-channel filter can be extended easily to meet different applications. Thirdly, two multi-functional balanced filters/balun filters have also been designed into the single-cavity-configuration dual-channel circuits, which can further reduce the size. By using the proposed dual- or multi-channel filtering circuits to replace several circuits in wireless systems, the number of circuits in the system can be greatly reduced, which would be useful for realizing miniaturized and high-integration wireless systems.

Chapter 5 Conclusions and Future Works

5.1 Conclusions

With the rapid development of wireless systems, microwave circuits are required to have a compact size and low power consumption. A lot of researches has been conducted to design microwave circuits and significant progress has been made. It is difficult to make further breakthroughs of miniaturization and low power consumption in the design of single-functional circuits under the current technological conditions. Therefore, co-designs of multiple circuits are proposed to integrate multiple circuits into a multi-functional circuit, which can reduce the size, reduce the loss or improve the efficiency by reducing the redundancy. This is of great significance for the development of wireless systems and the realization of green and energy-saving communication.

Relevant research has also been carried out previously. This thesis has summarized it and found that most co-designs are realized mainly based on planar PCB technology. The advantages in terms of size reduction in some reported designs are not obvious comparing to the cascaded designs. Also, the narrowband base station applications could not be satisfied due to the Q factor limitation and low power handling capability. In addition, most reported co-designs mainly integrate the two devices together to realize the two circuit functions, but the performance of the two circuits has not been improved. To solve these problems, this thesis studied the active and passive multi-function filtering circuits based on the co-design method using LTCC and DR techniques, which mainly includes the following contents.

Co-designs of filters and active circuits have been studied in **Chapter 2** for the purpose of improving the overall efficiency of power amplifier, switch, and filter. Filter switches have been designed based on LTCC and DR techniques. Compared with conventional cascaded designs, the loss in the ON-state is reduced and the

isolation in the OFF-state is improved. Then, to avoid the impedance mismatch between the power amplifier and filter and simplify the circuit structure, a DR filter with cross coupling and a power amplifier have been co-designed, where good filtering responses and high efficiency have been obtained.

Co-designs of filters and passive circuits have been conducted in **Chapter 3**. Miniaturized filtering balun and diplexer have been designed using multilayer LTCC structures with good circuit performance, which also have the advantages of simple structure and small size. Besides, a filtering rat-race coupler based on a quad-mode DR has been implemented with a single-cavity configuration. Compared to reported designs, the circuit size and insertion loss of the proposed multi-functional passive filtering circuits are effectively reduced.

Dual-/multi-channel active and passive filtering circuits have been presented in **Chapter 4**. Two or more filters/filtering circuits have been co-designed as one circuit to realize miniaturization and high integration. Firstly, a dual-channel filter has been proposed, which has also integrated with a two-input two-output Doherty power amplifier to achieve high integration and high efficiency. Then, multi-channel DR filters have been designed, showing the advantages of flexible expansion of the channel number and filter orders. Finally, two multi-functional balanced filters and balun filters are integrated together to form a highly integrated dual-channel balanced filter and balun filter, respectively. The proposed dual/multi-channel filtering circuits have achieved good circuit performance of each channel and high isolation between channels.

5.2 Future Works

According to the trend of the development of wireless communication, some works related to this thesis may be worthy of investigation.

For the first future work, the collaborative design techniques proposed in this

thesis on the LTCC and DR circuit designs can be applied to the integrated circuits and systems to improve the overall efficiency and reduce the size. For the wireless systems on chip (using CMOS, GaN or SiGe IC technology), it also includes a lot of circuits, such as the power amplifier, switch, low noise amplifier, mixer and so on. The IC technology has the characteristics of high integration, but the circuit losses are generally high which make it very difficult to realize a high efficiency of the whole system. The proposed collaborative-design techniques for active and passive multi-functional filtering circuits can be extended to the IC designs to reduce the loss and simplify the circuit structures, which would be helpful to improve the efficiency or reduce the noise fugure.

An example for the future work on IC designs using the collaborative design technique is detailed as follows. Figure 5.1 shows the schematic of a radio frequency (RF) front end in a time division duplexer (TDD) sub-system. It includes a SPDT switch, a power amplifier, and a low noise amplifier. In conventional solutions, the three circuits are independently designed with 50-Ω terminals and then they are cascaded in the system. Here, input and ouput matching networks (IMN and OMN) are needed in the power amplifier and low noise amplifier. By using the collaborative design technique, the SPDT switch can be designed with the impedance conversion function. Thus, the impedances desired by the transistors of the power amplifier and low noise amplifier can be directly matched to the SPDT switch. In this case, the OMN of the power amplifier and IMN of the low noise amplifier can be eliminated, and thus their losses are eliminated. Accordingly, the performance of the efficiency of the transmitter and noise figure of the receiver can be improved. Moreover, the system structure can also be simplified and size can be reduced.

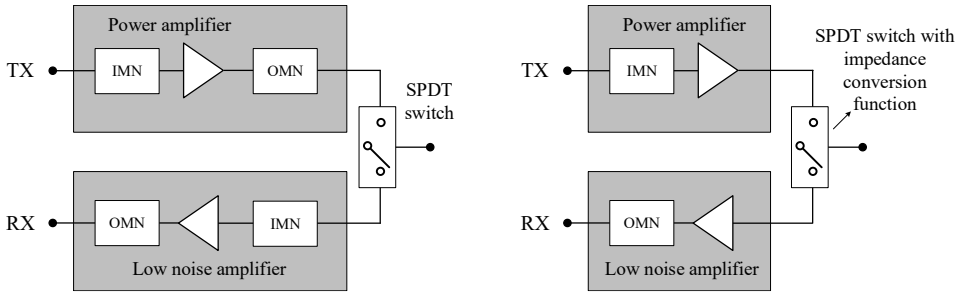

Figure 5.1. Schematic of an RF front end in IC technology (a) conventional solution; (b) collaborative-design solution.

For the second future work, it is the design of millimeter-wave (MMW) or terahertz multi-functional filtering circuits. In this thesis, the circuits are designed on the microwave frequency below 6 GHz. With the development of wireless technology, MMW and terahertz circuits play important roles in future wireless communications. The collaborative design techniques can also be extended to design the MMW or terahertz multifunction circuits, which may have a good application prospect in the future wireless communication.

Reference

[1]. Sheikhi A, Alipour A, Mir A. Design and Fabrication of an Ultra-Wide Stopband Compact Bandpass Filter[J]. IEEE Transactions on Circuits and Systems II: Express Briefs, 2019, 67(2): 265-269.

[2]. Liang G Z, Chen F C. A compact dual-wideband bandpass filter based on open-/short-circuited stubs[J]. IEEE Access, 2020, 8: 20488-20492.

[3]. Guo Q Y, Zhang X Y, Gao L, et al. Microwave and millimeter-wave LTCC filters using discriminating coupling for mode suppression[J]. IEEE Transactions on Components, Packaging and Manufacturing Technology, 2016, 6(2): 272-281.

[4]. Zhu Y Y, Li Y L, Chen J X. A novel dielectric strip resonator filter[J]. IEEE Microwave and Wireless Components Letters, 2018, 28(7): 591-593.

[5]. Zhang R, Mansour R R. Low-cost dielectric-resonator filters with improved spurious performance[J]. IEEE transactions on microwave theory and techniques, 2007, 55(10): 2168-2175.

[6]. Mansour R R. Filter technologies for wireless base stations[J]. IEEE Microwave Magazine, 2004, 5(1): 68-74.

[7]. Hosseinzadeh N, Medi A. Wideband 5 W Ka-band GaAs power amplifier[J]. IEEE Microwave and Wireless Components Letters, 2016, 26(8): 622-624.

[8]. Chen Y C, Lin Y H, Lin J L, Wang H. A Ka-Band Transformer-Based Doherty Power Amplifier for Multi-Gb/s Application in 90-nm CMOS[J]. IEEE Microwave and Wireless Components Letters, 2018, 28(12):1134-1136.

[9]. Sharma T, Darraji R, Ghannouchi F, Dawar N. Generalized continuous class-F harmonic tuned power amplifiers[J]. IEEE Microwave and Wireless Components Letters, 2016, 26(3): 213-215.

[10]. Siamak F, Mansour R R. Capacitive RF MEMS switches fabricated in

standard 0.35 μm CMOS technology[J]. IEEE Transact Microw Theory Tech, 2010, 58(2): 478-486.

[11]. Pal J, Zhu Y, Lu J, et al. High power and reliable SPST/SP3T RF MEMS switches for wireless applications[J]. IEEE Electron Device Letters, 2016, 37(9): 1219-1222.

[12]. Zhang X Y, Chen J X, Xue Q, et al. Dual-band bandpass filters using stub-loaded resonators[J]. IEEE Microwave and Wireless Components Letters, 2007, 17(8): 583-585.

[13]. Wang Y, Yu M. True inline cross-coupled coaxial cavity filters[J]. IEEE Transactions on Microwave Theory and Techniques, 2009, 57(12): 2958-2965.

[14]. Yassini B, Yu M. Ka-band dual-mode super *Q* filters and multiplexers[J]. IEEE Transactions on Microwave Theory and Techniques, 2015, 63(10): 3391-3397.

[15]. Lugo C, Papapolymerou J. Electronic switchable bandpass filter using PIN diodes for wireless low cost system-on-a-package applications[J]. IEE Proceedings-Microwaves, Antennas and Propagation, 2004, 151(6): 497-502.

[16]. Tu W H. Switchable microstrip bandpass filters with reconfigurable on-state frequency responses[J]. IEEE Microwave and Wireless Components Letters, 2010, 20(5): 259-261.

[17]. Chao S F, Lin W C. High-isolation switchable bandpass filter using connected-coupling line[J]. Electronics Letters, 2013, 49(16): 1004-1005.

[18]. Chao S F, Wu C H, Tsai Z M, et al. Electronically switchable bandpass filters using loaded stepped-impedance resonators[J]. IEEE transactions on microwave theory and techniques, 2006, 54(12): 4193-4201.

[19]. Lin Y S, Chang P Y, Hsieh Y S. Compact electronically switchable parallel-coupled microstrip bandpass filter with wide stopband[J]. IEEE Microwave and Wireless Components Letters, 2008, 18(4): 254-256.

[20]. Deng P H, Jheng J H. A switched reconfigurable high-isolation dual-band bandpass filter[J]. IEEE Microwave and Wireless Components Letters, 2011, 21(2): 71-73.

[21]. Dai G L, Xia M Y. Design of compact dual-band switchable bandpass filter[J]. Electronics letters, 2009, 45(10): 506-507.

[22]. Chen C S, Wu J F, Lin Y S. Compact single-pole-double-throw switchable bandpass filter based on multicoupled line[J]. IEEE Microwave and Wireless Components Letters, 2014, 24(2): 87-89.

[23]. Chao S F, Kuo C C, Tsai Z M, et al. 40-GHz MMIC SPDT and multiple-port bandpass filter-integrated switches[J]. IEEE Transactions on Microwave Theory and Techniques, 2007, 55(12): 2691-2699.

[24]. Chen C C, Wang S M. Design of an LTCC switchable filter for dual-band RF front-end applications[C]. TENCON 2007-2007 IEEE Region 10 Conference. IEEE, 2007: 1-3.

[25]. Chen S, Xue Q. A class-F power amplifier with CMRC[J]. IEEE Microwave and Wireless components letters, 2010, 21(1): 31-33.

[26]. Wang Z, Gao S, Nasri F, et al. High power added efficiency power amplifier with harmonic controlled by UWB filter with notched band at 6.42 GHz[C] WAMICON 2011 Conference Proceedings. IEEE, 2011: 1-4.

[27]. Chen K, Peroulis D. Design of highly efficient broadband class-E power amplifier using synthesized low-pass matching networks[J]. IEEE Transactions on Microwave Theory and Techniques, 2011, 59(12): 3162-3173.

[28]. Li Y C, Wu K C, Xue Q. Power amplifier integrated with bandpass filter for long term evolution application[J]. IEEE Microwave and Wireless Components Letters, 2013, 23(8): 424-426.

[29]. Gao L, Zhang X Y, Chen S, et al. Compact power amplifier with bandpass response and high efficiency[J]. IEEE Microwave and Wireless Components

Letters, 2014, 24(10): 707-709.

[30]. Chen K, Lee T C, Peroulis D. Co-design of multi-band high-efficiency power amplifier and three-pole high-Q tunable filter[J]. IEEE Microwave and Wireless Components Letters, 2013, 23(12): 647-649.

[31]. Guo Q Y, Zhang X Y, Xu J X, et al. Bandpass class-F power amplifier based on multifunction hybrid cavity–microstrip filter[J]. IEEE Transactions on Circuits and Systems II: Express Briefs, 2016, 64(7): 742-746.

[32]. Chen K, Lee J, Chappell W J, et al. Co-design of highly efficient power amplifier and high-Q output bandpass filter[J]. IEEE Transactions on Microwave Theory and Techniques, 2013, 61(11): 3940-3950.

[33]. Zheng S Y, Liu Z W, Pan Y M, et al. Bandpass filtering Doherty power amplifier with enhanced efficiency and wideband harmonic suppression[J]. IEEE Transactions on Circuits and Systems I: Regular Papers, 2016, 63(3): 337-346.

[34]. Li Y C, Xue Q, Zhang X Y. Single-and dual-band power dividers integrated with bandpass filters[J]. IEEE Transactions on Microwave Theory and Techniques, 2012, 61(1): 69-76.

[35]. Chau W M, Hsu K W, Tu W H. Filter-based Wilkinson power divider[J]. IEEE Microwave and Wireless Components Letters, 2014, 24(4): 239-241.

[36]. Deng P H, Chen Y T. New Wilkinson power dividers and their integration applications to four-way and filtering dividers[J]. IEEE Transactions on Components, Packaging and Manufacturing Technology, 2014, 4(11): 1828-1837.

[37]. Liu H W, Shi Z, Boutejdar A, et al. Harmonics suppression of Wilkinson power divider using spurlines with adjustable rejection bands[J]. Microwave and Optical Technology Letters, 2008, 50(3): 601-604.

[38]. Psychogiou D, Gómez-García R, Guyette A C, et al. Reconfigurable single/multi-band filtering power divider based on quasi-bandpass

sections[J]. IEEE Microwave and Wireless Components Letters, 2016, 26(9): 684-686.

[39]. Gao L, Zhang X Y, Xue Q. Compact tunable filtering power divider with constant absolute bandwidth[J]. IEEE Transactions on Microwave Theory and Techniques, 2015, 63(10): 3505-3513.

[40]. Yeung L K, Wu K L. A dual-band coupled-line balun filter[J]. IEEE Transactions on Microwave Theory and Techniques, 2007, 55(11): 2406-2411.

[41]. Jung E Y, Hwang H Y. A balun-BPF using a dual mode ring resonator[J]. IEEE Microwave and Wireless Components Letters, 2007, 17(9): 652-654.

[42]. Yang T, Tamura M, Itoh T. Compact hybrid resonator with series and shunt resonances used in miniaturized filters and balun filters[J]. IEEE Transactions on microwave Theory and Techniques, 2010, 58(2): 390-402.

[43]. Sun S, Menzel W. Novel dual-mode balun bandpass filters using single cross-slotted patch resonator[J]. IEEE Microwave and Wireless Components Letters, 2011, 21(8): 415-417.

[44]. Wu L S, Guo Y X, Mao J F, et al. Design of a substrate integrated waveguide balun filter based on three-port coupled-resonator circuit model[J]. IEEE Microwave and Wireless Components Letters, 2011, 21(5): 252-254.

[45]. Yeung L K, Wu K L. An LTCC balanced-to-unbalanced extracted-pole bandpass filter with complex load[J]. IEEE transactions on microwave theory and techniques, 2006, 54(4): 1512-1518.

[46]. Huang G S, Wu C H, Chen C H. LTCC balun bandpass filters using dual-response resonators[J]. IEEE Microwave and Wireless Components Letters, 2011, 21(9): 483-485.

[47]. Tamura M, Yang T, Itoh T. Very compact and low-profile LTCC unbalanced-to-balanced filters with hybrid resonators[J]. IEEE Transactions on Microwave Theory and Techniques, 2011, 59(8): 1925-1936.

[48]. Feng W, Che W, Xue Q. Balanced filters with wideband common mode suppression using dual-mode ring resonators[J]. IEEE Transactions on Circuits and Systems I: Regular Papers, 2015, 62(6): 1499-1507.

[49]. Wei F, Guo Y J, Qin P Y, et al. Compact balanced dual-and tri-band bandpass filters based on stub loaded resonators[J]. IEEE Microwave and Wireless Components Letters, 2014, 25(2): 76-78.

[50]. Guo X, Zhu L, Wu W. A New Concept of Partial Electric/Magnetic Walls for Application in Design of Balanced Bandpass Filters[J]. IEEE Transactions on Microwave Theory and Techniques, 2019, 67(4): 1308-1315.

[51]. Chen J X, Zhan Y, Qin W, et al. Analysis and design of balanced dielectric resonator bandpass filters[J]. IEEE Transactions on Microwave Theory and Techniques, 2016, 64(5): 1476-1483.

[52]. Chen J X, Zhan Y, Qin W, et al. Novel narrow-band balanced bandpass filter using rectangular dielectric resonator[J]. IEEE Microwave and Wireless Components Letters, 2015, 25(5): 289-291.

[53]. Chen J X, Li J, Zhan Y, et al. Design of balanced and balun filters using dual-mode cross-shaped dielectric resonators[J]. IEEE Transactions on Microwave Theory and Techniques, 2016, 65(4): 1226-1234.

[54]. Wang K X, Zhang X Y, Zheng S Y, et al. Compact filtering rat-race hybrid with wide stopband[J]. IEEE Transactions on Microwave Theory and Techniques, 2015, 63(8): 2550-2560.

[55]. Lin F, Chu Q X, Wong S W. Design of dual-band filtering quadrature coupler using $\lambda/2$ and $\lambda/4$ resonators[J]. IEEE Microwave and Wireless Components Letters, 2012, 22(11): 565-567.

[56]. Hagag M F, Khater M A, Sinanis M D, et al. Ultra-compact tunable filtering rat-race coupler based on half-mode siw evanescent-mode cavity resonators[J]. IEEE Transactions on Microwave Theory and Techniques, 2018, 66(12): 5563-5572.

[57]. Wang K X, Liu X F, Li Y C, et al. LTCC filtering rat-race coupler based on eight-line spatially-symmetrical coupled structure[J]. IEEE Access, 2017, 6: 262-269.

[58]. Shi J, Qiang J, Xu K, et al. A balanced filtering branch-line coupler[J]. IEEE Microwave and Wireless Components Letters, 2016, 26(2): 119-121.

[59]. Uchida H, Yoneda N, Konishi Y, et al. Bandpass directional couplers with electromagnetically-coupled resonators[C]. 2006 IEEE MTT-S International Microwave Symposium Digest. IEEE, 2006: 1563-1566.

[60]. Jiao L, Wu Y, Liu Y, et al. Concept for narrow-band filtering rat-race coupler using dual-mode cross-shaped dielectric[J]. Electronics Letters, 2015, 52(3): 212-213.

[61]. Srisathit S, Patisang S, Phromloungsri R, et al. High isolation and compact size microstrip hairpin diplexer[J]. IEEE Microwave and Wireless Components Letters, 2005, 15(2): 101-103.

[62]. Xiao J K, Zhu M, Li Y, et al. High selective microstrip bandpass filter and diplexer with mixed electromagnetic coupling[J]. IEEE Microwave and Wireless Components Letters, 2015, 25(12): 781-783.

[63]. Peng H S, Chiang Y C. Microstrip diplexer constructed with new types of dual-mode ring filters[J]. IEEE Microwave and Wireless Components Letters, 2014, 25(1): 7-9.

[64]. Chuang M L, Wu M T. Microstrip diplexer design using common T-shaped resonator[J]. IEEE Microwave and Wireless components letters, 2011, 21(11): 583-585.

[65]. Guan X, Yang F, Liu H, et al. Compact and high-isolation diplexer using dual-mode stub-loaded resonators[J]. IEEE microwave and wireless components letters, 2014, 24(6): 385-387.

[66]. Xiao J K, Zhang M, Ma J G. A Compact and High-Isolated Multiresonator-Coupled Diplexer[J]. IEEE Microwave and Wireless Components Letters,

2018, 28(11): 999-1001.

[67]. Brito-Brito Z, Llamas-Garro I, Navarro-Muñoz G, et al. Precise frequency and bandwidth control of switchable microstrip bandpass filters using diode and microelectro-mechanical system technologies[J]. IET microwaves, antennas & propagation, 2012, 6(6): 713-719.

[68]. Brito-Brito Z, Llamas-Garro I, Navarro-Munoz G, et al. Switchable bandpass filter for WiFi–UMTS reception standards[J]. Electronics Letters, 2010, 46(13): 930-931.

[69]. Weng S C, Hsu K W, Tu W H. Compact and switchable dual-band bandpass filter with high selectivity and wide stopband[J]. Electronics Letters, 2013, 49(20): 1275-1277.

[70]. Weng S C, Hsu K W, Tu W H. Independently switchable quad-band bandpass filter[J]. IET Microwaves, Antennas & Propagation, 2013, 7(14): 1113-1119.

[71]. Chuang M L, Wu M T. Switchable dual-band filter with common quarter-wavelength resonators[J]. IEEE Transactions on Circuits and Systems II: Express Briefs, 2015, 62(4): 347-351.

[72]. Guyette A C. Intrinsically switched varactor-tuned filters and filter banks[J]. IEEE Transactions on Microwave Theory and Techniques, 2012, 60(4): 1044-1056.

[73]. Lin Y C, Horng T S, Huang H H. Synthesizing a multiband LTCC bandpass filter with specified transmission-and reflection-zero frequencies[J]. IEEE Transactions on Microwave Theory and Techniques, 2014, 62(12): 3351-3361.

[74]. Chen J X, Zhan Y, Xue Q. Novel LTCC distributed-element wideband bandpass filter based on the dual-mode stepped-impedance resonator[J]. IEEE Transactions on Components, Packaging and Manufacturing Technology, 2015, 5(3): 372-380.

[75]. Dai X, Zhang X Y, Kao H L, et al. LTCC bandpass filter with wide stopband

based on electric and magnetic coupling cancellation[J]. IEEE Transactions on Components, Packaging and Manufacturing Technology, 2014, 4(10): 1705-1713.

[76]. Zhang X Y, et al. Compact LTCC bandpass filter with wide stopband using discriminating coupling[J]. IEEE Transactions on Components, Packaging and Manufacturing Technology, 2014, 4(4): 656-663.

[77]. Tsai C L, Lin Y S. Analysis and design of single-to-balanced combline bandpass filters with two independently controllable transmission zeros in LTCC technology[J]. IEEE Transactions on Microwave Theory and Techniques, 2010, 58(11): 2878-2887.

[78]. Zhang G, Wang J, Pan J, et al. Compact 60 GHz LTCC balun bandpass filter with two transmission zeroes[J]. Electronics letters, 2015, 51(8): 637-638.

[79]. Cameron R J. General coupling matrix synthesis methods for Chebyshev filtering functions[J]. IEEE Transactions on Microwave Theory and Techniques, 1999, 47(4): 433-442.

[80]. Pozar D M. Microwave engineering[M]. John Wiley & Sons, 2009.

[81]. Hong J S G, Lancaster M J. Microstrip filters for RF/microwave applications[M]. John Wiley & Sons, 2004.

[82]. Skyworks Solutions, Inc. SKY13370-374LF: 0.5 to 6.0 GHz SPDT Switch, 50 Ω Terminated[Datasheet]. http://www.skyworksinc.com/uploads/documents/SKY13370_374LF _201408G.pdf, Jan. 15, 2018.

[83]. RF Micro Devices, Inc. RFSW6223: 10-6000 MHz Symmetric DPDT Switch[Datasheet], http://www.qorvo.com/products/p/RFSW6223, Mar. 19, 2012.

[84]. Tomassoni C, Bastioli S, Snyder R V. Compact mixed-mode filter based on TE_{101} cavity mode and $TE_{01\delta}$ dielectric mode[J]. IEEE Transactions on Microwave Theory and Techniques, 2016, 64(12): 4434-4443.

[85]. Zhang R, Mansour R R. Dual-band dielectric-resonator filters[J]. IEEE Transactions on Microwave Theory and Techniques, 2009, 57(7): 1760-1766.

[86]. Memarian M, Mansour R R. Quad-mode and dual-mode dielectric resonator filters[J]. IEEE transactions on microwave theory and techniques, 2009, 57(12): 3418-3426.

[87]. Zhang Z C, Chu Q X, Wong S W, et al. Triple-mode dielectric-loaded cylindrical cavity diplexer using novel packaging technique for LTE base-station applications[J]. IEEE Transactions on Components, Packaging and Manufacturing Technology, 2016, 6(3): 383-389.

[88]. Chu Q X, Ouyang X, Wang H, et al. $TE_{01\delta}$-mode dielectric-resonator filters with controllable transmission zeros[J]. IEEE Transactions on Microwave Theory and Techniques, 2013, 61(3): 1086-1094.

[89]. Bastioli S, Snyder R V. Inline pseudoelliptic $TE_{01\delta}$-mode dielectric resonator filters using multiple evanescent modes to selectively bypass orthogonal resonators[J]. IEEE Transactions on Microwave Theory and Techniques, 2012, 60(12): 3988-4001.

[90]. Mini-Circuits, Brooklyn, NY, USA. ZMSW-1111, Coaxial Switch: 50 SPST Pin Diode Reflective 10 to 2500 MHz[Datasheet], http://www.minicircuits. com/pdfs/ZMSW-1111.pdf, Sep. 23, 2016.

[91]. Skyworks Solutions, Inc. SKY13347-360LF: 0.5 to 4.0 GHz SPST Switch, 50 Terminated [Datasheet], http://www.skyworksinc.com/uploads/documents/SKY13347_360LF_201393B. pdf, Nov. 10, 2015.

[92]. Skyworks Solutions, Inc. SKY13446-374LF: 0.1-6.0 GHz GaAs SPDT Switch[Datasheet], http://www.skyworksinc.com/uploads/documents/SKY13446_374LF_201843B.pdf, Mar. 14, 2013.

[93]. RF Micro Devices, Inc. RFSW8000: 2.5V to 5.0V, 5MHz to 6500MHz 10W SPDT Switch [Datasheet], http://www.rfmd.com/store/downloads/dl/file/id/27614/RFSW8000DS.pdf, Oct. 20, 2015.

[94]. Skyworks Solutions, Inc. SKY13348-374LF: 0.5 to 6.0 GHz SPDT Switch, 50 Terminated [Datasheet], http://www.skyworksinc.com/uploads/documents/SKY13348_374LF_201214E. pdf, Nov. 11, 2013

[95]. Analog Devices, Inc. ADGM1304: 0 Hz/DC to 14 GHz, Single-Pole, Four-Throw, MEMS Switch With Integrated Driver[Datasheet], http://www.analog.com/media/en/technical-documentation/data-sheets/adgm 1304.pdf, Oct. 2016.

[96]. Analog Devices, Inc. ADGM1004:0 Hz/DC to 13 GHz, 2.5 kV HBM ESD SP4T, MEMS Switch With Integrated Driver[Datasheet], http://www.analog.com/media/en/technical-documentation/data-sheets/adgm1004.pdf, Jan. 2017.

[97]. Wang C, Zaki K A. Dielectric resonators and filters[J]. IEEE microwave magazine, 2007, 8(5): 115-127.

[98]. Ang K S, Leong Y C, Lee C H. Analysis and design of miniaturized lumped-distributed impedance-transforming baluns[J]. IEEE Transactions on Microwave Theory and Techniques, 2003, 51(3): 1009-1017.

[99]. Zhou L H, Tang H, Chen J X, et al. Tunable filtering balun with enhanced stopband rejection[J]. Electronics letters, 2012, 48(14): 845-847.

[100]. Hui J N, Feng W J, Che W Q. Balun bandpass filter based on multilayer substrate integrated waveguide power divider[J]. Electronics Letters, 2012, 48(10): 571-573.

[101]. Yang T, Tamura M, Itoh T. Compact and high-performance low-temperature co-fired ceramic balun filter using the hybrid resonator and symmetric four-port network[J]. IET microwaves, antennas & propagation, 2012, 6(2): 121-126.

[102]. Tamura M, Ishizaki T, Hoft M. Design and analysis of vertical split ring resonator and its application to unbalanced–balanced filter[J]. IEEE Transactions on Microwave Theory and Techniques, 2009, 58(1): 157-164.

[103]. Tsai W L, Shen T M, Chen B J, et al. Design of single-branch laminated waveguide diplexers using modal orthogonality[J]. IEEE Transactions on Microwave Theory and Techniques, 2013, 61(12): 4079-4089.

[104]. Shang X, Wang Y, Xia W, et al. Novel multiplexer topologies based on all-resonator structures[J]. IEEE Transactions on Microwave Theory and Techniques, 2013, 61(11): 3838-3845.

[105]. Di Palma L, Bilotti F, Toscano A, et al. Design of a waveguide diplexer based on connected bi-omega particles[J]. IEEE Microwave and Wireless Components Letters, 2012, 22(3): 126-128.

[106]. Liu H, Xu W, Zhang Z, et al. Compact diplexer using slotline stepped impedance resonator[J]. IEEE Microwave and Wireless Components Letters, 2013, 23(2): 75-77.

[107]. Yang T, Chi P L, Itoh T. High isolation and compact diplexer using the hybrid resonators[J]. IEEE Microwave and Wireless Components Letters, 2010, 20(10): 551-553.

[108]. Duan Q, Song K, Chen F, et al. Compact wide-stopband diplexer using dual mode resonators[J]. Electronics Letters, 2015, 51(14): 1085-1087.

[109]. Bukuru D, Song K. Compact wide‐stopband planar diplexer based on rectangular dual spiral resonator[J]. Microwave and Optical Technology Letters, 2015, 57(1): 174-178.

[110]. Xue Q, Shi J, Chen J X. Unbalanced-to-balanced and balanced-to-unbalanced diplexer with high selectivity and common-mode suppression[J]. IEEE Transactions on Microwave Theory and Techniques, 2011, 59(11): 2848-2855.

[111]. Weng M H, Wu H W, Shu K. Design of compact microstrip diplexer with simple coupled resonators[J]. Microwave and Optical Technology Letters, 2007, 49(5): 1222-1225.

[112]. Chuang M L, Wu M T. Microstrip multiplexer and switchable diplexer with

joint T-shaped resonators[J]. IEEE Microwave and Wireless Components Letters, 2014, 24(5): 309-311.

[113]. Xue Q, Chen J X. Compact diplexer based on double-sided parallel-strip line[J]. Electronics Letters, 2008, 44(2): 123-124.

[114]. Cheng F, Lin X, Song K, et al. Compact diplexer with high isolation using the dual-mode substrate integrated waveguide resonator[J]. IEEE Microwave and Wireless Components Letters, 2013, 23(9): 459-461.

[115]. Fritz M, Wiesbeck W. A diplexer based on transmission lines, implemented in LTCC[J]. IEEE transactions on advanced packaging, 2006, 29(3): 427-432.

[116]. Tang C W, You S F. Design methodologies of LTCC bandpass filters, diplexer, and triplexer with transmission zeros[J]. IEEE transactions on microwave theory and techniques, 2006, 54(2): 717-723.

[117]. Chu H, Guo Y X, Song Y L, et al. 40/50 GHz diplexer design in LTCC technology[J]. Electronics letters, 2011, 47(4): 260-262.

[118]. Wu Y, Chin K S, Che W, et al. LTCC multilayered helical filters with a mixed electric and magnetic coupling structure[J]. IEEE Transactions on Components, Packaging and Manufacturing Technology, 2015, 5(8): 1050-1059.

[119]. Chin K S, Chang C C, Chen C H, et al. LTCC multilayered substrate-integrated waveguide filter with enhanced frequency selectivity for system-in-package applications[J]. IEEE Transactions on Components, Packaging and Manufacturing Technology, 2014, 4(4): 664-672.

[120]. Gao L, Zhang X Y, Hu B J, et al. Novel multi-stub loaded resonators and their applications to various bandpass filters[J]. IEEE Transactions on Microwave Theory and Techniques, 2014, 62(5): 1162-1172.

[121]. Shen G, Che W, Feng W, et al. Analytical design of compact dual-band filters using dual composite right-/left-handed resonators[J]. IEEE transactions on microwave theory and techniques, 2016, 65(3): 804-814.

[122]. Wong S W, Feng S F, Zhu L, et al. Triple-and quadruple-mode wideband bandpass filter using simple perturbation in single metal cavity[J]. IEEE Transactions on Microwave Theory and Techniques, 2015, 63(10): 3416-3424.

[123]. Zhou K, Zhou C X, Wu W. Substrate-integrated waveguide dual-mode dual-band bandpass filters with widely controllable bandwidth ratios[J]. IEEE Transactions on Microwave Theory and Techniques, 2017, 65(10): 3801-3812.

[124]. Wu Y, Shen J Y, Liu Y, et al. Miniaturized arbitrary phase-difference couplers for arbitrary coupling coefficients[J]. IEEE Transactions on Microwave Theory and Techniques, 2013, 61(6): 2317-2324.

[125]. Wu Y, Sun W, Leung S W, et al. Single-layer microstrip high-directivity coupled-line coupler with tight coupling[J]. IEEE Transactions on Microwave Theory and Techniques, 2013, 61(2): 746-753.

[126]. Lin C K, Chung S J. A Compact Filtering 180^{o} Hybrid[J]. IEEE Transactions on Microwave Theory and Techniques, 2011, 59(12): 3030-3036.

[127]. Wu L S, Xia B, Yin W Y, et al. Collaborative Design of a New Dual-Bandpass 180^{o} Hybrid Coupler[J]. IEEE Transactions on Microwave Theory and Techniques, 2013, 61(3): 1053-1066.

[128]. Shen T M, Huang T Y, Chen C F, et al. A laminated waveguide magic-T with bandpass filter response in multilayer LTCC[J]. IEEE Transactions on Microwave Theory and Techniques, 2011, 59(3): 584-592.

[129]. Lu Y L, Wang Y, Hua C, et al. Design of compact filtering rat-race hybrid with λ/2-resonators[J]. Electronics Letters, 2016, 52(21): 1780-1782.

[130]. Cheng Y J, Fan Y. Compact substrate-integrated waveguide bandpass rat-race coupler and its microwave applications[J]. IET microwaves, antennas & propagation, 2012, 6(9): 1000-1006.

[131]. Mansour R R. High-Q tunable dielectric resonator filters[J]. IEEE microwave magazine, 2009, 10(6): 84-98.

[132]. Xingdong P, Wei H, Tianyang Y, et al. Design and implementation of an active multibeam antenna system with 64 RF channels and 256 antenna elements for massive MIMO application in 5G wireless communications[J]. China communications, 2014, 11(11): 16-23.

[133]. Gao L, Zhang X Y, Xue Q. Miniaturised bandpass filter using novel feeding structure for harmonic suppression[J]. Electronics letters, 2012, 48(22): 1414-1415.

[134]. Chin K S, Chang C C, Chen C H, et al. LTCC multilayered substrate-integrated waveguide filter with enhanced frequency selectivity for system-in-package applications[J]. IEEE Transactions on Components, Packaging and Manufacturing Technology, 2014, 4(4): 664-672.

[135]. Cameron R J, Kudsia C M, Mansour R R. Microwave filters for communication systems: fundamentals, design, and applications[M]. John Wiley & Sons, 2018.

[136]. Wang Y, Yu M. True inline cross-coupled coaxial cavity filters[J]. IEEE Transactions on Microwave Theory and Techniques, 2009, 57(12): 2958-2965.

[137]. Chu Q X, Ouyang X, Wang H, et al. $TE_{01\delta}$-mode dielectric-resonator filters with controllable transmission zeros[J]. IEEE Transactions on Microwave Theory and Techniques, 2013, 61(3): 1086-1094.

[138]. Wang X, Jang G, Lee B, et al. Compact quad-mode bandpass filter using modified coaxial cavity resonator with improved *Q*-factor[J]. IEEE Transactions on Microwave Theory and Techniques, 2015, 63(3): 965-975.

[139]. Chen S, Cheng Z, Wang G, et al. Compact Doherty power amplifier design for 2 × 2 multiple-input multiple-output system[J]. IEEE Microwave and Wireless Components Letters, 2016, 26(3): 216-218.

[140]. Balanis C A. Advanced engineering electromagnetics[M]. John Wiley & Sons, 1999.

[141]. Chen J X, Zhan Y, Qin W, et al. Design of high-performance filtering balun based on $TE_{01\delta}$-mode dielectric resonator[J]. IEEE Transactions on Industrial Electronics, 2016, 64(1): 451-458.

Publications

Journal Papers

[1]. **J.-X. Xu**, H.-Y. Li, X. Y. Zhang, Y. Yang, Q. Xue and E. Dutkiewicz, "Compact dual-channel balanced filter and balun filter based on quad-mode dielectric resonator," *IEEE Trans. Microw. Theory Tech.,* vol. 65, no. 11, pp. 4636-4644, Feb. 2019. **[Chapter 4, Section 4.5]**

[2]. **J.-X. Xu,** X. Y. Zhang, H.-Y. Li, Y. Yang, E. Dutkiewicz and Q. Xue, "Ultra-compact multi-channel bandpass filter based on tri-mode dielectric resonator for 5G massive MIMO antenna system," *IEEE Trans. Microw. Theory Tech.,* vol. 68, no. 5, pp. 1668-1677, May 2020. **[Chapter 4, Section 4.4]**

[3]. **J.-X. Xu**, X. Y. Zhang, H.-Y. Li, and Y. Yang, "Narrow-band single-pole double throw filtering switch based on dielectric resonator," *IEEE Microw. Wireless Compon. Lett.*, vol. 28, no. 7, pp. 594-596, Jul. 2018. **[Chapter 2, Section 2.4]**

[4]. **J.-X. Xu**, L. Yang, Y. Yang, and X. Y. Zhang, "High-*Q*-factor tunable bandpass filter with constant absolute bandwidth and wide tuning range based on coaxial resonators," *IEEE Trans. Microw. Theory Tech.,* vol. 67, no. 10, pp. 4186-4195, Oct. 2019.

[5]. H.-Y. Li, **J.-X. Xu**, Y. Yang, and X. Y. Zhang, "Novel switchable filtering circuit with function reconfigurability between SPQT filtering switch and four-way filtering power divider," *IEEE Transactions on Microwave Theory and Techniques*, vol. 68, no. 3, pp. 867-876, Mar. 2020.

[6]. **J.-X. Xu** and X. Y. Zhang, "Single- and dual-band LTCC filtering witch with high isolation based on coupling control," *IEEE Trans. Ind. Electron.* vol. 64, no. 4, pp. 3137-3146, Apr. 2017. **[Chapter 2, Section 2.3]**

[7]. **J.-X. Xu** and X. Y. Zhang, "Compact high-isolation LTCC diplexer using

common stub-loaded resonator with controllable frequencies and bandwidths," *IEEE Trans. Microw. Theory Tech.,* vol. 67, no. 2, pp. 494-504, Nov. 2017. **[Chapter 3, Section 3.4]**

[8]. **J.-X. Xu** and X. Y. Zhang, "Dual-channel dielectric resonator filter and its application to Doherty power amplifier for 5G massive MIMO system," *IEEE Trans. Microw. Theory Tech.,* vol. 66, no. 7, pp. 3297-3305, Jul. 2018. **[Chapter 4, Section 4.3]**

[9]. **J.-X. Xu**, X. Y. Zhang and H.-Y. Li, "Compact narrow-band filtering rat-race coupler using quad-mode dielectric resonator," *IEEE Trans. Microw. Theory Tech.,* vol. 66, no. 9, pp. 4029-4039, Sep. 2018. **[Chapter 3, Section 3.5]**

[10]. X. Y. Zhang, **J.-X. Xu** and J. X. Chen, "High-power filtering witch with low loss and high isolation based on dielectric resonator," *IEEE Trans. Microw. Theory Tech.,* vol. 65, no. 6, pp. 2101-2110, Jun. 2017. **[Chapter 2, Section 2.4]**

[11]. **J.-X. Xu**, X. Y. Zhang and X. Q. Song, "High-efficiency filter-integrated class-F power amplifier based on dielectric resonator," *IEEE Microw. Wireless Compon. Lett.*, vol. 27, no. 9, pp. 827-829, Sep. 2017. **[Chapter 2, Section 2.5]**

[12]. **J.-X. Xu**, X. Y. Zhang and X. L. Zhao, "Compact LTCC balun with bandpass response based on Marchand balun," *IEEE Microw. Wireless Compon. Lett.*, vol. 26, no. 7, pp. 493-495, Jul. 2016. **[Chapter 3, Section 3.3]**

Conference Papers

[1]. **J.-X. Xu,** X. Y. Zhang and Y. Yang, "High-*Q*-factor dual-band bandpass filter and filtering witch using stub-loaded coaxial resonators," *2019 IEEE*

MTT-S International Wireless Symposium (IWS), Guangzhou, China, 2019, pp. 1-3.

[2]. H.-Y. Li, **J.-X. Xu**, X. Y. Zhang and Y. Yang, "Design of low-loss single-pole single-throw and single-pole double-throw filtering switches using coaxial resonators," *2019 International Conference on Microwave and Millimeter Wave Technology (ICMMT)*, Guangzhou, China, 2019, pp. 1-3.

Awards

[1]. **Best Student Paper Award:** H.-Y. Li, **J.-X. Xu**, X. Y. Zhang, and Y. Yang, "Design of low-loss single-pole single-throw and single-pole double-throw filtering switches using coaxial resonators," *2019 International Conference on Microwave and Millimeter Wave Technology*, Guangzhou, China, May 2019.